Karlsruher Institut für Technologie

ETP-KA/2020-2

Irradiation studies on n-in-p silicon strip sensors in the course of the CMS Phase-2 Outer Tracker Upgrade

Marius Metzler

Zur Erlangung des akademischen Grades eines
DOKTORS DER NATURWISSENSCHAFTEN
von der KIT-Fakultät für Physik des
Karlsruher Instituts für Technologie (KIT)

genehmigte

Dissertation

von

M.Sc.Marius Metzler
aus Karlsruhe

Tag der mündlichen Prüfung: 17.01.2020

Referent: Prof. Dr. Müller Institut für Experimentelle Teilchenphysik
Korreferent: Prof. Dr. Husemann Institut für Experimentelle Teilchenphysik

Contents

Part I.

Introduction and Basics

1 Introduction

Particle physics examines the nature of matter and its most basic components. The idea of matter being composed of elementary particles dates back to the 6th century BC [Rie96]. However, the starting signal for this new branch of physics was given at the end of the 19th century, when J. J. Thomson and other physicists discovered the electron. The groundbreaking work of theorists and experimentalists led to a better understanding of radiation, matter and its interactions in the following decades. The theory of the Standard Model (SM) emerged in the 1960s and was finalized in the mid-1970s. It introduces a zoo of elementary particles that can be grouped into three families: quarks, leptons and bosons. The SM has proven to be theoretically self-consistent and had huge success in providing precise experimental predictions. The experiments that were built to evaluate the physics postulated by the SM grew larger and more complex over the course of time, the reason being the nature of SM particles. Many SM particles are prohibited from existing isolated over a long period of time. Moreover, their sub-atomic size as well as the high energies which are required to isolate them, make it difficult the measure their properties. Ultimately, these issues demand a large number of measurements in order to present statistically relevant results. Therefore, one needs to build fast, high-precision detectors in addition to a source that can reliably produce high energy particles and interesting events in large numbers. A particle accelerator or particle collider is a machine with such characteristics. It uses experimentally available particles like leptons, protons or nuclei and accelerates them to typical energies of many GeV. The particle beams can be used to produce collisions at dedicated interaction points. The detectors are built around these interaction points. Depending on their purpose, they are using different materials and technologies to detect specific particles that are produced in the short time frame during the collision. Different detector types are required to measure the different particle properties. Some particles require specialized subdetectors to be detectable, while others are not directly detectable at all. A very common subdetector is the silicon tracker, which utilizes many layers of stacked silicon sensors in order to measure the trajectories of charged particles. The confirmation of the Higgs boson as the last remaining puzzle piece of the SM, took place in 2012 [Cha+12; Aad+12]. The measurement data were recorded by the CMS and ATLAS detectors at the Large Hadron Collider (LHC) in Geneva, Switzerland, which is until today the largest and highest-energy particle collider there is.

The studies presented in this thesis are mainly motivated by the upcoming High Luminosity LHC (HL-LHC) upgrade starting in 2024. The number of collisions per bunch crossing will be increased by an order of magnitude [CMS18]. The experiments are then able to generate the same amount of data within one year that has been collected since the start of operation in 2010. The run-time of the HL-LHC is expected to be ten years with a projected integrated luminosity of $3000\,\mathrm{fb}^{-1}$. An extension to $4000\,\mathrm{fb}^{-1}$ is already under consideration. It is crucial for the detectors to be able to run and detect efficiently over the course of the HL-LHC run-time. The detectors need to be adapted to the more challenging experimental environment as well. One of the severest issues that the engineers of the new detectors have to face is the increased radiation due to higher collision rates, which changes the electrical properties of the materials used for building these detectors. This thesis is centered around the characterization of different

sensor materials for the upgrade of the CMS Phase-2 Outer Tracker and their performance after irradiation.

The remaining chapters of Part I will introduce the LHC and the CMS experiment and present an overview of the basics of semiconductors and silicon sensors. Setups, measurements and measurement uncertainties will also be discussed. Relevant information about sensor materials and the sensor design will be shown at end of Part I. The first two chapters of Part II, Chapter 7 and Chapter 8, will summarizes the sensor R&D process of the last five years and will present the results of four qualification and irradiation campaigns, which were carried out with different sensor materials in order to find the most suitable candidate for the future silicon tracker of CMS. In Chapter 9 the obtained data is used to predict and evaluate the sensor performance over the course of the nominal HL-LHC run-time. The R&D process is usually focused on the center region of a sensor, which is sensitive for particle detection. However, Chapter 10 will investigate the properties of the sensor edge and how these properties change after irradiation. Understanding these properties is important for the evaluation of an unconventional biasing concept for silicon sensors, which is called frontside biasing. Part III will summarize the results and give a brief outlook.

2

The Large Hadron Collider and the CMS Experiment

2.1. The Large Hadron Collider

The Large Hadron Collider (LHC) is located at the European Organization for Nuclear Research (CERN) near Geneva, Switzerland. Built inside an underground tunnel, the accelerator ring has a circumference of 26.7 km. It is the world's largest and most powerful particle collider with a center-of-mass energy of $\sqrt{s} = 13\,\text{TeV}$. Two counter-rotating proton beams are forced into collision at four interaction points along the ring. Detectors are built around each of these interaction points in order to investigate and reconstruct the events which take place during the collision.

The protons pass through a number of pre-accelerators until they are injected into the LHC ring with an energy of 450 GeV where they are accelerated until they reach their peak energy of up to 7 TeV [EB08]. The CERN accelerator complex is illustrated in Figure 2.1. The beams are forced on their track by a sophisticated arrangement of superconducting magnets that create a maximum field of 8.3 T. The magnitude of these fields is the technological limitation for the LHC's center-of-mass energy. Generally, a circular hadron-hadron collider is significantly more powerful in achieving high $\sqrt{s}$ than a circular lepton-lepton collider of the same radius because of its comparably low synchrotron radiation, which has a $\frac{1}{m_0^4}$ mass dependency [Mes05]. Moreover, former colliders were usually designed to produce particle-antiparticle collisions. This is required for lower center-of-mass energies in order to produce new and interesting physics events due to particle-antiparticle annihilation. For example, a low energy proton-proton collision is dominated by the interaction between valence quarks and is, therefore, not suitable to investigate new physics. However, at high energies such as provided by the LHC, the interaction between sea quarks and gluons dominates. Therefore, high energies are required to reliably produce Higgs particles and to increase the new physics potential of the experiment. For example, the most probable way to produce a Higgs particle is if the two gluons combine to form a loop of virtual quarks [BD11]. Therefore, the LHC was designed as a circular proton-proton collider.

The proton beams are not continuous but consist of discrete packages known as bunches. A fully filled LHC stores 2808 bunches per beam. Each bunch consists of approximately $1.2 \cdot 10^{11}$ protons. They collide with a bunch crossing rate of 40 MHz. The magnitude of a collider's ability to produce collisions is given by its instantaneous luminosity $\mathcal{L}$:

$$\mathcal{L} = \frac{n \cdot N_1 \cdot N_2 \cdot f}{A}, \tag{2.1}$$

where n is the number of bunches per beam, N_1 and N_2 denote the number of protons per bunch, f the revolution frequency of a single bunch and A the cross section of the two particle beams [HM03]. Equation (2.1) shows that focusing the beam (reducing A) increases $\mathcal{L}$. This

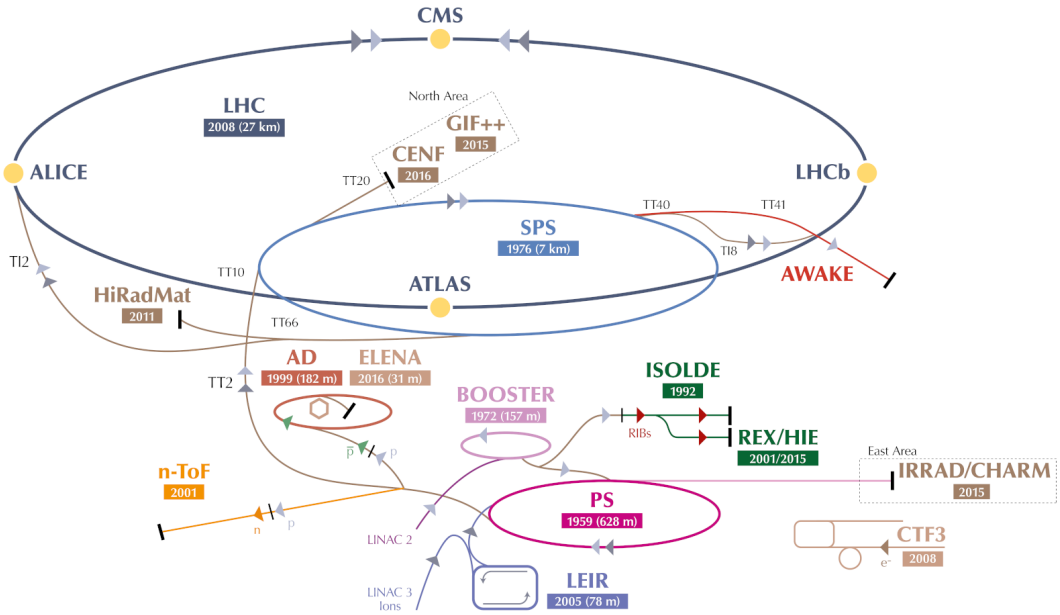

Figure 2.1.: The CERN accelerator complex [Mob16].

is how the luminosity was gradually increased since the first collision in 2008 (N_1 and N_2 were also increased in the beginning). Since May 2018 the LHC runs at $\mathcal{L} = 2 \cdot 10^{34}\,\mathrm{cm}^{-2}\mathrm{s}^{-1}$ which is double its design luminosity [CER18a]. Integrating $\mathcal{L}_{\mathrm{int}}$ over operation time yields the integrated luminosity $\mathcal{L}_{\mathrm{int}}$:

$$\mathcal{L}_{\mathrm{int}} = \int \mathcal{L} dt. \tag{2.2}$$

The integrated luminosity is a measure of the collected data size and is, therefore, an important value to characterize the performance of the LHC. It is measured in units of inverse femtobarn (fb^{-1}) [HM03].

2.2. The Compact Muon Solenoid Experiment

One of the two large general purpose detectors at LHC is called Compact Muon Solenoid (CMS). It is designed to cover a wide range of physics objectives. Figure 2.2 illustrates the CMS setup. The detector stands 15 m tall with a length of 27 m and a weight of 14 000 t. CMS is equipped with the world's largest superconducting magnet which provides a magnetic field of 3.8 T and, therefore, large bending power for tracking measurements. The four-layer niobium-titanium coil of the solenoid conducts a total current of 20 kA and stores a total energy of up to 2.6 GJ [The08]. As implied by the name, CMS provides a muon detection system which is embedded in the iron return yoke of the magnet. The iron yoke acts as a final absorber material to allow for a reliable detection of muons [CMS11]. The magnet circumferences the hadronic calorimeter which is responsible for measuring the energy of hadrons such as neutrons, protons, pions and kaons [Man+12]. Hadrons are absorbed by brass plates, which generates showers of secondary particles. The scintillation light of those particles is detected by an assembly of photodiodes and scintillators. Similarly, the crystal electromagnetic calorimeter,

being the next inner subdetector, measures the energy of electrons, positrons and photons. The high-density lead tungstate crystals used for the electronic calorimeter are highly transparent and scintillate when they absorbs said particles [CMS97].

The silicon tracker is the innermost subdetector of CMS. Its data is used to reconstruct the trajectories of charged particles right after the collision. Cylindrical layers of silicon sensors, known as barrel, are stacked around the beam pipe to cover particles with low pseudorapidity. The pseudorapidity η is a commonly used spatial coordinate in particle physics. Low η values correspond to large polar angles with respect to the vertical axis along the beam pipe ($\eta = 0$ corresponds to $\theta = 90°$). The coverage up to $|\eta| \approx 2.4$ ($\approx 10°$) is realized due to endcaps, disk-like sensor layers at both barrel heads. The magnetic field created by the solenoid forces charged particles on a bent trajectory. The radius R of such a track in combination with the magnitude of the magnetic field B is used to calculate the transverse momentum p_T of the particle:

$$p_T \left[\frac{\text{GeV}}{\text{c}}\right] = 0.3 \cdot B \cdot R\,[\text{Tm}]. \tag{2.3}$$

Hence, the curvature of particles with high transverse momentum is small compared to particles with lower transverse momentum, which limits the momentum resolution at the upper end of the momentum spectrum.

The reconstructed tracks are also used to assign the particles to their point of origin, the vertex. One can expect over 1000 tracks and 20 to 30 primary vertices per bunch crossing at $\mathcal{L} = 1 \cdot 10^{34}\,\text{cm}^{-2}\text{s}^{-1}$. The number of primary collisions per bunch crossing is often referred to as pile-up. The sensors closest to the collision point need to provide a sufficient granularity in order to cope with pile-up . The sensitive volume of these sensors is subdivided into rectangular pixel cells. The Inner Tracker (pixel detector) of CMS is currently separating vertices with an accuracy of 40 µm to 50 µm. Such a resolution is necessary in order to resolve secondary vertices [CMS12]. The CMS Outer Tracker, beginning at a radial distance of $r > 200\,\text{mm}$ with respect to the beam pipe, consists of an arrangement of single and double-sided strip modules. The decreasing track density towards the outer layers of the tracker allow for a reduction of the sensor granularity without giving up too much on track separation performance. Using strip sensors for the outer layers of a tracker instead of pixel sensors significantly lowers the overall costs. Reducing the number of readout channels in the Outer Tracker also decreases the amount of generated data. The total extent of the current tracker is about $z = \pm 2500\,\text{mm}$ and $r = 1100\,\text{mm}$. The cross-section of one quarter of the current tracker is shown in Figure 2.3.

2.3. The CMS Trigger System

When combining the information of all subdetectors, the data per event can amount up to 1 MB [The08]. At $\mathcal{L} = 1 \cdot 10^{34}\,\text{cm}^{-2}\text{s}^{-1}$ one can expect a total amount of 40 TB per second of generated data. Processing or storing such an amount of data at a rate of 40 MHz would not be feasible. Data filtering mechanisms had to be implemented in order to reduce the amount of data that is effectively read out and passed on to the CMS computer farm.

The first stage of data selection is referred to as the Level-1 trigger (L1). This low-level hardware filtering mechanism uses information from calorimeters and muon system to select events with predefined signatures within a time frame of 3.4 µs. The L1 trigger decision determines if information is rejected or stored in the readout buffer before it is passed on to

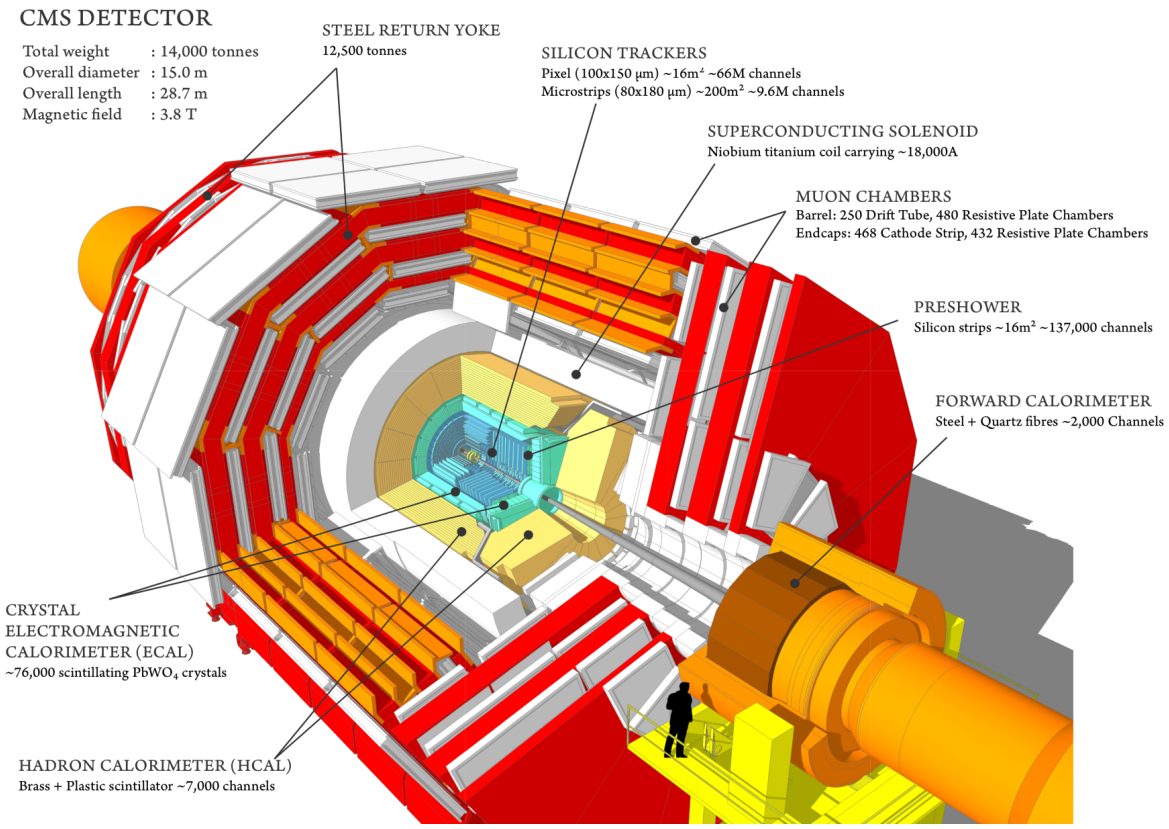

Figure 2.2.: Illustration of the Compact Muon Solenoid (CMS) detector as at November 2011 [Tay11].

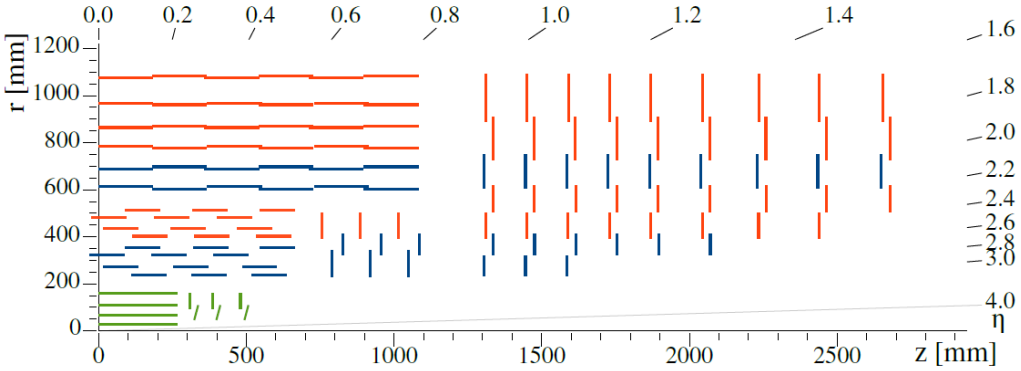

Figure 2.3.: Illustration of the current CMS Tracker (Phase-1) [CMS18]. The silicon pixel detector is shown in green. The single and double-sided silicon strip modules of the Outer Tracker are depicted in red and blue, respectively.

the second stage of the trigger system. The rejection of insignificant data already reduces the overall readout frequency from 40 MHz (bunch-crossing rate of the LHC) to 100 kHz [CMS17a]. The second stage of the data filtering is known as High Level Trigger (HLT). It runs on a computer cluster and offers a great amount of flexibility regarding the selection criteria. The HLT uses information of all subdetectors to ultimately reduce the average data rate for offline event storage to 400 Hz [CMS17a].

3

The Phase-2 Upgrade of CMS Outer Tracker

3.1. The High-Luminosity LHC

The LHC is currently in Long Shutdown 2 (LS2). The following operation period is called Run 3 and is scheduled for 2021 until 2023 where LHC will reach an instantaneous luminosity of $\mathcal{L} = 2.5 \cdot 10^{34}\,\mathrm{cm}^{-2}\mathrm{s}^{-1}$ and a center-of-mass energy of $\sqrt{s} = 14\,\mathrm{TeV}$. The integrated luminosity since beginning of Run 1 will then amount to roughly $300\,\mathrm{fb}^{-1}$. However, the search for new physics, which is often a search for high-mass particles or very rare processes, requires more data. The LHC and some of its experiments will therefore undergo a major upgrade during the LS3 scheduled from 2024 to 2026. The High-Luminosity LHC (HL-LHC) will then reach a peak luminosity of $\mathcal{L} = 5 \cdot 10^{34}\,\mathrm{cm}^{-2}\mathrm{s}^{-1}$ resulting in $3000\,\mathrm{fb}^{-1}$ after ten years. The ultimate performance scenario of the HL-LHC even assumes a peak luminosity of $\mathcal{L} = 7.5 \cdot 10^{34}\,\mathrm{cm}^{-2}\mathrm{s}^{-1}$ which would result in an integrated luminosity of $4000\,\mathrm{fb}^{-1}$ [CMS17b]. The project schedule is illustrated in Figure 3.1.

3.2. The Phase-2 Outer Tracker Upgrade

The degradation of the CMS Tracker performance due to radiation damage after Run 3 will render a continuous operation for another ten years impossible. Besides, the technology of the current tracker cannot cope with the demands set by the design luminosity of the HL-LHC. Therefore, the new tracker design underwent numerous adjustments compared to the current one. The Phase-2 Tracker will be installed during LS3, completely replacing the current tracker. The Phase-2 Outer Tracker is composed of six barrel layers (TB2S and TBPS) with a length of roughly 2400 mm and a radius of about 1120 mm. Including the five endcap double discs (TEDD) on each side, the total tracker length amounts to roughly 5400 mm. An illustration of one quarter of the Phase-2 Outer Tracker can be found in Figure 3.2. In combination with the Inner Tracker, the pseudorapidity coverage is going to increase from currently $|\eta| = 2.4$ to $|\eta| = 4$. More details about the Inner Tracker upgrade can be found in Ref. [CMS18] and are not further discussed here. The main features of the Phase-2 Outer Tracker design can be summarized as follows:

- **Increased Granularity:** The granularity of the tracker is increased in order to cope with the expected pile-up of 140 to 200 per bunch-crossing and to ensure a low occupancy of the readout channels. This is realized, firstly, by increasing the channel density of the sensors. Secondly, the Outer Tracker will be separated into two regions: 2S (outer layers) and PS region (inner layers). Strip sensors are solely used for the 2S region while a mix of macro-pixel and strip sensors is used for the PS region. The implementation of macro-pixel sensors results in a significantly higher channel density among the inner layers of the Outer Tracker [CMS18].

- **Increased radiation tolerance:** A replacement of the Phase-2 Outer Tracker during the nominal or even extended HL-LHC run-time is not envisaged. The modules need to be

Figure 3.1.: Current schedule of the LHC upgrade project [CMS17b].

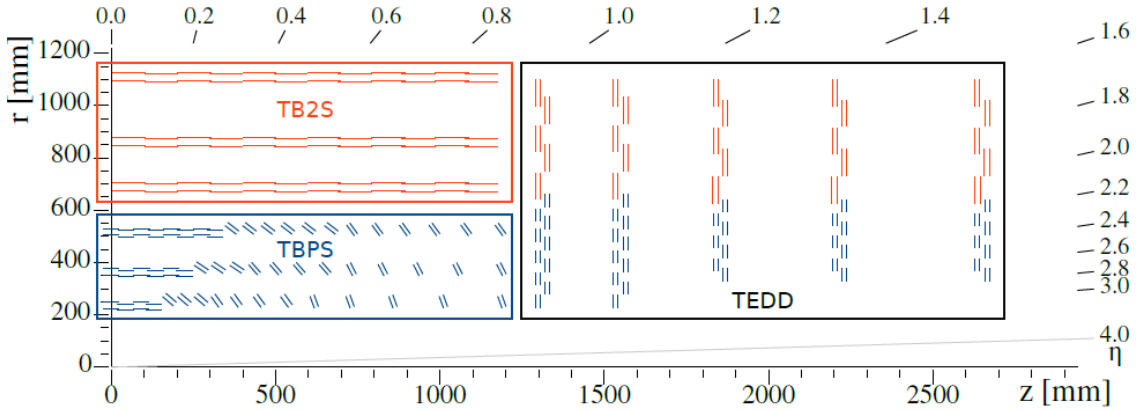

Figure 3.2.: Illustration of one quarter of the Phase-2 Outer Tracker. The Inner Tracker is not incorporated in this illustration.

operable and able to detect particles efficiently at every stage of the operation. Electronics and support material need to withstand the extreme radiation conditions as well. The accumulated radiation damage at $3000\,\mathrm{fb}^{-1}$ was estimated via the FLUKA simulation tool [Fer+05]. A margin of +50% ($\approx 4500\,\mathrm{fb}^{-1}$) is targeted in order to account for FLUKA uncertainties as well as a potential $4000\,\mathrm{fb}^{-1}$ extension [CMS18]. The radiation environment of the Phase-2 Outer Tracker is described in more detail Section 3.4. The development and characterization of radiation hard sensor materials is the main focus of this thesis and is presented in Part II.

- **L1 Trigger contribution and binary readout:** The algorithm of the current L1 Trigger becomes inefficient under high pile-up conditions and increasing event rates. The algorithm can be improved by including track information in the L1 Trigger decision, which can reduce the trigger rates below 750 kHz without increasing the p_T threshold. However, the additional information would ultimately increases the trigger latency. In order to cope with this issue, the Phase-2 Outer Tracker modules are able to preselect high p_T particles, which are particularly interesting for HEP analysis, at a rate of 40 MHz. Moreover, the Phase-2 Upgrade introduces binary readout chips in contrast to the analog readout approach of the current tracker as a means to reduce the generated data even

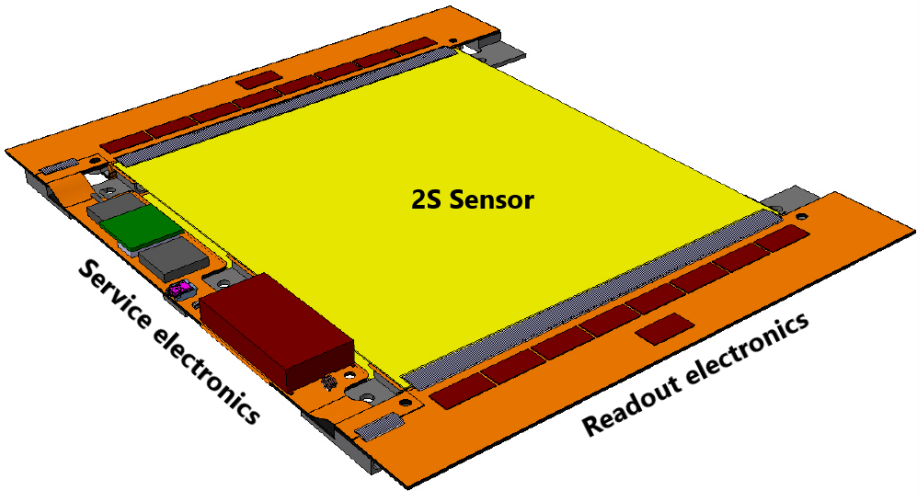

Figure 3.3.: Illustration of the 2S module [CMS18].

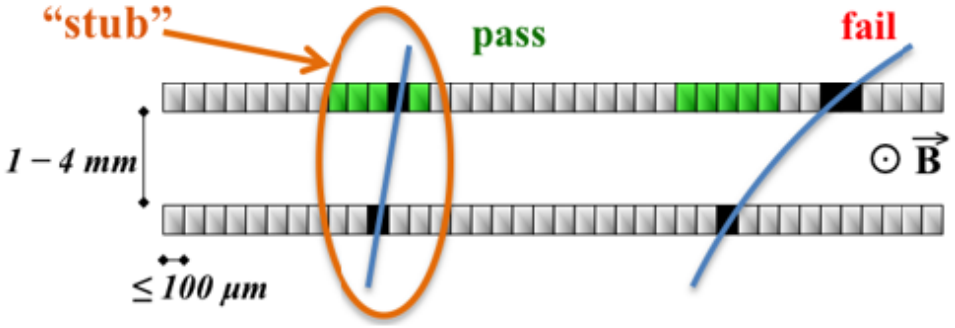

Figure 3.4.: Illustration of the stub-finding concept of p_T modules [CMS18].

further. The binary hit information of the preselected high p_T particles is fed directly into the Track Finder, an FPGA farm which reconstructs the particle tracks and eventually identifies and filters high p_T particles for the L1 Trigger [CMS18]. The p_T discrimination that takes place on the module level is explained in more detail in Section 3.3.

3.3. The Phase-2 Outer Tracker Modules

The Phase-2 Outer Tracker is composed of thousands of stand-alone units. These units are called modules and incorporate sensors, readout and service electronics as well as support structures. A 2S module uses two strip senors (2S sensors) with an area of about $10 \cdot 10\,\mathrm{cm}^2$. The 2S sensor is designed with a mid segmentation along its strips. This results in two rows with 1016 strips with a length of 5 cm and a pitch of 90 µm (distance between two neighboring strips). A technical drawing of a 2S module is presented in Figure 3.3. The PS module uses a strip (PS-s) and a macro-pixel sensor (PS-p) with an area of $5 \cdot 10\,\mathrm{cm}^2$ each. The PS-s, also designed with a mid segmentation, provides two rows of 960 strips with a length of about 2.4 cm and a pitch of 100 µm. The PS-p provides 30208 long macro-pixels with a length of 1467 µm and a pitch of 100 µm. Wire-bonds are used to connect the strips to the channels of the readout

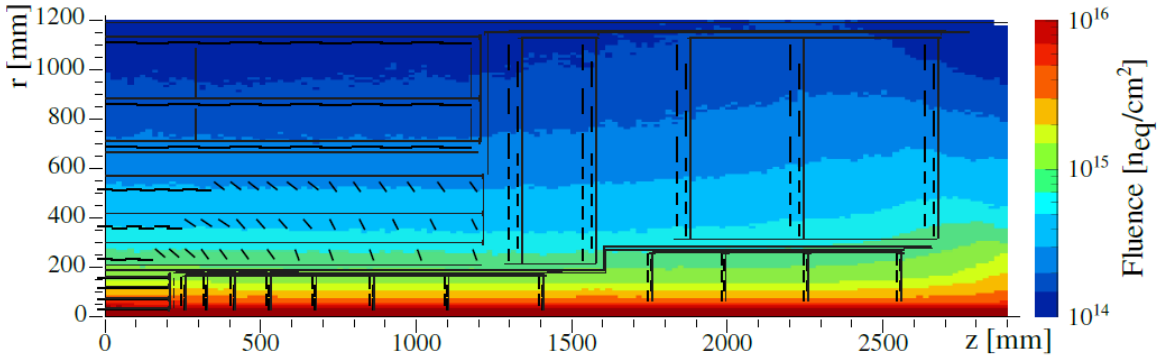

Figure 3.5.: Fluence spectrum at 3000 fb^{-1} expected for the CMS Phase-2 Tracker according to FLUKA simulations [CMS18].

electronics. The common technology for connecting pixelated sensors and readout electronics is called bump bonding. Tiny solder balls have to be put on every cell with relatively high precision. The readout chip is then flipped and placed onto the sensor. The respective readout chips are called CBC [Uch+18] for the 2S, SSA [Car+16] for the PS-s and MPA [Cer+14] for the PS-p sensor. The sensors are positioned on top of each other in the module. The front-side of strip sensors always faces outwards. The front-side of the PS-p faces inwards. Three different spacings of 1.6 mm, 2.6 mm and 4.0 mm are foreseen for PS modules, whereas 2S modules come with a 1.8 mm and 4.0 mm spacing. The sensor spacing decreases with the distance from the interaction point in order to compensate for increasing incident angles (angle between the particle track and the surface normal of the sensor plane). The sensors are mechanically aligned with a precision of at least 400 µrad (tilt angle between cut edges of top and bottom sensor) during module assembly, which corresponds to a maximum misalignment of about half the sensor pitch.

As mentioned earlier, the front-end readout electronics of the Phase-2 modules can discriminate between traversing particles with high and low transverse momentum and are therefore called p_T modules [Fou+05]. The p_T discrimination algorithm compares the hit position of a traversing particle in top and bottom sensor. If the second hit is within a certain acceptance window with respect to the first one, the particle track is flagged as a *stub*. The algorithm is therefore more commonly referred to as stub-finding algorithm. Equation (2.3) shows that the curvature of low p_T particles in the presence of a magnetic field is described by a smaller radius compared to high momentum particles. Thus, the concept allows for an easy adjustment of the accepted minimum particle momentum by tuning the width of the acceptance window. The stub-finding concept is illustrated in Figure 3.4. The stub information is passed on to the Track Finder FPGA farm [Cie+17], that reconstructs the full particle tracks and eventually feeds its output into the L1 Trigger.

3.4. The Phase-2 Outer Tracker Radiation Environment

All parts of the detector are exposed to a vast particle flux. The particles will generate microscopic damage in the detector material, which changes the electrical properties, e.g., modules become less efficient in detecting particles. The radiation damage in the detector material can be quantified by the accumulated 1 MeV neutron equivalent fluence Φ_{eq}, which is explained in Section 4.5.3. The result of a FLUKA simulation for one quarter of the Phase-2 Tracker at 3000 fb^{-1} is shown in Figure 3.5. The highest nominal Outer Tracker fluence for the 2S region amounts to $3 \cdot 10^{14}\, n_{eq} cm^{-2}$. The highest nominal PS fluence is estimated to be

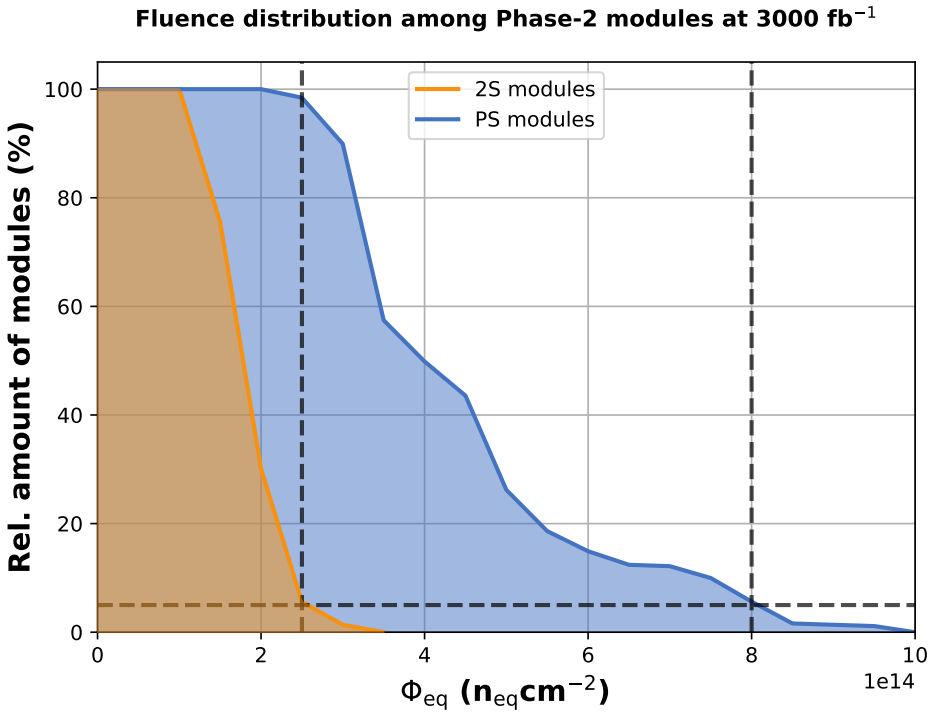

Figure 3.6.: Distribution of Phase-2 Outer Tracker modules with respect to their expected maximum fluence at 3000 fb^{-1} according to FLUKA simulations. The horizontal line highlights a 5% margin. The vertical lines indicate at which fluence the relative amount of modules is around 5%.

$9.4 \cdot 10^{14}$ $n_{eq}cm^{-2}$. Figure 3.6 illustrates the fluence distribution among Outer Tracker modules at 3000 fb^{-1} in more detail. The horizontal line highlights a 5% margin. The vertical lines indicate at which fluence the relative amount of modules is around 5%. The data plot shows that only 5% of 2S modules are expected to accumulate more than $2.5 \cdot 10^{14}$ $n_{eq}cm^{-2}$. For the PS modules the relative amount of modules falls below the 5% margin at $8 \cdot 10^{14}$ $n_{eq}cm^{-2}$. Nevertheless, the expected maximum fluences at 3000 fb^{-1} are considered the reference fluences for the R&D process of components for the Phase-2 Outer Tracker.

Another important aspect of the radiation environment is the varying particle composition with respect to the position in the tracker. Results presented in this thesis show that the radiation damage generated by charged and neutral particles can have different impact on certain sensor parameters. Therefore, it is important for the R&D process to know how the particle composition looks like. Figure 3.7 depicts the result of FLUKA simulations with respect to this subject. The plot illustrates the expected ratio of neutral particles in the Outer Tracker for a $z = 0$ (barrel) and $z = 250$ (endcap) as a function of the radial distance from beam pipe. The PS region is dominated by charged particles ($\sim 60\%$), which results from the fact that the vast majority of collision products are pions. The radiation environment of the 2S region is dominated by neutrons ($\sim 80\%$), which is a consequence of backscattering from the calorimeters [CMS18].

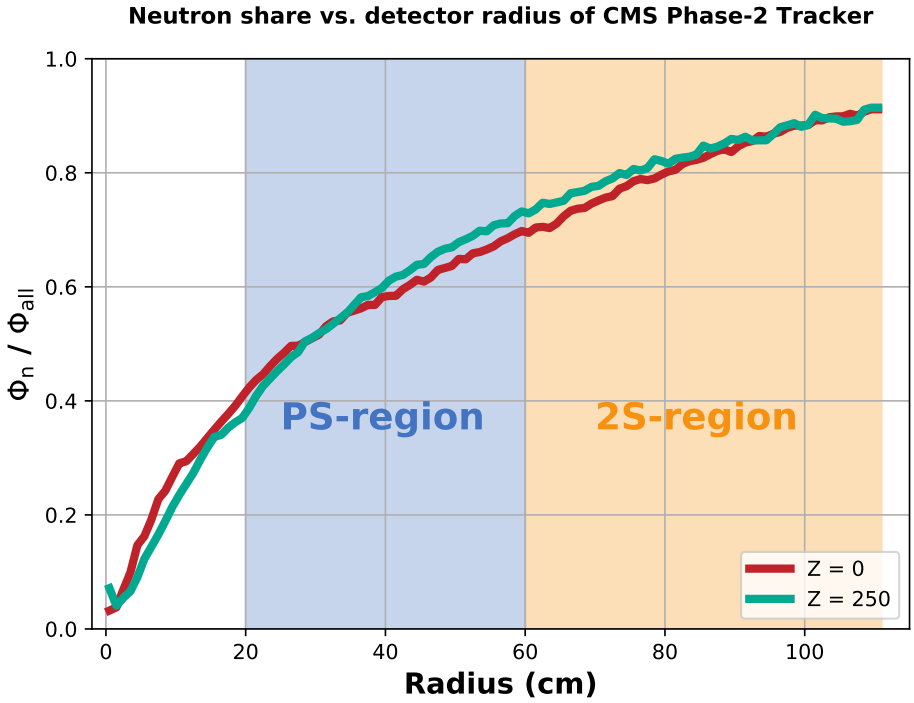

Figure 3.7.: Composition of neutral and charged particles in Phase-2 Outer Tracker with respect to the radial distance from beam pipe. The composition is given by the fraction of the expected 1 MeV neutron equivalent fluence of neutrons Φ_n in silicon normalized by the fluence of all particles Φ_{all}. The data is originally shown in Ref. [CMS15].

4

Principles of Silicon Strip Sensors

4.1. The Band Model

Electron transport in solids can be approximated on the basis of the quantum mechanical problem of a particle (electron) in an one-dimensional periodically-repeating environment (periodic crystal). The energy eigenstates can be written as Bloch waves. The definition of the Bloch waves for the general case is as follows [AM11]:

$$\Phi_{n\boldsymbol{k}}(\boldsymbol{r}) = \exp(i\boldsymbol{k}\boldsymbol{r})u_{n\boldsymbol{k}}(\boldsymbol{r}) \ , \tag{4.1}$$

where $\boldsymbol{r}$ is position, $u_{n\boldsymbol{k}}$ is a periodic function with the same periodicity as the environment and $\boldsymbol{k}$ the wave vector. For the one-dimensional case one can write $\boldsymbol{r} = x$ and $\boldsymbol{k} = k$. Regarding the periodic nature of the environment, it is sufficient to reduce the problem to the first Brillouin zone, which is the uniquely defined primitive cell in the reciprocal lattice where each $\boldsymbol{k}$ is unique. For each value of $\boldsymbol{k}$ there are multiple solutions of the Schrödinger equation, which are indexed by n. The index n is called band index. The dispersion relation or band structure for the given problem (also known as nearly free electron model) is depicted in Figure 4.1. One can see how the free electron parabola is distorted near the edge of the Brillouin zone by the weak periodic potential (red lines). Because of the imposed Bragg condition at the edge, the Schrödinger equation yields exactly two solutions for $k = \pm\frac{\pi}{a}$, which is reflected in the bend of the parabolas at the edge of the Brillouin zone. In conclusion, the band structure represents the allowed eigenenergies of an electron in the periodic potential of lattice atoms. A band gap refers to an uncovered range of energy in which no allowed electron state exists.

Electrons are fermions and therefore follow the Pauli-Dirac statistic as was stated in the first paragraph. One can construct the ground state of the system by starting to fill the states in the lowest band, the quantum numbers of an electron being $\boldsymbol{k}$ and spin $S = \frac{1}{2}, -\frac{1}{2}$. The last occupied state defines the Fermi energy E_F. The highest partly or completely filled band is called valence band. If the valence band is completely filled, then the Fermi level lies between the valence band and the next higher band, which is called conduction band. The energy that is required for an electron to occupy another unoccupied state within the same band is almost negligible. However, additional energy is required in order to occupy a state of the next higher band. The band gap energy E_G is defined as the difference between the highest occupied and lowest unoccupied state. The term indirect band gap is used if the maximum of the valence band and the minimum of the conduction band have different wave vectors (different momenta), which is the case for silicon. Hence, the energy that is required to occupy a state in the conduction band is $E_\mathrm{G} + E_\mathrm{P}$, where E_P is the minimum energy that is required to create a phonon, which transfers momentum to the crystal.

The mechanism of electrical conduction depends on the number of free charge carriers and their mobility. The smaller the band gap energy, the easier it is for electrons to occupy free states and generate a current in the presence of an electric field E. Therefore, the band

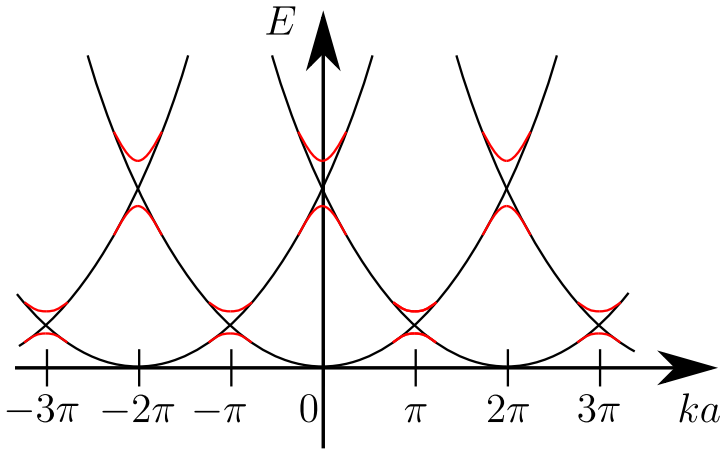

Figure 4.1.: Band structure of nearly free electron model in the repeated Brillouin zone scheme [Akh+19].

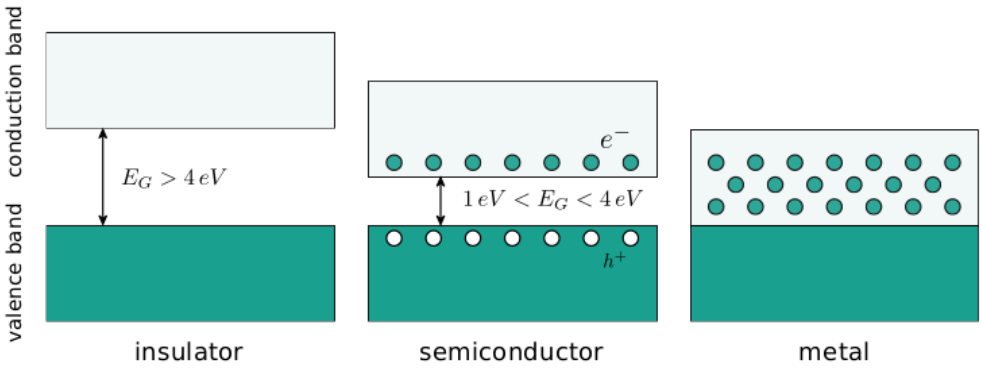

Figure 4.2.: Classification of solids according to their band gap energy E_G [Sch15].

gap energy is a valid tool for characterizing solids and their electrical properties as shown in Figure 4.2. A material is called semiconductor if $1\,\mathrm{eV} < E_\mathrm{G} < 4\,\mathrm{eV}$. The term insulator is used for materials with larger band gaps. Metals have no band gap at all and are, therefore, nearly ideal conductors [AM11].

4.2. Effects of Doping

It is a common procedure to adapt the electrical properties of a semiconductor by introducing dopants into their crystal lattice. In the case of silicon, which is an element of the fourth main group of the periodic table and has four lattice electrons, one uses dopants from the third and fifth main group. Typical dopants from the third main group are aluminum or boron. Introducing such a dopant into the silicon lattice produces positively charged holes since it is equipped with only three valence electrons. These dopants are called acceptors and the material is labeled p-doped. Acceptors create additional states within the band gap close to the valence band. On the other hand, a dopant from the fifth main group like phosphorus provides an additional weakly bound electron. It is called donor and the material is labeled n-doped. Introducing donors into the lattice creates states near the conduction band. Macroscopically, the material is still electrically neutral, since the dopants not only have a different number of valence electrons but also a similarly different number of protons in the nucleus. The concept

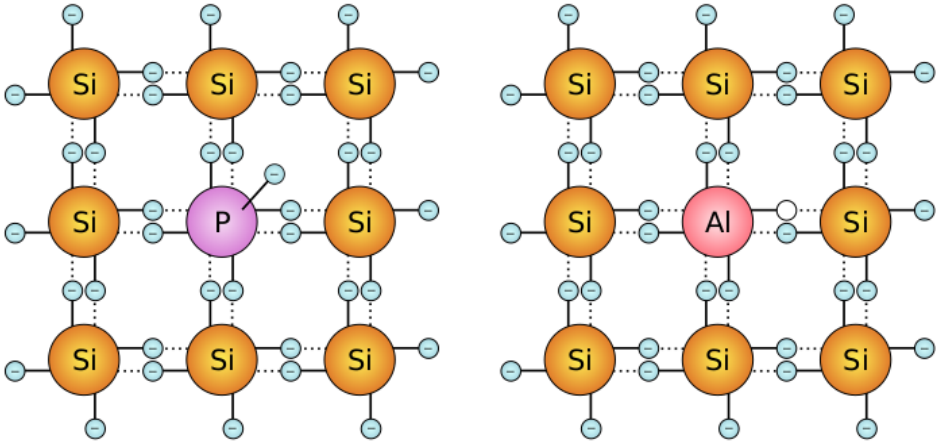

Figure 4.3.: Illustration of a n-doped and p-doped silicon lattice. On the left: n-doped silicon lattice with phosphorus [Hen15a]. On the right: p-doped silicon lattice with aluminum [Hen15b].

is outlined in Figure 4.3. The grade of doping is characterized by the doping concentration N. Typical values are between $10^{12}\,\mathrm{cm}^{-3}$ and $10^{18}\,\mathrm{cm}^{-3}$.

4.3. The pn-Junction

A pn-junction is created by connecting a n-doped and p-doped semiconductor layer. Under neutral conditions the different Fermi levels of these layers force surplus carriers to diffuse from one interface region into the other, ionizing donor and acceptor atoms close to the junction. The emerging space charge region is depleted of mobile charge carriers. Eventually, the electrical force cancels out this diffusion process. This mechanism is depicted in Figure 4.4. If the layers are connected to an electrical circuit one can use its polarity to manipulate the width of the space charge region. A positive terminal connected to the p-doped region and negative terminal to the n-doped region mitigates the electric field at the junction and reduces the width of the space charge region. Charge carriers can flow unhindered to their respective electrode as soon as the applied voltage is high enough to completely remove the space charge. This is known as forward biasing. Connecting the terminals the other way around is called reverse biasing. The electrons of the neutral n-doped region are collected by the positive electrode and the holes of the neutral p-doped region are collected by the negative electrode. Free charged carriers are removed and the width of the space charge region increases. The width w is therefore proportional to the bias voltage V_{bias}, see e.g. Ref. [Har17]:

$$w = \sqrt{2\epsilon\mu\rho V_{\mathrm{bias}}}\ , \tag{4.2}$$

where ϵ is the permittivity, ρ the resistivity and μ the carrier mobility. Strictly speaking, the bias voltage is the difference between the natural built-in voltage V_{bi} at the junction and the external voltage V_{ext}:

$$|V_{\mathrm{ext}}| - |V_{\mathrm{bi}}| = |V_{\mathrm{bias}}| \approx |V_{\mathrm{ext}}|. \tag{4.3}$$

Since V_{bi} ($\sim 0.7\,\mathrm{V}$ in silicon at room temperature) is usually considerably smaller compared to V_{ext}, the applied external voltage is always referred to as the bias voltage in the scope of this thesis.

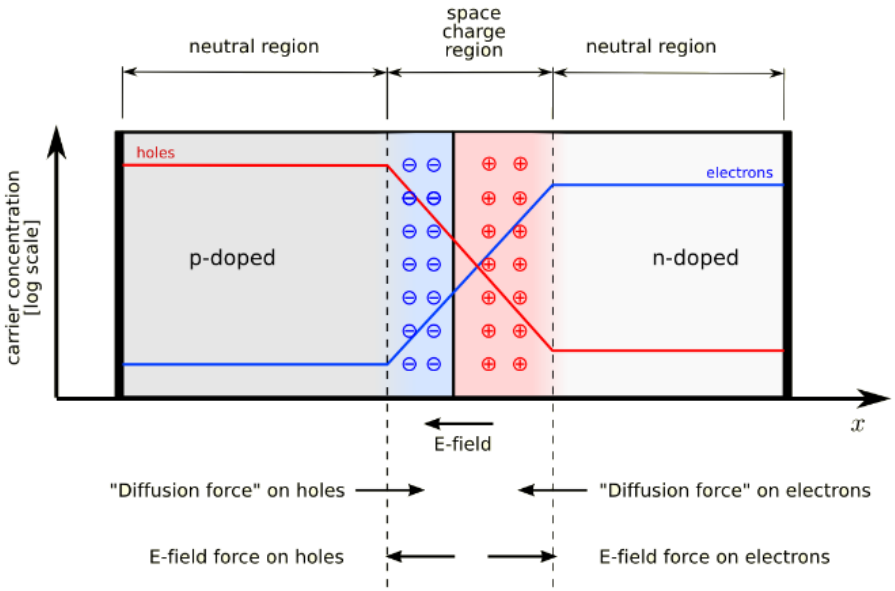

Figure 4.4.: Illustration of a pn-junction under electrically neutral conditions [Adu07].

The simplest pn-device is a diode. The p-doped and n-doped layers of a diode are sandwiched by two parallel metal electrodes. The configuration is comparable to a plate capacitor. Thus, the capacitance of a diode is given by the field constants ϵ, the area of the diode A and the width of the depletion zone w:

$$C = \epsilon \frac{A}{w}. \tag{4.4}$$

The bias voltage at which the diode/sensor is fully depleted is called full depletion voltage V_{fd}. The width w is then equal to the thickness d of the device, which results in a constant capacitance. The full depletion voltage of a diode can be easily deduced from Equation (4.2). The field configuration at the front-side of a silicon sensor is more sophisticated compared to a diode, which is a consequence of the complex design shown in Section 4.8. Equation (4.4) still suffices qualitatively for sensors ($C \sim \frac{A}{w}$). An approach to calculate the full depletion voltage by using the semi-analytical solution of Poisson's equation for strip sensors is presented in Ref. [Bar+94]:

$$\frac{V_{\text{dep, diode}}}{V_{\text{dep, sensor}}} = \left(1 + \frac{2p}{d} f\left(\frac{s}{p}\right)\right)^{-1}, \tag{4.5}$$

where p is the pitch (distance between the center of two neighboring strips) and s is the width of a strip implant. The universal function $f(x)$ is given by:

$$f(x) = -0.00111x^{-2} + 0.0586x^{-1} + 0.24 + 0.0651x + 0.3555x^2 \tag{4.6}$$

By inserting the typical values for strip sensors presented in this thesis ($d = 290\,\mu\text{m}$, $p = 90\,\mu\text{m}$, $s = 22\,\mu\text{m}$), one finds the full depletion voltage of a diode to be about 24% smaller then of a strip sensor.

4.4. Resistivity

This section is an adjusted version of Section 3 in Ref. [Bas+18] (myself being the main author) which summarizes textbook knowledge relevant for Chapter 10. The inverse of the conductivity σ is called resistivity ρ. It significantly impacts the electrical properties of a semiconductor device and must, therefore, be chosen carefully for any given application. Equation (4.12) shows that V_{fd} is inversely proportional to the resistivity of the material. Silicon sensors are usually operated at voltages above V_{fd}, which is explained in Section 4.7. The usage of high resistivity materials is, therefore, preferred in HEP experiments since it allows for low operation voltages. Typical resistivities are between $2\,\mathrm{k\Omega\,cm}$ and $10\,\mathrm{k\Omega\,cm}$. The resistivity can be expressed as a function of the electron charge q, the carrier densities p and n as well as the carrier mobilities μ_{h} and μ_{e}. This is shown e.g. in Ref. [Sze81]:

$$\rho = \frac{1}{\sigma} = \frac{1}{q(n\mu_{\mathrm{e}} + p\mu_{\mathrm{h}})} \ . \tag{4.7}$$

The intrinsic carrier density n_{i} can be written as a function of the effectively available number of states in the conduction and valence band, N_{c} and N_{v}, in addition to the band gap energy E_{G} [Sze81]:

$$n_{\mathrm{i}} = \sqrt{N_{\mathrm{v}} N_{\mathrm{c}}} \exp\Big(- \frac{E_{\mathrm{G}}}{2kT} \Big) \ . \tag{4.8}$$

From this equation one can derive the mass action law. It states that the product of p and n is constant:

$$np = n_{\mathrm{i}}^2 \ . \tag{4.9}$$

The temperature dependence of n_{i} is determined by N_{v} and N_{c}. Higher states in the conduction and deeper states in the valence band become more accessible as the thermal energy increases. One finds that n_{i} is proportional to $T^{\frac{3}{2}}$ with c being a combination of constants:

$$n_{\mathrm{i}} = 2(cT)^{\frac{3}{2}} \exp\Big(- \frac{E_{\mathrm{G}}}{2kT} \Big) \ . \tag{4.10}$$

As shown by Equation (4.7), ρ is a function of carrier mobility and density, which are both dependent on temperature. Dopants are completely ionized in a temperature range between roughly $-170\,^{\circ}\mathrm{C}$ and $130\,^{\circ}\mathrm{C}$ ($100\,\mathrm{K}$ and $300\,\mathrm{K}$). The carrier density is determined by the doping concentration in this temperature range and is, therefore, constant. Thus, Equation (4.7) can be written as a function of the effective doping concentration N_{eff}, which is defined by the difference between acceptor and donor concentration if one charge carrier type dominates [Har17]:

$$\rho = \frac{1}{q\mu|N_{\mathrm{eff}}|} \ . \tag{4.11}$$

With this knowledge one can derive a relation between ρ, full depletion voltage V_{fd}, the thickness d of a device and the electric field constants:

$$\rho = \frac{d^2}{2\mu\epsilon V_{\mathrm{fd}}} \ . \tag{4.12}$$

Because of the constant carrier density, the temperature range between roughly −170 °C and 130 °C is referred to as the extrinsic or saturation region [Zeg07; Gru10; Lut07]. The measurements presented in this thesis were all performed in a temperature range between −20 °C and 20 °C. Following Equation (4.7), the resistivity is, therefore, determined by the carrier mobility. The total carrier mobility μ_t is a superposition of mainly two processes. As stated by Matthiessen's law, these two contributions are related to phonons and impurities:

$$\frac{1}{\mu_\mathrm{t}} = \frac{1}{\mu_\mathrm{imp}} + \frac{1}{\mu_\mathrm{pho}} \ . \tag{4.13}$$

At low temperatures the carrier mobility is driven by increasing ionization and impurity scattering, which is represented by a dominating μ_imp-term. Phonon scattering begins to dominate for higher temperatures, which leads to an inverted temperature dependency [Sze81; Gru10]:

$$\mu_\mathrm{imp} \sim T^{\frac{3}{2}} \ , \tag{4.14}$$

$$\mu_\mathrm{pho} \sim T^{-\frac{3}{2}} \ . \tag{4.15}$$

The exponents of T are derived by theoretical evaluations. An experimental evaluation of the carrier mobilities of extrinsic silicon is presented in Ref. [Jac+77] for a broad temperature spectrum and different impurity concentrations. Near room temperature the mobility is found to be proportional to $T^{-2.42}$ for a doping concentration $N \leq 10^{12}\,\mathrm{cm}^{-3}$, which corresponds to the expected N of the samples used in the scope of this thesis. The exponent $a = -2.42$ differs from the theoretically expected value of $a = -1.5$ in Equation (4.15) because of additional scattering mechanisms [Sze81]. As stated by Equation (4.7), resistivity is inversely proportional to carrier mobility, which yields the expected temperature dependency of ρ for silicon devices:

$$\rho \sim T^{2.42} \ . \tag{4.16}$$

4.5. Interaction between Particles and Matter

4.5.1. Heavy Charged Particles

The mean rate of energy loss of a heavy charged particle (e.g. high-energy muons) in matter is described by the Bethe formula. It postulates an interaction only between particle and shell electrons (ionization). The inelastic scattering processes result in a deposition of energy. The Bethe formula includes the Avogadro constant N_A, the classical electron radius r_e, the electron mass m_e, the speed of light c, the proton number Z, the mass number A, the velocity-speed-of-light-ratio β, the Lorentz factor γ, the density effect correction δ, the mean excitation energy I and the maximum kinetic energy which can be transferred to the electron in a single collision T_max:

$$-\left\langle \frac{dE}{dx} \right\rangle = 4\pi N_\mathrm{A} r_\mathrm{e}^2 m_\mathrm{e} c^2 z^2 \frac{Z}{A\beta} \left[\frac{1}{2} \ln \left(\frac{2 m_\mathrm{e} c^2 \beta^2 \gamma^2 T_\mathrm{max}}{I^2} \right) - \beta^2 - \frac{\partial \delta(\gamma)}{2} \right] \ . \tag{4.17}$$

This is also known as the *mass stopping power*. The mass stopping power over $\beta\gamma = p/Mc$ (muon momentum) for a muon traversing a copper solid is shown in Figure 4.5. The stopping power decreases approximately with v^{-2} for increasing energies. It reaches its minimum at $\beta\gamma = 3$. Ionization is a key mechanism for particle detection. In semiconductors ionization produces

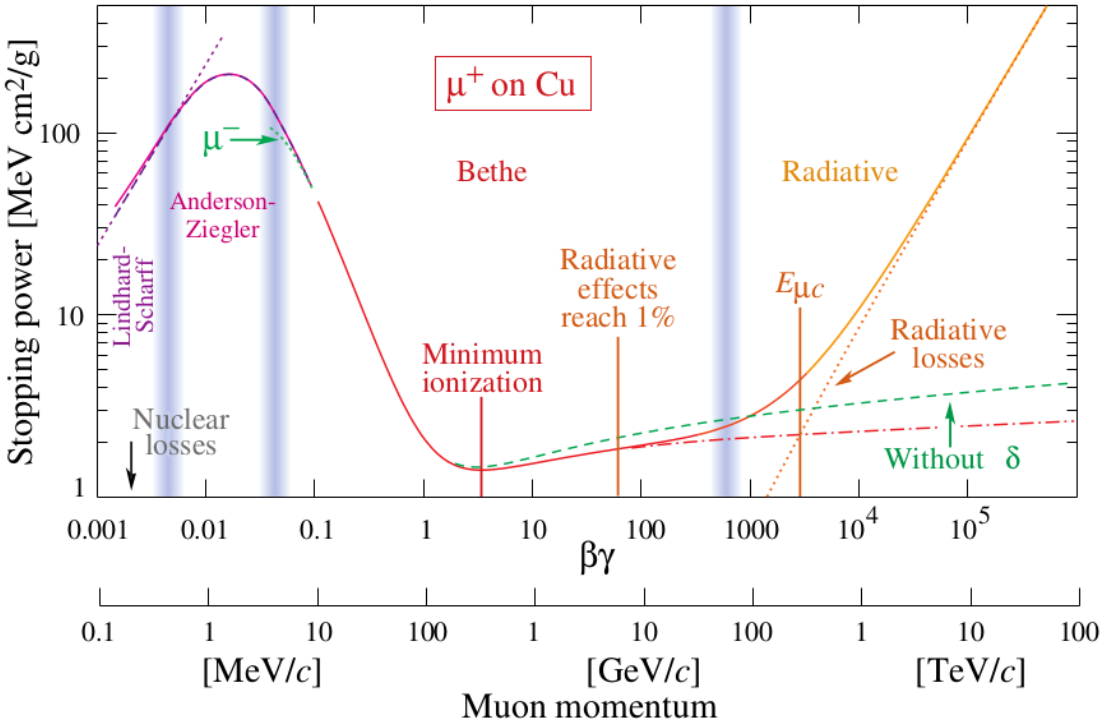

Figure 4.5.: Mass stopping power as a function of $\beta\gamma = p/Mc$ (muon momentum) for a μ^+ traversing a copper solid [BK16]. The transparent vertical lines highlight certain boundaries between approximations discussed in the reference.

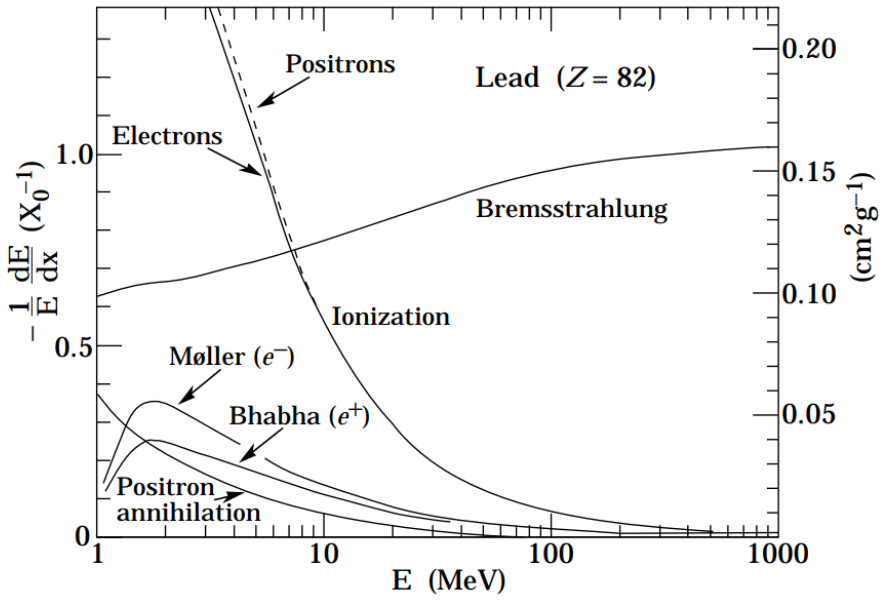

Figure 4.6.: Fractional energy loss per radiation length in lead as a function of electron energy [Tan+18].

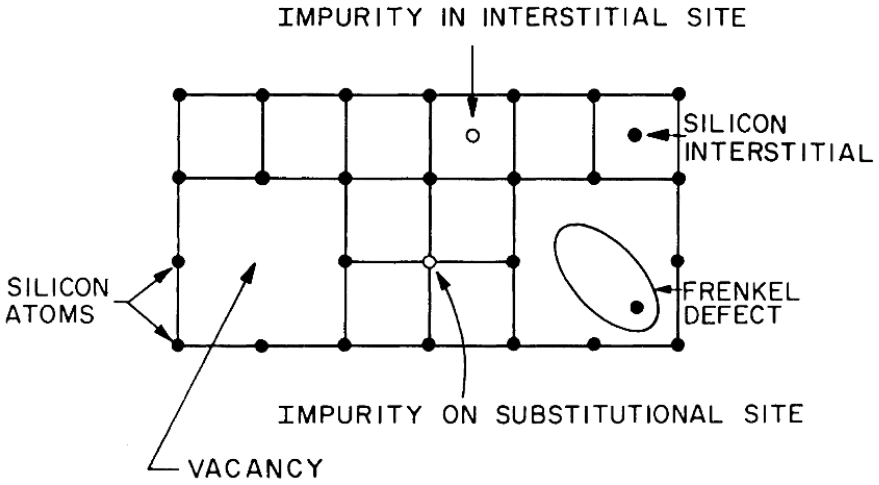

Figure 4.7.: Summary of lattice defects that might occur naturally or due to displacement [Lut07].

electron-hole pairs (e^-h^+-pairs) which can be separated and measured in the presence of an electric field. Particles with $\beta\gamma$ of 3 to 4 are usually referred to as *minimum ionizing particles* (MIPs). The corresponding momentum is a typical value for relativistic particles. Figure 4.5 also shows the limits of the basic Bethe approach for low and high energies ($0.1 \lesssim \beta\gamma \lesssim 1000$ for materials with intermediate Z). Various correction terms are used to extend the range of validity [BK16].

4.5.2. Other Particles

The energy loss of light or massless particles differs from the loss of charged heavy particles, which can be related to their kinematics, charge, spin or, in the case of an electron, their indistinguishability. At low energies, the energy loss of electrons is dominated by ionization via elastic scattering. Bremsstrahlung becomes the dominating interaction mechanism above energies of a few tens of MeV for most materials. The characteristics are shown in Figure 4.6, where the fractional energy loss per radiation length in lead is plotted as a function of electron energy. The radiation length X_0 is the characteristic amount of matter traversed by these particles. For electrons it is defined as the mean distance over which they lose all but $1/e$ of their energy by bremsstrahlung [Tan+18]. For photons the dominating processes are ionization, Compton scattering and e^+e^--pair production. Photon interaction is the least important interaction in the scope of this thesis. A typical example of a heavy electrically neutral particle is the neutron. There is no Coulomb interaction between a neutron and shell electrons or the nuclei of the lattice atoms. The prominent interaction process for such a particle is via nuclear forces, although the cross-section is relatively low because of the small spatial extent of the nuclei and the short range of the force [Tan+18].

4.5.3. Radiation Damage and NIEL Scaling

High energy particles, may they be charged or uncharged, can interact with the nuclei of the material they are traversing. In the case of silicon, an interaction energy larger than 25 eV will displace a lattice atom [Lin+80]. If the initial particle energy and the energy of the recoiled atom are high enough, they can generate a cascade of displacements. Low recoil energies usually create isolated point defects, while energies above about 5 keV generate a dense agglomeration

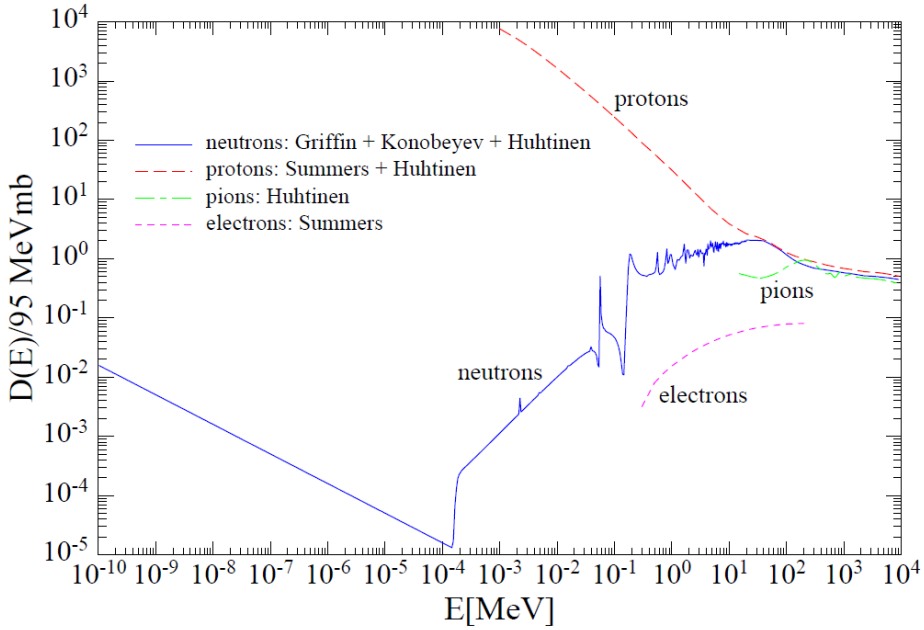

Figure 4.8.: Displacement damage function $D(E)$ normalized to 95 MeV mb for different particles. Due to the normalization of the y-axis, it represents the damage equivalent to a 1 MeV neutron [Rav06].

of defects at the end of the displaced atom's track. The resulting irregularities in the crystal structure are classified as different types of lattice defects as shown in Figure 4.7. The most prominent defects caused by displacement are vacancies, interstitials and Frenkel defects.

The Non Ionizing Energy Loss (NIEL) hypothesis introduces the possibility to normalize the damage of a hadron or lepton to the equivalent damage created by a 1 MeV neutron [Rav06]. It postulates a linear scaling between any displacement-induced change in the material and the transferred energy during the collision. Figure 4.8 shows the normalized displacement damage function $D(E)$ for different particles. The actual particle fluence Φ_{par} can then be replaced by the 1 MeV neutron equivalent fluence Φ_{eq} [Mol99]:

$$\Phi_{\text{eq}} = \kappa \cdot \Phi_{\text{par}}, \tag{4.18}$$

where the unit of Φ_{eq} is $\text{n}_{\text{eq}}\text{cm}^{-2}$ and the conversion factor is called hardness factor κ. The value of κ depends on particle type and particle energy. The precise experimental determination of κ is described in Ref. [Mol99].

4.6. Silicon as a Sensor Material

The silicon crystal has a diamond lattice structure with a lattice constant of 5.43 Å. Its indirect bandgap has a magnitude of 1.12 eV, effectively 3.6 eV. For years, silicon has been the dominating material for tracking devices in HEP experiments. Other candidates like germanium, gallium arsenide or diamond could not compete with the advantages of silicon detectors so far. The main advantages can be summarized as follows [Har17]:

- **Fast readout**: Silicon has a high intrinsic carrier mobility of $\mu_e = 1350\,\text{cm}^2\,\text{V}^{-1}\,\text{s}$ and $\mu_p = 450\,\text{cm}^2\,\text{V}^{-1}\,\text{s}$, which results in a drift velocity of $10\,\mu\text{m}\,\text{ps}^{-1}$ for an electric field over $5 \cdot 10^4\,\text{V}\,\text{cm}^{-1}$. This results in readout times below 10 ns for typical sensor thicknesses

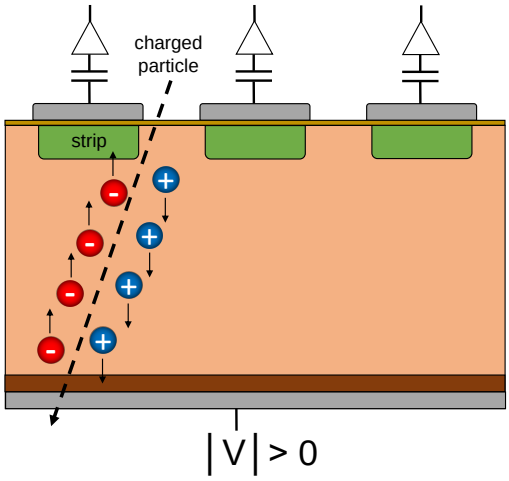

Figure 4.9.: Sketch of a MIP traversing a silicon strip detector. The components of a silicon strip sensor are explained in Section 4.8. The electric field between front-side implants (strips) and backplane leads to a separation e^-h^+-pairs. Regarding strip sensors presented in this thesis, the collected charge is read out capacitatively and amplified by the readout electronics. This is indicated by the capacitor and the amplifier symbol.

of a few 100 µm. Regarding the bunch crossing rate of the LHC of 25 ns, a high drift velocity is absolutely necessary.

- **Low costs and high accessibility**: Silicon is a very common resource on earth. It is therefore highly available and cheap. It can be considered the standard material for integrated circuits and can be produced at very high quality and purity.
- **Good energy resolution**: Every 3.6 eV (magnitude of silicon's effective bandgap) deposited by a traversing charged particle in a silicon bulk generates one e^-h^+-pair. That is about one order of magnitude less than the energy required to ionize a gas molecule in a gaseous detector. Silicon also has a high density. The average energy loss of a MIP in silicon is 390 eV µm^{-1}, generating 108 e^-h^+-pairs per 1 µm (the effective collected number being lower due to statistical reasons as explained later).
- **Existence of a natural oxide:** As will be explained later, AC-coupled silicon strip sensors rely on the existence of a natural oxide since it can be grown on a silicon wafer easily.

4.7. Particle Detection

A traversing charged particle ionizes atoms of the silicon lattice (see Section 4.5) and generates e^-h^+-pairs along its way. The electrons and holes are separated and drift to their respective electrodes in the presence of an electric field as depicted in Figure 4.9. The electrical signal can then be read out and interpreted by the readout electronics. The energy deposition of a MIP in

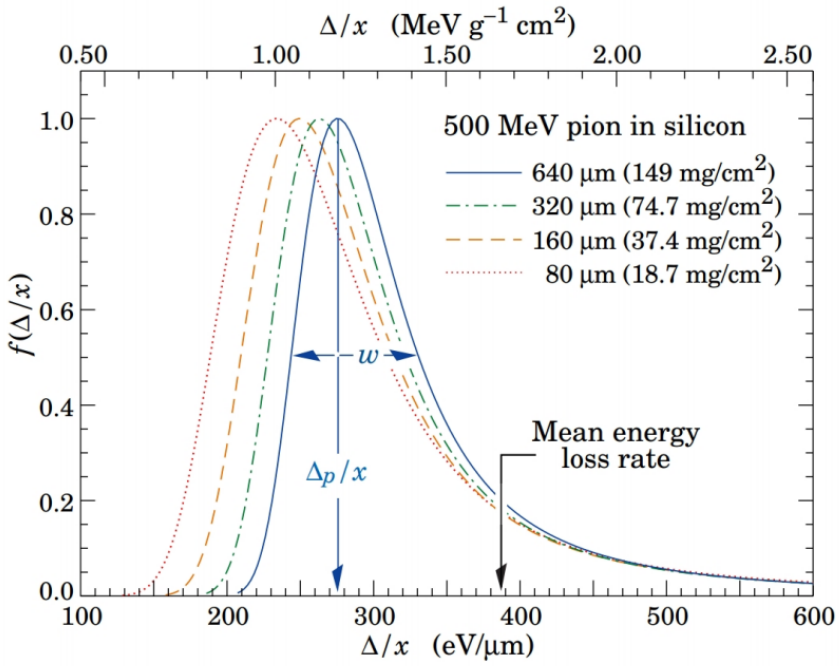

Figure 4.10.: Normalized energy deposition per micron of a muon with an energy of 500 MeV in silicon for different thicknesses. The energy deposition follows a Landau distribution [Par12].

silicon follows a Landau distribution. The rising tail of the Landau accounts for the fact that the number of collisions per MIP passage fluctuates. The transferred energy per interaction varies, which is described by Landau's straggling function and represented by the falling tail of the distribution. The Landau distribution also accounts for the rare production of δ-electrons towards high charge deposits. The shape of the Landau-distributed energy deposition in silicon is depicted in Figure 4.10. In practice, an adjustment of the Landau distribution is necessary in order to accurately describe the signal distribution of a sensor. This is related to the electronic noise of the readout electronics. The distribution is described best by a Landau-Gaussian convolution. The most probable value (MPV) of the Landau-Gaussian convolution is the conventional measure of the sensor signal. The MPV is around 30% lower than the mean, which results in a reference value of 75 $e^-h^+/\mu m$ generated by a traversing MIP in silicon [Har17].

It is obvious that the signal background of a sensor must be kept well below the expected signal. The signal background in an unbiased sensor is given by thermally generated e^-h^+-pairs. At room temperature this background can be approximated by multiplying the intrinsic charge carrier density $n_i = 1.45 \cdot 10^{10}\,cm^{-3}$ with the sensor thickness d and its area A:

$$N_b = n_i \cdot d \cdot A \tag{4.19}$$

The background N_b of a sensor with $d = 300\,\mu m$ and $A = 1\,cm^2$ is approximately $N_b = 4.35 \cdot 10^8$. The corresponding signal generated by a MIP in such a sensor would be $S = 22500\,e^-$ which is three orders of magnitude below N_b. Such a silicon sensor would not be able to detect a MIP. Cooling can be a way to reduce thermally generated background. However, the main solution for solving this issue is to deplete the sensor from free charge carriers by operating it under reverse bias. The highest detection efficiency is realized for bias voltages above V_{fd}.

4.8. Basic Design of a n-in-p Silicon Strip Sensor

A silicon strip sensor is, at its core, an arrangement of parallel connected diodes with a common base and biasing circuit. The spatial resolution x of a strip sensor is given by the pitch p (for binary readout as it is used in for CMS Phase-2 Outer Tracker sensors) [Har17]:

$$x = \frac{p}{\sqrt{12}}. \tag{4.20}$$

The term *n-in-p* refers to a p-doped bulk with n^+-doped strip implants. The $^+$ indicates a higher doping concentration. The typical design of such an n-in-p silicon strip sensor is illustrated in Figure 4.11. The strips are circumferenced by the bias ring (aluminum ring and n^+-doped bias implant). The direct connection between aluminum electrode and implant is realized by vias (vertical electrical connection through silicon). Strips and bias ring are connected by small, meandering polysilicon resistors (bias resistors). During operation the bias ring is connected to a ground terminal (GND) by wire bonds which also grounds the strip implants. The region between strips, bias ring and backside is called active region. The sensor backside is coated with aluminum in order to connect the bulk to the negative high voltage (-HV) terminal. A p^{++} backside implant can be found between bulk and the aluminum backplane to impede the formation of a Schottky contact. A Schottky contact describes a potential barrier which arises due to the Fermi level and band characteristics of a metal-semiconductor interface. The width of the barrier is inversely proportional to the doping concentration of the semiconductor. Thus, a highly doped implant reduces the barrier width and creates an ohmic contact to the backside metallization.

The DC pads are physically connected to the strip implants for qualification purposes. The AC pads, which are connected to the readout electronics via wire bonds during operation, are separated from the strip implants. The two structures sandwich a SiO_2 layer that functions as a dielectric. Charge that is collected by the strips is read out capacitatively. This strip-implant capacitor separates the induced signal of a traversing particle from the DC-share of the bias circuit, which is the main advantage of this approach. The n-in-p design requires an additional implant between strips to ensure a sufficient interstrip resistance. The degeneration of the interstrip resistance (mostly after irradiation) originates from electrons accumulating at the Si-SiO_2 interface, attracted by positively charged defects in the oxide. The accumulation layer shortens neighboring strips, which increases cross-talk. The development of the p-stop and p-spray technology that breaks the electron accumulation layer is documented in Ref. [Pri16].

Silicon sensors are produced on wafers. After the processing, the wafer structures are mechanically separated by dicing. The mechanical separation creates a rather amorphous edge region with conductive properties. Thus, the whole edge region is set to backside potential (-HV) during operation. The potential difference between edge and active region (on ground potential) leads to high currents, which would make it very difficult to operate a sensor. Therefore, the active region is protected by a n^+-doped guard ring, which reduces the potential difference between active region and the edge to almost zero. Moreover, it prevents the depletion zone from reaching the edge region. The guard ring is usually set to floating ground (not electrically connected). The p^{++} edge implant is a additional protection implant which is located close to the edge. The edge region on the front-side of the sensor is covered with aluminum (edge ring), which provides alignment marks for module assembly, strip numbers, which is helpful to identify individual strips, and contact pads for front-side biasing (explained in Chapter 10). Finally, the sensor surface is passivated by an oxide layer. Passivation openings are available at certain positions in order to electrically connect, probe or wire-bond the sensor properly.

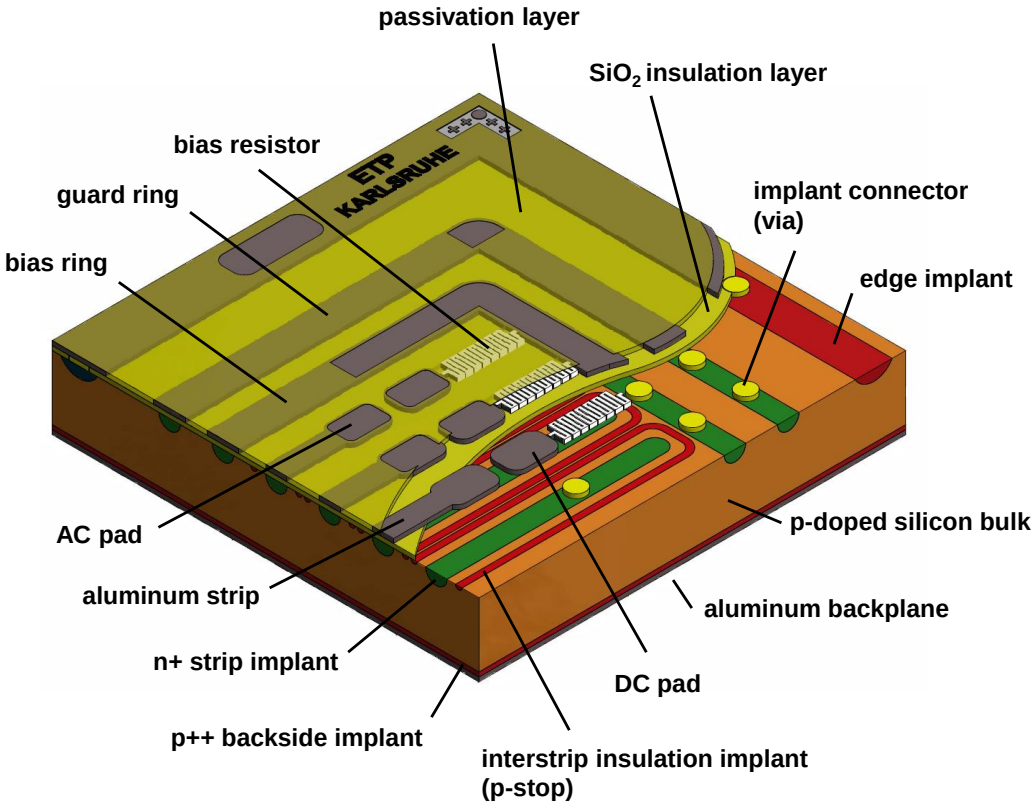

Figure 4.11.: Details of an n-in-p silicon strip sensor. The n^+-doped implants are marked as green, p^{++} implants in red and p-doped silicon in orange. The original image is taken from Ref. [Har17].

4.9. Leakage Current

The leakage current I_{tot} refers to the current which flows under reverse biased conditions. It results from thermally generated e^-h^+-pairs within the depletion zone. Generally, the leakage current is dominated by the carrier generation lifetime τ_L:

$$I_{\text{tot}} = -\frac{e}{2}\frac{n_{\text{i}}}{\tau_{\text{L}}} w \cdot A \ , \tag{4.21}$$

with A being the area of the junction. It is easy to see that I_{tot} is proportional to the width of the depletion zone. Taking into account Equation (4.2) this leads to:

$$I_{\text{tot}} \sim \sqrt{V_{\text{bias}}} \qquad (V \leq V_{\text{fd}}). \tag{4.22}$$

Theoretically, the leakage current saturates for $V > V_{\text{fd}}$. However, additional states within the band gap introduced by impurities, process induced defects, defects at the Si-SiO_2 interface, edge and front-side defects increase the leakage current generation [Mol99]. Leakage current contributes weakly to the system noise and is a noticeable source of heat dissipation in the detector. Leakage current is strongly dependent on temperature since the number of thermally

generated electrons increases with T according to Fermi-Dirac statistics (temperature dependence of n_i) [Har17]. Cooling systems are mandatory to suppress the radiation induced leakage current in the detector. If a cooling system cannot cope with the heating power of the sensor, the circular dependency of temperature, leakage current and heating power can eventually lead to *thermal runaway*, especially after irradiation, when the leakage current increases by a few orders of magnitude (see Section 4.11).

The voltage at which the leakage current rises dramatically is called breakdown voltage V_{bd}. It results from a collapsing space charge region or emerging conductive channels through the space charge region due to electric field values which exceed approximately $3 \cdot 10^5\,\mathrm{Vcm}^{-1}$ [Sch19]. A low breakdown voltage is usually a hint towards potential flaws in the manufacturing process. If the exponential rise of the leakage current is weak enough to be able to continue operation, one refers to the issue as soft breakdown. This vague definition is stated more precisely in Chapter 5.2.

In some cases it is helpful to be able to scale a measured leakage current to a given temperature. This can be done by using following formula:

$$I(T) = I_{\mathrm{tot}} \cdot \left(\frac{T}{T_0}\right)^2 \cdot e^{-\frac{E^*}{2k_{\mathrm{B}}}\left(\frac{1}{T_0}-\frac{1}{T}\right)}\,, \tag{4.23}$$

where I_{tot} is the measured leakage current at T_0, T is the given temperature and k_{B} the Boltzmann constant. The parameter $E^* = 1.21\,\mathrm{eV}$ denotes the adjusted band gap energy of silicon [Chi13]. The additional leakage current ΔI per volume unit due to radiation damage increases linearly with fluence, which was shown primarily in Ref. [Mol99]. The slope of this linear characteristic is called current related damage rate α:

$$\frac{\Delta I}{V} = \alpha \cdot \Phi_{\mathrm{eq}}\,. \tag{4.24}$$

Figure 4.12 shows the normalized increase of leakage current for different fluences after a heat treatment of 80 min at 60 °C, measured at bias voltages slightly above V_{fd}.

4.10. Signal versus Noise

The signal-to-noise ratio (SNR) is a key design feature for sensors. The signal can only be tweaked by changing the sensor thickness. This is, however, constrained by the desire to reduce leakage current, depletion voltage and multiple scattering in the detector, which is expected to favors thin sensors. The sensor noise, on the other hand, is related to various design choices. The strip-to-backplane capacitance C_{back} depends on sensor thickness and strip dimensions [Bar+94]. The thickness of the oxide, the aluminum strip and strip implant dimensions determine the coupling capacitance C_{c}. The interstrip capacitance C_{int} is determined by the strip implant length and the strip pitch. The noise of the parallel bias resistors, the aluminum strip resistance and the leakage current contribute as well. A common quantity that is used to express the noise is the equivalent noise charge (ENC) given in e^-. The different contributions sum up quadratically:

$$ENC = \sqrt{ENC_{\mathrm{C}}^2 + ENC_{\mathrm{I}}^2 + ENC_{\mathrm{R_P}}^2 + ENC_{\mathrm{C_S}}^2}, \tag{4.25}$$

where ENC_{C} denotes the electrical noise, the contribution of the load capacitance, and ENC_{I} the shot noise ($\sim \sqrt{I_{\mathrm{tot}}}$). The parallel thermal noise $ENC_{\mathrm{R_P}}$ is related to the resistance of

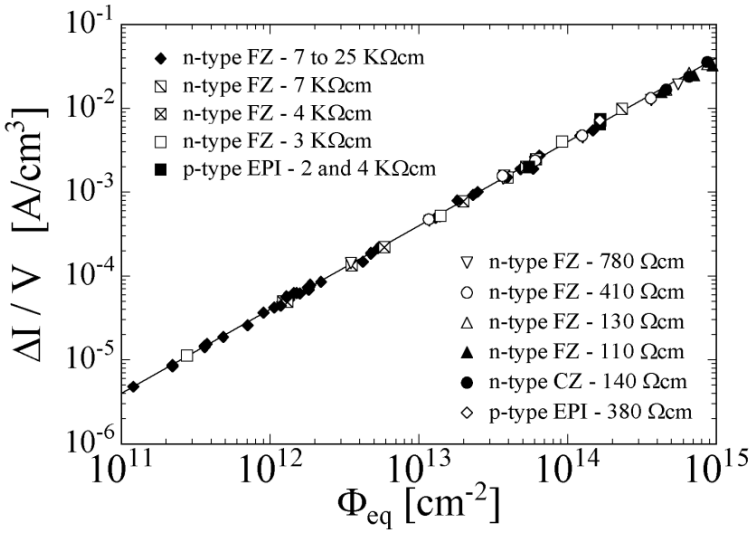

Figure 4.12.: Additional leakage current induced by irradiation versus fluence. Diodes of various process technologies and materials were measured after a heat treatment for 80 min at 60 °C [Mol99].

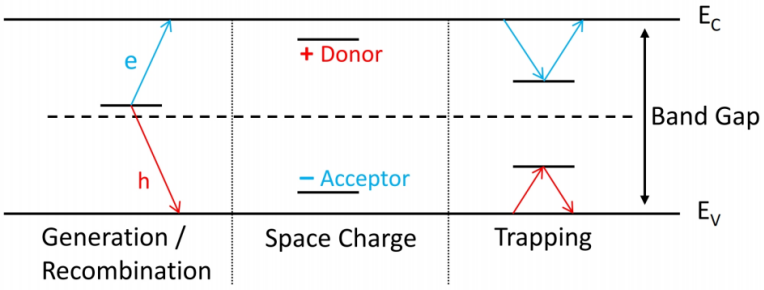

Figure 4.13.: Additional states within the band gap due to radiation damage in the sensor bulk [Ebe13].

the bias resistor and the serial thermal noise ENC_{R_S} is related to the metal strip resistance. The dominating term is ENC_C, which depends on the capacitances mentioned above. A more detailed overview about the noise contributions can be found e.g. in Ref. [Har17].

4.11. Sensor Degradation due to Irradiation

The microscopic impact of irradiation has been described in Section 4.5. The generated defects introduce additional states within the band gap which can be characterized by their depth. This is depicted in Figure 4.13. The generation and recombination centers close to the center of the band gap allow electrons to access the conduction band more easily. As a result, the leakage current increases by several orders of magnitude. Cooling is the most impactful tool to reduce leakage current. Typical operation temperatures of silicon sensors of modern HEP experiments are therefore between −30 °C and −20 °C.

The additional donors and acceptor states increase the effective doping concentration N_{eff}. According to Equation (4.11), this results in an increase of V_{fd}. Sensors are still able to detect MIPs even if V_{fd} surpasses the operation voltage of the device during the experiment. However,

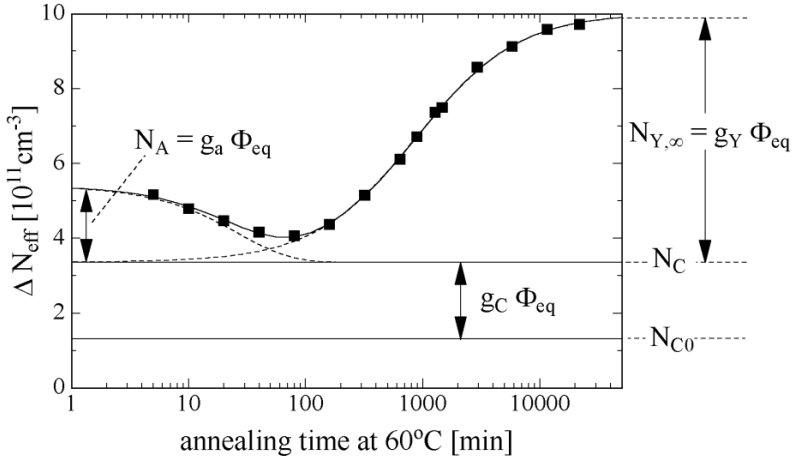

Figure 4.14.: Radiation induced changes of the effective doping concentration ΔN_{eff} measured over annealing time at 60 °C [Mol99].

the charge collection efficiency will gradually decrease since the undepleted volume is not sensitive for particle detection.

Defects can also trap charge carriers for a certain amount of time. A MIP can only be detected if an adequate number of generated electrons reach the readout electrode within the same readout cycle. In other words, the collected charge must be larger than the readout threshold or else the event is rejected. The sensor efficiency, therefore, decreases with increasing trapping probability. In the case of the Phase-2 Tracker the front-end readout frequency is 40 MHz which equates to a readout every 25 ns.

The sensor noise is also expected to increases after irradiation due to an increase of the shot noise and electrical noise. The main noise contribution originates from electrical noise. This is related to the change of the depletion behavior of the device. As stated by Equation (4.4), the strip-to-back capacitance and the bulk capacitance increase for partially depleted sensors (which depends on the operation voltage).

The decrease of the SNR of CMS Phase-2 Outer Tracker strip sensors after irradiation appears to be driven by the decrease in signal due to trapping and insufficient depletion rather than an increase in noise. The degradation of the signal within the expected fluence range of the Phase-2 Outer Tracker at 3000 fb^{-1} and $V_{\text{bias}} = 600$ V is between 20% and 50% with respect to the signal before irradiation (see Chapter 8). Preliminary, unpublished results of a beam test study which was conducted by ETP personnel in May 2019 revealed a negligible increase of the system noise. Miniature versions of the 2S sensor with a similar strip length, were read out with a prototype version of the future 2S readout chip while being exposed to an electron beam. At this point, the reader is referred to future publications of the CMS Tracker, since noise studies are outside the scope of this thesis.

4.12. Annealing

The cold operation of silicon sensors suppresses the diffusion of defect-related atoms in the sensor. However, if an irradiated sensor is exposed to room temperature or higher temperatures, defects

can anneal and rearrange. Firstly, this results in a decrease of leakage current. The magnitude of this effect falls off exponentially over time. Nevertheless, one can expect a decrease of leakage current of over 40% for annealing times of more than 20 weeks (see Chapter 8). Secondly, defect annealing reduces N_{eff} and, therefore, the depletion voltage up to roughly two weeks at room temperature or 80 min at 60 °C as claimed by Ref. [Mol99]. This phenomenon is referred to as beneficial annealing. Longer annealing gradually increases the depletion voltage again. This is called reverse annealing. The radiation induced change of the effective doping concentration ΔN_{eff} was measured over annealing at 60 °C in said reference and is shown in Figure 4.14.

The cooling system of the the CMS Phase-2 Outer Tracker can be shut down during the year-end maintenance period. The envisaged annealing time is two weeks per year. The exact annealing time depends on the reverse annealing of the signal and will be determined according to the results of irradiation studies presented in this thesis. Annealing studies during the R&D phase are performed using higher annealing temperatures to accelerate the annealing process. The annealing time at room temperature can be calculated using the parameterization of the damage rate presented in Ref. [Mol99].

5 Electrical Characterication of Silicon Strip Sensors

5.1. ETP Probe Stations

The electrical qualification of sensors and diodes was carried out with two custom-made probe stations. Measurements were performed between $-20\,°C$ and $20\,°C$ in a temperature controlled environment located inside a lightproof aluminum box. The device under test is placed on a polished aluminum chuck. Peltier elements are located beneath the chuck in order to adjust the temperature of the device. The temperature is measured via several temperature sensors which are attached to the chuck. The chuck itself is mounted on an assembly of three high-precision, motorized, linear stages. Furthermore, the environment is flushed with dry air in order to enable measurements at a relative humidity below 5%. A low humidity is required to decrease the dew point of the environment. This prevents condensation on cooled surfaces at low temperatures. Probing needles are used to contact the front-side of the device under test. The bias needle holder is placed on a small ledge that is fixated to the chuck. Additional needle holders are located on a side ledge which is fixated to the housing. This configuration allows for automated strip scans while maintaining the bias connection at all times. The measurement devices are located outside the aluminum housing. They are connected to a PCB[1] with integrated relays. The measurements are automated by utilizing different relay patterns that are activated by computer hard- and software.

The ability to cool the samples and to perform automated strip scans are key features for irradiation studies and sensor qualification. However, these features are hardly provided by commercial probe stations or else very expensive. This is why ETP has always relied on custom-made probe stations which are designed, built and refined by ETP personnel. Both probe stations underwent a major refurbishment between 2018 and 2020. This included new chucks, motor stages, relay board and needle holders. A new python [Pyt14] based software framework was developed simultaneously, which eventually replaced the outdated LabView [Nat17] based measurement software. The temperature and humidity control was completely outsourced and is now independently controlled via an Arduino microcontroller [Ard]. The last remaining items which have to be replaced (by the time this thesis was written) are the probe station housings, the mechanical fixations (for e.g. the microscope) and the rack for the required measurement devices. The probe stations are scheduled to be disassembled and then reassembled including the remaining items in a new laboratory which satisfies clean room standards by beginning of 2020.

ETP will act as a sensor quality control (SQC) center and an irradiation test (IT) center during the upcoming production of 2S modules starting by 2021. The produced 2S sensors will be distributed among SQC centers, which will fully characterize about one to two sensors

[1] Printed circuit board

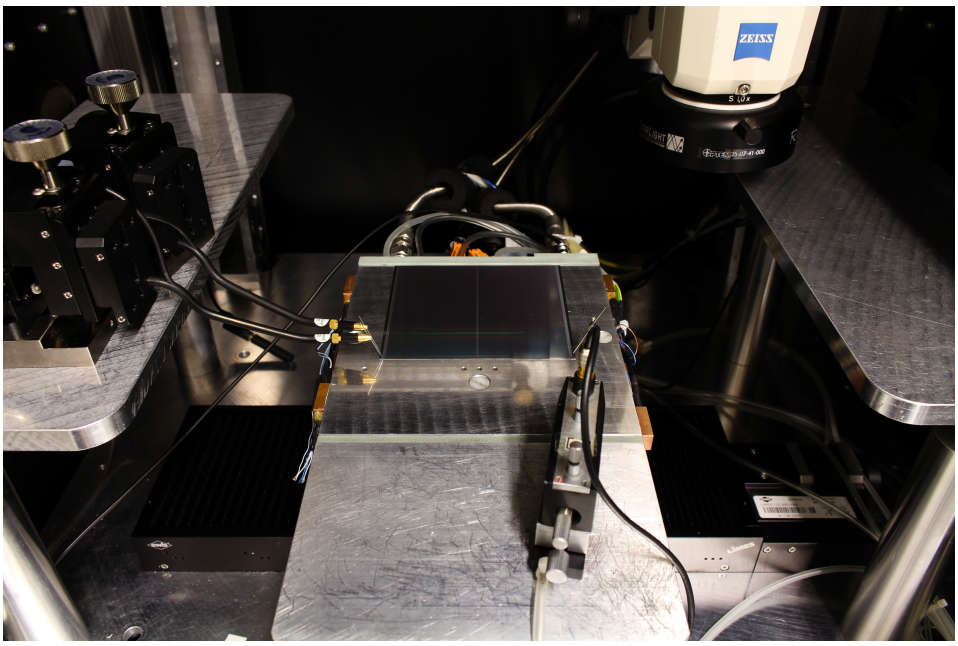

Figure 5.1.: The inside of the ETP probe station. A 2S sensor is placed on the chuck in the center of the image. The bias needle holder is positioned on the ledge of the chuck. The strip needle holders are positioned on the side ledge.

per batch. The typical batch size will presumably be 30 wafers per batch (each containing one 2S sensor). Simultaneously, process quality control (PQC) centers will check the process quality of a batch by characterizing a certain number of test structure sets which are located on every wafer. More information about the quality control during production can be found in Ref. [CMS18]. If the measured sensor and material parameters are within specifications, then the batch will be cleared for module production. In order to realize a sufficient throughput, an SQC center like ETP has to qualify at least one 2S sensor per day. Furthermore, ETP has to cope with the additional workload generated by irradiation test. Due to the hardware and software updates the ETP Hardware Group was able to sufficiently increase the measurement speed of their probe stations. The measurement time for a full characterization of a 2S sensor with over 2000 strips currently takes about 7 h. By utilizing both probe stations for SQC and IT, which have demonstrated their reliability throughout the past year, ETP can provide sufficient capacity in order to cope with the given task.

5.2. IV Characteristics

The IV characteristic is expected to follow Equation (4.22) until the whole bulk is depleted. In practice, the leakage current does not saturate for $V_{\text{bias}} > V_{\text{fd}}$ but increases steadily. The characteristic depends on a variety of macroscopic and microscopic defects in the sensor/diode (see Section 4.9). Figure 5.2 illustrates three typical IV characteristics of strip sensors used for studies presented in this thesis measured at $T = 20\,°\text{C}$. The IV characteristic of a first-grade strip sensor is represented by the green curve. The leakage current follows Equation (4.22) until it is fully depleted ($V_{\text{dep}} \approx 250\,\text{V}$). Afterwards, the leakage current increases moderately appearing almost linearly in this case (within the measurement range of 1000 V). The leakage current generation can also follow an exponential characteristic. The magnitude of the exponential increase depends on the number of macroscopic and microscopic defects (see Section 4.9). Such

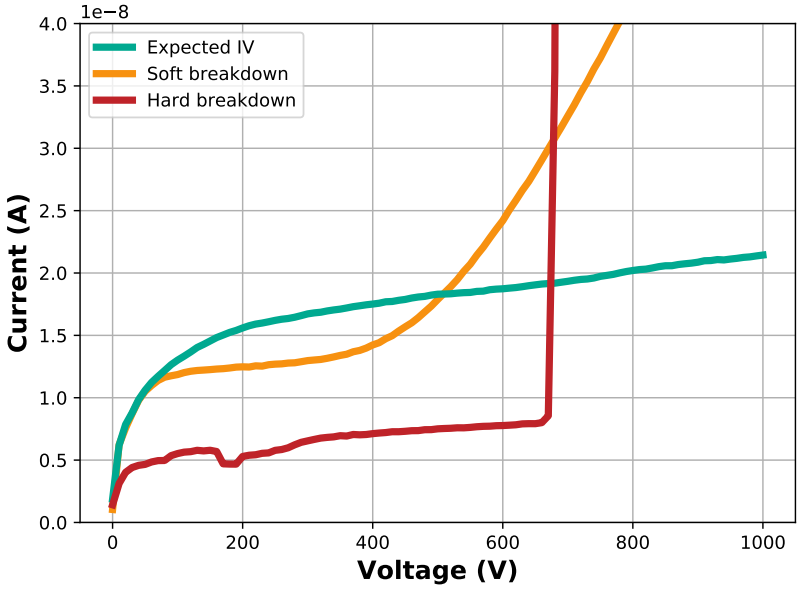

Figure 5.2.: IV characteristics of three different strip sensors. The expected IV characteristic for typical strip sensors presented in this thesis is depicted in green. The orange curve represents a strip sensor with a soft breakdown behavior. A hard breakdown at roughly $V_{\text{bias}} = 650\,\text{V}$ is shown by the red curve.

a characteristic is represented by the orange curve. The moderately exponential increase is referred to as a soft breakdown. Sensors that show a soft breakdown behavior can be efficiently operable until high bias voltages. A hard breakdown at roughly $V_{\text{bias}} = 650\,\text{V}$ is shown in the red curve. The technical design report (TDR) of the CMS Phase-2 Tracker Upgrade specifies the accepted range for soft and hard breakdowns before irradiation as follows [CMS18]:

$$V_{\text{break}} > 700\,\text{V}, \tag{5.1}$$

$$3 \cdot I_{500} > I_{700}, \tag{5.2}$$

where I_i denotes the leakage current and the index the applied bias voltage. Applying Relation (5.2) to the data of the orange curve yields $3 \cdot I_{500} \approx 54\,\text{nA} > I_{700} \approx 33\,\text{nA}$. Thus, the orange characteristic represents a sensor, which does not meet the specification defined by Relation (5.2).

5.3. Extraction of the Full Depletion Voltage

The full depletion voltage of a sensor/diode can be extracted from its CV characteristic by finding the voltage at which the capacitance becomes constant. It is common practice to plot the inverse square of the capacitance over the bias voltage. One expects a linear increase of the $C^{-2}V$ characteristic for $V < V_{\text{fd}}$. The full depletion voltage can then be easily determined by calculating the point of interception of the individual straight line fits of the slope and the horizontal segment (saturation region). The CV characteristics presented in this thesis always comply with the $C^{-2}V$-representation ($C^{-2}V \equiv CV$). A typical CV characteristic of a diode is depicted in the in Figure 5.3a. In order to identify the two segments one needs to locate the knee of the curve. The data can then be separated into two chunks and individually

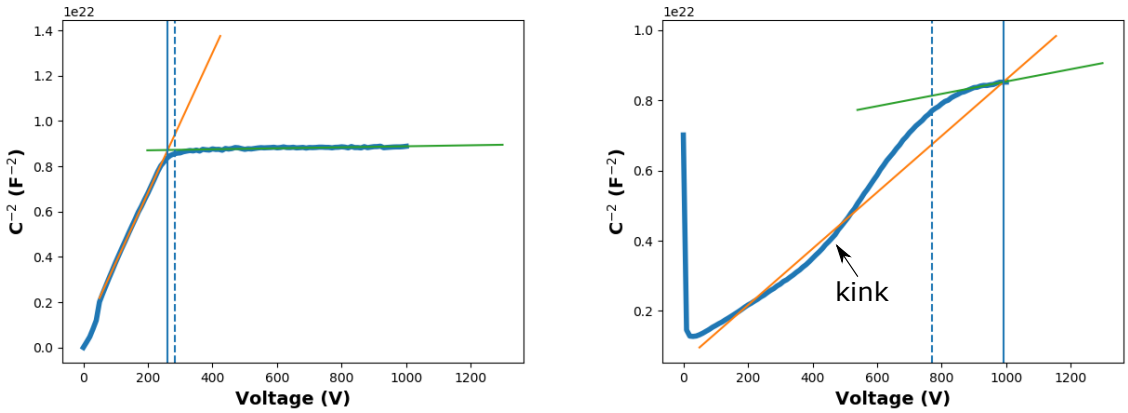

(a) (b)

Figure 5.3.: Typical CV characteristics (a) before and (b) after irradiation of a diode with a typical thickness of 290 µm. The data is analyzed with the automated V_{fd}-finding procedure. The dashed vertical line highlights the knee of the curve. The slope and horizontal segment to the left and the right of the knee are fitted, which is illustrated by the orange and green lines. The voltage at the point of interception, highlighted by the vertical blue line, is the full depletion voltage.

fitted by straight lines. The estimation of the knee location V_{knee} can be done manually for each measurement. The analysis written in the scope of in this thesis, however, automates the V_{fd}-finding procedure. The knee of the curve is approximated by using the Kneedle algorithm presented in Ref. [Sat+11], which evaluates the point of maximum curvature in a continuous function. The CV data is adjusted in order to improve the performance of the algorithm. Small spikes in the CV characteristics due to measurement noise can sometimes lead to misinterpretations. The CV data is, therefore, smoothened via a Savitzky-Golay filter. Moreover, the smoothened curve is parameterized by a high degree polynomial in order to increase the number of data points (usually from 10 V to 1 V steps). Lastly, data points which satisfy Relation (5.3) are used for the line fit of the slope. Data points which satisfy Relation (5.4) are used for the line fit of the horizontal segment.

$$V_{\text{bias}} < (1 - \epsilon) \cdot V_{\text{knee}} \tag{5.3}$$

$$V_{\text{bias}} > (1 + \epsilon) \cdot V_{\text{knee}} \tag{5.4}$$

A limit parameter of $\epsilon = 0.1$ proved to be decent choice for the analysis of unirradiated samples. A typical CV characteristic before irradiation is presented in Figure 5.3a. The dashed vertical line highlights the knee of the curve which is determined by the Kneedle algorithm using a sensitivity parameter of $S = 10$. This parameter determines how aggressive the algorithm is in terms of detecting knees: the larger S, the more conservative the knee detection. The line fits of the slope and saturation segment to the left and the right of the knee are represented by the orange and green lines. The voltage at the point of interception, highlighted by the vertical blue line, is the full depletion voltage. Knee and V_{fd} are similar before irradiation. The difference is used as a means to quantify the uncertainty of the procedure, which is discussed in Section 5.8.2.

The point of full depletion after irradiation is more difficult to determine. The sharp transition from slope to saturation region that is typical for CV characteristics before irradiation

transforms into a broadly bent segment, whose extent is dependent on the accumulated fluence of the sample. A typical CV characteristic of a high-fluence diode is shown in Figure 5.3b. Firstly, the distance between knee and V_{fd} increases. Secondly, the saturation region is usually not as horizontal as it is before irradiation. This results in a skewed line fit which shifts the intersection point to the left. Thirdly, the maximum measurement range of $V_{\mathrm{bias}} = 1000\,\mathrm{V}$ eventually limits the validity of the line fit of the saturation region. In order to account for these circumstances it proved sufficient to adjust the limit parameter to $\epsilon = 0.2$, since the distance between knee and saturation region increases. By increasing ϵ one reduces the number of available data points for the line fit of the saturation region. Therefore, it is practical to cap the limits defined in Relation (5.3) and Relation (5.4) to a value of $V_{\mathrm{knee}} \pm 150\,\mathrm{V}$. Moreover, the characteristic of the slope segment is not linear anymore. A kink emerges within the slope region, which decreases the validity of the straight line fit. The higher the fluence, the flatter the initial slope and the more pronounced the kink becomes. Nevertheless, the point of intersection shown in Figure 5.3b coincides with the voltage at which the capacitance saturates. The results of the V_{fd}-finding algorithm for irradiated sensors were validated by comparing the extracted full depletion voltages with the corresponding signal versus voltage characteristics. The algorithm performs excellent for irradiated samples with fluences up to $\Phi_{\mathrm{eq}} \leq 3 \cdot 10^{14}\,\mathrm{n_{eq}cm^{-2}}$. Uncertainties become larger for increasing fluences until the algorithm finally starts to fail. In some cases the automated V_{fd}-finding procedure is able to approximate V_{fd} beyond the measurement range up to roughly 1100 V, if the Kneedle algorithm manages to determine the knee of the data set. This is possible because of the parameterization of the CV characteristic.

The estimation of V_{knee} is often done manually. By choosing the knee and adjusting the line fits *by eye*, one introduces a certain level of arbitrariness to the evaluation of V_{fd}, especially after irradiation where the estimation is more difficult. The automated approach used in this thesis produces consistent results.

5.4. Strip Measurements

Next to the IV and CV measurements, the electrical qualification incorporates six strip measurements, which require two different needle configurations in case of two available strip needles. The characterization of the strip parameters is, therefore, performed in two steps. The strip leakage current I_{leak}, coupling capacitance C_{c}, the resistance of the polyresistors R_{poly} and I_{diel}, the current between implant and aluminum strip, are measured with a configuration that contacts DC and AC pad of a single strip. The interstrip capacitance C_{int} and interstrip resistance R_{int} are determined in a second series of measurements where the strip needles contact two neighboring DC pads. The six measurements could also be performed with a configuration of three strip needles in one go. The measurement parameters for each strip measurement are shown in Table 5.1. The asterisk highlights obsolete parameter sets that were changed during the probe station update process in 2019. The adjustment of the measurement frequency of C_{c} was motivated by an increase of the LCR measurement speed as well as improvements regarding the measurement reliability. The latter also motivated the adjustment of the voltage ramp of the R_{int} measurement to $[0, 5]\,\mathrm{V}$ in 1 V steps. This is explained more precisely in Section 5.8.3.

One of the major challenges of conducting strip measurements over a large number of strips is maintaining a sufficient contact between strip needle and pad. A bad contact is usually easy to detect: currents and capacitances are decreased to unrealistically low and resistances to unrealistically high values. An unexpectedly high R_{poly} value is the best indicator of a bad

Table 5.1.: Strip measurements performed in the course of a full electrical sensor characterization. The asterisk highlights obsolete parameter sets, that were changed during the probe station update process in 2019. The exclusion limits are used to exclude outliers from the mean value calculation, which are related to bad contacts. The I_{diel} measurement is only used to check for pinholes. A mean value calculation is not performed for this parameter. Typical values refer to values before irradiation and strip sensors presented in this thesis.

Strip parameter	Measurement parameter	Connected pads	Exclusion limit	Typical value
I_{leak}	-	DC	$< 1.5\,\text{nA}\,\text{cm}^{-1}$	$\geq \mathcal{O}(10^{-12})\text{A}\,\text{cm}^{-1}$
I_{diel}	10 V	AC	-	$< \mathcal{O}(10^{-12})\text{A}$
C_{c}	1 kHz	DC, AC	$< 15\,\text{pF}\,\text{cm}^{-1}$	$1.3\,\text{pF}/(\text{cm}\,\mu\text{m})$
C_{c}*	100 Hz	DC, AC	$< 15\,\text{pF}\,\text{cm}^{-1}$	$1.3\,\text{pF}/(\text{cm}\,\mu\text{m})$
C_{int}	1 MHz	DC, DC	$< 0.1\,\text{pF}\,\text{cm}^{-1}$	$0.4\,\text{pF}/\text{cm}$
R_{poly}	[0, 2] V, 2 V step	DC	$< 5\,\text{M}\Omega$	$1.8\,\Omega$
R_{int}	[0, 5] V, 1 V steps	DC, DC	$> 10\,\text{T}\Omega$	$\mathcal{O}(10^{12})\Omega\,\text{cm}$
R_{int}*	[0, 1] V, 0.2 V steps	DC, DC	$> 10\,\text{T}\Omega$	$\mathcal{O}(10^{12})\Omega\,\text{cm}$

DC pad contact and is usually one to three orders of magnitude above the typical R_{poly} value (see Table 5.1). The parameter is obtained by measuring the current between DC pad and the bias ring at 2 V and is, therefore, independent of the AC contact. An unexpectedly low C_{c} value is the best indicator of a bad AC pad contact. The measured value is then about one order of magnitude below the typical C_{c} value. The parameter is obtained by measuring the capacitance between AC pad and strip implant, which is independent of the DC contact. The integration of an algorithm which automatically detects bad measurements and repeats them with higher surface pressure is currently developed for the ETP measurement framework. Such an algorithm was not available for the ETP probe stations during the measurement campaigns presented in this thesis. Measurement data can, therefore, contain bad values originating from insufficient contact. Bad values are excluded from the mean calculations, which are performed during the strip measurement analysis in order to obtain more representative values for a sensor. The exclusion principles are listed in Table 5.1. The defined exclusion principles do not interfere with the actual process of detecting bad strips or significant variations of designed strip parameters. The strip measurement analysis still compares every measured strip parameter to the maximum or minimum values specified in the TDR and flags broken or noisy strips.

5.5. ETP ALiBaVa Setup

Signal measurements and annealing studies on sensors were carried out with a custom-made setup including the ALiBaVa readout system [Mar+07]. This test setup can measure the sensor signals generated by traversing MIPs, which are emitted by a radioactive source. The section describes the individual components of the setup, while the measurement and the analysis is explained in Section 5.6. The ALiBaVa daughter board provides two analogue front-end readout chips, known as Beetle chips, with 128 channels each, which were developed in the scope of the LHCb experiment [Löc02]. The Beetle chip channels are connected to a fan-in for better accessibility. The fan-in is connected to a pitch adapter, which is eventually used

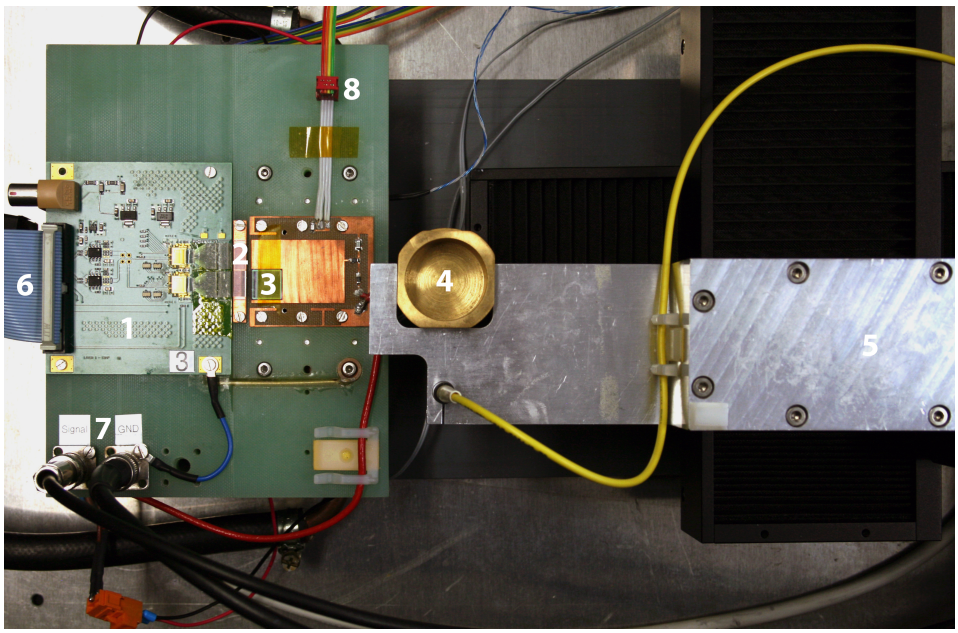

Figure 5.4.: The inside of the ETP ALiBaVa setup [Bra17]: (1) ALiBaVa daughter board, (2) pitch adapter, (3) PCB, (4) collimator, (5) aluminum arm which is mounted on the linear stages, (6) ribbon cable which connects ALiBaVa daughter board and motherboard, (7) sockets for ground and HV connection and (8) connection for the temperature sensor on the PCB.

to connect the AC pads of the strip sensor under test with the readout channels. The sensor under test is fixated onto a copper clad laminate PCB via polyamid tape. The daughter board and the PCB are mounted on a GRP[2] carrier, which also includes the biasing circuit for the sensor and sockets for ground and HV connection. The GRP carrier can be mounted onto the copper bridge, which houses Peltier elements in order to adjust the measurement temperature. The typical operation temperatures range between $-20\,°C$ and $20\,°C$. Temperatures of $60\,°C$ and $80\,°C$ are usually used to anneal irradiated sensors. Temperature sensors on the PCB and the copper bridge are used to monitor the measurement temperature and control the power of the Peltier elements. The signal measurements presented in this thesis were exclusively performed with a Sr^{90} source, that is used to generate signals in the sensor. However, an e^-h^+-pair generation via a laser beam is also possible with the setup. In order to control the position of a collimator and a focusing lens, the setup includes an assembly of three motorized, linear stages. The collimator limits the emitted particles of the radioactive source to a typical spot size of about 4.5 mm. The emitted particles traverse the sensor and the PCB before they can be detected by a plastic scintillator below the copper bridge. The GRP carrier as well as the copper bridge provide cavities in order to minimize the amount of absorption. All of these components are located inside a lightproof aluminum box that is flushed with dry air to allow for low measurement temperatures. A snapshot of these components is presented in Figure 5.4. Daughter board and scintillator are connected with the ALiBaVa motherboard located outside the box. The motherboard houses an FPGA that processes and digitizes the analogue data from the Beetle chips. Moreover, it processes the trigger input signal sent by the scintillator. Finally, the motherboard is connected to a PC, which stores the measurement files and provides an interface with which the measurement and hardware components can be

[2]Glass fiber reinforced plastic

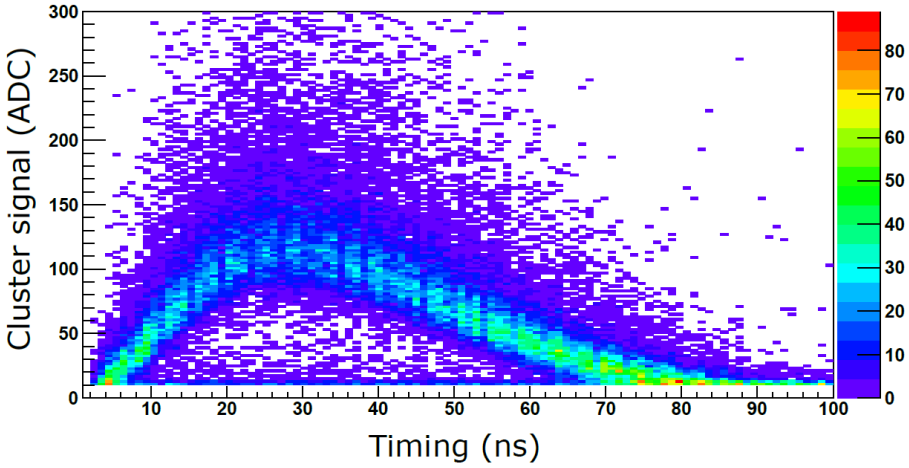

Figure 5.5.: Cluster signal versus timing with respect to the 100 ns window of the TDC. The color map indicates the number of clusters. The measured sensor has an active thickness of 290 µm and an accumulated fluence of $3 \cdot 10^{14}\,\mathrm{n_{eq}cm^{-2}}$. The measurement was conducted at $V_{\mathrm{bias}} = 600\,\mathrm{V}$ after an annealing of two weeks at room temperature.

controlled. Power supplies for Peltier elements, scintillator and sensor as well as a amperemeter for current measurements are also located outside the aluminum box.

5.6. Signal Measurement

Signal measurements are usually performed in a range between 300 V and 900 V, because this covers the operation voltage range of the Phase-2 Outer Tracker throughout the extended HL-LHC run time. The first stage of the measurement is the evaluation of the background signal and the noise of the system (readout chip and sensor). The ALiBaVa motherboard triggers the Beetle chip readout randomly for e.g. 3000 times. The data is used to calculate the mean background signal of every channel that is wire-bonded to the sensor. This background is called pedestal P_i with i being the channel index. Its variation (standard deviation of all measured signals of a channel) is the channel noise σ_i. The noise of the Beetle chip is comparable to the noise of the CBC, the read-out chip used in 2S modules, which is presented in Table 5.2.

Secondly, one has to perform a calibration run in order to extrapolate the conversion factor between the arbitrary units provided by the motherboard (analog-to-digital counts: ADCs) and an electric charge produced in the sensor. The Beetle chip provides integrated calibration capacitors for each channel, which can be used to inject a charge pulse of adjustable amplitude. The most accurate way to find the conversion factor, also called gain, is to perform a charge scan for every channel. Different amounts of electric charge are hereby injected into each channel and the ADC signal is measured. The gain per channel is derived by calculating the inverse slope of the individual ADC over charge characteristic. Since this characteristic is not linear across a large charge range, one could improve the ADC conversion in the analysis by parameterizing the gain per charge characteristic per channel. However, tests have shown that the improvement is marginal at least for a typical sensor signal between 5000 $\mathrm{e^-}$ to 24000 $\mathrm{e^-}$. The Beetle chip calibrations at ETP is carried out with a fixed electric charge of 15720 $\mathrm{e^-}$. This approach saves time during the calibration and the analysis. Moreover, it is accurate enough in order to acquire a sufficient sensitivity in the expected signal region.

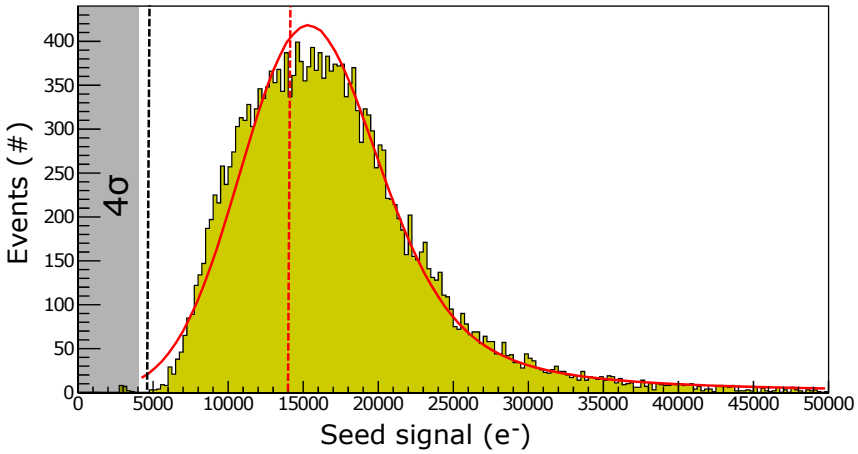

Figure 5.6.: Typical seed signal distribution of an irradiated strip sensor. The distribution is fitted with by a Landau-Gaussian convolution, which is indicated by the solid red line. The MVP of the distribution located at $S = 14000\,\mathrm{e}^-$ is highlighted by the red dashed line. A third of the MVP is highlighted by the black dashed line. The gray area represents the signal range that is below the 4σ threshold of the CBC.

The plastic scintillator below the sensor triggers the readout of the Beetle chip. The timing of the incoming trigger pulse is measured with respect to a 100 ns window of a time-to-digital converter (TDC) with a precision of around 1 ns. The exact timing is defined by the time between incoming trigger pulse and the falling edge of the TDC. The falling edge of the TDC also triggers the read out of Beetle chip. This results in a temporal distribution of the measured cluster signals within a 100 ns window. A typical distribution is shown in Figure 5.5 for a sensor with an active thickness of 290 µm and an accumulated fluence of $3 \cdot 10^{14}\,\mathrm{n_{eq}cm^{-2}}$. The measurement was conducted at $V_{\mathrm{bias}} = 600\,\mathrm{V}$ after an annealing of two weeks at room temperature. The color map indicates the number of clusters per data point. One can clearly see a maximum of the measured cluster signals around 30 ns. This is related to the properties of the shapers of the Beetle chip channels and the timing of the traversing particle. The storage cell which is read out due to the incoming trigger pulse does not necessarily contain the maximum of the measured charge pulse. Eventually, the analysis accounts for this feature by only including signals which are located at ±20% around the maximum of this distribution.

The ETP analysis uses a seed cut of 5σ above the noise to identify seeds. Seeds are strips which collect the large majority of the charge generated by a traversing MIP (about 80% to 90% of the cluster signal before irradiation). After identifying a seed strip, the algorithm evaluates the signal of neighboring strips. They are associated with the same cluster, if their signal exceeds 2σ. A typical cluster size for strip sensors presented in this thesis is about 1.5 to 2 strips. Since the CBC and SSA work in binary mode, the charge collection studies for the Phase-2 Outer Tracker focus on the seed signal rather than the cluster signal [Ada+17].

5.7. Sensor Efficiency and Signal Specifications

As described before, a generated signal needs to be higher than the readout threshold in order to be accepted. The threshold needs to be well above the noise σ of the readout electronics.

Table 5.2.: Information about the Phase-2 Outer Tracker readout chips [CMS18]. The 12σ margin represents a conservative estimation regarding the minimum signal that is required to ensure a sensor efficiency of at least 99.5%.

Name	Sensor	σ (e^-)	4σ-Threshold (e^-)	12σ-margin (e^-)
CBC	2S	1000	4000	12000
SSA	PS-s	800	3200	9600
MPA	PS-p	200	1200	2400

Table 5.2 lists the readout chips that will be used in the Phase-2 Outer Tracker. The usage of two different module types and three different sensor types demands for three different readout chips. A 4σ-threshold is usually a sufficient measure in order to eliminate fake hits (noise spikes interpreted as traversing particles). The hit efficiency of a sensor is defined as the number of detected particles divided by the number of particles that actually traversed the sensor. Although not directly specified in the TDR, the CMS Outer Tracker Sensor Working Group is aiming at a minimum efficiency of 99.5%. The hit efficiency of a sensor can only be determined in a test beam experiment which provides a realistic particle beam and information about the particle tracks. However, a test beam study is expensive, time-consuming and requires a lot of preparation. It is, therefore, only performed on a few selected samples in the course of the Phase-2 sensor R&D and not part of the irradiation studies presented in this thesis.

The efficiency can be well-approximated by performing signal measurements with a setup like the ETP ALiBaVa setup. Moreover, a setup like that has a larger measurement throughput, which is perfect for large sample numbers and annealing studies. A sensor is assumed to be fully efficient if $S_{\text{seed}}/3 > 4\sigma$. The relation can be written as follows:

$$S_{\text{seed}} > 12\sigma, \tag{5.5}$$

where S_{seed} denotes the MPV of the seed signal. The 12σ-approach is empirically motivated and was formulated during the Phase-2 R&D process within the CMS Outer Tracker Sensor Working Group. A typical seed signal distribution is presented in Figure 5.6, which corresponds to the measurement shown in Figure 5.5. The distribution is fitted by a Landau-Gaussian convolution, which is indicated by the solid red line. The MPV of the distribution located at about $14000\,e^-$ is highlighted by the red dashed line. The black dashed line highlights the $S_{\text{seed}}/3$ value. The gray area represents the signal range that is below the 4σ threshold of the CBC of $4000\,e^-$.

Preliminary results of test beam studies performed by ETP personal indicated that a threshold of 10σ or even 9σ is probably sufficient in order to operate a 2S sensors efficiently. Therefore, the 12σ-approach can be considered conservative enough in order to compensate for the relatively large uncertainty of the signal measurement of up to $\pm 1000\,e^-$ (see Section 5.8.4).

5.8. Measurement Uncertainties and Systematics

The following subsections describe the expected statistical and systematic uncertainties of measurements and procedures used in this thesis. The estimated uncertainties are summarized in Table 5.3. As a general remark, one is mainly interested in the variation of the measured

Table 5.3.: Estimated uncertainties of measurements and procedures. The given uncertainty of the full depletion voltage is only valid for unirradiated sensors.

Procedure or measured quantity	Uncertainty
Current	$\pm 100\,\mathrm{fA}$
Strip current	$\pm(I_{\mathrm{leak}} \cdot 0.04)$ [A]
Current (ALiBaVa)	$\pm 1.89\,\mathrm{pA}$
Capacitance	$\pm 4\,\mathrm{fF}$
Full depletion voltage	$\pm 10\,\mathrm{V}$
Signal	$\pm 1000\,\mathrm{e}^-$
Temperature	$\pm 1\,^\circ\mathrm{C}$
Temperature (AliBaVa, drying oven)	$\pm 2\,^\circ\mathrm{C}$
Annealing	$\pm(a_{\mathrm{t}} \cdot 0.1)$ [h]
Irradiation	$\pm(\Phi_{\mathrm{eq}} \cdot 0.2)$ [$\mathrm{n_{eq}cm^{-2}}$]

parameter of a sample in the scope of this thesis, e.g. the variation of the leakage current of the strips of a 2S sensor. Usually, every parameter is only measured once, e.g the leakage current of one strip or the leakage current of a sensor at a certain voltage. Therefore, the standard deviation of the mean is not relevant. If not stated otherwise the mean value of a measured parameter is always presented together with the standard deviation of the distribution of measurement values ($\mu \pm \sigma$) as a measure of their spread. The uncertainties presented in Table 5.3 are not included in the depiction of the results.

5.8.1. Current Measurements

A resolution of about $r_{\mathrm{I}} = 100\,\mathrm{fA}$ is sufficient for academic research and more than is required for SQC centers during Phase-2 production. The leakage current of an unirradiated 2S sensor is about six to seven orders of magnitude larger than r_{I}. The strip leakage current of a 2S sensor is about two orders of magnitude larger than r_{I}. Such a resolution is only required to sufficiently resolve the interstrip current during R_{int} measurements for high interstrip resistances as they are expected before irradiation. However, this is not necessarily mandatory, since one is mostly interested in detecting bad strips or bad sensor components during SQC, which are identified by high currents. Test measurements performed at one of the ETP probe stations revealed that the measurement noise of an open circuit current measurement is $112\,\mathrm{fA} \approx r_{\mathrm{I}}$ (I_{leak} relay configuration and needles floating), which is shown in Figure A.1a and Figure A.1b. This coincides with the accuracy provided by the measurement device in the lowest available range (see data sheet of Keithley 6485 [Kei10]). As expected, there is no permanently noticeable dark current contribution during an open circuit measurement. Outliers occur predominantly during the first seconds of the measurement, which could be related to a short settling time of the device. The settling time of a measurement device can easily be increased. This ultimately increases the measurement time, which is always tried to be kept as low as possible. For example, an increase of the settling time by 100 ms increases the total measurement time of an 2S sensor during SQC by approximately 15 min which would be acceptable. The fine tuning of the ETP probe station for SQC is still on-going.

Figure 5.7a shows the repeatedly measured strip current of one strip of a 2S sensor with

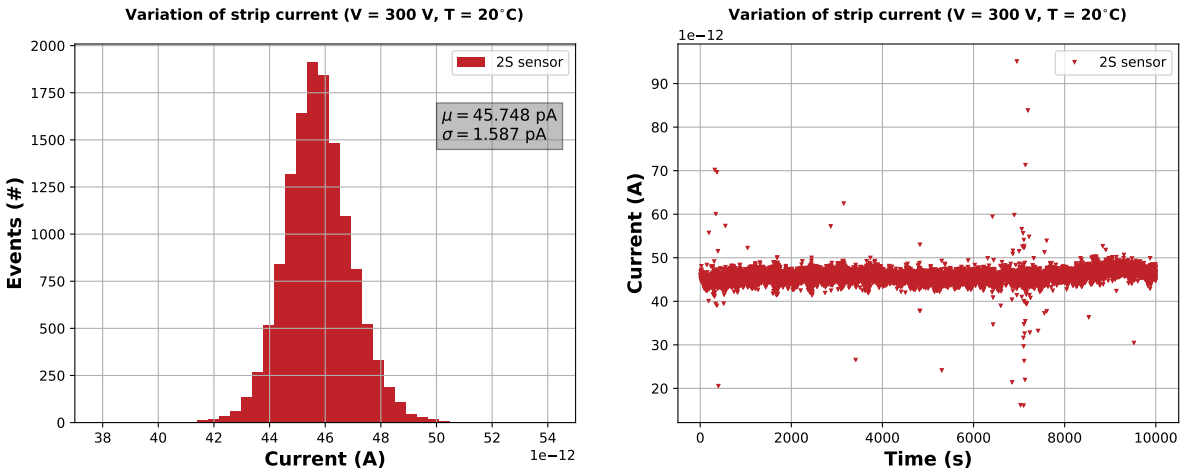

(a) (b)

Figure 5.7.: Variation of strip current of a 2S sensor with a typical active thickness of 290 µm measured at $V_{\text{bias}} = 300\,\text{V}$ and $T = 20\,°\text{C}$. The probe needle was positioned on a single strip and I_{leak} was measured for about 2.8 h, which resulted in approximately 13300 data points. The distribution of the measured current values is presented in (a). The current over time is shown in (b).

a typical active thickness of 290 µm. The probe needle contact was maintained throughout the measurement, which was conducted at $V_{\text{bias}} = 300\,\text{V}$ and $T = 20\,°\text{C}$ for about 2.8 h which resulted in approximately 13300 measurements. The allowed maximum strip current of a 2S sensor (5 cm long strip) is roughly 10 nA according to the TDR specifications [CMS18]. The data yield a mean strip current of about 45.75 pA and a standard deviation of 1.587 pA. The standard deviation corresponds to a measurement noise of about 4% and is expected to scale with the strip current. The noise within one standard deviation can be expected to originate from intrinsic leakage current fluctuations. Figure 5.7b, which illustrates the same data plotted over time, shows several severe outliers over the course of the measurement (±50 pA). Most of them are concentrated around 7000 s. These spikes are most likely hardware related and could originate from variations of the main power line or ground potential of the setup. In conclusion, one has to be aware of potential current spikes during the strip measurements. However, current spikes of ±50 pA are negligibly small with respect to the specified maximum strip current parameters in the TDR.

An open circuit measurement at the ETP ALiBaVa setup was carried out while having a GPR carrier with daughter board mounted on the cooling bridge. The measurement yields $\sigma = 1.89\,\text{pA}$ (see Figure A.2). Annealing studies of irradiated miniature versions of the 2S sensor are carried out with this setup. The said resolution is sufficient to accurately measure the current of irradiated sensors which is several orders of magnitude larger than σ. However, the resolution of the setup is one order of magnitude lower despite using the same amperemeter as the ETP probe stations. This is related to the dark current of the setup or large variations in the main power line.

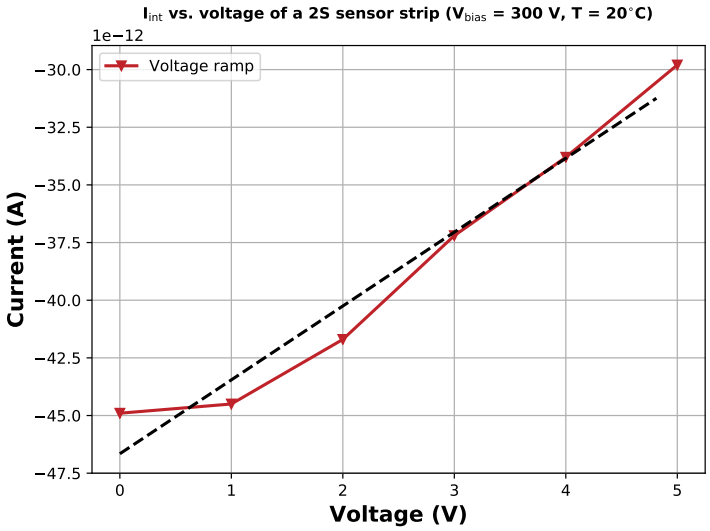

Figure 5.8.: IV measurement of a single strip of a 2S sensor at $V_{\text{bias}} = 300\,\text{V}$ and $T = 20\,°\text{C}$. The interstrip resistance R_{int} is calculated from the inverse slope of the fit, represented by the dashed line.

5.8.2. Capacitance Measurements and V_{dep} Extraction

Following Equation (4.4), the capacitance of a pn-device should be relatively large at low voltages because of the small width of the depletion zone. In practice, the LCR meter can sometimes return unexpectedly low capacitance values at $V_{\text{bias}} = 0\,\text{V}$, which is illustrated in Figure 5.3b. This measurement artifact originates from measuring ground against a 0 V potential and has no physical relevance. The accuracy of the device is about 4 fF, which was evaluated by an open circuit measurement with the C_{int} relay configuration of one of the ETP probe stations after performing an open correction. The capacitance was measured at 1 MHz (see Fig A.3). This is sufficient in order to resolve the expected interstrip capacitances of strip sensors (0.4 pF/cm) with typical strip lengths between 1 cm to 5 cm.

The uncertainty of the V_{fd}-finding procedure before irradiation is estimated by comparing the difference of the knee voltage with the the voltage at the point of intersection of the two straight line fits, which yields the approximate width of the transition region between slope and horizontal segment. The standard deviation of the calculated differences of all measured CV characteristics is about 10 V, which the is the estimated uncertainty of the procedure. A full depletion voltage within the measurement range of 1000 V is difficult to determine for high-fluence samples. The uncertainty for $V_{\text{fd}} > 900\,\text{V}$ is estimated to be $\pm 75\,\text{V}$.

5.8.3. R_{int} Measurements

The R_{int} value is extracted by applying a voltage ramp to two neighboring strips and calculating the inverse slope of the resulting characteristic in order to minimize the influence of the background. A sufficient interstrip isolation is the consequence of a high interstrip resistance and, thus, a low interstrip current. This current is especially low before irradiation. Precisely determining R_{int} is challenging regarding the measurement noise which originates from the variation of the strip leakage current. The typical strip leakage current value of a 2S sensor is $I_{\text{leak}} \approx 45\,\text{pA}$. The variation of I_{leak} during repeated measurements is about 4% of the mean value (see Figure 5.7a). Figure 5.8 shows the measured current between two strips for a voltage

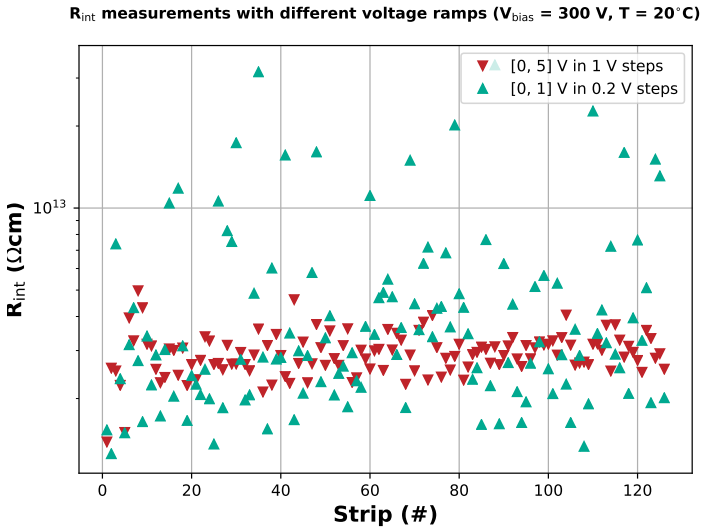

Figure 5.9.: R_{int} for different voltage ramps measured on a miniature version of a 2S sensor. The measurement was conducted at $V_{\text{bias}} = 300\,\text{V}$ and $T = 20\,°\text{C}$.

ramp between 0 V and 5 V. The positive interstrip current increases up about 15 pA. It is easy to see that interstrip current for voltages below 1 V is in the order of $\mathcal{O}(10^{-12})$ A, which is similar to the variation of I_{leak}. A fit in this range would yield a significantly larger interstrip resistance. Due to the variation of the background, the fit can even have negative slopes. The measurement is even more challenging if one tries resolve I_{int} of an irradiated strip sensor with sufficient interstrip resistance. With a strip current in the order of e.g. $\mathcal{O}(10^{-7})$ A (this depends on the accumulated fluence and the sensor dimensions) the device has to switch into the $I < 200\,\mu\text{A}$ range, which provides a precision of only $\mathcal{O}(10^{-8})$ A. The interstrip current is not measurable if it is in the order of $\mathcal{O}(10^{-9})$ A. Thus, the R_{int} measurement is problematic for sufficient interstrip resistances and high strip leakage currents. In conclusion, larger voltage ramps increase the reliability of the fit, because higher interstrip currents are easier to distinguish from the background.

Figure 5.9 illustrates the difference between an R_{int} measurement conducted with a voltage ramp of [0, 5] V in 1 V steps (red) and a ramp of [0,1] V in 0.2 V steps (green). The measurement was carried out with an unirradiated miniature version of the 2S sensor with an equivalent strip length at $V_{\text{bias}} = 300\,\text{V}$ and $T = 20\,°\text{C}$. It is easy to see that the variation of R_{int} is larger with a voltage ramp of [0,1] V. Moreover, ten of the green data points were excluded because the fit yielded a negative slope. The two approaches yield a $R_{\text{int, 5V}} = 587 \pm 105\,\text{T}\Omega\,\text{cm}$ and $R_{\text{int, 1V}} = 858 \pm 845\,\text{T}\Omega\,\text{cm}$. This is the reason for picking a voltage ramp of [0, 5] V in 1 V steps.

5.8.4. Signal Measurement

Signal measurements are conducted with the ETP ALiBaVa setup. The usage of an Sr^{90} source and only one scintillator adds a minor fraction of low energetic electrons to the spectrum, increasing the average deposited energy by about 2% [Ada+17]. Another source of uncertainty is the fit of the seed signal. The seed signal roughly follows a Landau-Gaussian convolution as shown in Figure 5.6. Typical seed signals of sensors presented in this thesis range between 24000 e^- (before irradiation) and 5000 e^- (for severely underdepleted sensors after irradiation)

with an uncertainty on the fitted MPV between $50\,e^-$ and $100\,e^-$. The seed signals are, therefore, rounded to the nearest ten.

A significant, hardware-based uncertainty originates from the accuracy of the injected charge during the calibration. The variations of the calibration capacitors of the Beetle chip are expected to result in a gain uncertainty of 2% [Löc06]. The signal measurements presented in Chapter 7 were conducted with different daughter boards, which makes the comparison of signals less reliable. The results presented in Chapter 8 were produced with a single daughter board. This should improve the comparability. However, one cannot assure that ALiBaVa systems used two Beetle chips of the same wafer for the assembly of the daughter board. A gain uncertainty of 2% results in a signal uncertainty between $100\,e^-$ and $480\,e^-$ with respect to the expected signal range.

Eventually, one wants to compare signals of different fluences during irradiation studies. The uncertainty of the radiation procedure between 10% and 20% does not impact the measurement directly, but adds a level of uncertainty to the evaluation of results. In conclusion, the most conservative estimation of the measured signal is $\pm 1000\,e^-$. The 12σ approach is conservative enough to account for this uncertainty.

5.8.5. Temperature Measurement and Annealing Procedure

The annealing procedure performed in the ALiBaVa setup and the drying oven are both monitored with similar temperature sensors (Pt100/1000). These sensors are also used for the probe stations. The accuracy of these sensors is about $\pm 0.5\,°C$ according to the datasheet. The actual sensor temperature can deviate from the reference value, because of the environment temperature or a non-optimal conduction between Peltier elements and sensor backside. The effective uncertainty of the temperature measurement is, therefore, estimated to be $\pm 1\,°C$ in the probe station and $\pm 2\,°C$ in the ALiBaVa setup and the drying oven. The uncertainty of the annealing procedure is driven by the heating and cooling periods. The setup takes about 2 min to increase the usual measurement temperature to annealing temperature. The annealing time is counted as soon as the temperature is stabilized. Not accounting for the annealing which takes place during the rise and fall time adds an uncertainty of about 10% to the annealing procedure (depending on the temperature).

5.9. Margins of the Signal Evaluation

The studies presented in this thesis examine the electrical properties of n-in-p sensors after irradiation in general. However, they were conducted in the scope of the CMS Phase-2 Upgrade and are, therefore, always evaluated with respect to the CMS Phase-2 Outer Tracker specifications and frame conditions. In this context there are a number of CMS specific margins that need to be mentioned. The 12σ margin, which is used for the signal evaluation, already includes an intrinsic margin of presumably $+2\sigma$ (see Section 5.7). Secondly, the irradiation studies presented in this thesis used fluences, which included safety margins of up to +50% with respect to the expected fluences determined by simulations (see Section 7.2 and Section 8.3). Hence, the qualified sensors are significantly more damaged by radiation than the sensor of the future tracker will be. Thirdly, the irradiations were carried out with reactor neutrons and low energy protons (see Section 6.4). A study presented in Ref. [Har+16] reported that low energy protons impact the charge collection efficiency more severely than pions. Since pions represent the vast majority of charged particles in the tracker, this adds another indirect margin to the evaluation process.

6
Samples and Irradiation

6.1. Sensor Material

The RD50 Collaboration, founded by CERN in 2002, has been conducting studies in order to find radiation hard semiconductor material for high luminosity colliders [CER18b]. Based on the promising results of the RD50 Collaboration, the CMS Phase-2 Upgrade Sensor Working Group carried out a large-scale sensor development campaign between 2010 and 2015 in order to find the optimal material and design parameters for the sensors of the future tracker. Sensors with different geometries as well as test structures were solely produced by Hamamatsu Photonics (HPK) [Ham19] on 6-inch silicon wafers. The single-sided processed wafers contained either n-in-p or p-in-n structures. The wafers were sliced out of a silicon ingot that was either grown with the Magnetic Czochralski [Czo18] or the Float Zone [Pfa58] process. The available thicknesses ranged from 50 µm to 320 µm. The adjustment of the thickness was achieved by either epitaxial growth, physical thinning, deep-diffusion or direct bonding of a thinned wafer onto a support wafer.

The deep-diffused technology is based on the fact that a heavily doped backside implant restricts the extent of the depletion zone. Heat is used to drive the dopants deep into the material. It can be assumed that temperature and heating time are the parameters that control the extent of the deep-diffused implant. The reduction of the active sensor region due to deep diffusion is more cost efficient than physical thinning and was, therefore, considered a promising candidate for the final material choice. A similar technology is utilized for the HPK standard float zone material with a physical thickness of 320 µm. Its active region is reduced to 290 µm by a 30 µm deep implant. Epitaxial growth and direct bonding were not considered as a potential base material for sensors of the Outer Tracker, mainly because of financial reasons. Wafers with active thicknesses of $d < 200\,\mu\text{m}$ are also uninteresting for Outer Tracker sensors because of their small signal. To give an example, a sensor with an active thickness of 150 µm has an expected signal of $11250\,\text{e}^-$ before irradiation, which is already below the lower limit of the 2S signal specification of $12000\,\text{e}^-$ (see Section 5.7). The results for thinned and deep-diffused material with $d \geq 200\,\mu\text{m}$ were summarized in Ref. [Ada+17], which identified n-in-p type silicon as the most suitable material for the new Phase-2 Outer Tracker. A comparison of the seed signal after irradiation of n-in-p and p-in-n sensors processed on the HPK standard material is shown in Figure 6.1. Based on these results, n-in-p type material became the baseline for CMS Phase-2 Outer Tracker sensors. The remaining R&D process for the future Outer Tracker focused on

- finding the optimal sensor thickness for the different regions of the Outer Tracker
- the characterization of the finalized sensor design of the 2S sensor
- the evaluation of different pixel designs for the PS-p
- the inspection of the process quality over the course of several sensor batches

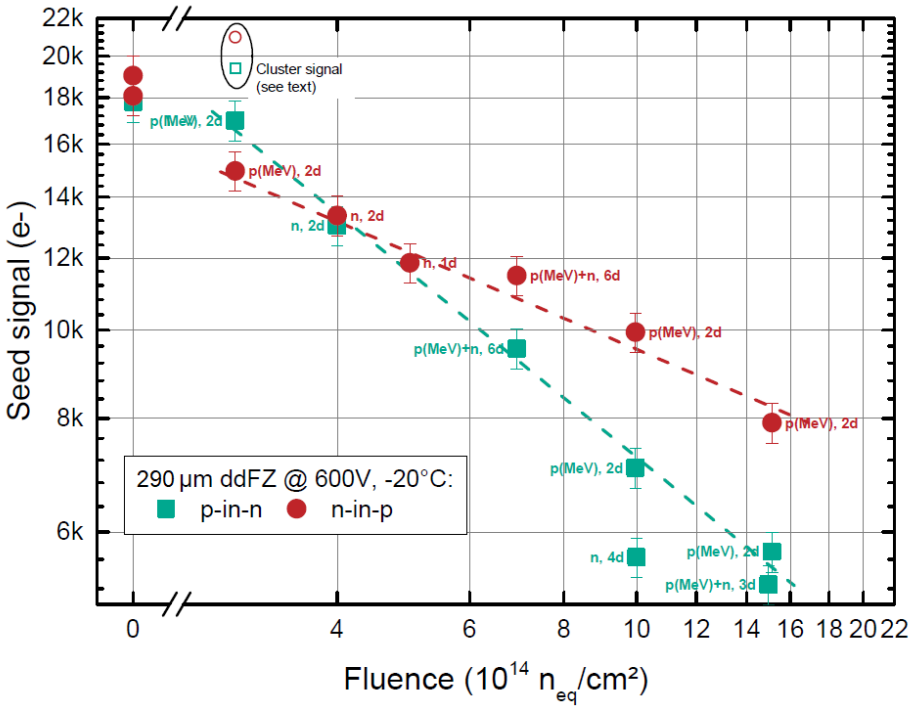

Figure 6.1.: Comparison of the seed signal after irradiation of n-in-p and p-in-n sensors processed on the HPK standard material with active thickness of 290 µm. The measurements were conducted at $V_{\text{bias}} = 600\,\text{V}$ and $T = -20\,°\text{C}$ [Ada+17]. The labels next to the markers state the irradiation composition of the sensor as well as the annealing time. The label *p(MeV)* denotes 23 MeV protons and *n* denotes reactor neutrons (see Section 6.4). The digit followed by a *d* indicates the annealing time scaled to days at room temperature.

The studies presented in this thesis were carried out with 2S and 2S-like strip sensors. Investigations regarding the macro pixel sensors for the Outer Tracker, the PS-p, can be found in Ref. [Sch19].

6.2. The 2S Wafer

The investigations of different strip sensor geometries led to the final design of the 2S sensor. The sensor has an area of roughly $10\,\text{cm}^2$ and 2032 strips with a length of about 5 cm. The strips are segmented in the center of the sensor providing an additional row of AC and DC pads on each side. The interstrip isolation is realized by p-stop or p-spray technology. Sensors with both technologies were produced during the R&D process. Next to the 2S sensor located in the center of the wafer, one can find different miniature sensors, diodes and test structures. The most important sample designs are the strip sensors Irradiation, KIT Test, Baby and PCommon. The Irradiation is the smallest miniature version of the 2S sensor. It was mainly designed for irradiation studies because of the limited container or carrier space for the irradiation process. The irradiation of smaller sensors is also more cost efficient. The KIT Test design comprises short strips which are segmented by a bias rail in the center of the sensor. The strips of the Baby sensor are not segmented but are of the same length as the strips of the 2S sensor and, therefore, the sensor provides the same load capacitance for noise and CBC studies. The PCommon differs from the base design of the 2S since it features a common p-stop

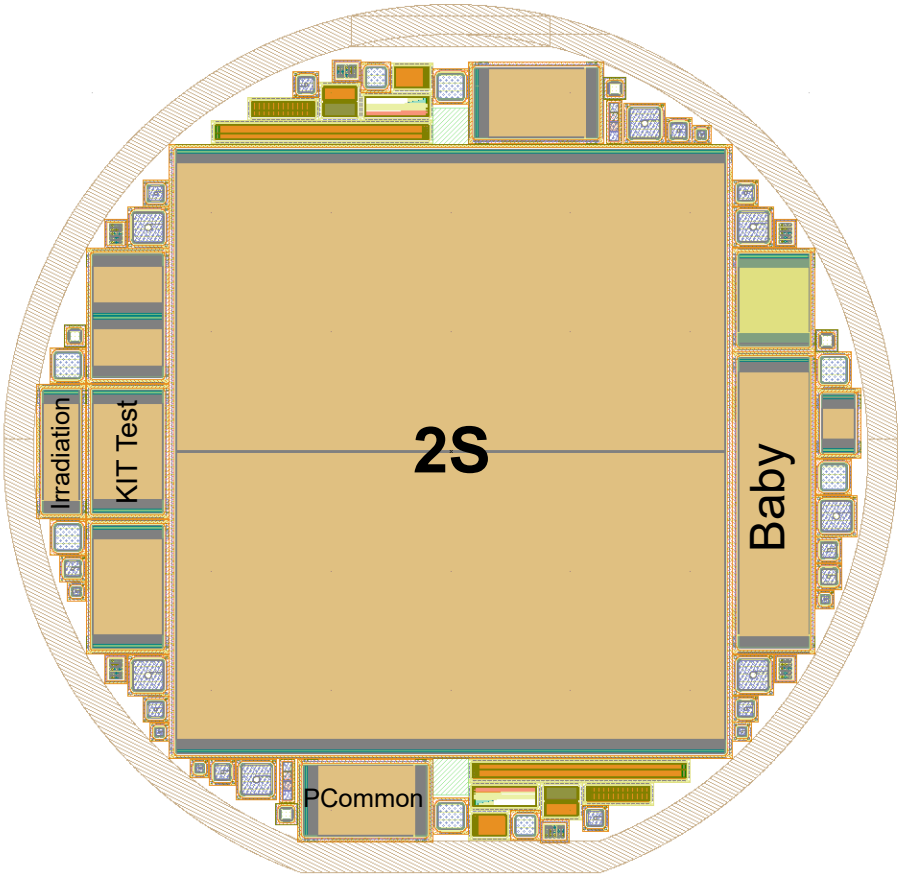

Figure 6.2.: Illustration of the 2S wafer with the 2S sensor in the center. The miniature sensors, which are relevant for this thesis, are called Irradiation, KIT Test, Baby and PCommon.

Table 6.1.: General layout and process details of the strip sensors of the 2S wafer.

Parameter	Value
Strip pitch	90 µm
Strip implant width	22 µm
Aluminum strip width	32 µm
Implant doping conc.	$\sim 10^{19}\,\mathrm{cm}^{-3}$
Bulk doping conc.	$\sim 10^{12}\,\mathrm{cm}^{-3}$
Bulk resistivity	$\sim 3\,\mathrm{k}\Omega\,\mathrm{cm}$

Table 6.2.: Sample specific design parameters. The active are is defined as the area within the center line of the guard ring.

Parameter	2S	Irradiation	KIT Test	Baby	PCommon	DiodeL
Number of strips	2032	64	254	127	127	-
Segmentation of strips	Yes	No	Yes	No	No	No
Active area length (µm)	101060	20616	20616	48522	20616	5300
Active area width (µm)	91840	6125	11701	11860	11735	5300
Active area (mm)	9281.35	127.27	241.33	575.47	241.93	28.09

implant instead of separate p-stop implants circumferencing each strip. The 2S wafer provides four different diode designs. The standard diode used for characterization is the largest diode (DiodeL). Material and design details are summarized in Table 6.1 and Table 6.2.

6.3. Sensor Materials and Nomenclature

The base material of each batch is the HPK standard float zone material, which has a physical thickness of 320 µm. The first two received 2S batches characterized in Chapter 7 were produced with deep diffused technology. The first batch had an active thickness of 240 µm and is called ddFZ240, where *dd* is the abbreviation for deep diffused, *FZ* for float zone and the 3 digit number denotes the active thickness in µm. The second batch is referred to as ddFZ200, since it has a active thickness of 200 µm. The materials characterized in Chapter 8 are referred to as FZ290, which is the HPK standard material with an active thickness of 290 µm, and thFZ240. The latter was exposed to the same front-side processing as FZ290, but was physically thinned to a thickness of 240 µm afterwards. The backside of thFZ240 sensors is protected by a shallow implant only. The original nomenclature of the samples is a combination of the material acronym, the active thickness, wafer number and the sample name. For simplicity and in order to reduce the legend size of the plots, it was decided to consecutively number the sensors and diodes that are relevant. These sensors are summarized in Table 6.3 and Table 6.4.

6.4. Irradiation Procedure

The neutron irradiation was performed at the TRIGA Mark II reactor [SŽT11] at Jozef Stefan Institute (JSI) [Insb] in Ljubljana, Slovenia. The samples were exposed to the reactor neutrons

Table 6.3.: List of relevant sensor names and their abbreviations, which are used in the text and for plots in Chapter 7. The full sample name incorporates the sensor material, wafer number and the sensor design.

Sample name	Full sample name	Sample name	Full sample name
S01	ddFZ240 04 Irradiation	S30	ddFZ200 07 Irradiation
S02	ddFZ240 07 Irradiation	S31	ddFZ200 09 Irradiation
S03	ddFZ240 08 Irradiation	S32	ddFZ200 11 Irradiation
S04	ddFZ240 18 Irradiation	S33	ddFZ200 14 Irradiation
S05	ddFZ240 22 Irradiation	S34	ddFZ200 01 KIT Test
S06	ddFZ240 23 Irradiation	S35	ddFZ200 02 KIT Test
S07	ddFZ240 29 Irradiation	S36	ddFZ200 07 KIT Test
S08	ddFZ240 33 Irradiation	S37	ddFZ200 09 KIT Test
-	-	S38	ddFZ200 10 KIT Test
-	-	S39	ddFZ200 11 KIT Test
-	-	S40	ddFZ200 12 KIT Test
S09	ddFZ240 07 KIT Test	S41	ddFZ200 15 KIT Test
S10	ddFZ240 08 KIT Test	S42	ddFZ200 06 PCommon
S11	ddFZ240 15 KIT Test	S43	ddFZ200 07 PCommon
S12	ddFZ240 16 KIT Test	S44	ddFZ200 10 PCommon
S13	ddFZ240 23 KIT Test	-	-
S14	ddFZ240 03 Baby	-	-
S15	ddFZ240 07 Baby	-	-
S16	ddFZ240 15 Baby	-	-
S17	ddFZ240 11 Baby	-	-
S18	ddFZ240 03 PCommon	-	-
S19	ddFZ240 07 PCommon	-	-
S20	ddFZ240 08 PCommon	-	-

Table 6.4.: List of relevant sensor names and their abbreviations, which are used in the text and for plots in Chapter 8. The full sample name incorporates the sensor material, wafer number and the sensor design.

Sample name	Full sample name	Sample name	Full sample name
S50	FZ290 11 Irradiation	S70	thFZ240 11 Irradiation
S51	FZ290 12 Irradiation	S71	thFZ240 15 Irradiation
S52	FZ290 13 Irradiation	S72	thFZ240 17 Irradiation
S53	FZ290 15 Irradiation	S73	thFZ240 18 Irradiation
S54	FZ290 19 Irradiation	S74	thFZ240 19 Irradiation
S55	FZ290 22 Irradiation	S75	thFZ240 20 Irradiation
S56	FZ290 26 Irradiation	S76	thFZ240 38 Irradiation
S57	FZ290 27 Irradiation	S77	thFZ240 39 Irradiation
S58	FZ290 29 Irradiation	S78	thFZ240 40 Irradiation
S59	FZ290 30 Irradiation	S79	thFZ240 41 Irradiation
S60	FZ290 33 Irradiation	S80	thFZ240 42 Irradiation
S61	FZ290 40 Irradiation	-	-
S62	FZ290 19 KIT Test	-	-
S63	FZ290 02 2S	S83	thFZ240 14 2S
S64	FZ290 12 2S	S84	thFZ240 17 2S
S65	FZ290 26 2S	S85	thFZ240 40 2S
-	-	S86	thFZ240 41 2S
D10	FZ290 02 TS12 DiodeL	D30	thFZ240 31 TS08 DiodeL
D11	FZ290 03 TS12 DiodeL	-	-
D12	FZ290 04 TS12 DiodeL	-	-
D13	FZ290 05 TS12 DiodeL	-	-
D14	FZ290 08 TS12 DiodeL	-	-
D15	FZ290 10 TS12 DiodeL	-	-
D16	FZ290 11 TS12 DiodeL	-	-
D17	FZ290 12 TS12 DiodeL	-	-
D18	FZ290 13 TS12 DiodeL	-	-
D19	FZ290 14 TS12 DiodeL	-	-
D20	FZ290 15 TS12 DiodeL	-	-
D21	FZ290 20 TS12 DiodeL	-	-

for a few minutes at 40 °C followed by a 30 minute period at 30 °C in the irradiation channel for deactivation. The spectroscopy takes place at room temperature and lasts for at least one hour. The samples are shipped back within one day. They are cooled via ice packs which provide temperatures that suppress annealing for roughly eight hours. The proton irradiations were mostly carried out with 23 MeV protons at −30 °C at the Zyklotron AG (ZAG) [Zyk] with the Karlsruhe Cyclotron (KAZ) [Zyk], which is located on the same campus as ETP. The samples collect minimal amounts of annealing time at room temperature during transport, preparation and spectroscopy. They are stored below −5 °C in between those procedures. The proton irradiation of the thFZ240 sensors was carried out with the MC40 Cyclotron at the University of Birmingham [All+17], England, which works similarly to the KAZ and provides proton energies of 11 MeV to 38 MeV. All in all, one can estimate a total amount of undesired annealing time of 20 h at room temperature for an external irradiation procedure and negligible annealing for an irradiation at KAZ.

Part II.

Irradiation Studies

7

Qualification of Deep Diffused Float Zone Material

The first major decisions regarding the Outer Tracker sensors was made after the initial Phase-2 sensor qualification campaign between 2010 and 2015 described in Section 6.1. The campaign evaluated various materials processed by HPK, which emerged as the vendor with the highest product quality during the R&D process. The conclusions drawn in this campaign emphasized float zone silicon as the more favorable substrate. Moreover, it was shown that the CMS sensor design was radiation harder in the n-in-p version beyond fluences of $5 \cdot 10^{14} \mathrm{n_{eq}cm^{-2}}$ compared to p-in-n or other sensor technologies. The degradation of the interstrip isolation after irradiation, which had been a major disadvantage of the n-in-p doping strategy in the past, turned out to be containable with the introduction of p-stop and p-spray technology. HPK initially proposed a flexible and cost efficient alternative to thinned wafers: n-in-p sensors produced on deep diffused float zone wafers, which have the benefit of an adjustable active thickness without generating additional costs for physical thinning. More information about the materials, sensors and their nomenclature is provided in Chapter 6.

The first batch of 30 deep diffused 2S wafers with an active thickness of 240 µm (ddFZ240), containing the final 2S sensor as well as similarly designed miniature sensors and diodes, was received in 2016. The ddFZ240 material was estimated to be a well-balanced compromise between sufficient signal, low leakage current and depletion voltage, combining the advantages of both 300 µm and 200 µm material. The second batch of deep diffused 2S wafers with an active thickness of 200 µm (ddFZ200) was received in 2017.

The main goal of the irradiation study of ddFZ240 and ddFZ200 was to characterize the material with respect to the signal specifications for 2S and PS region of the Phase-2 Outer Tracker. While the full-sized 2S sensors were mainly characterized by other institutes participating in the CMS Outer Tracker Sensor Working Group, the measurements at ETP were focused on qualifying the deep diffused material properties on miniature sensors and carrying out irradiation studies. Moreover, the community had to decide between the p-stop and p-spray interstrip isolation approach. Both batches therefore contained sensors with either technology.

The results presented in this chapter were partly published in my master's thesis [Met16] and the bachelor's thesis of J. Braach [Bra17], who performed measurements and analysis under my supervision.

7.1. Electrical Characterization of ddFZ240 and ddFZ200 before Irradiation

The electrical characterization is a major part of the material evaluation process. It includes a variety of characteristic measurements, which are described in Chapter 5. Table 7.1 shows

Table 7.1.: Mean leakage current of $|I_{500}|$ at $V_{\text{bias}} = 500\,\text{V}$ and mean full depletion voltage V_{fd}. Measurements were conducted at $T = 20\,°\text{C}$. The full depletion voltage was extracted from CV measurements performed at $f = 1\,\text{kHz}$. The standard deviation of the distribution of V_{fd} is not included because it is smaller than the estimated uncertainty of V_{fd} of $\pm 10\,\text{V}$.

Material	Design	$\lvert I_{500}\rvert$ (nA/mm^3)	V_{fd} (V)	Number of samples
ddFZ240	Irradiation	0.44 ± 0.03	203	8
	KIT Test	0.24 ± 0.02	216	12
	PCommon	0.14 ± 0.01	198	4
	Baby	0.11 ± 0.03	210	5
	DiodeL	0.14 ± 0.03	175	4
	2S	0.24	219	1
ddFZ200	Irradiation	1.82 ± 0.12	170	6
	KIT Test	1.76 ± 0.09	176	14
	PCommon	1.29 ± 0.03	157	5
	Baby	2.61	174	1
	DiodeL	-	-	0
	2S	0.89 ± 0.11	181	5

Table 7.2.: Mean values of normalized strip parameters before irradiation of all strips of every measured sensor at $V_{\text{bias}} = 300\,\text{V}$ and $T = 20\,°\text{C}$. The coupling capacitance C_{c} was measured at $f = 100\,\text{Hz}$ and the interstrip capacitance C_{int} to one next neighbor was measured at $f = 1\,\text{MHz}$. The values of the *Check* column indicate whether or not the TDR specifications are met [CMS18].

Material	Parameter	Value	No. of strips	Check
ddFZ240	I_{leak} (nA/cm)	0.050 ± 0.039	~ 2900	✓
	C_{c} (pF/(cm µm))	1.29 ± 0.05	~ 2900	✓
	R_{poly} (MΩ)	1.67 ± 0.08	~ 3000	X
	C_{int} (pF/cm)	0.423 ± 0.039	~ 2000	✓
	R_{int} (TΩ cm)	2.82 ± 0.32	~ 2800	✓
	Detected pinholes	0	~ 2900	-
ddFZ200	I_{leak} (nA/cm)	0.232 ± 0.052	~ 2600	✓
	C_{c} (pF/(cm µm))	1.35 ± 0.04	~ 2600	✓
	R_{poly} (MΩ)	1.92 ± 0.03	~ 2600	X
	C_{int} (pF/cm)	0.447 ± 0.03	~ 2000	✓
	R_{int} (TΩ cm)	1.35 ± 0.15	~ 2000	✓
	Detected pinholes	1	~ 2600	-

the mean values of the leakage current at $V_{\text{bias}} = 500\,\text{V}$ and $T = 20\,°\text{C}$ for different sample designs. The leakage current is normalized by sensor volume for better comparability. The TDR specification of $I_{500} \leq 2\,\text{nA/mm}^3$ can be met by ddFZ240 samples, easily. There is no outlier among the 34 tested ddFZ240 samples. No hard breakdowns were encountered and a soft breakdown tendency was not ascertainable. The normalized mean leakage current of ddFZ200 samples is about one order of magnitude higher compared to ddFZ240. One ddFZ200 miniature sensor showed a breakdown at 450 V and could not be used for the campaign. Many of the 31 ddFZ200 samples showed soft breakdown tendencies above about 600 V, especially sensors with p-spray isolation and 2S sensors. Five ddFZ200 sensors showed leakage currents which were about 1 to $2\,\text{nA/mm}^3$ above the I_{500} specification. The mentioned samples were flagged as high current samples and are listed in Table A.1. Nevertheless, the samples were well-operable and could be used for further measurements.

The absolute leakage current of ddFZ200 sensors is significantly larger than the leakage current of ddFZ240 sensors, which contradicts the classical expectation, where I_{tot} is proportional to the active thickness. Firstly, the heat treatment of the deep diffusion process can be expected to create additional defects in the active volume of the sensor. The longer the treatment, the more defects are generated, which results in more leakage current [Jun11]. This feature was already observed during the initial Phase-2 sensor campaign. Secondly, the soft breakdown tendencies are an indicator of a decreasing production quality. The discrepancy between the two batches is all the more pronounced due to the excellent quality of the ddFZ240 batch. Differences between p-stop and p-spray technology can also be observed in the IV characteristics of both batches. These differences are most pronounced on 2S sensors. IV measurements of 2S sensors of both batches are presented in Figure A.4a, Figure A.4b, A.5a and Figure A.5b [CMS17c][1]. The measurements were conducted by HPK directly after dicing and before the sensors were shipped. The ddFZ240 2S sensors with p-spray technology show unstable IV characteristics above 600 V, which follow a zig-zag-like pattern. Every measured ddFZ200 2S sensor with p-spray technology shows a soft breakdown at low bias voltages, which results in higher leakage currents. On the other hand, 2S sensors with p-stop technology produce stable IV characteristics.

A typical feature of deep diffused material as its fuzzy depletion characteristic. The transition of the slope to saturation region of the CV characteristic is less defined and the saturation region is not as horizontal as it is for other materials. This is a result of an on-going saturation process of the region around the interface of active volume and deep diffused backside. However, this feature has no impact on the estimated uncertainty of the V_{fd}-finding algorithm (Section 5.3). The uncertainty is estimated to be $\pm 10\,\text{V}$ (see Section 5.8.2). Besides, this is a minor effect which is not supposed to have any negative impact on the sensor efficiency. The full depletion voltage for ddFZ240 sensors is between 198 V and 219 V and between 157 V and 181 V for ddFZ200 sensors. There is no specification in terms of full depletion voltage available for 240 µm material. For 200 µm material the TDR states $V_{\text{fd}} < 150\,\text{V}$, which is not met by ddFZ200 sensors. The PCommon sensors stand out in both cases as the design with the lowest full depletion voltage. The 2S sensor has the highest full depletion voltage in both cases. The variations in V_{fd} can stem from thicknesses or N_{eff} variations. This indicates a fixed temperature gradient during the heat treatment of the deep diffused wafers. Sensors located at the wafer edge show a lower V_{fd} as the center sensor (2S). In case of thickness variation, the temperature at the edges would be high and decrease towards the center. A higher temperature results in a larger extent of the highly doped backside. The PCommon sensor would therefore be the

[1] The plots are taken from an internal presentation given in the scope of a meeting of the CMS Outer Tracker Sensor Working Group in October 2017 at CERN

thinnest sensor on the wafer among the tested designs. Overall, these variations take place on a small scale and are acceptable. Diodes require about 20% less bias voltage than sensors to reach full depletion, which is a result of the more homogeneous field configuration (see Equation (4.5)).

The strip and interstrip measurements before irradiation were conducted at $V_{\text{bias}} = 300\,\text{V}$ and $T = 20\,°\text{C}$. The strip leakage current I_{leak}, interstrip capacitance C_{int} and interstrip resistance R_{int} are normalized to the strip length. The coupling capacitance C_{c} is normalized to strip length and the strip width of 22 µm. The mean strip parameters were calculated using the exclusion principles explained in Section 5.4. They are presented in Table 7.2. The deviations between C_{c} between ddFZ240 and ddFZ200 are within two standard deviations, which is most probably related to small differences in the oxide thickness. The deviations between C_{int} are marginal and within one standard deviation. A fixed value is to be expected since the interstrip capacitance mainly depends on the strip dimension and pitch, which are given by design. The interstrip resistance is sufficient in both cases. The exact values are not of importance in the measured orders of magnitude since they usually correspond to measurement noise and not any realistically measured current (see Section 5.8.3. The strip leakage currents of ddFZ240 and ddFZ200 differ by one order of magnitude, which corresponds to the differences in I_{tot}. Strips with $I_{\text{leak}} > 2\,\text{nA/cm}$ and strips for which a pinhole had been detected ($I_{\text{diel}} > 2\,\text{nA}$ at 10 V) were flagged as bad strips. Groups of 23 to 29 adjacent leaky strips were found on two ddFZ240 samples. One leaky strip was detected on four additional ddFZ240 samples. Four leaky strips were found among three ddFZ200 samples. Only a single pinhole was detected during the initial characterization of the sensors. Table A.2 and Table A.3 present details about samples with flagged strips. The magnitude of the polyresistor changed by roughly 15% from batch to batch. The TDR specification demands a value of $R_{\text{poly}} = 1.5 \pm 0.3\,\text{M}\Omega$. The ddFZ200 sensors are out of specifications in that regard. In this case however, the TDR value is not written in stone and could be adjusted accordingly. The more important specification regarding R_{poly} is its homogeneity across the sensor. The TDR states a maximum deviation of 5% among all strips of a single sensor. The calculated standard deviations are below 5% for both batches. The polyresistors therefore satisfy that requirement.

7.2. Irradiation Program

Three fluences were chosen for the irradiation of ddFZ240 samples in order to roughly cover the fluence spectrum in the Phase-2 CMS Outer Tracker. A fluence of $1 \cdot 10^{14}\,\text{n}_{\text{eq}}\text{cm}^{-2}$ represents the lowest fluence in the Outer Tracker at the end of the nominal HL-LHC run-time (Low 2S). The latest FLUKA [Fer+05] simulations at that time estimated the highest occurring fluence among 2S modules to be approximately $5 \cdot 10^{14}\,\text{n}_{\text{eq}}\text{cm}^{-2}$. After adding a safety margin to compensate for FLUKA uncertainties, it was concluded to pick $6 \cdot 10^{14}\,\text{n}_{\text{eq}}\text{cm}^{-2}$ as an ultimate 2S fluence, which also served as a candidate for covering a medium PS fluence. The top-end for this campaign was chosen to be the nominally highest fluence among PS modules of $1 \cdot 10^{15}\,\text{n}_{\text{eq}}\text{cm}^{-2}$. The previous Phase-2 sensor qualification campaign presented in Ref. [Ada+17] was carried out with mixed irradiated samples (proton and neutron irradiation) to emulate the radiation environment of the detector more accurately. Increased expenses and the logistical effort that is required for neutron irradiations as well as time constraints lead to the decision to carry out the study solely with 23 MeV proton irradiations performed at KAZ. Mixed irradiated and purely neutron irradiated samples were added during the ddFZ200 irradiation campaign when it became obvious that neutron and proton irradiation led to different results with deep diffused material, which is explained in the following sections. The irradiation program is depicted in the first half of Table 7.3.

Table 7.3.: Summary of the irradiation program of the ddFZ240 and ddFZ200 campaign with respect to the accumulated fluences after neutron (Φ_n) and proton (Φ_p) irradiation as well as the ionizing dose. The fluences were chosen according to FLUKA predictions for different regions in the CMS Phase-2 Outer Tracker. The nominal fluence represents the highest expected fluence for 2S as well as PS region at 3000 fb^{-1}. The ultimate fluence incorporates safety margins compensating FLUKA uncertainties and a potential 4000 fb^{-1} extension of the HL-LHC. Low 2S and PS fluences represent the lowest expected fluence at 3000 fb^{-1}. Start 2S emulates the state of an Outer Tracker sensor within the first year of operation.

Region	Φ_n ($10^{14}\,n_{eq}cm^{-2}$)	Φ_p ($10^{14}\,n_{eq}cm^{-2}$)	Dose (kGy)
ddFZ240			
Low 2S	0	1	150
Ultimate 2S	0	6	900
Ultimate 2S	3	3	450
Nominal PS	0	10	750
ddFZ200			
Start 2S	0	0.1	15
Start 2S	0.1	0	0.1
Low 2S	0	1	150
Low 2S	1	0	1
Nominal 2S	0	3	450
Nominal 2S	3	0	3
Ultimate 2S	0	6	900
Ultimate 2S	6	0	6
Ultimate 2S	3	3	453
Nominal PS	0	10	1500
Nominal PS	10	0	10
Ultimate PS	0	15	2250
Ultimate PS	15	0	15

The fluence spectrum for the ddFZ200 campaign was extended, which was partly related to changes in the design of the tracker geometry that led to an update of the FLUKA predictions. The fluence expectations generally decreased for the outer layers of the tracker. Up to now, the highest expected fluence for the 2S region is $3 \cdot 10^{14}\,\mathrm{n_{eq}cm^{-2}}$ at $3000\,\mathrm{fb^{-1}}$. The fluence of $6 \cdot 10^{14}\,\mathrm{n_{eq}cm^{-2}}$ was kept as the ultimate 2S fluence with respect to a potential $4000\,\mathrm{fb^{-1}}$ extension of the HL-LHC and for comparability. Moreover, it was decided to add a ultimate PS fluence with incorporated margins for the $4000\,\mathrm{fb^{-1}}$ extension and an additional lower-end fluence of $1 \cdot 10^{13}\,\mathrm{n_{eq}cm^{-2}}$, which represents a sensor state within the first year of HL-LHC operation (Start 2S). It is important to note that the nominal fluences are only accumulated by less than 5% of the 2S and PS modules at $3000\,\mathrm{fb^{-1}}$ (see Figure 3.6). The second half of Table 7.3 summarizes the program of the ddFZ200 campaign. The annealing program for both campaigns is depicted in Table A.4. Table 7.3 also shows the total ionizing dose of the irradiation. The ionizing dose that is accumulated during the neutron irradiation is a result of an unavoidable gamma emission in the reactor. The expected dose in the Phase-2 Outer Tracker at $3000\,\mathrm{fb^{-1}}$ is in the order of 10 kGy for the 2S and 800 kGy for the PS region.

7.3. Electrical Characterization of ddFZ240 after Irradiation

The reference value of the damage rate, which is derived from the radiation damage induced leakage current increase after irradiation is $\alpha_{\mathrm{para}} = 4.14 \cdot 10^{-17}\,\mathrm{Acm^{-1}}$ [Mol99]. The experimentally found value for a fixed annealing time of 80 min at 60 °C in said reference is $\alpha_{\mathrm{Moll}} = 3.99 \cdot 10^{-17}\,\mathrm{Acm^{-1}}$. The value for α_{para} is derived from the parameterization of the damage rate for different annealing times. Since this parameterization is used very frequently in this thesis, e.g. to calculate the annealing equivalent at room temperature, it seemed more consistent to use α_{para} as the reference value. Figure 7.1 shows the radiation damage induced leakage current increase at $V_{\mathrm{bias}} = 600\,\mathrm{V}$, after a heat treatment of 80 min at 60 °C. The leakage current is scaled to $T = 20\,^{\circ}\mathrm{C}$ and sensor volume in cubic centimeters. The fit of the original data set (solid markers) yields $\alpha = (2.94 \pm 0.51) \cdot 10^{-17}\,\mathrm{Acm^{-1}}$, which is represented by the dashed black line. This value is 29% lower than the reference value. One has to address, that there is a methodical difference between the damage rate determination in Ref. [Mol99] and this thesis. In said reference, the bias voltage was always kept above the full depletion voltage of the measured sample. Regarding the Phase-2 Upgrade, one is mainly interested in determining the performance at a fixed bias voltage, like the maximum desired operation voltage of the CMS Outer Tracker of 600 V. Besides, the full depletion voltages of strip sensors exceed the measurement range of 1000 V for high fluences, which is discussed in the next paragraph and shown in Figure 7.7. Therefore, the dynamic bias voltage approach is not feasible. Moreover, α_{Moll} was deduced by using diodes. The studies presented in this chapter were carried out by using strip sensors, since the number of available diodes at ETP was limited (the majority of diodes was distributed among other institutes). The leakage current of sensors is usually higher because of the electric field configurations around the strips and a noticeable amount of surface currents. One could therefore expect to find larger damage rates from strip sensors.

The deviation between the reference value and α is mainly driven by two outliers at the nominal PS fluence of $1 \cdot 10^{15}\,\mathrm{n_{eq}cm^{-2}}$ (`S03` and `S07`). Their leakage current is about 25% lower than the leakage current of equally irradiated sensors (`S11` and `S18`), which significantly decreases the slope of the fit. The leakage current at high fluences might generally be smaller than expected due to an underdepletion, as a result of the fixed bias voltage approach. But this effect does not equally affect all sensors at the given fluence and can, therefore, not explain the

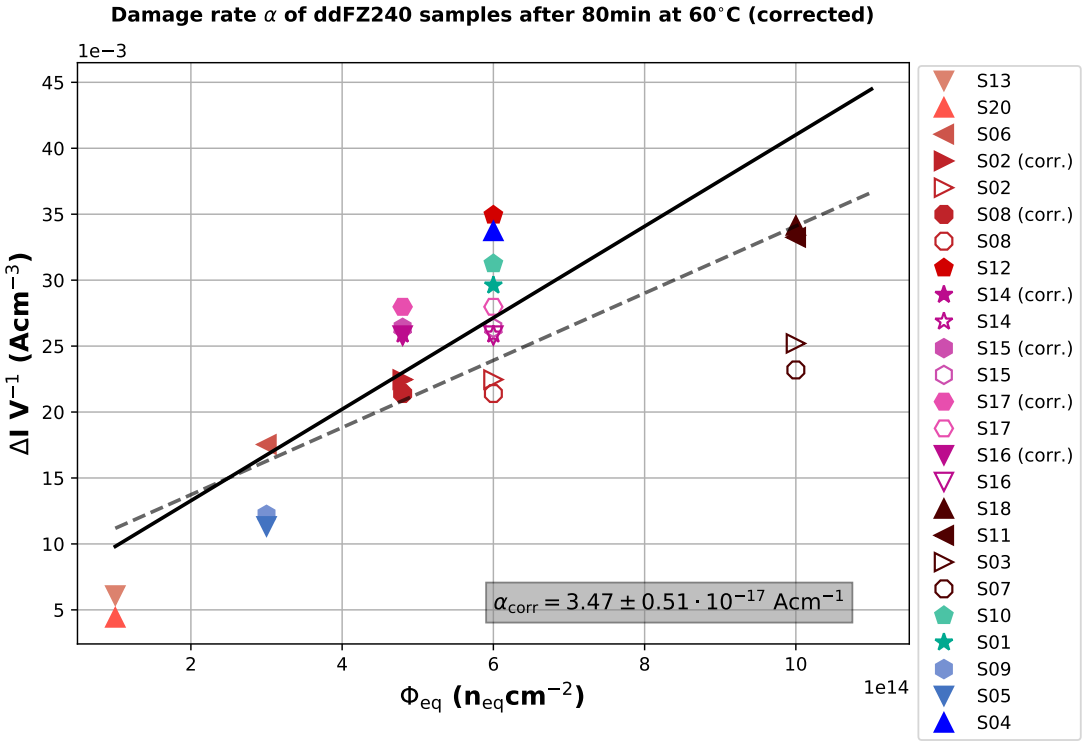

Figure 7.1.: Damage rate α of ddFZ240 at $V_{\text{bias}} = 600\,\text{V}$, after a heat treatment of 80 min at 60 °C. The current is normalized to sensor volume and $T = 20\,°\text{C}$. Proton irradiated samples are depicted in red and purple, neutron irradiated samples in blue and mixed irradiated samples in green. The fit of the initial data set yields a damage rate of $\alpha = (2.94 \pm 0.51) \cdot 10^{-17}\,\text{Acm}^{-1}$ (dashed black line). Investigations of the leakage current, CV and signal characteristics led to adjustments of the data, which are described in the text. The replaced or excluded data points are represented by hollow markers. The fit of the corrected data set yields a value of $\alpha_{\text{corr}} = (3.47 \pm 0.51) \cdot 10^{-17}\,\text{Acm}^{-1}$ (solid black line).

low leakage current of S03 and S07. An *underirradiation* could be another possible explanation, which should have noticeable impact on the signal. But the comparison between the signal of S03 and S18 presented in Section 7.4 does not indicate any severe deviation from the nominal fluence. At the ultimate 2S fluence of $6 \cdot 10^{14}\,\mathrm{n_{eq}cm^{-2}}$ one also finds large deviations among the measured leakage currents of ddFZ240 samples. The highest deviation (lowest leakage currents) can be observed for S8 and S2.

Unfortunately, the available CV data of irradiated ddFZ240 samples are incomplete. Technical issues with the LCR meters at the probe stations at the time the measurements were conducted, corrupted many of the measured CV characteristics. Furthermore, CV characteristics after annealing are not available since the ALiBaVa setup, in which the annealing studies of the sensors were performed, is not equipped with an LCR meter. An optimal evaluation of the full depletion voltage would require CV characteristics for different annealing steps in order to document the progression of V_{fd} over time. The available CV characteristics of irradiated ddFZ240 samples, measured at $T = -20\,^{\circ}\mathrm{C}$ and before heat treatment are presented in Figure 7.2. The values for knees and full depletion voltages are extracted by the V_{fd}-finding algorithm presented in Section 5.3. Since the plot incorporates samples with different sensor area, the capacitances in the plot were multiplied by different scaling factors in order to pull the plateaus to a similar level for better comparison. The scaling factors are denoted by s and can be found in the legend of the plot.

At the low 2S fluence of $1 \cdot 10^{14}\,\mathrm{n_{eq}cm^{-2}}$ the sensor S13 shows a fast depletion behavior with a knee around 230 V. The segment that follows the knee is not as horizontal as expected. This indicates delayed depletion processes. The V_{fd}-finding algorithm yields a full depletion voltage of 237 V. However, one can expect to see a slight increase of the signal for voltages above V_{fd} for sensors with such a CV characteristic. The purely neutron irradiated sample S05 with a fluence of $3 \cdot 10^{14}\,\mathrm{n_{eq}cm^{-2}}$ shows a full depletion voltage of 867 V with a knee located at 695 V. The CV characteristic of S14 clearly reveals an *underirradiation* of the sample. Its nominal accumulated fluence is $6 \cdot 10^{14}\,\mathrm{n_{eq}cm^{-2}}$, but the knee of its CV characteristic is located at 445 V with $V_{\mathrm{fd}} = 566\,\mathrm{V}$. For comparison, the similarly irradiated sensor S12 has an approximated full depletion voltage of 1137 V with a knee located at 817 V. Based on the results of other irradiation campaigns presented in this thesis, one would rather expect V_{fd} values close to 1000 V at this fluence before heat treatment. One can assume that the accumulated fluence of S14 is still within the most conservatively estimated range of uncertainty of the irradiation procedure of ±20%. This yields an adjusted fluence of $4.8 \cdot 10^{14}\,\mathrm{n_{eq}cm^{-2}}$, which appears to be more realistic compared to other data. The CV characteristic of the mixed irradiated sample S10 has its knee at 687 V and $V_{\mathrm{fd}} = 844\,\mathrm{V}$. The knee of the CV characteristic at the nominal PS fluence of $1 \cdot 10^{15}\,\mathrm{n_{eq}cm^{-2}}$ is located at 940 V. The full depletion voltage can no longer be determined with the V_{fd}-finding algorithm since it is outside the range of validity.

In conclusion, the CV data indicate that the degradation of mixed irradiated samples is driven by the neutron induced defects. This is shown in the comparison between the mixed irradiated sample S10 with an accumulated fluence of $6 \cdot 10^{14}\,\mathrm{n_{eq}cm^{-2}}$ and the neutron irradiated sample S05 with an accumulated fluence of $3 \cdot 10^{14}\,\mathrm{n_{eq}cm^{-2}}$. One can hardly see a difference in the depletion behavior despite the fact that S10 was exposed to an additional proton irradiation of $3 \cdot 10^{14}\,\mathrm{n_{eq}cm^{-2}}$. Moreover, the CV characteristic of S14 has led to an adjustment of its fluence value to $4.8 \cdot 10^{14}\,\mathrm{n_{eq}cm^{-2}}$. The comparison between S14 and the purely neutron irradiated sample S05, which accumulated a fluence of $3 \cdot 10^{14}\,\mathrm{n_{eq}cm^{-2}}$, indicates a stronger degradation due to neutron induced defects.

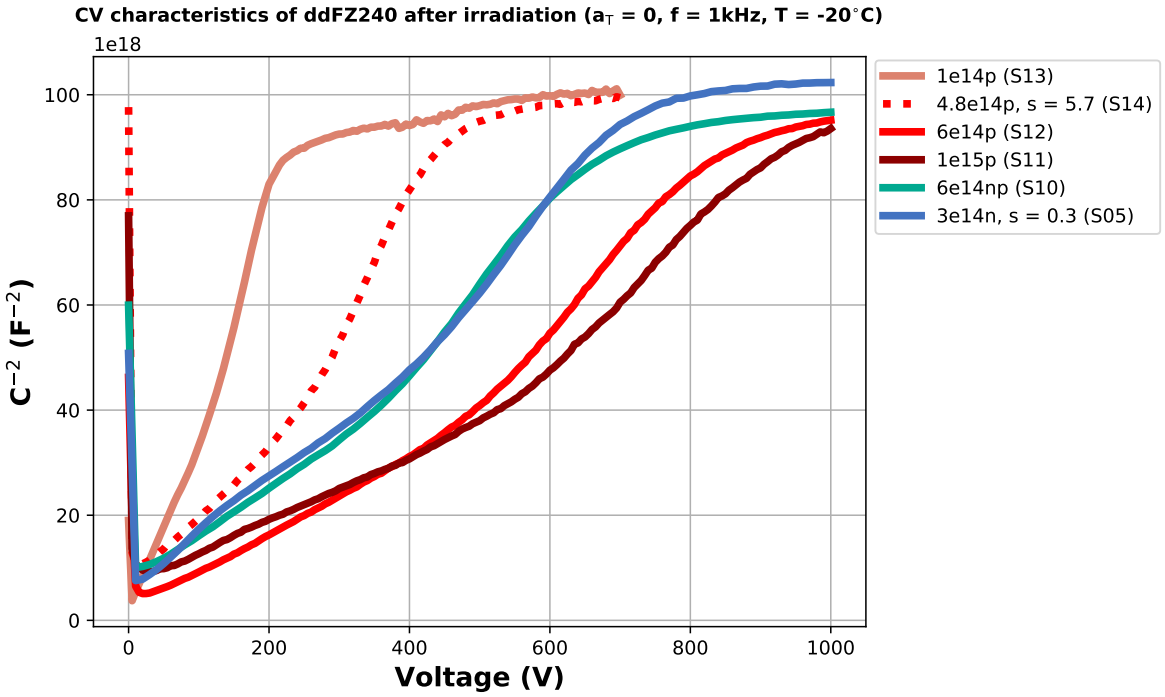

Figure 7.2.: CV characteristics of ddFZ240 for different fluences, measured at $T = -20\,°C$ with a frequency of 1 kHz and before heat treatment. Proton irradiated samples are depicted in red, neutron irradiated samples in blue and mixed irradiated samples in green. Since the plot incorporates samples with different sensor area, the capacitances of `S05` and `S14` are multiplied by scaling factors (s) in order to pull the plateaus to a similar level for better comparison. The sample `S14` has a nominally accumulated fluence of $6 \cdot 10^{14}\,\mathrm{n_{eq}cm^{-2}}$, but based on the unexpectedly low full depletion voltage, its fluence value was adjusted to $4.8 \cdot 10^{14}\,\mathrm{n_{eq}cm^{-2}}$.

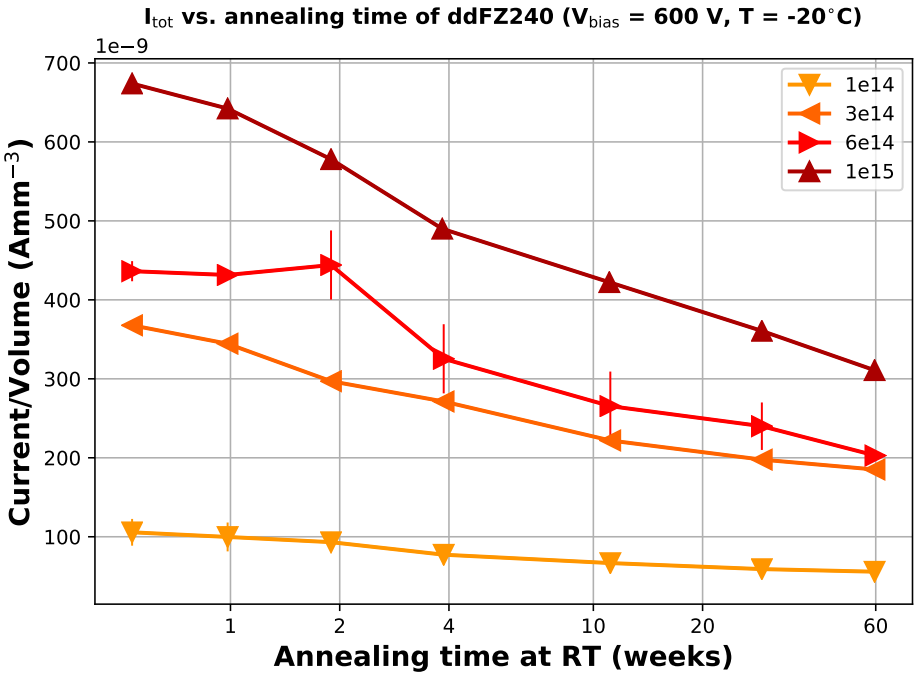

Figure 7.3.: Leakage current versus annealing time of ddFZ240 at $T = -20\,°\mathrm{C}$ and $V_{\mathrm{bias}} = 600\,\mathrm{V}$ for different fluences. The annealing time is scaled to weeks at room temperature. The data points represent the calculated mean values of the available samples. The error bars correspond to the standard deviation of the distribution of measurement values.

Based on the investigation of the CV characteristics, one can apply a number of justifiable corrections to the data presented in Figure 7.1 in order to increase the viability of the ddFZ240 study. The root of the unexpectedly low leakage current of `S03` and `S07` could not be identified. The data is not representative of sensors of this fluence and are, therefore, excluded from the fit. The set `S14 - S17` (purple markers) was irradiated in a separate batch for a test beam study. One can expect the same *underirradiation* for all of them. Thus, their fluence is adjusted by -20%, which is the most conservatively estimated uncertainty of the irradiation procedure. There are no CV characteristics available for `S08` and `S02`. However, the measurements of `S02` presented in Section 7.4 show a signal that is comparable to sensors with an accumulated fluence of $3 \cdot 10^{14}\,\mathrm{n_{eq}cm^{-2}}$. In combination with the unexpectedly low leakage current, one could argue that an *underirradiation* is likely and apply the same fluence adjustments for `S08` and `S02`. The replaced or excluded data points are represented by hollow markers. This shifts the result of the fit to $\alpha = (3.47 \pm 0.51) \cdot 10^{-17}\,\mathrm{Acm^{-1}}$ (solid black line), which deviates by 16% from the reference value, which corresponds to 1.3 standard deviations. This deviation appears acceptable, considering the underdepletion of `S11` and `S17` as a result of the fixed bias voltage approach.

The mean leakage current at $T = -20\,°\mathrm{C}$ at a bias voltage of 600 V for different annealing times and fluences is shown in Figure 7.3. The current is normalized to sensor volume. The data show that the leakage current is significantly reducible due to annealing. The envisaged annealing time for sensors in the Phase-2 Outer Tracker is two weeks per year or 20 weeks after ten years. The leakage current at $1 \cdot 10^{14}\,\mathrm{n_{eq}cm^{-2}}$ and 20 weeks of room temperature annealing is about $60\,\mathrm{nA\,mm^{-3}}$ which corresponds to a relative reduction of 40% with respect to the leakage current value after the first annealing step. At $6 \cdot 10^{14}\,\mathrm{n_{eq}cm^{-2}}$ the leakage current after

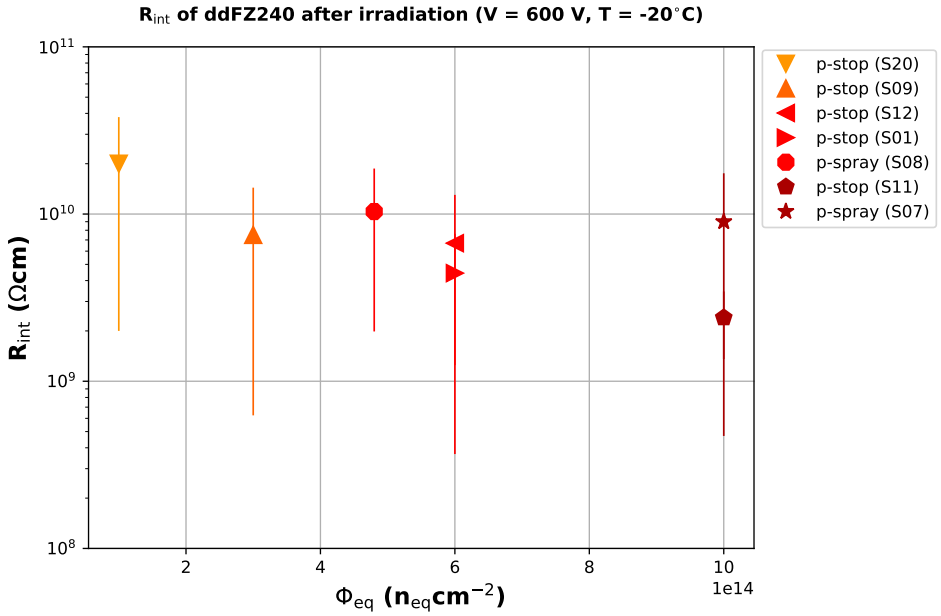

Figure 7.4.: Interstrip resistance of ddFZ240 after irradiation at $T = -20\,°\mathrm{C}$ and $V_{\mathrm{bias}} = 600\,\mathrm{V}$ for different fluences.

20 weeks of room temperature annealing is about $250\,\mathrm{nA\,mm^{-3}}$ which corresponds to a relative reduction of 50%. The data points for a fluence of $1 \cdot 10^{15}\,\mathrm{n_{eq}cm^{-2}}$ only include contributions from `S18`. The leakage current decreases by 60% to a value of $391\,\mathrm{nA\,mm^{-3}}$. As claimed in Ref. [Mol99], the expected relative leakage current reduction should be similar among irradiated (fully depleted) samples. The observed differences are most probably related to *underdepletion* and surface current annealing, which is not accounted for in the parameterization of the damage rate in said reference. The leakage current after irradiation and its annealing characteristic is an important input for thermal simulations of the modules. The leakage current is proportional to the power consumption per sensor. An upper limit for the leakage current after irradiation is not specified, yet.

The strip measurements after irradiation were conducted at $V_{\mathrm{bias}} = 600\,\mathrm{V}$ and $T = -20\,°\mathrm{C}$. The capacitances C_{int} and C_{c} are practically not affected by irradiation since they are dominated by geometrical effects and the strip and implant dimensions as well as the pitch are still the same. The strip leakage current naturally increases relative to the increase of I_{tot}. The resistance of the polyresistors is also not significantly affected by the radiation since their microscopic structure is amorphous. The calculated mean value is $R_{\mathrm{poly}} = 2.01 \pm 0.01\,\mathrm{M\Omega}$. The resistivity of the polyresistors is inversely proportional to temperature and therefore increases at low measurement temperatures. The two most important strip measurements after irradiation are the pinhole check and the interstrip resistance measurement. Two pinholes were detected among all irradiated ddFZ240 samples, which were not seen before irradiation. The samples are listed in Table A.3. Figure 7.4 shows R_{int} for different fluences normalized to the strip length. The TDR specification of $R_{\mathrm{int}} > 100\,\mathrm{M\Omega\,cm}$ can easily be met even at the highest available fluence.

7.4. Signal Measurements of ddFZ240

The seed signal over annealing time for different fluences of ddFZ240 samples measured at $V_{\text{bias}} = 600\,\text{V}$ and $T = -20\,^{\circ}\text{C}$ is depicted in Figure 7.5 starting at the first annealing step. The annealing time is normalized to weeks at room temperature. The transparent black lines at $12000\,\text{e}^-$ and $9600\,\text{e}^-$ highlight the lower limit of the 2S and PS-s signal specifications. The dashed black line emphasizes the envisaged annealing time of the Phase-2 Tracker of 20 weeks for $3000\,\text{fb}^{-1}$. The plot shows that sensors with $\Phi_{\text{eq}} \leq 3 \cdot 10^{14}\,\text{n}_{\text{eq}}\text{cm}^{-2}$ are well above the 2S signal specification at $V_{\text{bias}} = 600\,\text{V}$. Reverse annealing is not observable. Instead, the annealing has a beneficial effect on the seed signal throughout the study. The only deviation from this characteristic is observable after 60 weeks of annealing when the signal of the neutron irradiated sample decreases by around $1000\,e^-$.

The sensor `S02` was nominally irradiated to a fluence of $6 \cdot 10^{14}\,\text{n}_{\text{eq}}\text{cm}^{-2}$ with protons. Based on the unexpectedly low leakage current and the low difference between its signal and the signal of `S06` , it was concluded to assume an *underirradiation*. The fluence was therefore adjusted by -20% which yields $4.8 \cdot 10^{14}\,\text{n}_{\text{eq}}\text{cm}^{-2}$.

At the ultimate 2S fluence of $6 \cdot 10^{14}\,\text{n}_{\text{eq}}\text{cm}^{-2}$ one can clearly see the impact of neutron irradiation. The signal characteristic of the mixed irradiated sensor `S01` has a shape that is comparable to the one of `S02` or `S03`, which are both irradiated with protons. The shape changes significantly if more neutrons are added to the irradiation composition. The purely neutron irradiated sensor `S04` shows beneficial annealing of the signal by about $2200\,\text{e}^-$ up to the expected value of two weeks corresponding to 80 min at 60 °C, where the absolute seed signal is at $12300\,e^-$. This value is comparable to the signal of `S01`. The following reverse annealing decreases the signal by about $3500\,e^-$. The data indicate that defects generated by neutrons increase the degeneration of the charge collection of a strip sensor compared to proton generated defects at high fluences. These defects appear to be very sensitive to annealing. As a consequence, sensors that accumulate high neutron fluences limit the amount of annealing time that is beneficial for the detector. The maximum accumulated neutron fluence of CMS Phase-2 Outer Tracker modules is estimated to be $5 \cdot 10^{14}\,\text{n}_{\text{eq}}\text{cm}^{-2}$, which is represented by the ultimate 2S and PS fluences. Such a neutron fluence is expected only for a very small number of Outer Tracker modules in a potential $4000\,\text{fb}^{-1}$ scenario of the HL-LHC (plus additional safety margins). Therefore, the magnitude of reverse signal annealing as it is observed for `S04` is not expected for a realistic irradiation scenario. Nevertheless, at 800 V the signal of `S04` increases by roughly $2000\,e^-$ and is larger than the lower limit of the 2S signal specification of $12000\,e^-$ up to 29 weeks of annealing. Generally, the signals of ddFZ240 sensors are very responsive to an increase of the bias voltage above the desired maximum operation voltage of $V_{\text{bias}} = 600\,\text{V}$ (*bias voltage boosting*). A bias voltage boost up to 200 V at the end of the nominal HL-LHC run-time and especially during a potential $4000\,\text{fb}^{-1}$ scenario was already discussed within the CMS Tracker Community. The boost is considered acceptable if it can ensure a prolonged efficient operation of the sensors.

At the nominal PS fluence of $1 \cdot 10^{15}\,\text{n}_{\text{eq}}\text{cm}^{-2}$ the solely proton irradiated sensors show a similar behavior compared to the proton irradiated sensors of lower fluences. Beneficial annealing can be observed for longer than the expected two weeks. Reverse annealing is only observable at the end of the annealing study. The signal after 20 weeks for both sensors is around $11100\,e^-$, which is well above the lower limit of the PS-s signal specification of $9600\,e^-$. The ultimate PS fluence of $1.5 \cdot 10^{15}\,\text{n}_{\text{eq}}\text{cm}^{-2}$ was not part of the ddFZ240 irradiation study. However, based on the large signal margin of `S18` and `S03` at 600 V and the responsiveness of ddFZ240 towards

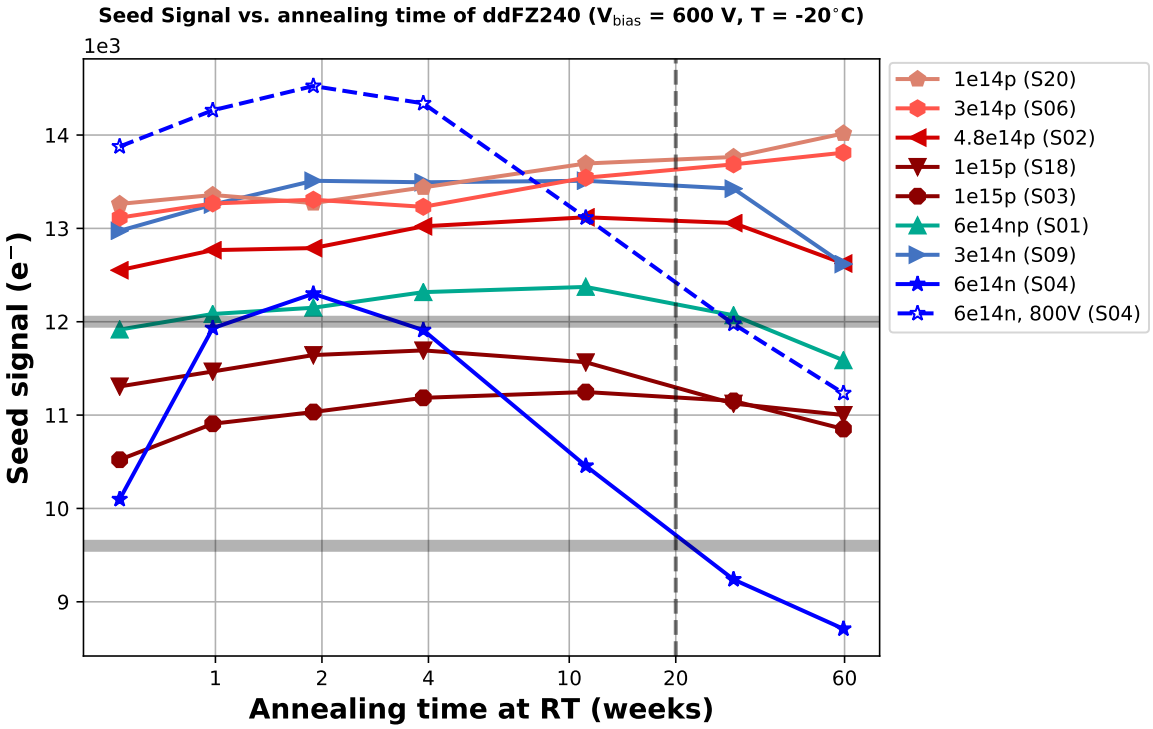

Figure 7.5.: Seed signal over annealing time normalized to weeks at room temperature of ddFZ240 at $V_{\text{bias}} = 600\,\text{V}$ and $T = -20\,°\text{C}$. A signal at $V_{\text{bias}} = 800\,\text{V}$ was added for `S04` which is represented by the dashed blue graph. The transparent black lines at $12000\,\text{e}^-$ and $9600\,\text{e}^-$ highlight the lower limit of the 2S and PS-s signal specifications. The dashed black line emphasizes the envisaged annealing time of the Phase-2 Tracker of 20 weeks at $3000\,\text{fb}^{-1}$.

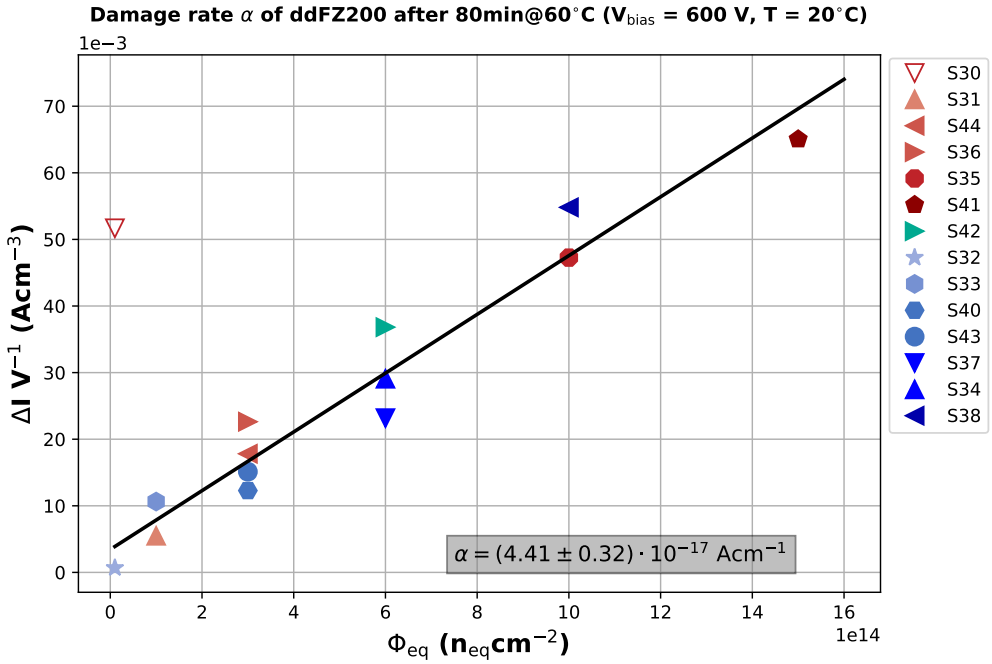

Figure 7.6.: Damage rate α of ddFZ200 at $V_{\text{bias}} = 600\,\text{V}$ after a heat treatment of 80 min at 60 °C. The current is normalized to volume and $T = 20\,°\text{C}$. Proton irradiated samples are depicted in red, neutron irradiated samples in blue and mixed irradiated samples in green. The sample `S30` was excluded from the fit because of a soft breakdown characteristic.

bias voltage boosting, one can safely assume that ddFZ240 sensors are efficiently operable after accumulating the ultimate PS fluence. In conclusion, the ddFZ240 sensors can meet the 2S and PS-s signal specifications for the nominal as well as the ultimate HL-LHC scenario. A bias voltage boost might be necessary during the $4000\,\text{fb}^{-1}$ extension.

7.5. Electrical Characterization of ddFZ200 after Irradiation

Figure 7.6 shows the radiation damage induced leakage current increase at $V_{\text{bias}} = 600\,\text{V}$, after a heat treatment of 80 min at 60 °C. The leakage current is normalized to $T = 20\,°\text{C}$ and sensor volume in cubic centimeters. The leakage current distribution of ddFZ200 samples is more consistent than the one of ddFZ240 and follows the expected characteristic quite nicely. The sensor `S30` is the only significant outlier, which is a result of a soft breakdown after irradiation. This data point was excluded from the fit. The fit yields $\alpha = (4.41 \pm 0.32) \cdot 10^{-17}\,\text{Acm}^{-1}$. The expected value of $\alpha_{\text{para}} = 4.14 \cdot 10^{-17}\,\text{Acm}^{-1}$ is within the limits of one standard deviation. The sources that can lead to deviations are explicitly described in Section 7.3.

The technical issues regarding CV measurements of irradiated samples were solved during the ddFZ240 irradiation campaign and CV data is therefore complete. The CV characteristics before heat treatment measured at $-20\,°\text{C}$ are shown in Figure 7.7. The plot incorporates sensors with different areas. In order to fit all graphs in one plot, the capacitances are multiplied by different scaling factors (s) for better comparability. The proton irradiated samples with an accumulated fluence of $1 \cdot 10^{13}\,\text{n}_{\text{eq}}\text{cm}^{-2}$ and $1 \cdot 10^{14}\,\text{n}_{\text{eq}}\text{cm}^{-2}$ show a fast depletion behavior with a knee located around 139 V and 246 V, respectively. However, the knee is followed by

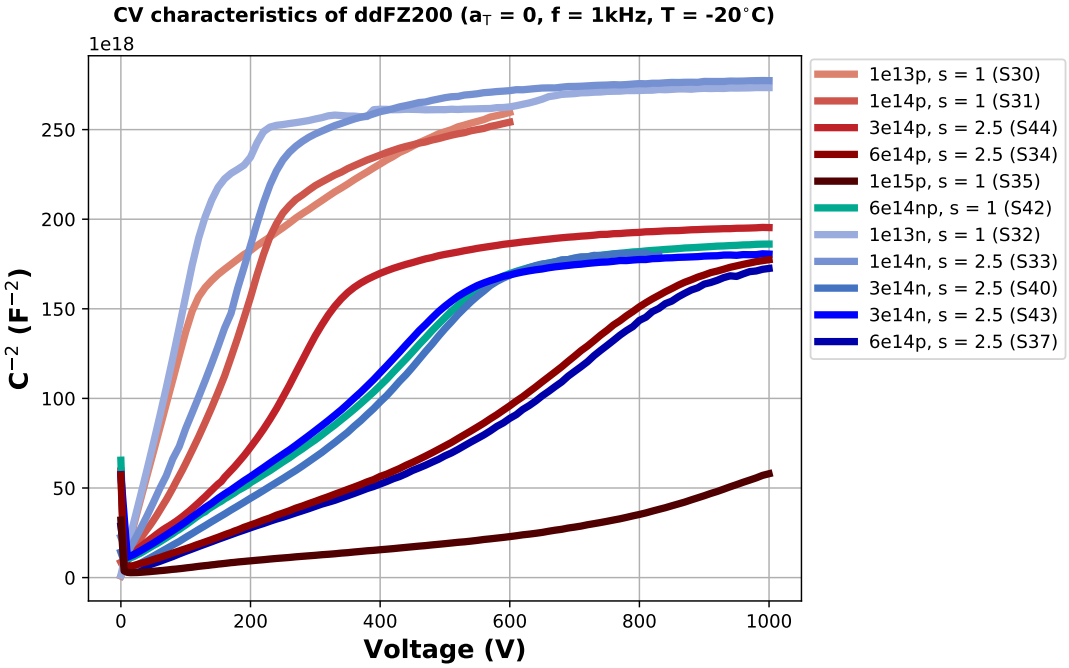

Figure 7.7.: CV characteristics of ddFZ200 strip sensors for different fluences, measured at $T = -20\,°C$ with a frequency of 1 kHz and before heat treatment. Proton irradiated samples are depicted in red, neutron irradiated samples in blue and mixed irradiated samples in green.

an unexpectedly steep saturation region. This behavior is not observed for neutron irradiated samples with equivalent fluences. Their full depletion voltage is located at 203 V and 274 V, respectively. The on-going depletion after the knee of the CV characteristic was also observed on a low-fluence proton irradiated ddFZ240 sensor. This feature is, therefore, related to the damage generated by proton irradiation. The full depletion voltage at the nominal 2S fluence is located at 436 V for proton and 623 V for neutron irradiation. At a fluence of $6 \cdot 10^{14}\,\mathrm{n_{eq}cm^{-2}}$ the proton and neutron irradiated sensors fully deplete outside the measured range of 1000 V. Their knee is located around 850 V. The characteristic of the mixed irradiated sample is similar to the ones with an accumulated fluence of $3 \cdot 10^{14}\,\mathrm{n_{eq}cm^{-2}}$, as if the proton irradiation did not generate any additional degradation. However, the degradation is observable in the increase of leakage current as shown Figure 7.6. The knee of CV characteristics at the nominal PS fluence of $1 \cdot 10^{15}\,\mathrm{n_{eq}cm^{-2}}$ is outside the measurement range.

The mean leakage currents of ddFZ200 samples for different annealing steps and fluences are depicted in Figure 7.8. The leakage current is normalized to sensor volume and was measured at $-20\,°C$ and 600 V. The only sample available at the ultimate PS fluence of $1.5 \cdot 10^{15}\,\mathrm{n_{eq}cm^{-2}}$ started to break down at 400 V during the annealing study. The remaining data points for this sample were approximated by applying the relative leakage current reduction obtained from the next lower fluence. Breakdowns during annealing studies or after irradiation also occurred randomly at lower fluences. Since the existing data follows the expected characteristic, these assumptions seem justifiable. A soft breakdown emerged during the annealing study of `S31` irradiated with $1 \cdot 10^{14}\,\mathrm{n_{eq}cm^{-2}}$ (protons). The data were also excluded from the mean calculation. Similarly to ddFZ240 measurements, the absolute leakage current reduction due to annealing is more pronounced the higher the accumulated fluence of the sample, which

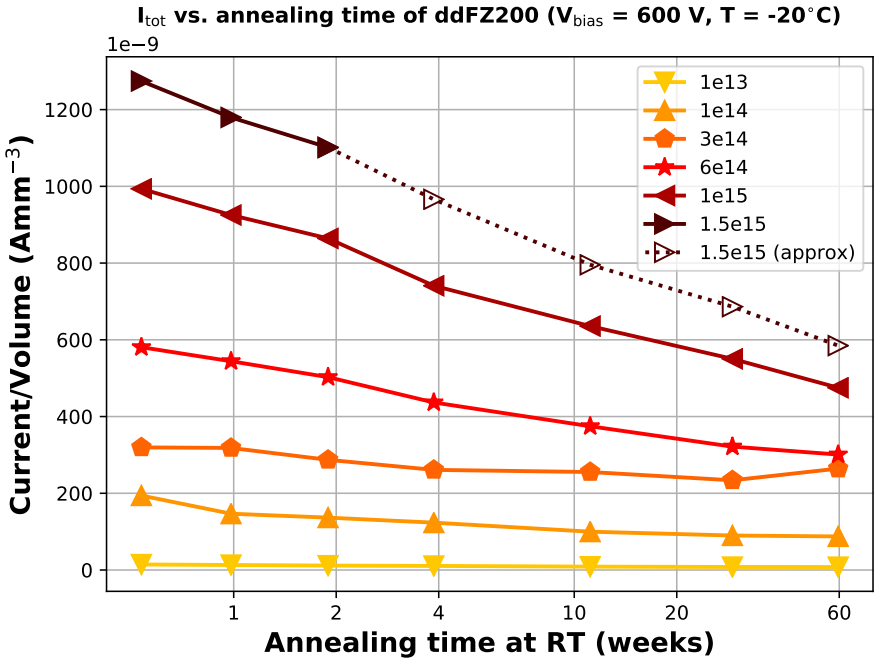

Figure 7.8.: Mean leakage current versus annealing time of ddFZ200 at $V_{\text{bias}} = 600\,\text{V}$ and $T = -20\,°\text{C}$ for different fluences normalized to volume. Only one sample was irradiated to a fluence of $1.5 \cdot 10^{15}\,\text{n}_{\text{eq}}\text{cm}^{-2}$ which broke down during the annealing study. The dotted line with hollow markers represents approximated values. The approximation is motivated in the text.

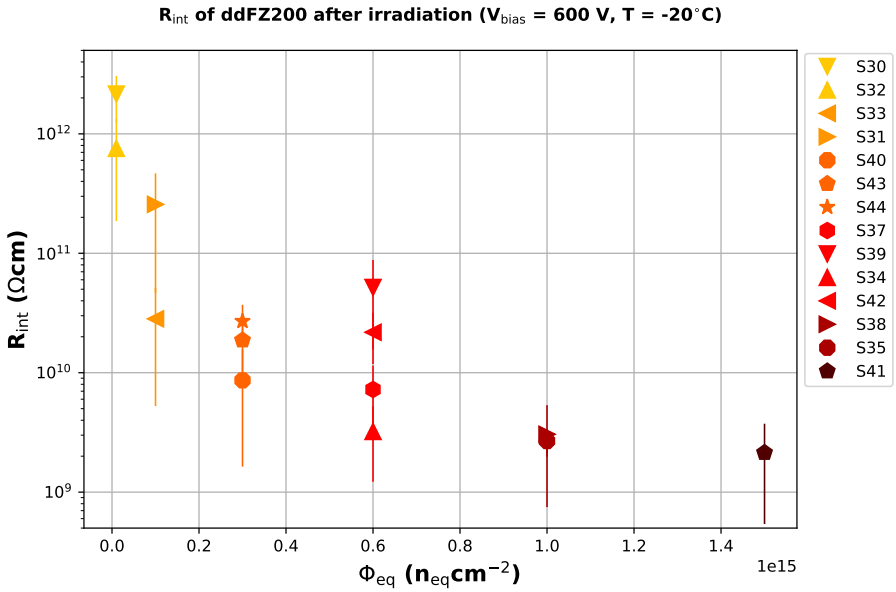

Figure 7.9.: Interstrip resistance of ddFZ200 strip sensors with p-stop isolation after irradiation at $T = -20\,°\text{C}$ and $V_{\text{bias}} = 600\,\text{V}$ for different fluences.

deviates from the conclusion made in Ref. [Mol99]. At a fluence of $1 \cdot 10^{13}\,\mathrm{n_{eq}cm^{-2}}$ and after an annealing time of 20 weeks at room temperature the material shows a mean leakage current of $8\,\mathrm{nA\,mm^{-3}}$, which corresponds to a relative leakage current reduction of 45% with respect to the value before heat treatment. At a fluence of $1 \cdot 10^{14}\,\mathrm{n_{eq}cm^{-2}}$ the leakage current amounts to $95\,\mathrm{nA\,mm^{-3}}$ which corresponds to a relative reduction of 49%. At $6 \cdot 10^{14}\,\mathrm{n_{eq}cm^{-2}}$ the leakage current is about $350\,\mathrm{nA\,mm^{-3}}$ and at $1 \cdot 10^{15}\,\mathrm{n_{eq}cm^{-2}}$ it is about $590\,\mathrm{nA\,mm^{-3}}$. This corresponds to a relative reduction of 40% and 41%, respectively. As already mentioned, an upper limit for the leakage current after irradiation is not specified, yet. The best way to evaluate the material performance in that regard, is to compare it to ddFZ240, which is done in Section 7.8.

The outcome of the strip measurements after irradiation is very similar to ddFZ240 strip measurements. The resistance of the polyresistors is increased due to the low measurement temperature to $R_{\mathrm{poly}} = 2.11 \pm 0.01\,\mathrm{M\Omega}$. The impact of irradiation on C_{int} and C_{c} is negligible. The strip currents increased with respect to the increase of I_{tot}. Three pinholes were detected among the irradiated samples which are listed in Table A.3. Figure 7.9 shows the normalized interstrip resistance after irradiation at 600 V and $-20\,^{\circ}\mathrm{C}$. Only sensors with p-stop isolation were irradiated in this campaign. R_{int} decreases with fluence but stays well above the specified value of $100\,\mathrm{M\Omega\,cm}$. The interstrip resistance appears to saturate above fluences of $6 \cdot 10^{14}\,\mathrm{n_{eq}cm^{-2}}$.

7.6. Signal Measurements of ddFZ200

Figure 7.10a depicts the seed signal over annealing time for different fluences of ddFZ200 samples measured at 600 V and $-20\,^{\circ}\mathrm{C}$. The annealing time is normalized to weeks at room temperature. The black dashed line highlights the envisaged annealing time at $3000\,\mathrm{fb^{-1}}$. The two solid black lines at $12000\,\mathrm{e^-}$ and $9600\,\mathrm{e^-}$ represent the lower limit of the signal specification for 2S and PS-s sensor, respectively. Proton irradiated samples are depicted in red, neutron irradiated samples in blue and mixed irradiated samples in green. As mentioned in Section 7.5, `S41` ($\Phi_{\mathrm{eq}} = 1.5 \cdot 10^{15}\,\mathrm{n_{eq}cm^{-2}}$) broke down during the annealing study. The data points for the missing annealing steps were approximated by using the relative signal change of `S35`, which is the sensor with next lower fluence. The flaws of this approach were already mentioned in Section 7.5. Nevertheless, it appears to be valid for a qualitative evaluation since the available data set of `S41` as well as the data set of the other highly irradiated sensors follow a similar characteristic. The proton irradiated sensors `S31` ($\Phi_{\mathrm{eq}} = 1 \cdot 10^{14}\,\mathrm{n_{eq}cm^{-2}}$) and `S44` ($\Phi_{\mathrm{eq}} = 3 \cdot 10^{14}\,\mathrm{n_{eq}cm^{-2}}$) had to be excluded from the plot because of corrupted Beetle chip calibrations. Since the 2S radiation environment is dominated by neutrons (Figure 3.7), the purely neutron irradiated samples should suffice to evaluate the performance of ddFZ200 for the low and nominal 2S fluence.

The purely neutron irradiated sensor `S40` which accumulated a fluence of $3 \cdot 10^{14}\,\mathrm{n_{eq}cm^{-2}}$ indicates the fluence margin under which these sensors are efficiently operable for the 2S region, since its signal characteristic exactly follows the $12000\,\mathrm{e^-}$ line. Signal annealing is hardly observable for this sensor. The signal characteristic of `S32` shows that 600 V suffices to operate a sensor with an accumulated fluence of $1 \cdot 10^{13}\,\mathrm{n_{eq}cm^{-2}}$ at full efficiency. Again, signal annealing is not observable. However, at a fluence of $1 \cdot 10^{14}\,\mathrm{n_{eq}cm^{-2}}$ the sensor `S33` shows slight beneficial annealing throughout the study.

The seed signal of samples with an accumulated fluence of $6 \cdot 10^{14}\,\mathrm{n_{eq}cm^{-2}}$ is very similar

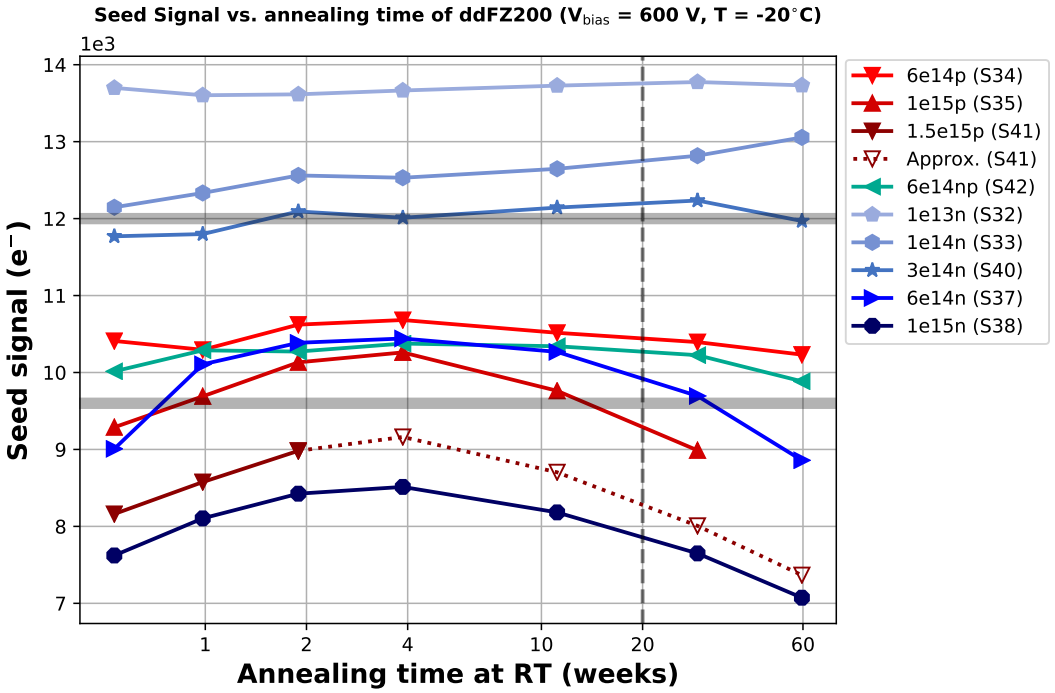

(a)

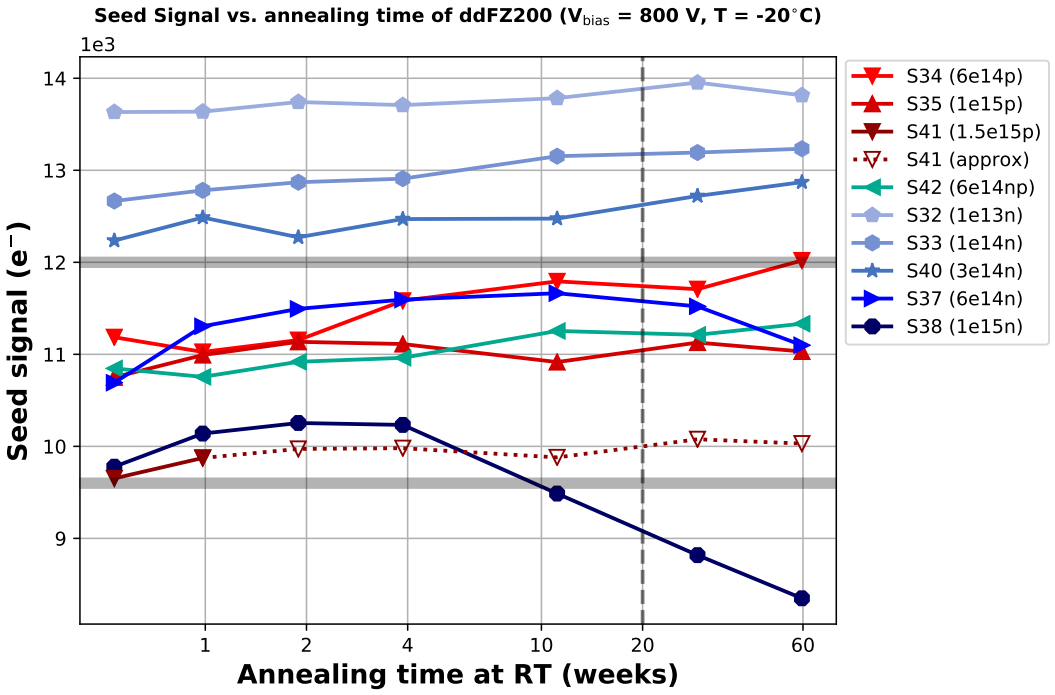

(b)

Figure 7.10.: Seed signal over annealing time normalized to weeks at room temperature of ddFZ200 at (a) 600 V, (b) 800 V and −20 °C. The transparent black lines at 12000 e^- and 9600 e^- highlight the lower limit of the 2S and PS-s signal specifications. The dashed black lines emphasizes the envisaged annealing time of the Phase-2 Tracker of 20 weeks at 3000 fb^{-1}. The dotted graphs with hollow markers represent approximated values. Proton irradiated samples are depicted in red, neutron irradiated samples in blue and mixed irradiated samples in green.

ranging between 10300 e^- and 10600 e^- after two weeks of annealing. The proton and mixed irradiated samples hardly show reverse annealing of the signal throughout the study. The neutron irradiated sample `S37` shows a beneficial annealing of the signal by about 1400 e^- followed by a reverse annealing of about 1500 e^-. The higher sensitivity of neutron irradiated sensors at this fluence towards signal annealing was already observed for ddFZ240 sensors. The effect was more pronounced for the thicker material. This indicates that the amount of signal annealing also depends on the thickness and, therefore, the width of the depletion volume. None of the available samples at this fluence manages to meet the 2S signal specifications at 600 V.

The most pronounced difference between neutron and proton irradiation can be observed at the highest available fluences. The signal of the proton irradiated sample `S41` with an accumulated fluence of $1.5 \cdot 10^{15}\,n_{eq}cm^{-2}$ is comparable to the signal of the neutron irradiated sample `S38` with an accumulated fluence of $1 \cdot 10^{15}\,n_{eq}cm^{-2}$, despite the fluence difference of 33%. In fact, `S38` shows the lowest measured signal of the ddFZ200 irradiation campaign, which is around 2000 e^- below the lower limit of the PS-s signal specification after 20 weeks of room temperature annealing. A similar observation can be made for the the proton irradiated sensor `S35` ($\Phi_{eq} = 1 \cdot 10^{15}\,n_{eq}cm^{-2}$) and the neutron irradiated sensor `S37` ($\Phi_{eq} = 6 \cdot 10^{14}\,n_{eq}cm^{-2}$), where the fluence difference of 40%. This indicates a stronger degradation of the signal due to neutron generated defects. As already mentioned in Section 7.4, the highest expected neutron fluence in the CMS Phase-2 Outer Tracker is $5 \cdot 10^{14}\,n_{eq}cm^{-2}$, which is accumulated by only a small fraction of modules at 4000 fb^{-1}. The high degradation of `S37` and `S38` is not expected in a realistic irradiation scenario.

Figure 7.10b depicts the measured signals of ddFZ200 at 800 V. The approximated values for `S41` are again calculated by applying the relative signal change of `S35` from step to step. The signal boost can improve the performance of ddFZ200 sensors noticeably, but does not suffice to increase the signal above 12000 e^- for accumulated fluences of $6 \cdot 10^{14}\,n_{eq}cm^{-2}$. Therefore, the usage ddFZ200 sensors is not sufficient for the 2S region in case of a 4000 fb^{-1} extension of the HL-LHC. The material is sufficient for the PS region up to 3000 fb^{-1} at 800 V. The suitability of ddFZ200 for the PS region up to 4000 fb^{-1} cannot be clearly evaluated. The signal of the approximated data for the ultimate PS fluence of $1.5 \cdot 10^{15}\,n_{eq}cm^{-2}$ meets the PS-s signal specification. However, the radiation damage generated by neutrons, as part of the realistic irradiation scenario in the detector, is expected to increase the degradation as well as the reverse annealing of the signal. To summarize the results of both plots, the material can provide sufficient signal up to 3000 fb^{-1} for 2S and PS region if the bias voltage is boosted to 800 V. Nevertheless, it fails to satisfy the 2S and, presumably, PS-s signal requirements for a potential 4000 fb^{-1} extension of the HL-LHC.

7.7. Impact of the Oxygen Concentration in Deep Diffused Material

The CV and signal data of the deep diffused irradiation campaign show differences in the degradation of the material after neutron and proton irradiation, which is more pronounced the higher the accumulated fluence. According to results of the initial Phase-2 sensor campaign carried out between 2010 and 2015 this was not expected to such an extent. The deep diffused material shows a strongly pronounced tolerance towards proton generated irradiation damage. Former studies like the ones presented in Ref. [WVK02; Lin+01] revealed that this feature can be attributed to a high oxygen concentration of a material. A typical oxygen concentration of a non-oxygenated silicon sensor is in the order of $1 \cdot 10^{15}$ O-atoms per cm^{-3}. HPK does not

provide detailed information about their manufacturing processes. However, measurements presented in Ref. [The20] have shown that the oxygen concentration in deep diffused material is in the order of $5.5 \cdot 10^{17}\,\mathrm{cm}^{-3}$. The oxygen concentration of HPK standard material (FZ290), which is characterized in Chapter 8, is in the order of $1.5 \cdot 10^{17}\,\mathrm{cm}^{-3}$. One can, therefore, expect a similar tolerance towards proton irradiation.

The degradation of a silicon sensor after irradiation is driven by the increase of V_{fd}, which is related to the change of N_{eff}, in the expected fluence range. It has been shown that the formation of electrically active V_2O defects (two vacancies that merged with an oxygen atom) play an important role in that process [Lin+01]. The V_2O defects act as additional acceptor states. The formation of $VO + V \rightarrow V_2O$ is suppressed if the possibility of a migrating vacancy to react with a oxygen atom is high enough $V + O \rightarrow VO$. The VO and emerging V_2O_2 defects are electrically neutral and do not take part in the degradation process [WVK02]. The difference between the defect generation of neutrons and charged particles manifests itself in the introduction rate of isolated point defects (e.g. vacancies). This introduction rate is high for charged particles. The reactions that were just mentioned are therefore typical for proton irradiated silicon sensors. Neutrons, on the other hand, produce mainly defect clusters, densely-spaced regions with high defect concentration, where the formation of V_i and eventually V_2O defects are more likely to happen. Thus, the radiation hardness of proton irradiated silicon sensors is more sensitive to oxygen concentration. Simulations which illustrate the different vacancy generation due to neutron and proton irradiation are presented in Ref. [Huh02].

The fact that neutrons and protons have a different impact on the degeneration of the depletion behavior is in its core a violation of the NIEL hypothesis. An improvement of the model is required in order to describe the damage scaling in oxygen-rich sensor materials which will be used for the CMS Phase-2 Tracker. The extension of the NIEL hypothesis is a research topic which is currently within the RD50 collaboration. Nevertheless, the 1 MeV neutron equivalent damage scaling works quite well because the radiation damage in the tracker is heavily dominated by fast hadrons (except for the 2S region).

7.8. Comparison of ddFZ240 and ddFZ200

The results of the electrical characterization of ddFZ240 and ddFZ200 before and after irradiation as well as signal measurements were presented in the previous sections. Both materials meet the electrical specifications, but the performance of ddFZ240 is superior to ddFZ200 in almost every aspect. The normalized leakage current of ddFZ240 at 500 V before irradiation is about one order of magnitude lower on average. The leakage current after irradiation, for two and 20 weeks of annealing at room temperature, measured at $T = -20\,^{\circ}\mathrm{C}$ and $V_{\mathrm{bias}} = 600\,\mathrm{V}$ is depicted in Figure 7.11. In order to compare the absolute leakage current generation of materials with different active thicknesses, measured on differently sized miniature sensors, one has to normalize I_{tot} to sensor area. The data points are extracted from the data presented in Figure 7.3 and Figure 7.8. Figure 7.11 shows that ddFZ240 produces a similar or even lower leakage current after irradiation. The power consumption per sensor at a certain fluence can be estimated by following formula:

$$P = I_{\mathrm{norm}} \cdot A_{\mathrm{2S}} \cdot V_{\mathrm{bias}} \ , \tag{7.1}$$

where I_{norm} is the leakage current normalized to sensor area and A_{2S} is the area of a 2S sensor. The power consumption depends on the applied bias voltage. This can vary between different

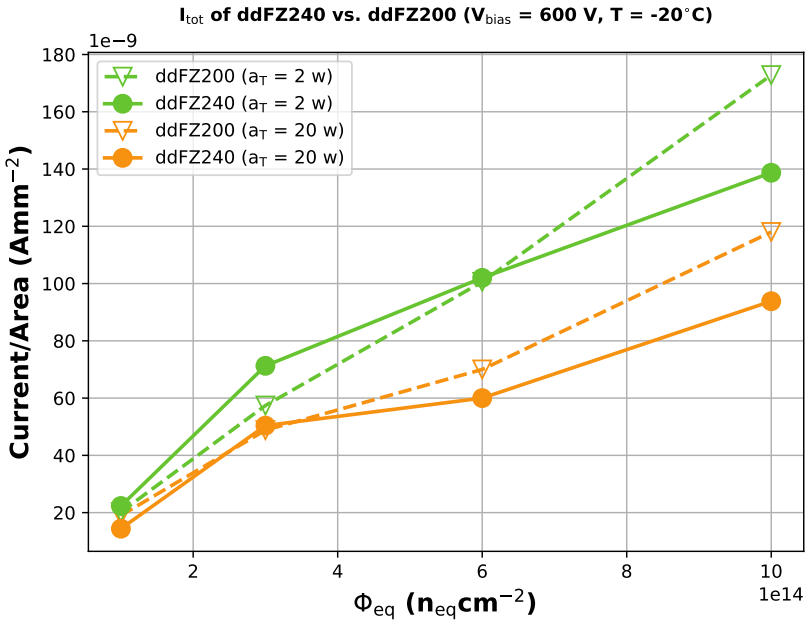

Figure 7.11.: Mean leakage current over fluence for ddFZ240 and ddFZ200 after two weeks and 20 weeks of annealing at room temperature, measured at $T = -20\,°\mathrm{C}$ and $V_{\mathrm{bias}} = 600\,\mathrm{V}$. Leakage current is normalized to area in order to compare the values of both materials.

sectors in the tracker. Moreover, ddFZ240 and ddFZ200 sensors require different bias voltages at different stages of the HL-LHC run-time (depending on annealing and fluence) in order to operate efficiently. For simplicity, one can compare the power consumption at a fixed bias voltage of 600 V, which is then equivalent to the characteristic shown in Figure 7.11. The anticipated benefit of ddFZ200 sensors, namely less leakage current and, therefore, less power consumption, cannot be confirmed at this voltage. The *underdepletion* that is observed for ddFZ240 sensors at high fluences and $V_{\mathrm{bias}} = 600\,\mathrm{V}$ is responsible for leakage current values that are below expectations. Moreover, ddFZ240 sensors show a better responsiveness towards leakage current annealing. This is most pronounced at high fluences and large annealing times.

The seed signals of ddFZ240 (circular markers) and ddFZ200 samples (triangular markers) for different fluences at 20 weeks of annealing at room temperature, measured at $T = -20\,°\mathrm{C}$ and $V_{\mathrm{bias}} = 600\,\mathrm{V}$ are depicted in Figure 7.12. The color code of the markers represents the irradiation composition. Signals at $V_{\mathrm{bias}} = 800\,\mathrm{V}$ were added for samples which do not meet the signal specification at the desired maximum operation voltage of 600 V. These signals are represented by hollow markers. All signal values were approximated by calculating the average of the measured signals at 11 and 29 weeks. The orange and yellow sectors highlight the required signal range for strip sensors in the 2S and PS region. The plot summarizes the available states of Phase-2 strip sensors with respect to $3000\,\mathrm{fb}^{-1}$ and $4000\,\mathrm{fb}^{-1}$. The fluence spectrum covers the expected fluences of all Outer Tracker layers in addition to the expected fluences at $4000\,\mathrm{fb}^{-1}$. The signals at $V_{\mathrm{bias}} = 600\,\mathrm{V}$ were fitted for both materials in order to highlight the signal trend, qualitatively. The quantitative validity is limited because of the inconsistent irradiation compositions that were used for the ddFZ240 and ddFZ200 campaign. Furthermore, the data points at the ultimate PS fluence of $1.5 \cdot 10^{15}\,\mathrm{n_{eq}cm^{-2}}$ were derived from approximations as was explained in Section 7.6. All signal specifications are met by ddFZ240. The material is suited for a $4000\,\mathrm{fb}^{-1}$ extension, where a bias voltage boost might be required.

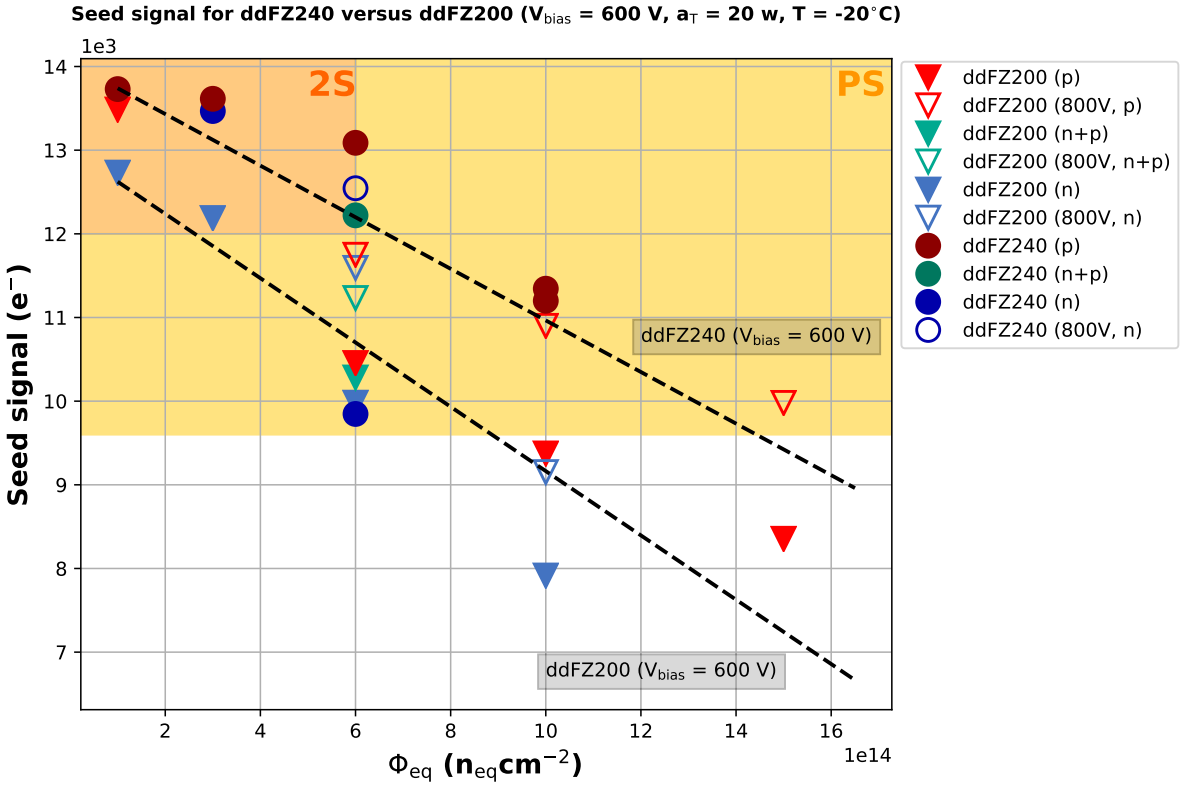

Figure 7.12.: Seed signal over fluence for ddFZ240 and ddFZ200 after 20 weeks of annealing at room temperature, measured at $T = -20\,°C$. Solid triangular markers represent results for ddFZ200 samples at $V_{bias} = 600\,V$. Solid circular markers represent signals of ddFZ240 samples. Hollow markers indicate signals at $V_{bias} = 800\,V$. The dashed lines represent fits of the signals at $V_{bias} = 600\,V$. The orange and yellow sectors highlight the required signal range for strip sensors in the 2S and PS region.

The ddFZ200 material can be used for 2S and PS region up to $3000\,fb^{-1}$. However, the data indicate that ddFZ200 sensors lack the required signal for a $4000\,fb^{-1}$ extension even at 800 V.

As a general outcome of the electrical characterization of ddFZ240 and ddFZ200 before and after irradiation, one can state that the interstrip resistance is sufficient up to the highest measured fluence of $1.5 \cdot 10^{15}\,n_{eq}cm^{-2}$. The p-stop and p-spray technology are both valid approaches to provide a sufficient interstrip resistance for n-in-p type silicon strip sensors. However, sensors with p-stop isolation appear to be more stable regarding leakage current and breakdown behavior. Besides, HPK implied that they are more confident in producing p-stop rather than p-spray sensors. This makes the p-stop technology the more favorable approach for Phase-2 Outer Tracker sensors. As discussed in Section 7.7, the high oxygen concentration of deep diffused material is responsible for a higher radiation tolerance towards proton irradiation. The signals of solely proton irradiated sensors show less reverse annealing and less degradation of the signal especially at higher fluences.

7.9. Conclusion

The results of the qualification and irradiation campaign performed on deep diffused sensors present ddFZ240 (deep diffused material with an active thickness of 240 µm) as a well-suited material choice for Phase-2 Outer Tracker sensors. A further reduction of the active thickness to 200 µm cannot be recommended because of an insufficient signal for a potential extension of the HL-LHC run-time as well as higher required bias voltages at the end of the nominal HL-LHC run-time. Moreover, ddFZ200 sensors did not show any significant benefit regarding the total leakage current after irradiation.

One has to address the fact that the initial conclusions presented in Ref. [CMS18] were drawn from a comparison of solely proton irradiated ddFZ240 sensors ($\Phi_{\text{eq}} = 6 \cdot 10^{14}\,\text{n}_{\text{eq}}\text{cm}^{-2}$) with other mixed irradiated HPK materials ($\Phi_{\text{eq}} = 7 \cdot 10^{14}\,\text{n}_{\text{eq}}\text{cm}^{-2}$). When irradiated with protons only, ddFZ240 shows a signal that is around $1000\,\text{e}^-$ above the lower limit of the 2S signal specification of $12000\,\text{e}^-$ at a fluence of $6 \cdot 10^{14}\,\text{n}_{\text{eq}}\text{cm}^{-2}$ and an annealing of 20 weeks at room temperature. The signal at an equal fluence decreases as soon as neutrons are involved in the irradiation process. With a neutron fraction of 50% the signal only ends up marginally above the specified value. Moreover, ddFZ240 hardly shows reverse annealing of the signal if only irradiated with protons. But the higher the neutron fraction of the irradiation mixture, the more apparent does the reverse annealing of the signal become. The additional radiation tolerance towards proton generated defects originates from a high oxygen concentration in deep diffused material. The magnitude of this effect was not understood until the end of this irradiation campaign. Overall, the material performance of ddFZ240 is sufficient but not as good as initially concluded in the TDR.

Regarding the general design features of the 2S sensor, one can state that the 2S design did not show any particular flaws that demand further adjustment. Most importantly, the interstrip resistance is sufficient up to the highest investigated fluence of $1.5 \cdot 10^{15}\,\text{n}_{\text{eq}}\text{cm}^{-2}$. The p-stop and p-spray technology are both valid approaches to contain a sufficient interstrip resistance for n-in-p type silicon sensors. However, sensors with p-stop isolation appear to be more stable regarding leakage current and breakdown behavior. The fact that HPK also favors p-stop over p-spray makes the p-stop technology the more favorable approach for Phase-2 Outer Tracker sensor design.

8

FZ290 and thFZ240 Irradiation Campaign

In 2018, HPK declared that deep diffused material can no longer be offered as a substrate for the CMS Phase-2 Outer Tracker sensor production. At this point, HPK had turned out to be the only company that complied with the CMS requirements for silicon sensor vendors and was able to provide sensors that met the Phase-2 sensor specifications. The CMS community was left with two remaining material offers: HPK standard float zone material (FZ290) or physically thinned float zone wafers. Based on the performance of ddFZ240 presented in Chapter 7 the community chose 240 µm as the thickness for the thinned material (thFZ240). One batch of 2S wafers of each material was ordered and received in November 2018 and January 2019. The results of this final 2S qualification and irradiation campaign were presented to the CMS Tracker community in September 2019. It was concluded to pick FZ290 as the material for all Phase-2 Outer Tracker sensors, based on the results presented in this chapter.

The results of the FZ290 and thFZ240 qualification and irradiation campaign were partly published in the master's thesis of J.-O. Gosewisch [Gos18] and the bachelor's thesis of U. Elicabuk [Eli19], who performed measurements and analyses under my supervision.

8.1. Electrical Characterization of FZ290 and thFZ240 before Irradiation

Table 8.1 shows the mean leakage current at $V_{\text{bias}} = 500\,\text{V}$ and $T = 20\,°\text{C}$ for different sensors/diodes. The leakage current is normalized to the sensor volume. The volume generated leakage current of FZ290 is exceptionally small and about two orders of magnitude below the TDR specification of $I_{500} \leq 2\,\text{nA/mm}^3$ [CMS18]. Two out of 111 measured samples were flagged because of a soft breakdown characteristic and excluded from the mean calculation. One sample showed a breakdown at 650 V, which is high enough in order to include it into the characterization process. The IV curves of FZ290 samples show a distinct characteristic, located in a bias voltage range of approximately 200 V to 300 V. The feature is presented in Figure 8.1a, which shows typical IV curves of three different sample designs (Irradiation, 2S and DiodeL), measured at $T = 20\,°\text{C}$ and normalized to sensor volume. The slopes of the curves increase exponentially and settle again at the end of the interval, which results in a step-like progression of the leakage current. It is likely that this effect is exclusively observed on FZ290 samples because of the small magnitude of their leakage current, rather than being a specific characteristic of the FZ290 material.

The normalized leakage current of thFZ240 sensors is higher than of FZ290 sensors, but still about one order of magnitude below the specified maximum value in the TDR. A comparison of the mean values of the total leakage currents shows that I_{tot} of a full-sized FZ290 strip sensor is 14% lower than the total leakage current of a full-sized thFZ240 strip sensor. This outcome does not follow the conventional expectation of the relation between active thickness and leakage current. The higher leakage current of thFZ240 is most likely related to the

Table 8.1.: Mean leakage current of $|I_{500}|$ at $V_{\text{bias}} = 500\,\text{V}$ and full depletion voltage V_{fd} of every tested sample. Measurements were conducted at $T = 20\,°\text{C}$. The capacitance was measured at $f = 1\,\text{kHz}$. The standard deviation of the distribution of V_{fd} is not included because it is smaller than the estimated uncertainty of V_{fd} of $\pm 10\,\text{V}$.

Material	Design	$\lvert I_{500}\rvert$ (nA/mm^3)	V_{fd} (V)	Number of samples
FZ290	Irradiation	0.048 ± 0.002	284	15
	KIT Test	0.047 ± 0.005	298	23
	PCommon	0.052 ± 0.021	292	6
	Baby	0.048 ± 0.027	290	24
	DiodeL	0.032 ± 0.004	252	17
	DiodeM	0.052 ± 0.007	241	18
	2S	0.086 ± 0.088	293	8
thFZ240	Irradiation	0.371 ± 0.036	195	13
	KIT Test	0.149 ± 0.047	205	16
	PCommon	0.290 ± 0.006	199	4
	Baby	0.158 ± 0.017	198	15
	DiodeL	0.119 ± 0.001	190	14
	DiodeM	0.228 ± 0.004	194	15
	2S	0.122 ± 0.024	205	5

Table 8.2.: Mean values of normalized strip parameters before irradiation of strip sensors at $V_{\text{bias}} = 300\,\text{V}$ and $T = 20\,°\text{C}$. Coupling capacitance was measured at $f = 1000\,\text{Hz}$ and interstrip capacitance to one next neighbor was measured at $f = 1\,\text{MHz}$. The values of the *Check* column indicate whether or not the TDR specifications are met [CMS18].

Material	Parameter	Value	No. of strips	Check
FZ290	I_{leak} (nA/cm)	0.008 ± 0.004	~ 1600	✓
	C_{c} (pF/(cm µm))	1.31 ± 0.01	~ 1500	✓
	R_{poly} (MΩ)	1.89 ± 0.01	~ 1500	X
	C_{int} (pF/cm)	0.485 ± 0.008	~ 800	✓
	R_{int} (TΩ cm)	1.89 ± 0.19	~ 800	✓
	Detected pinholes	0	~ 1600	-
thFZ240	I_{leak} (nA/cm)	0.021 ± 0.015	~ 1600	✓
	C_{c} (pF/(cm µm))	1.22 ± 0.01	~ 1600	✓
	R_{poly} (MΩ)	1.84 ± 0.01	~ 1600	X
	C_{int} (pF/cm)	0.461 ± 0.01	~ 1100	✓
	R_{int} (TΩ cm)	1.16 ± 0.3	~ 1100	✓
	Detected pinholes	37	~ 1600	-

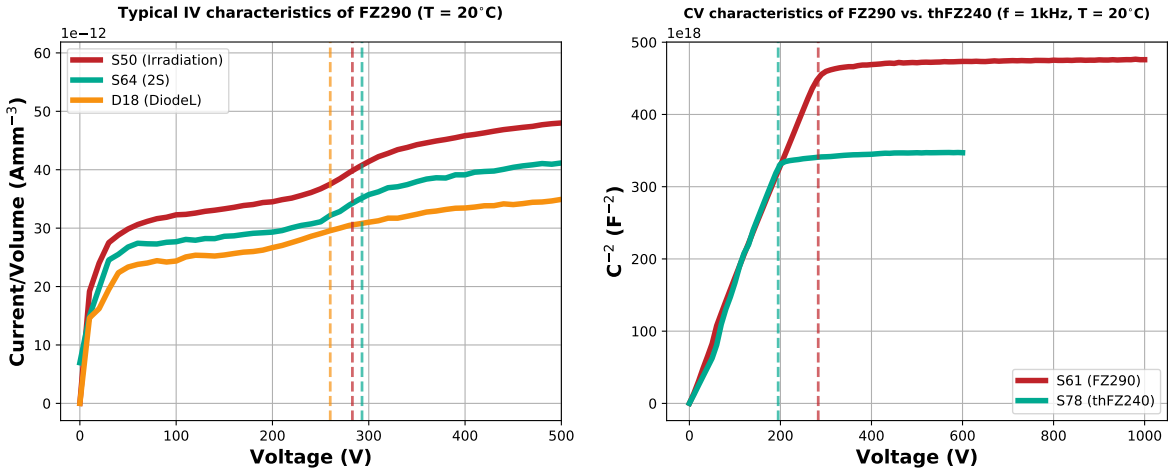

(a) (b)

Figure 8.1.: (a) Typical IV characteristics of FZ290 samples measured at $T = 20\,°C$ and normalized to sample volume for a range of 0 V to 500 V. The range was chosen in order to highlight the step-like characteristic of the curves within a bias voltage range of approximately 200 V to 300 V. The data stem from an Irradiation and 2S sensor as well as a large diode. The dashed vertical lines highlight the measured full depletion voltages of these samples. (b) Typical CV characteristics of FZ290 and thFZ240 sensors measured at $T = 20\,°C$.

thinning process. The thinning can be expected to create additional lattice defects close to the backside region of the sensor. This backside region is active for thFZ240 sensors, which increases the overall leakage current. FZ290 sensors benefit from the 30 µm thick backside implantation which protects the active region from such defects. Both batches were produced from the same base material and were processed on the same production line. As confirmed by HPK, the front-side processing of both FZ290 and thFZ240 is identical. The thinning and metallization of the backside of thFZ240 is an additional process step performed afterwards. In terms of miniature sensors and diodes, only one out of 77 measured samples showed a leakage current above the specified maximum value during the initial measurement. However, the qualification process revealed substantial issues of the thFZ240 material. The thFZ240 senors are sensitive towards mechanical stress and scratches on the sensor backside. This resulted in soft breakdowns, ohmic IV characteristics and increased leakage currents during repeated measurements in the probe station. The issue occurred mainly among 2S sensors and was only observed on a single miniature sensor. The issue is presented in more detail in Section 8.2. The FZ290 and thFZ240 sensors, which were flagged because of unexpectedly high current, are listed in Table A.1.

The depletion behavior of both materials is fairly distinct as shown in Figure 8.1b. This was to be expected for thinned sensors because the active volume and, therefore, the extent of the depletion zone are strictly limited by the shallow backside implant and the aluminum backplane. One has to be aware of the fact that the 30 µm backside implant of FZ290 is created via (deep) diffusion. Therefore, one could have expected a similar fuzziness of the depletion behavior as it was observed for ddFZ240 and ddFZ200. Since this is not the case, one can assume that this feature only occurs for backside implants larger than 30 µm. The mean depletion voltage for each sample design is listed in Table 8.1. The approximate uncertainty for each value is ±10 V (see Section 5.8.2). The full depletion voltage for FZ290 sensors is between

284 V and 298 V. The material meets the TDR specification of $V_{\mathrm{fd}} < 300\,\mathrm{V}$. The range of full depletion indicates that the step-like effect in the FZ290 IV characteristics is related to the extent of the depletion zone. It can be assumed that the depletion zone begins to penetrate the backside region of the material around 200 V when the effect starts to show. The leakage current follows the expected characteristic after the whole sensor is depleted. The thinned samples deplete at low voltages with a V_{fd} between 195 V and 205 V. The thFZ240 diodes show a full depletion voltage that is quite similar to the value found for sensors. From measurements on deep diffused as well as FZ290 diodes one could have expected a full depletion voltage that is about 20% lower compared to V_{fd} of sensors. This is also indicated by a theoretical evaluation using Equation (4.5). For both materials one finds the KIT Test and the 2S sensor design to show the highest full depletion voltage. A similar observation is described in Section 7.1, where design specific variations of V_{fd} were attributed to a potential systematic temperature gradient of the heating device that controls the diffusion process during fabrication. The base material of FZ290 and thFZ240 is processed similarly. Potential variations of N_{eff} due to the heat gradient could still be noticeable after thinning. The depth of the N_{eff} variation in the base material with a physical thickness of 320 µm would have to exceed 80 µm (amount of material that is removed during the thinning process of thFZ240). However, measurements regarding the change of N_{eff} over depth are not available.

The strip and interstrip measurements before irradiation were conducted at $V_{\mathrm{bias}} = 300\,\mathrm{V}$ and $T = 20\,^{\circ}\mathrm{C}$. The interstrip capacitance C_{int} to one next neighbor was measured at $f = 1\,\mathrm{MHz}$. The coupling capacitance C_{c} was measured at $f = 1000\,\mathrm{Hz}$. The adjustment of the C_{c} measurement frequency from 100 Hz to 1000 Hz took placed in the beginning of the FZ290 qualification campaign. A handful of samples were still measured at 100 Hz, though. The increase of the measurement frequency results in a decrease of C_{c} by about 5%. Another measurement parameter that was adjusted during the campaign is the voltage ramp of the interstrip resistance measurement. The motivation for adjusting these measurement parameters is explained in Section 5.4 in greater detail. The strip leakage current I_{leak}, C_{int} and the interstrip resistance R_{int} are normalized to the strip length. The coupling capacitance is normalized to strip length and strip width. The mean strip parameters were calculated using the exclusion principles explained in Section 5.4. The results of the mean value calculation are presented in Table 8.2.

The strip leakage current roughly follows the trend of the total leakage currents that were observed for both materials. The sample `S62` showed a mean leakage current that was within the specifications but two orders of magnitude above the mean value of every other measured FZ290 sensor. It was excluded from the mean value calculation (Table 8.2). Three leaky strips with a current above 2 nA/cm were found on two FZ290 sensors (Table A.2). The mean values of C_{c} obtained from thFZ240 samples is close to the minimum specified value in the TDR and about 8% lower than the mean value found among FZ290 samples. This indicates differences in the oxide properties. There is no observable difference between mean interstrip capacitance, which is to be expected because of the equivalent strip and pitch dimensions. The mean resistance of the polyresistors is similar but slightly outside the specified range of $R_{\mathrm{poly}} = 1.5 \pm 0.3\,\mathrm{M\Omega}$. This tendency was already observed among the latest deep diffused batch. As stated before, the specified value can easily be adjusted if HPK is more comfortable with producing polyresistors with a resistance closer to 2 MΩ rather than 1.5 MΩ. The most important feature regarding these resistors is their uniformity among the sensor. The TDR states a maximum deviation of 5% among all strips. The calculated standard deviations are below 1% for both batches. The interstrip resistance is sufficient in both cases. No pinholes were detected for FZ290 sensors. The 37 pinholes that were detected for thFZ240 were found on a single sample (Table A.3). This indicates extensive oxide damage on this particular sensor.

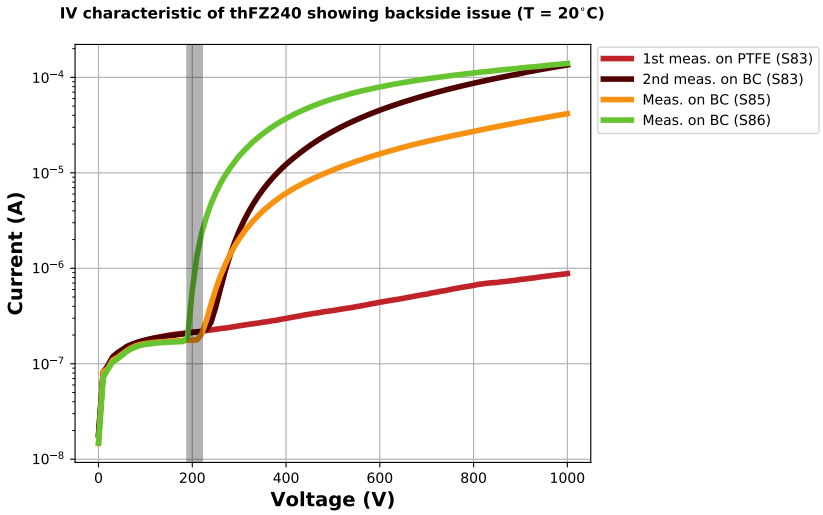

Figure 8.2.: IV characteristic of thFZ240 2S sensors measured at $T = 20\,°\text{C}$, which developed high leakage currents due to scratches on the backside. The sensor `S83` was initially measured on a chuck covered with PTFE foil in order to create a soft surface. The sensor started to break down after remeasuring it on a bare aluminum chuck (BC). The IV measurements of `S85` and `S86` were also carried out on a bare aluminum chuck.

8.2. Sensitivity of thFZ240 Sensors

A certain amount of robustness is mandatory for Phase-2 Outer Tracker sensors, because mechanical stress and backside scratches are unavoidable. The FZ290 sensors meet this requirement. Issues were not observed among deep diffused or FZ290 sensors because of their physical thickness of 320 µm and a passive, highly doped backside implant of at least 30 µm. The backside implant protects the sensor from distortions in the aluminum backplane and reduces the backside sensitivity significantly. The thFZ240 sensors revealed a severe sensitivity regarding mechanical stress and scratches on the sensor backside during the measurement campaign. The issue is mainly limited to 2S sensors. Only one incident can be reported where such an issue was observed on a miniature sensor. Scratches and mechanical stress appear to be responsible for soft breakdowns, ohmic IV characteristics and increased leakage currents which occurred during repeated measurements in the probe station. This was reported from all institutes within the CMS Outer Tracker Sensor Working Group which were involved in the 2S characterization process. All 2S sensors were initially received by HEPHY [Insa], measured once and then distributed among the other institutes. The issue was not observed during this initial measurement. In order to clearly identify scratches as the root of the issue, the chuck of a ETP probe station was covered with PTFE[1] foil. The foil was pierced atop the vacuum holes to enable vacuum fixation. The sensors were operated via front-side biasing, which allows the operation of the sensor via two front-side connections (see Chapter 10). The five thFZ240 2S sensors which were included in the calculations presented in Table 8.1 were measured with this configuration. Thereby, irreversible damage of the sensors could be avoided. Typical IV curves that outline the issue are presented in Fig 8.2. The initial IV measurement of `S83` was carried out on a PTFE surface and revealed nothing abnormal (red curve). A high leakage current as a result of a strongly pronounced soft breakdown was observed as the sensor was measured for a second time on the bare aluminum chuck (darkish red curve). The two other 2S sensors

[1] Polytetrafluoroethylene

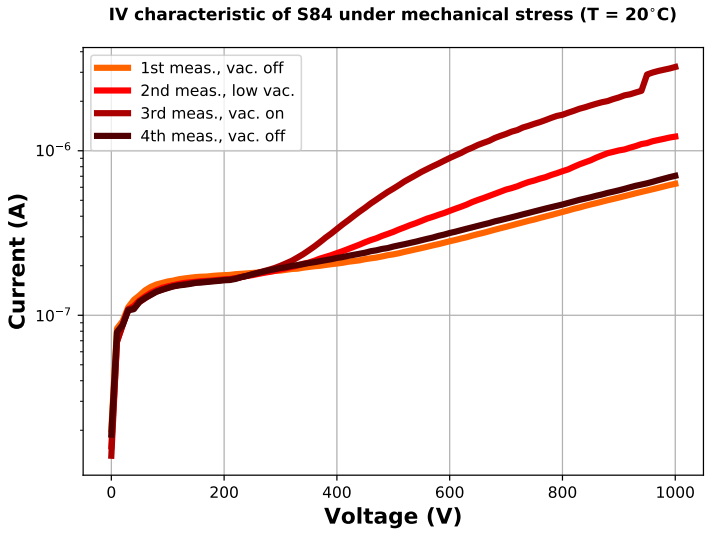

Figure 8.3.: IV characteristic of the 2S sensor `S84` at $T = 20\,°\mathrm{C}$. The chuck surface was covered with a PTFE foil in order to avoid scratches on the backside. The sensor was exposed to different levels of mechanical stress by turning the vacuum system on and off and using different vacuum hole configurations.

in the plot were also measured on a bare chuck and showed a similar abnormality right away. The transparent black line at roughly $V_{\mathrm{bias}} = 200\,\mathrm{V}$ highlights the region in which the break down started to occur. This value corresponds to the full depletion voltage of thFZ240 sensors and indicates a significant increase of the electric field as soon as the depletion zone reaches the backside. Furthermore, it was observed that mechanical stress directly translates into a reversible change of the IV characteristic, which is shown in Figure 8.3. The plot shows four consecutive measurements of `S84` that were carried out with different vacuum configurations on the PTFE foil-covered chuck. The first and fourth measurement were conducted without vacuum fixation. They show the expected IV characteristic throughout the measurement. Only a small set of vacuum holes was used for the second and all available vacuum holes for the third measurement. The sensor develops a soft breakdown at around 300 V as a consequence of the fixation. The slope of this soft breakdown characteristic can be controlled by varying the mechanical stress acting upon the sensor. The start of the soft breakdown is clearly above the full depletion voltage of the sensors. The root of this phenomenon is, therefore, different to the one illustrated in Figure 8.2 and not related to mechanical damage on the backside.

In reality, sensors are not flat, but usually convexly bent. Wafer bow and wafer warpage are common features that result from merging different materials with different lattice coefficients, which creates tension within the compound. In order to evaluate the bow of the sensors, qualitatively, the absolute surface height was measured at 15 locations on the sensor via a digital microscope. The data set was smoothened by calculating a bivariate B-spline representation of the given surface. Figure 8.4a and Figure 8.4b depict the interpolated surfaces of `S63` (FZ290) and `S83` (thFZ240). The x-position corresponds to the strip axis (parallel to to the strips). The y-position represents the position perpendicular to the strips. The sensors were measured along their full y-range and from cut edge to the strip segmentation in the center. The full sensor surface could not be measured because of the limited travel of the microscope. Since the nominal sensor thickness represents a mere offset in the obtained z-values, the data were normalized by subtracting the nominal sensor thickness (320 µm for FZ290 and 240 µm for thFZ240). The measured locations were chosen equidistantly according to alignment marks

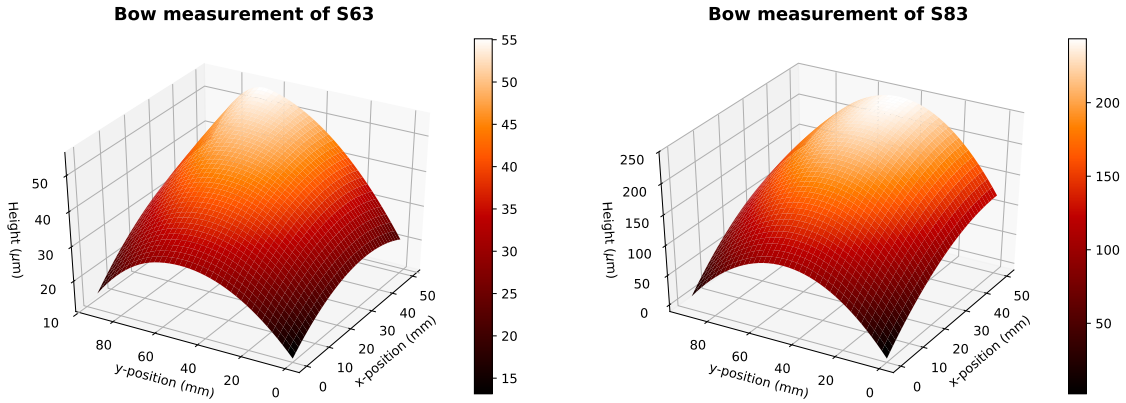

(a) **(b)**

Figure 8.4.: Results of a bow measurement of a (a) FZ290 and a (b) thFZ240 2S sensor. The x-position correspond to the strip axis (in parallel to to strips). The y-position represents the position perpendicular to the strips. The sensors were measured along their full y-range and from cutting edge to the strip segmentation in the center. The z-values were normalized by subtracting the nominal sensor thickness. The measurement yields a maximum bow of $b_{\mathrm{FZ290}} = 45\,\mu\mathrm{m}$ and $b_{\mathrm{thFZ240}} = 240\,\mu\mathrm{m}$.

located at the periphery of the sensor. The outermost data points represent a position about 320 µm away from the cut edge. The uncertainty of this optical measurement approach is hard to estimate. These kind of measurements are usually carried out with specialized metrology stations. The lowest measured point for `S63` is 13 µm larger than the expected thickness of the sensor of 320 µm. For `S83` the difference is 14 µm. Thus, a conservative estimation of the measurement uncertainty appears to be ±20 µm. The uncertainty of the manufacturing process itself is stated as ±10 µm by the vendor. In the end, the measurement yields a maximum bow of $b_{\mathrm{FZ290}} = 45\,\mu\mathrm{m}$ and $b_{\mathrm{thFZ240}} = 240\,\mu\mathrm{m}$. Bow measurements performed at other institutes yielded similar results. The qualitative outcome of this investigation is that the bow of the sensors is more pronounced the smaller their physical thickness. Therefore, the mechanical stress for thFZ240 sensors can be expected to be high during the vacuum fixation, where the sensors are sucked onto the chuck and are flattened out.

Scratches are created during the placement and fixation of the sensor on a chuck. Corner and edge region of the sensors carry most of the weight as a result of the sensor bow and slide outwards during the vacuum fixation. The backside of thFZ240 and FZ290 sensors were examined with a digital microscope. Figure 8.5a shows a snapshot of a corner section of `S84` before it was measured in a probe station at ETP. The scratches are mostly superficial, but the picture illustrates the increased exposure of the corner and edge section. The red box highlights a typical scratch mark that can be found on several and only on thFZ240 2S sensors. The scratch marks were not produced during measurements. They are assumed to be produced at HPK as part of a sensitivity test, which would indicate that HPK was aware of the backside issues (HPK never confirmed nor denied that). However, the sensors are protected from defective regions and high currents that emerge at the edges by the guard ring and the edge implants. These scratches should not affect the sensor performance at all. Typical scratches within the active region of the sensor backside are presented in Figure 8.5b. They can be caused by tiny metal chips or burrs at the chuck surface. Pressure marks from vacuum holes were observed as

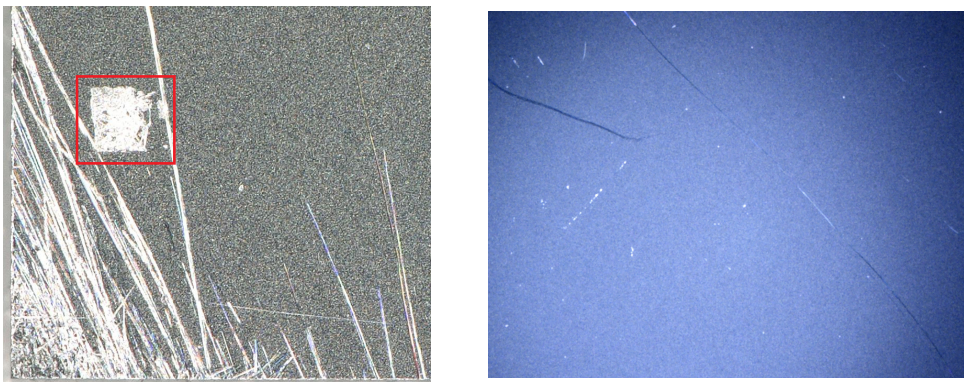

(a) (b)

Figure 8.5.: (a) Backside scratches in the corner region of a thFZ240 2S sensor. The red box highlights a scratch mark that was not produced during a measurement. These scratch marks were found on several thFZ240 2S sensors. The pictures was taken before the sensor was measured at ETP. (b) Typical backside scratches inside of the active region of a 2S sensor as they are produced during placement and fixation on a chuck.

well. The aluminum layer on the backside is about 1 µm thick. The digital microscope was not able to clearly resolve the depth of these scratches, which indicates that the depth is below 1 µm.

As already mentioned, this issue was observed by every institute that was involved in the 2S qualification of thFZ240. The custom-made chucks of the ETP probe stations are made from aluminum, which is a standard material for these kind of applications. Their surface was deburred and polished. Other institutes use commercial chucks with gold alloy finish or the like. Therefore, the issue occurred with different kinds of chucks and vacuum hole configurations. If this issue only appeared at one institute, one could attribute the thFZ240 issues to the chuck material, its design or surface quality. But since these issue were observed everywhere, one has to conclude that large thFZ240 sensors are oversensitive. The sensitivity of the thFZ240 sensors would be a major problem during the Phase-2 module production. The sensor qualification centers are going to fully qualify at least one sensor per batch in their probe stations. If sensors frequently broke during the qualification process, the batches could not be cleared for further usage. Even if the probe station chucks were covered with PTFE, which turned out to be the only surface material with which backside damage was avoidable, the sensors would need to pass additional steps and tests during module assembly. During this process the sensors are placed on different types of chucks for handling, gluing or other measurements. The backside is exposed to potential surface damage on multiple occasions. Moreover, the sensors are going to be fixated on support structures in the final module and undergo temperature cycles on multiple occasions which creates mechanical stress.

8.3. Irradiation Program

Fluences for the FZ290 and thFZ240 irradiation campaign were chosen according to updated FLUKA [Fer+05] predictions for the Phase-2 Outer Tracker presented in Ref. [CMS18]. The nominal fluence corresponds to the highest expected values of the 2S and PS region at 3000 fb^{-1}. Since less than 5% of the modules are exposed to this amount of radiation, it was decided to add a lower representative 2S and PS fluence to the program. The ultimate fluences incorporate ad-

Table 8.3.: Summary of the irradiation program of the final 2S irradiation campaign with respect to the accumulated fluences after neutron and proton irradiation as well as the ionizing dose. The approximate fluences of the respective regions of the CMS Phase-2 Outer Tracker are split into a low and the nominally highest fluence as well as an ultimate fluence, which includes several safety margins with respect to a potential 4000 fb^{-1} extension. The total fluence is composed of a neutron and a proton share which corresponds to the predicted ratio of neutrons and charged particles in the CMS Phase-2 Outer Tracker.

Set	Neutron irrad. ($10^{14}\,\mathrm{n_{eq}cm^{-2}}$)	Proton irrad. ($10^{14}\,\mathrm{n_{eq}cm^{-2}}$)	Total fluence ($10^{14}\,\mathrm{n_{eq}cm^{-2}}$)	n-fraction	Dose (kGy)
Low 2S	0.75	0.25	1	75%	37.5
Low PS	1	2	3	33%	300
Nom. 2S	2.5	0.5	3	83%	75
Nom. PS	4	6	10	40%	900
Ult. 2S	5	1	6	83%	150
Ult. PS	5	10	15	33%	1500

ditional margins that compensate for FLUKA uncertainties and a potential 4000 fb^{-1} extension of the HL-LHC performance scenario. The final values were matched to the ones chosen for the deep diffused irradiation campaigns for comparability. The irradiation program is presented in Table 8.3. The results of irradiation campaign presented in Chapter 7 have shown that proton and neutron irradiation have different effects on annealing characteristic and charge collection efficiency for materials with high oxygen concentration (explained in Section 7.7). Therefore, it was decided to perform mixed irradiations. The neutron and proton shares correspond to the predicted ratio of neutrons and charged particles in the tracker (Figure 3.7). The particle composition of the 2S region is dominated by a neutron share of roughly 80%. This is a consequence of the backscattering from the hadronic calorimeters. The PS region on the other hand, is dominated by charged particles, primarily pions. The charged particle share is about 66%. The expected dose in the Phase-2 Outer Tracker at 3000 fb^{-1} is in the order of 10 kGy for the 2S and 800 kGy for the PS region. The ionizing dose that is accumulated during the neutron irradiation is a result of unavoidable gamma emission in the reactor and is in the order of 1 kGy per $1 \cdot 10^{14}\,\mathrm{n_{eq}cm^{-2}}$. The dose accumulation during the irradiation with 23 MeV protons is 150 kGy per $1 \cdot 10^{14}\,\mathrm{n_{eq}cm^{-2}}$.

There are two Irradiation sensors and two diode sets (consisting of 2 to 3 diodes each) for each of the six fluence combinations. The annealing program of the sensors was changed compared to the former annealing routine. The goal was to create a smoother and more granular signal over annealing characteristic. The steps are summarized in Table A.5. Sensors were annealed in the ALiBaVa setup during automated annealing and charge collection studies. Diodes were annealed in a drying oven whose temperature is controlled via the same type of temperature sensor that is used in the ETP probe stations and ALiBaVa setup. The reduced annealing program for diodes is summarized in Table A.6.

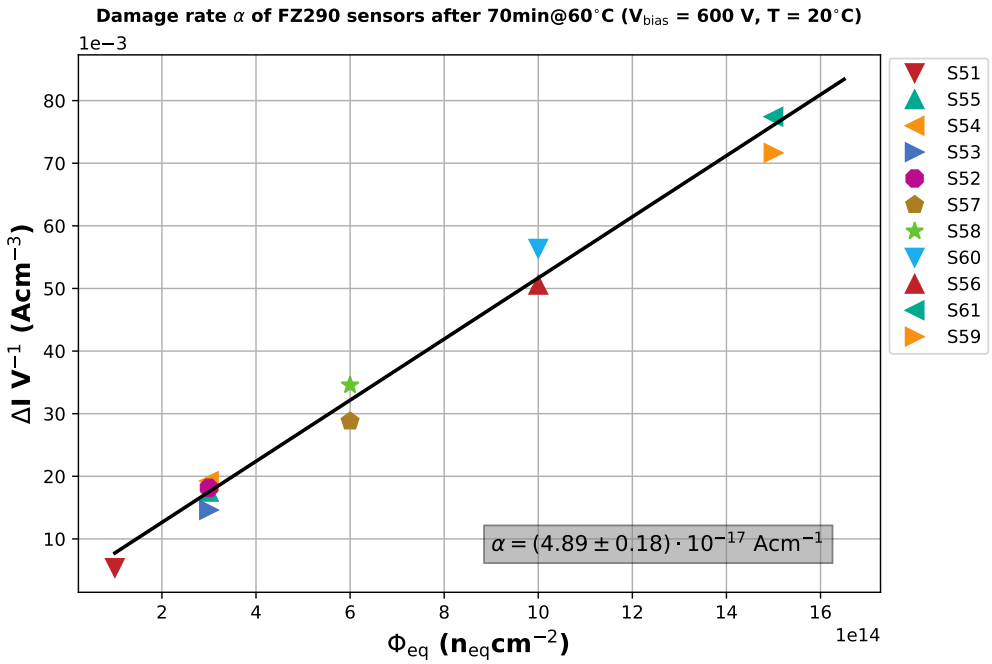

Figure 8.6.: Damage rate α of FZ290 sensors at $V_{\text{bias}} = 600\,\text{V}$ after a heat treatment of 70 min at 60 °C. The current is normalized to volume and $T = 20\,°\text{C}$.

8.4. Electrical Characterization of FZ290 after Irradiation

Figure 8.6 depicts the radiation damage induced leakage current increase at $V_{\text{bias}} = 600\,\text{V}$ and after a heat treatment of 70 min at 60 °C scaled to $T = 20\,°\text{C}$ and normalized to sample volume. Because of the reduced heat treatment the sensors should be slightly below the point of maximum beneficial annealing of 80 min at 60 °C as claimed by Ref. [Mol99]. The expected damage rate for diodes is $\alpha_{\text{para}} = 4.23 \cdot 10^{-17}\,\text{Acm}^{-1}$. The fit of the given data set yields $\alpha = (4.89 \pm 0.18) \cdot 10^{-17}\,\text{Acm}^{-1}$ which deviates by 16% from the reference value. The sensor `S50` was excluded, because of a soft breakdown that occurred during the annealing study, which resulted in a leakage current in the order of 100 µA. The (relatively small) deviation from the reference value is related to the fixed bias voltage of 600 V and the resulting underdepletion of the sensors at high fluences. This is indicated by Figure 8.9, which shows CV characteristics of irradiated diodes. This results in lower leakage currents. As already mentioned, diodes have smaller depletion voltages than sensors because of the shape of the electric field close to the strips. Nevertheless, diodes which accumulated $\Phi_{\text{eq}} \geq 6 \cdot 10^{14}\,\text{n}_{\text{eq}}\text{cm}^{-2}$ fully deplete far above $V_{\text{bias}} = 600\,\text{V}$. The underdepletion leads to lower leakage currents. By increasing the number of data points and measured fluences, one would most probably find a non-linear characteristic emerging between fully depleted and underdepleted sensors.

As shown by all damage rate plots in this thesis so far, the leakage current of irradiated sensors deviates from the reference value presented in Ref. [Mol99]. The deviation is mainly caused by the fact that the parameterization in this reference was obtained from diode measurements at a bias voltage slightly above V_{fd}. Compared to diodes, sensors have larger surface currents as well as higher electric fields emerging at the front-side around the strips. Diodes were added to the irradiation study to evaluate the bulk generated leakage current more precisely. The leakage current of the FZ290 diodes was measured after a heat treatment of 80 min at 60 °C and is presented in Figure 8.7. The measured damage rate is $\alpha = (4.27 \pm 0.12) \cdot 10^{-17}\,\text{Acm}^{-1}$

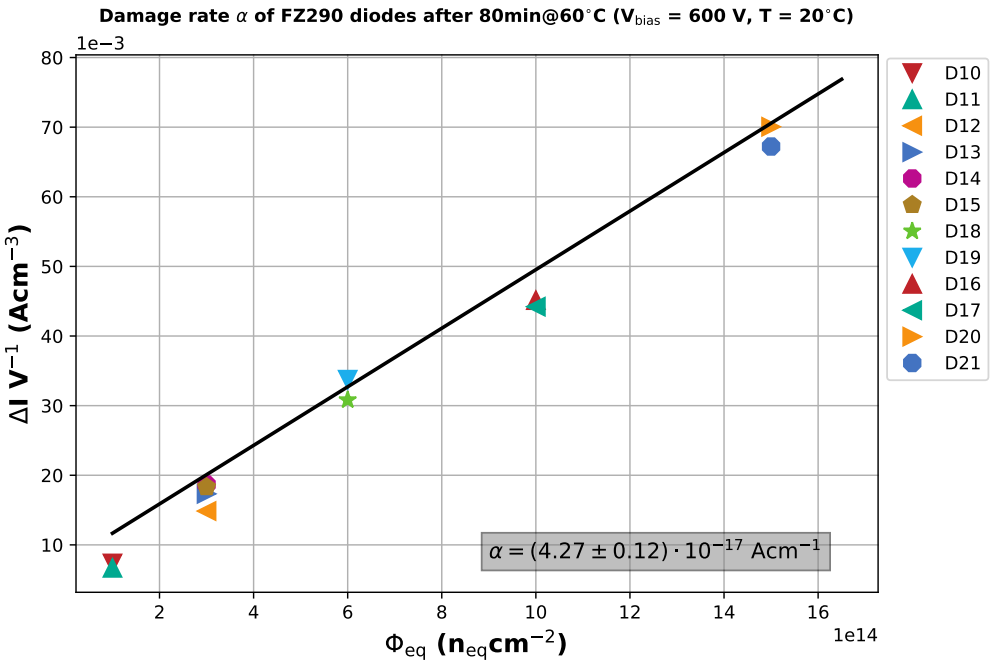

Figure 8.7.: Damage rate α of FZ290 at $V_{\text{bias}} = 600\,\text{V}$ after a heat treatment of 80 min at 60 °C. The current is normalized to volume and a $T = 20\,°\text{C}$.

and deviates by only 3% from the reference value, which shows that the fixed bias voltage approach is accurate enough the study the bulk generated leakage current of the material with diodes.

The mean leakage current for different fluences and annealing times is presented in Figure 8.8. The current was measured at $T = -20\,°\text{C}$, $V_{\text{bias}} = 600\,\text{V}$ and was normalized to volume. The annealing time is scaled to weeks at room temperature. The plot shows the benefit of leakage current annealing especially at higher fluences. The envisaged annealing time for sensors in the Phase-2 Outer Tracker is two weeks per year or 20 weeks at $3000\,\text{fb}^{-1}$. The leakage current at $1 \cdot 10^{14}\,\text{n}_{\text{eq}}\text{cm}^{-2}$ and 20 weeks is about $64\,\text{nA}\,\text{mm}^{-3}$. This yields a relative reduction of 46% with respect to the leakage current after the first annealing step of 10 min at 60 °C, which corresponds to two days of annealing at room temperature. At $3 \cdot 10^{14}\,\text{n}_{\text{eq}}\text{cm}^{-2}$ the leakage current after 20 weeks is about $183\,\text{nA}\,\text{mm}^{-3}$ which corresponds to a relative reduction of 50%. The leakage current at $6 \cdot 10^{14}\,\text{n}_{\text{eq}}\text{cm}^{-2}$ decreased by 47% to a value of $352\,\text{nA}\,\text{mm}^{-3}$. The leakage current at $1 \cdot 10^{15}\,\text{n}_{\text{eq}}\text{cm}^{-2}$ decreased by 49% to a value of $632\,\text{nA}\,\text{mm}^{-3}$. The data set for a fluence of $1.5 \cdot 10^{15}\,\text{n}_{\text{eq}}\text{cm}^{-2}$ reveals a reducibility of the leakage current to a value close to the next lower fluence. Here, the leakage current after 20 weeks is about $694\,\text{nA}\,\text{mm}^{-3}$ which corresponds to a reduction ratio of 85%. This contradicts the conclusions made in Ref. [Mol99], which states that the relative reduction ratio is equal for every fluence (for fully depleted diodes). A similar observation was already reported in Chapter 7. The deviations are related to the fixed bias voltage and the resulting *underdepletion* at higher fluences.

The evaluation of the full depletion voltage after irradiation is based on CV measurements performed with FZ290 diodes shown in Figure 8.9. The diodes were annealed in a drying oven according to the annealing program shown in Table A.6 and measured in an ETP probe station. Figure 8.10 presents the extracted full depletion voltages of FZ290 diodes for different

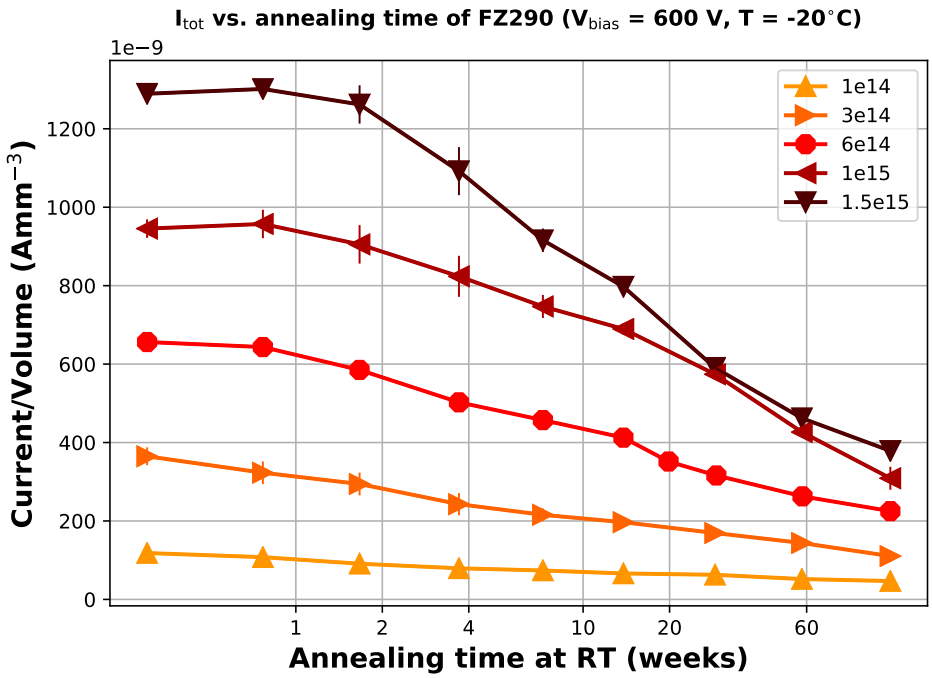

Figure 8.8.: Leakage current of FZ290 sensors, measured at $T = -20\,°C$, for different annealing times and fluences. The annealing time is scaled to weeks at room temperature.

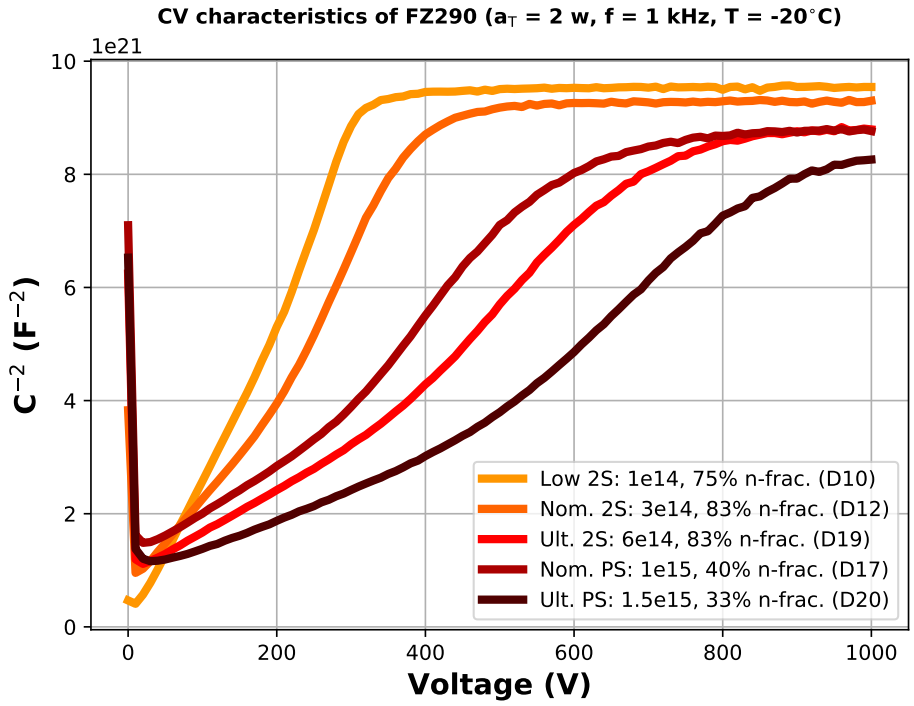

Figure 8.9.: CV characteristics of FZ290 diodes for different fluences measured at $T = -20\,°C$ with a frequency of 1 kHz and an annealing of 80 min at 60 °C, which corresponds to two weeks at room temperature.

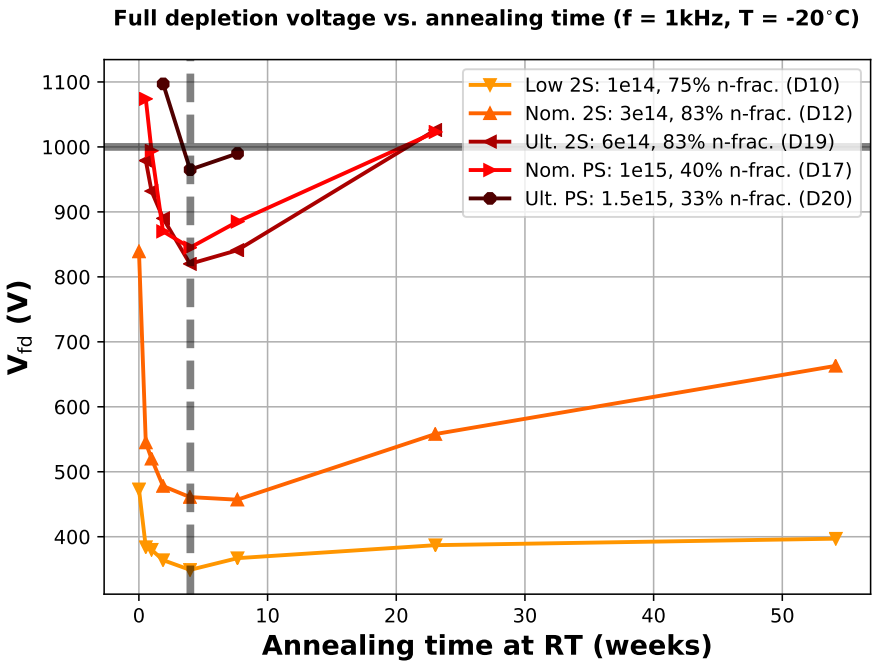

Figure 8.10.: Full depletion voltage of FZ290 for different fluences and annealing times. The annealing time is scaled to weeks at room temperature. The full depletion voltage is extracted from CV measurements performed at $T = -20\,°\mathrm{C}$ and a frequency of 1 kHz. The upper limit of the measurement range is indicated by the solid black line. The minima of the characteristics are highlighted by the dashed black line at four weeks of room temperature annealing. Uncertainties are estimated to $\pm 75\,\mathrm{V}$ for $V_{\mathrm{fd}} > 900\,\mathrm{V}$ and $\pm 15\,\mathrm{V}$ for full depletion voltages below that value.

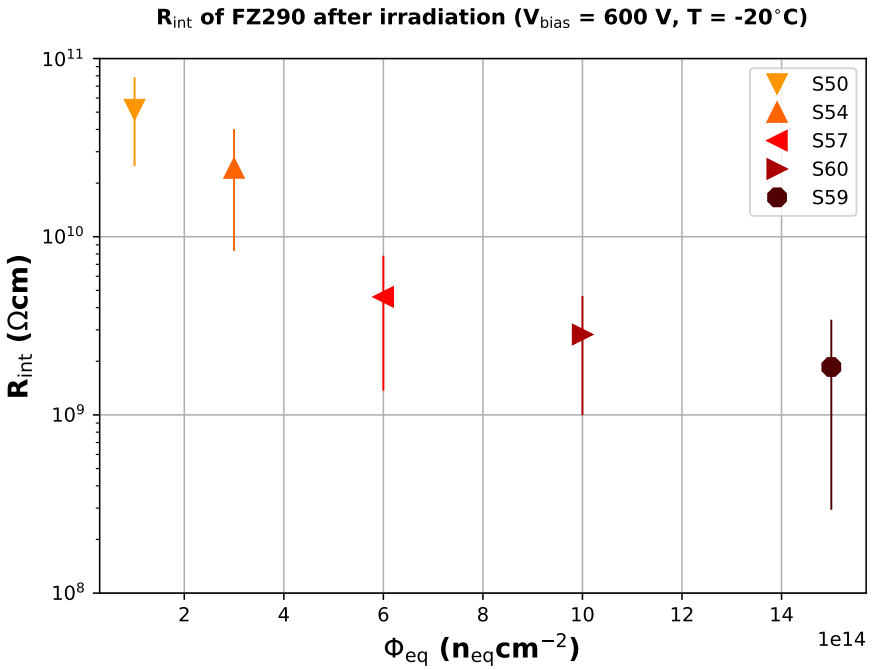

Figure 8.11.: Interstrip resistance of FZ290 after irradiation at $T = -20\,°\mathrm{C}$ and $V_{\mathrm{bias}} = 600\,\mathrm{V}$ for different fluences.

fluences measured at $T = -20\,°\mathrm{C}$ and a frequency of 1 kHz. The solid black line indicates the measurement range of 1000 V. The algorithm which extracts V_{fd} is explained in Section 5.3. It is able to approximate full depletion voltages which lie slightly above the upper limit of the measurement range. However, the algorithm did not converge for some of the high-fluence samples because they deplete far above 1000 V. The uncertainty of data points with $V_{\mathrm{fd}} > 900\,\mathrm{V}$ is estimated to be $\pm 75\,\mathrm{V}$. The saturation region of the CV characteristic is sufficiently detectable for full depletion voltages below that value, which reduces the estimated uncertainty to $\pm 20\,\mathrm{V}$ (see Section 5.8.2).

The characteristic of the extracted full depletion voltages indicates a beneficial annealing up to four weeks at room temperature, which is longer than what is claimed in Ref. [Mol99]. This is highlighted by the dashed black line in Figure 8.10. An annealing time of four weeks at room temperature appears to be the minimum of every measured characteristic. Furthermore, the CV characteristics at the ultimate 2S fluence of $6 \cdot 10^{14}\,\mathrm{n_{eq}cm^{-2}}$ and the nominal PS fluence of $1 \cdot 10^{15}\,\mathrm{n_{eq}cm^{-2}}$ are quite similar even though the absolute fluence differs by 40%. The accumulated neutron fluence at the ultimate 2S fluence, however, is 20% larger (see Table 8.3). This indicates that the degradation of mixed irradiated samples is driven by the neutron share of the irradiation. A similar phenomenon was observed with ddFZ samples, which is presented in Chapter 7. The proton induced damage after a neutron irradiation has less of an effect as it normally would, in terms of the degradation of V_{fd}. This is a result of the high oxygen concentration of the HPK standard material as is explained in Section 7.7. The oxygen impurities specifically target and neutralize defects which drive the degradation of V_{fd}. The measurement data reveal that the oxygen concentration in FZ290 is high enough in order to show a similar resilience towards proton generated radiation damage.

The evaluation of the strip and design parameters after irradiation was carried out extensively during the deep diffused irradiation campaign which is presented in Chapter 7. Significant changes of the strip and interstrip capacitances as well as the resistance of the polyresistor were not observed. Therefore, strip scans after irradiation were only performed sporadically for FZ290. The obtained data does not reveal any significant abnormalities. The strip leakage currents scale with fluence and follows the increase of I_{tot}. The interstrip resistance of three selected fluences is depicted in Figure 8.11. The characteristic is similar to what was already discussed in Chapter 7. The p-stop technology is sufficient even at high fluences. The interstrip resistance saturates for fluences larger than $6 \cdot 10^{14}\,\mathrm{n_{eq}cm^{-2}}$ at a value between $1\,\mathrm{G\Omega\,cm}$ and $10\,\mathrm{G\Omega\,cm}$, which is well above the specified minimum value ($R_{\mathrm{int}} > 100\,\mathrm{M\Omega\,cm}$).

8.5. Signal Measurements of FZ290

The seed signal over annealing time for different fluences of FZ290 samples measured at $V_{\mathrm{bias}} = 600\,\mathrm{V}$ and $T = -20\,°\mathrm{C}$ is depicted in Figure 8.12 starting at the second annealing step which corresponds to 30 min at 60 °C. The annealing time is scaled to weeks at room temperature. One of the sensors with an accumulated fluence of $1.5 \cdot 10^{15}\,\mathrm{n_{eq}cm^{-2}}$ (`S61`) developed a breakdown at 550 V during the annealing study. Moreover, data of `S53` for annealing times between four weeks and 120 weeks is not available because of a malfunction of the automated annealing procedure. Both sensors were not included into the analysis.

At an accumulated fluence of $1 \cdot 10^{14}\,\mathrm{n_{eq}cm^{-2}}$ the sensors show only beneficial annealing throughout the annealing study. Reverse annealing of the signal is observable for sensors with an accumulated fluence of $3 \cdot 10^{14}\,\mathrm{n_{eq}cm^{-2}}$ above ten weeks at room temperature. The different

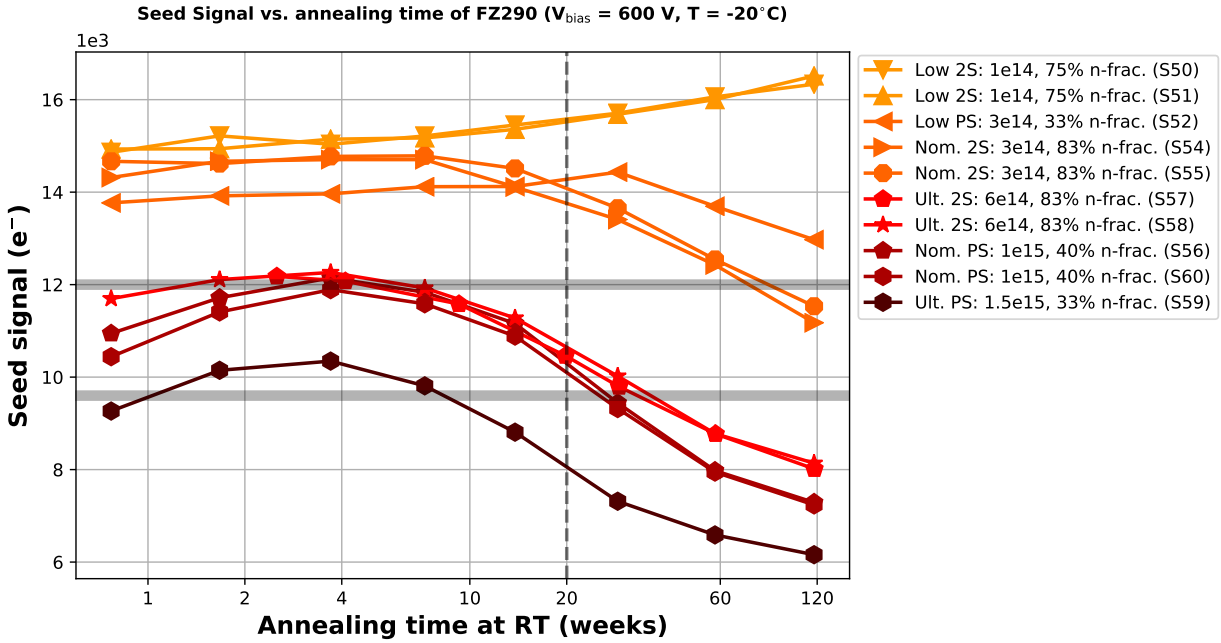

Figure 8.12.: Seed signal over annealing time scaled to weeks at room temperature of FZ290 sensors at $V_{\text{bias}} = 600\,\text{V}$ and $T = -20\,°\text{C}$. The transparent black lines at $12000\,\text{e}^-$ and $9600\,\text{e}^-$ highlight the lower limit of the 2S and PS-s signal specifications, respectively. The dashed black line emphasizes the envisaged annealing time of the Phase-2 Tracker of 20 weeks at $3000\,\text{fb}^{-1}$.

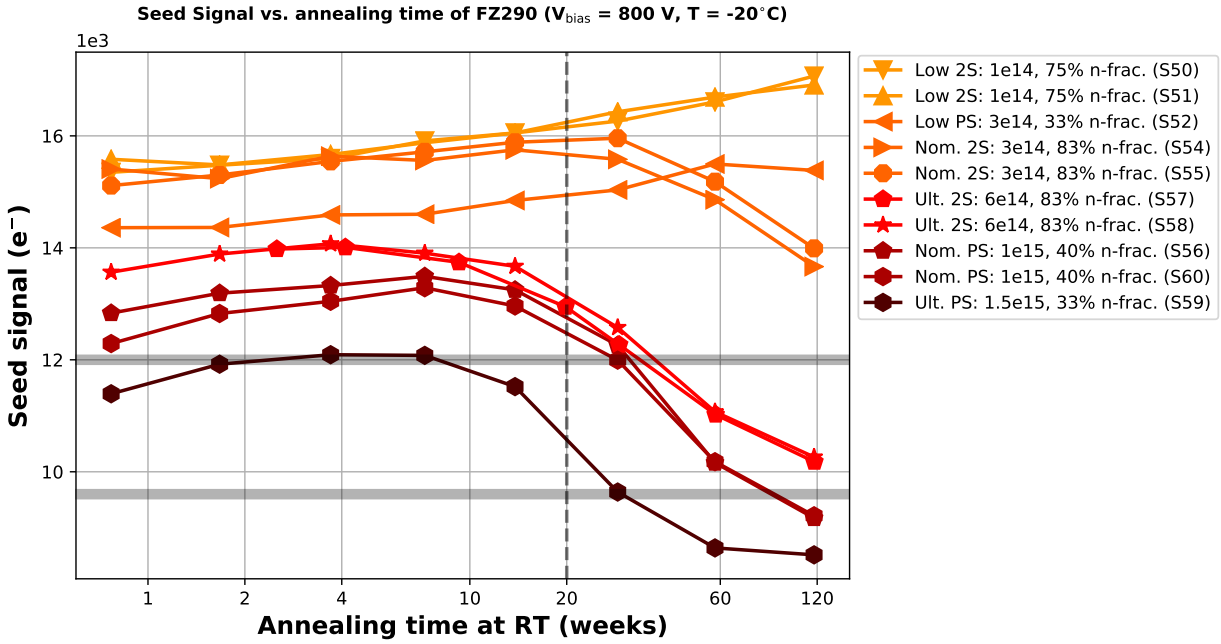

Figure 8.13.: Seed signal over annealing time scaled to weeks at room temperature of FZ290 sensors at $V_{\text{bias}} = 800\,\text{V}$ and $T = -20\,°\text{C}$. The transparent black lines at $12000\,\text{e}^-$ and $9600\,\text{e}^-$ highlight the lower limit of the 2S and PS-s signal specifications, respectively. The dashed black line emphasizes the envisaged annealing time of the Phase-2 Tracker of 20 weeks at $3000\,\text{fb}^{-1}$.

neutron shares of the nominal 2S and low PS irradiation composition do not result in any significant difference regarding the signal characteristic up to 20 weeks at room temperature. Differences only occur for larger annealing times where the reverse annealing of the signal is more pronounced for `S55` and `S55` (neutron fraction of 83%). The signal values after 20 weeks of annealing are around 14000 e^-, which is well above the 2S signal specification for 2S modules at 3000 fb^{-1}.

Sensors with a higher accumulated fluence show very similar signal characteristics. The signal peaks at around four weeks of annealing. This correlates with the results shown in Figure 8.10, where the minimum full depletion voltage was found after four weeks of room temperature annealing. The following reverse annealing decreases the signal of highly irradiated sensors by about 1500 e^- to 2000 e^- with respect to an annealing time of 20 weeks at room temperature. Sensors with a fluence of $1 \cdot 10^{15}\,n_{eq}cm^{-2}$ show a signal that is larger than the PS-s signal specification of 9600 e^- up to 30 weeks of annealing. In conclusion, FZ290 can meet the signal specifications for 2S and PS region up to 3000 fb^{-1} at 600 V. At this bias voltage, the signal is sufficient at the point of maximum beneficial annealing only for a potential 4000 fb^{-1} extension of the HL-LHC .

By comparing the signal at the ultimate 2S fluence of $6 \cdot 10^{14}\,n_{eq}cm^{-2}$ and the nominal PS fluence of $1 \cdot 10^{15}\,n_{eq}cm^{-2}$, one can see that the magnitude of the signal appears to be determined by the neutron share of the total fluence. The fluence that was accumulated during neutron irradiation is $5 \cdot 10^{14}\,n_{eq}cm^{-2}$ (ultimate 2S) versus $4 \cdot 10^{14}\,n_{eq}cm^{-2}$ (nominal PS). The additional proton irradiation has no noticeable impact on the charge collection efficiency of the sensors at this bias voltage. The only difference can be observed for very large annealing times. Similar observations were already described in Chapter 7. This coincides with the data presented in Figure 8.10, where the degradation of V_{fd} is similar for ultimate 2S and nominal PS fluence. This phenomenon originates in the radiation tolerance towards proton irradiation of FZ290. The proton generated defects which are responsible for the degradation of V_{fd} are partly neutralized by the oxygen impurities in the material, which is described in more detail in Section 7.7. Similar observations were also reported in Ref. [Gos18], which investigated the difference between neutron and proton irradiation on n-type silicon sensors with low and high oxygen concentration.

The data also show that the signal of `S59` ($\Phi_{eq} = 1.5 \cdot 10^{15}\,n_{eq}cm^{-2}$) is clearly below the signal of `S57` and `S58` ($\Phi_{eq} = 6 \cdot 10^{14}\,n_{eq}cm^{-2}$). All three samples accumulated a fluence of $5 \cdot 10^{14}\,n_{eq}cm^{-2}$ during the neutron irradiation. The degradation of the charge collection coincides with the increased degradation of V_{fd} of `S59` shown in Figure 8.10. This illustrates the high amount of additional proton irradiation ($\Phi_{eq} = 1 \cdot 10^{15}\,n_{eq}cm^{-2}$) that is required to significantly reduce the signal of neutron irradiated sensors. The degradation of the charge collection is also impacted by trapping. The studies presented in Ref. [WVK02; Lin+01] did not report any effect of oxygen impurities on the defects responsible for trapping. Hence, trapping is expected to increase for higher fluences.

As already mentioned in Chapter 7, the CMS community has agreed upon a potential increase of the Phase-2 Outer Tracker operation voltage up to 800 V in case of a potential 4000 fb^{-1} extension if it can ensure a prolonged efficient operation of the sensors. The measured signals at 800 V are depicted in Figure 8.13. The difference in the signal annealing between the samples at $3 \cdot 10^{14}\,n_{eq}cm^{-2}$ becomes more pronounced compared to $V_{bias} = 600$ V. The neutron share of the low PS fluence is only 33% in contrast to a 83% share of the nominal 2S fluence. The signal annealing of the proton dominated fluence does not show reverse annealing, whereas the signals for the nominal 2S fluence decrease after 20 weeks of annealing. Most importantly,

the FZ290 material is responsive towards signal boosting (about 2000 e^- increase in signal for +200 V). At 20 weeks of room temperature annealing one can observe an increase by over 2000 e^- among all samples. As a consequence, sensors irradiated to the ultimate 2S and PS fluence show a sufficient signal up to 30 weeks of annealing. An efficient operation of FZ290 is, therefore, possible during the ultimate HL-LHC performance scenario.

8.6. Electrical Characterization of thFZ240 after Irradiation

First of all, one has to mention that the irradiation procedure of thFZ240 samples did not go according to plan. Two diodes missed the irradiation at JSI completely because of human failure. Technical issues at KAZ delayed the irradiation for months. Since the CMS community expected the material decision for the Outer Tracker in September, it was eventually decided to carry out the proton irradiation of the sensors at the University of Birmingham (information about the irradiation facilities can be found in Section 6.4). Two sensors cracked due to mechanical stress during the removal of the polyamid tape that was used to fixate the sensors during the irradiation process. This incident is another example of how fragile the thFZ240 material is. The irradiation of the diodes could not be carried out in time because the technical issues at KAZ remained until the end of 2019, when this thesis was submitted.

Figure 8.14 depicts the radiation damage induced leakage current increase at $V_{\text{bias}} = 600\,\text{V}$ and after a heat treatment of 70 min at 60 °C normalized to $T = 20\,°\text{C}$ and sensor volume, represented by hollow markers. The expected damage rate for a heat treatment of 70 min at 60 °C is $\alpha_{\text{para}} = 4.23 \cdot 10^{-17}\,\text{Acm}^{-1}$ [Mol99]. The fit of the data points represented by hollow markers yields a value of $\alpha = (6.39 \pm 0.35) \cdot 10^{-17}\,\text{Acm}^{-1}$ which is represented by the dashed black line. The results deviates from the reference value by 44%. The deviation from the reference value originates from the fixed bias voltage approach and the usage of strip sensors instead of diodes, which was already explained in Section 7.3. In comparison with the damage rate found for FZ290 sensors, one finds a difference of 24%. However, this is not necessarily an indication of a severe *overirradiation* of the thFZ240 sensors. The difference of the damage rate originates from the fact that the FZ290 sensors are underdepleted at a bias voltage of 600 V for high fluences as was mentioned in Section 8.4. The thFZ240 sensors, on the other hand, are fully depleted at 600 V even at the highest available fluence and before annealing, which is shown in Figure 8.16a. Therefore, the damage rate of thFZ240 sensors at $V_{\text{bias}} = 600\,\text{V}$ is presumably a more representative value for sensors, since it is methodically closer to the original approach presented in Ref. [Mol99], even though it deviates severely from the reference value. For a more meaningful comparison of the two materials, one can calculate the damage rate of thFZ240 sensors at a bias voltage at which the high-fluence samples are similarly underdepleted as high-fluence FZ290 sensors at 600 V. The CV characteristics of thFZ240 sensors reveal that high-fluence thFZ240 sensors are underdepleted at 400 V, while low-fluence thFZ240 sensors are still fully depleted (before annealing). The data points in Figure 8.14 measured at $V_{\text{bias}} = 400\,\text{V}$ are represented by solid markers. The fit (solid black line) yields $\alpha_{400} = (4.44 \pm 0.28) \cdot 10^{-17}\,\text{Acm}^{-1}$, which only deviates by 9% from the value found for FZ290 sensors at $V_{\text{bias}} = 600\,\text{V}$ and 5% from the reference value. This indicates that the accumulated fluences of the samples in this campaign are similar.

The mean leakage current of thFZ240 sensors at $T = -20\,°\text{C}$, normalized to volume, at a bias voltage of 600 V for different fluences and annealing times is shown in Figure 8.15. The leakage current for sensors irradiated with $1.5 \cdot 10^{15}\,\text{n}_{\text{eq}}\text{cm}^{-2}$ after 20 weeks of annealing at room temperature amounts to $1359\,\text{nA}\,\text{mm}^{-3}$ which corresponds to a relative reduction of 16%

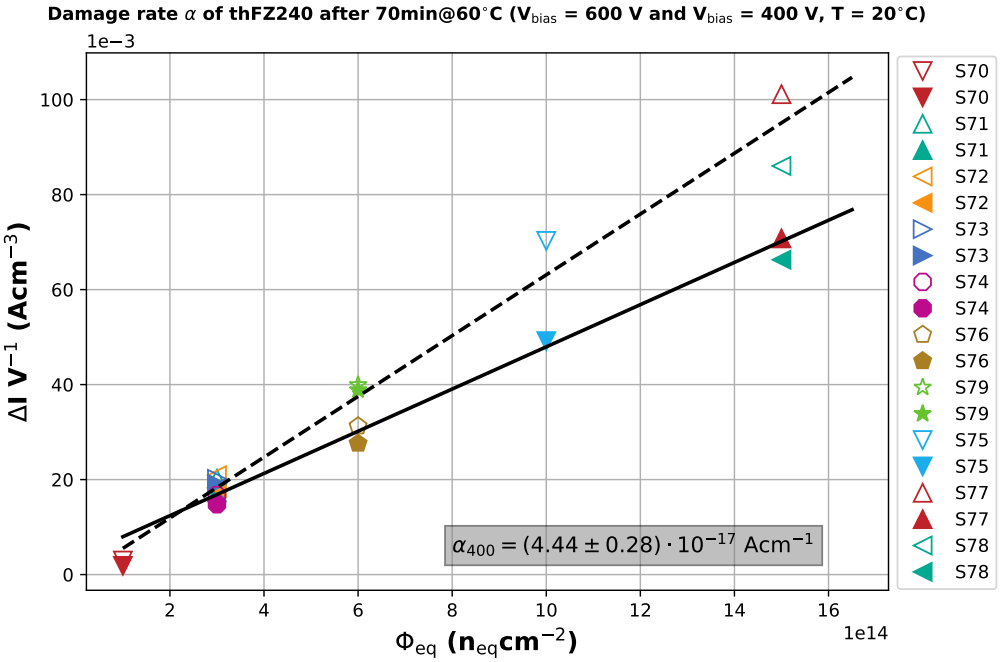

Figure 8.14.: Damage rate α of thFZ240 sensors after a heat treatment of 70 min at 60 °C. The current is normalized to sensor volume and scaled to $T = 20\,°C$. The hollow markers represent the measured values at $V_{\text{bias}} = 600\,\text{V}$. The corresponding fit yields $\alpha = (6.39 \pm 0.35) \cdot 10^{-17}\,\text{Acm}^{-1}$ and is represented by the dashed black line. The measured values at $V_{\text{bias}} = 400\,\text{V}$ are represented by solid markers. The fit for these data points is represented by the solid black line and yields a damage rate of $\alpha_{400} = (4.44 \pm 0.28) \cdot 10^{-17}\,\text{Acm}^{-1}$.

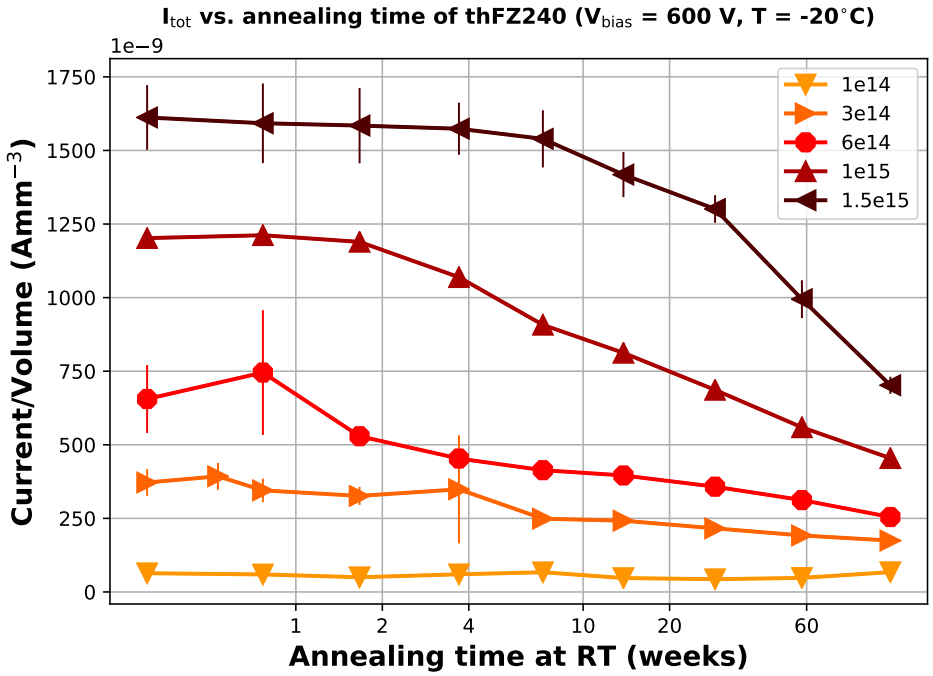

Figure 8.15.: Leakage current versus annealing time of thFZ240 sensors at $T = -20\,°C$ for different fluences. The annealing time is scaled to weeks at room temperature.

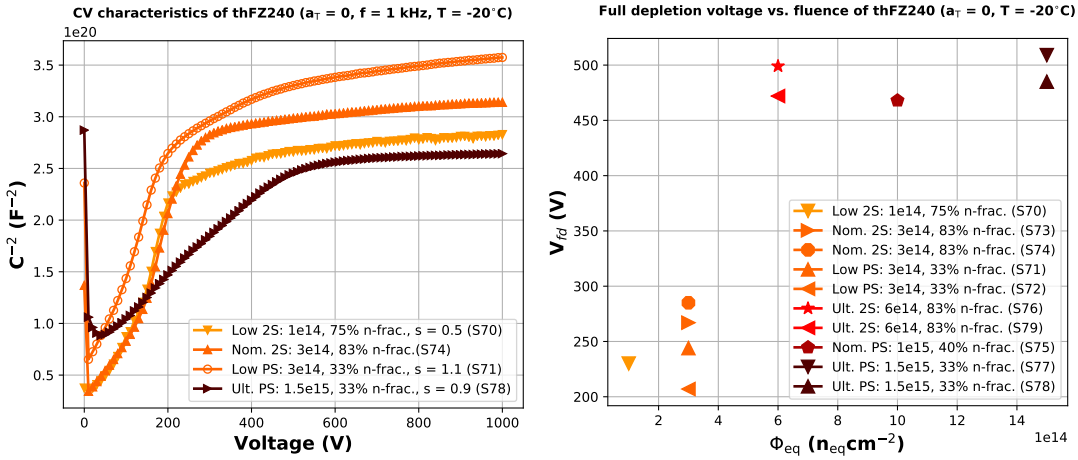

(a) (b)

Figure 8.16.: (a) Selected CV characteristics of thFZ240 sensors after irradiation, measured at $T = -20\,°C$ with a frequency of 1 kHz and before heat treatment. The capacitances are multiplied by a scaling factor s for better visibility of the individual curves. (b) Extracted full depletion voltages of thFZ240 sensors from CV characteristics.

with respect to the measured value after 10 min at 60 °C. At a fluence of $1 \cdot 10^{15}\,\mathrm{n_{eq}cm^{-2}}$ the leakage current after 20 weeks is $749\,\mathrm{nA\,mm^{-3}}$ which corresponds to a reduction of 38%. The leakage current for the next lower fluences are $377\,\mathrm{nA\,mm^{-3}}$, $229\,\mathrm{nA\,mm^{-3}}$ and $45\,\mathrm{nA\,mm^{-3}}$. The relative reduction is 43%, 39% and 30%, respectively. In comparison to other materials in this thesis, the leakage current annealing is less pronounced. The relative leakage current reduction varies between 16% and 43%, which does not follow the claims made in Ref. [Mol99].

Generally, the thFZ240 material shows exceptionally low full depletion voltages even at the highest available fluences. Even the nominally thinner ddFZ200 sensors did not show such low full depletion voltages. The full depletion voltages of thFZ240 sensors without heat treatment are depicted in Figure 8.16b. This result shows the benefit of physically thinned materials. The low bias voltage that is required to operate such sensors at its full capacity, can potentially reduce the overall power consumption of the tracker. The subject is further discussed in Section 8.8. On the other hand, the depletion behavior of thFZ240 reduces the effectiveness of a potential bias voltage boost that might be required during the ultimate HL-LHC performance scenario. The signal of thFZ240 sensors must, therefore, be sufficient at 600 V at all times. This is investigated in Section 8.7. Figure 8.16a shows a number of selected CV characteristics. The saturation region after the knee of the CV characteristic is relatively steep for `S70` and `S71`. The irradiation composition of these sensors is dominated by protons. Similar characteristics were observed on purely proton irradiated samples in Chapter 7. The efficiency is expected to increase noticeably beyond the knee. The full depletion voltages of sensors which accumulated $\Phi_{eq} \geq 1 \cdot 10^{14}\,\mathrm{n_{eq}cm^{-2}}$ are located around 500 V, which show the expected saturation after the knee. Similar to observations made on other materials, the degradation is driven by the radiation damage generated by neutrons. The accumulated fluence due to neutrons is similar for all these sensors. An additional proton irradiation hardly impacts the degradation.

Section 8.2 outlines the thFZ240 backside issue that was encountered during the thFZ240 qualification campaign. The issue was mainly observed on full-sized sensors and only one

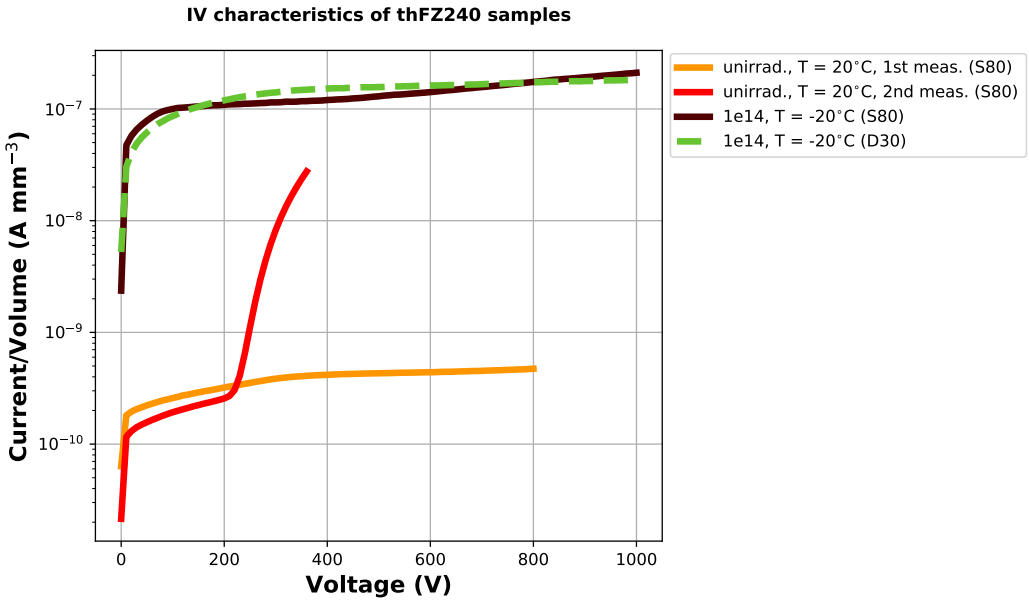

Figure 8.17.: Illustration of how the thFZ240 backside issue is impacted by irradiation. The IV characteristics are measured at $T = 20\,°\mathrm{C}$ (before irradiation) and $T = -20\,°\mathrm{C}$ (after irradiation). The leakage current is normalized to volume. The initial measurement shows the expected result (yellow). As a consequence of the thFZ240 backside issue the sensor developed a breakdown close to the full depletion voltage (red). The breakdown vanishes after irradiation (dark red). The leakage current is in the expected range for a fluence of $1 \cdot 10^{14}\,\mathrm{n_{eq}cm^{-2}}$. The leakage current of a thFZ240 diode (green) with an equal fluence was added for comparability.

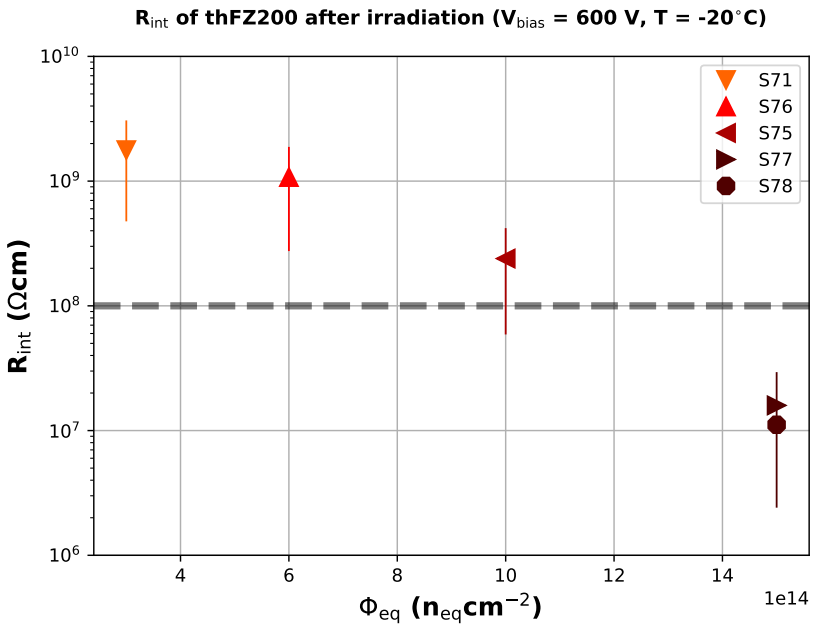

Figure 8.18.: Interstrip resistance of thFZ240 sensors after irradiation at $T = -20\,°\mathrm{C}$ and a bias voltage of 600 V for different fluences. The dashed line highlights the specified minimum value of $R_{\mathrm{int}} > 100\,\mathrm{M\Omega\,cm}$.

miniature sensor. This sensor was irradiated with a fluence of $1 \cdot 10^{14}\,\mathrm{n_{eq}cm^{-2}}$ in order to investigate the impact of radiation damage on the breakdown voltage. Figure 8.17 shows the outcome of this investigation. The IV characteristics are measured at $T = 20\,^{\circ}\mathrm{C}$ before irradiation and $T = -20\,^{\circ}\mathrm{C}$ after irradiation. The leakage current is normalized to sample volume. The initial measurement shows the expected characteristic of the leakage current (yellow). As a result of the thFZ240 backside issue the sensor developed a breakdown close to the full depletion voltage (red). The breakdown vanishes after irradiation (dark red). The leakage current of a diode (green) with equal fluence was added for comparability. It shows that the leakage current of the sensor is in the expected range. The fact that early breakdown can be cured by irradiation is an important statement. For whatever reasons and independent of the base material, a sensor might develop an early breakdown during module assembly. Time and resources that were invested during the assembly process are not completely wasted, because this module might still be usable as a backup.

As already mentioned in Section 8.4, strip scans after irradiation were only performed sporadically because the extensive investigation of strip parameters and their sensitivity towards irradiation was studied during the deep diffused campaign presented in Chapter 7. The impact of irradiation on strip and interstrip capacitances as well as the resistance of the polyresistor is negligible. The strip leakage current increases relative to the total leakage current of the sensor. The interstrip resistance for different fluences are depicted in Figure 8.11. The data show that the degradation of R_{int} at high fluences is significantly larger than observed for FZ290 or the deep diffused batches. At the highest available fluence it is even below the specified minimum value of $R_{\mathrm{int}} > 100\,\mathrm{M\Omega\,cm}$. Although HPK claims that the front-side processing of both materials is equal, the stronger degradation of R_{int} indicates otherwise. One has to mention that HPK ensures a radiation tolerance up to only $1 \cdot 10^{15}\,\mathrm{n_{eq}cm^{-2}}$. Technically, the sensor parameters specified in the TDR [CMS18] are also only valid up said fluence. The thFZ240 sensors, therefore, meet the specifications. Moreover, signal measurements presented in Section 8.7 show that the degradation of the interstrip resistance does not interfere with the ability to sufficiently detect MIPs. The average cluster size is comparable among all presented sensors. This phenomenon is currently investigated by the ETP Hardware Group. Overall, the TDR specification appears to be too conservative regarding the minimum specified value of R_{int}. The subject should be reevaluated in a test beam experiment.

8.7. Signal Measurements of thFZ240

Figure 8.19 shows the seed signal over annealing time scaled to weeks at room temperature of thFZ240 at $V_{\mathrm{bias}} = 600\,\mathrm{V}$ and $T = -20\,^{\circ}\mathrm{C}$. The data show that the signals of thFZ240 sensors do not meet the 2S signal specifications at 600 V. The thFZ240 material can be operated efficiently up to a fluence of $1 \cdot 10^{14}\,\mathrm{n_{eq}cm^{-2}}$. Sensors which accumulated the nominal 2S or the ultimate 2S fluence show a signal that is about $500\,\mathrm{e^-}$ to $1000\,\mathrm{e^-}$ below the lower limit for 2S sensors of $12000\,\mathrm{e^-}$. Beneficial as well as reverse annealing of the signal is not observable for sensors with $\Phi_{\mathrm{eq}} \leq 3 \cdot 10^{14}\,\mathrm{n_{eq}cm^{-2}}$. Sensors with $\Phi_{\mathrm{eq}} \geq 6 \cdot 10^{14}\,\mathrm{n_{eq}cm^{-2}}$ show reverse annealing of the signal above 20 weeks of annealing at room temperature. The sensor `S75` ($\Phi_{\mathrm{eq}} = 1 \cdot 10^{15}\,\mathrm{n_{eq}cm^{-2}}$) can meet the PS-s signal specification for an annealing scenario of 10 to 50 weeks at room temperature. The material would fail to provide a sufficient signal in case of a $4000\,\mathrm{fb^{-1}}$ extension for the PS region.

Because of the low full depletion voltages of thFZ240 sensors, one cannot expect significant benefit from increasing the bias voltage to 800 V. This assumption is corroborated by the

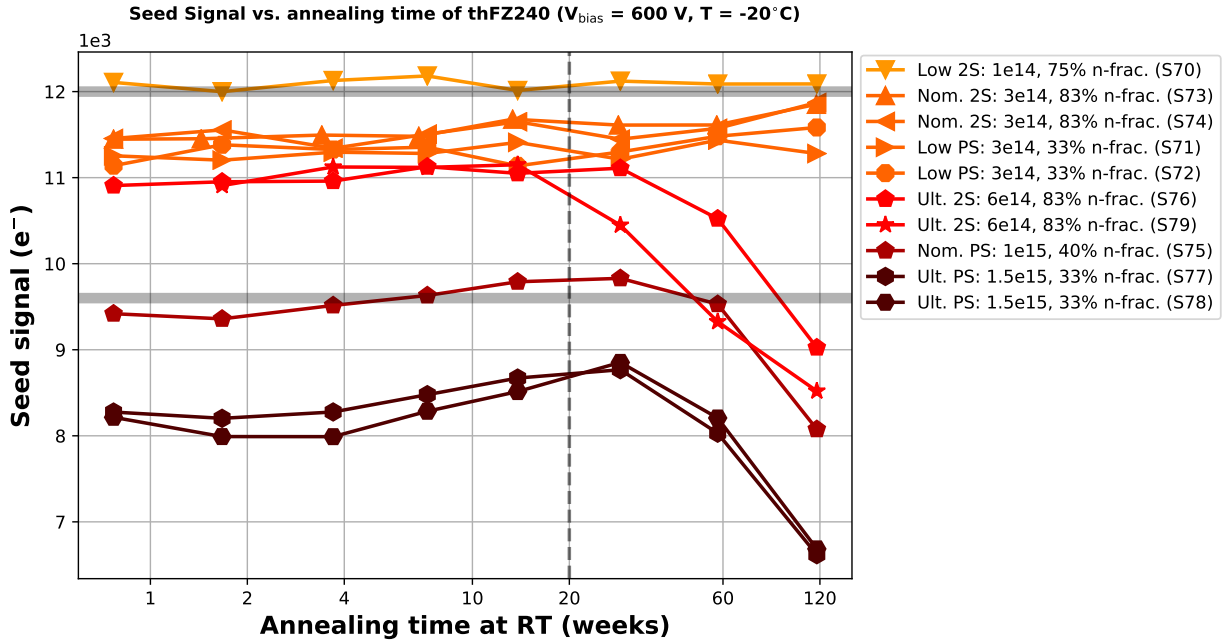

Figure 8.19.: Seed signal over annealing time scaled to weeks at room temperature of thFZ240 at $V_{\text{bias}} = 600\,\text{V}$ and $T = -20\,°\text{C}$. The transparent black lines at $12000\,\text{e}^-$ and $9600\,\text{e}^-$ highlight the 2S and PS-s signal specifications. The dashed black line emphasizes the envisaged annealing time of the Phase-2 Tracker of 20 weeks at $3000\,\text{fb}^{-1}$.

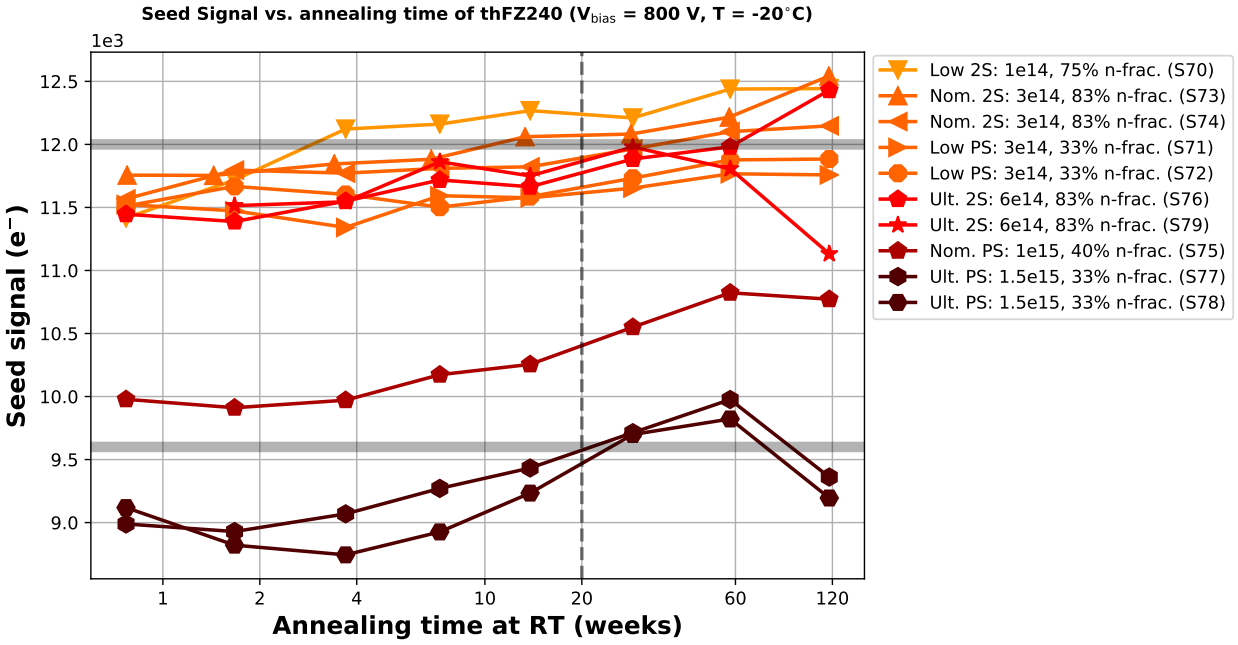

Figure 8.20.: Seed signal over annealing time scaled to weeks at room temperature of thFZ240 at $V_{\text{bias}} = 800\,\text{V}$ and $T = -20\,°\text{C}$. The transparent black lines at $12000\,\text{e}^-$ and $9600\,\text{e}^-$ highlight the 2S and PS-s signal specifications. The dashed black line emphasizes the envisaged annealing time of the Phase-2 Tracker of 20 weeks at $3000\,\text{fb}^{-1}$.

signal measurements at $V_{\text{bias}} = 800\,\text{V}$ presented in Figure 8.20. At the crucial point of 20 weeks of annealing at room temperature the signal of sensors irradiated with low 2S, low PS, nominal 2S and ultimate 2S fluence show an increase of about $500\,\text{e}^-$. Their signals are located in a region between 11500^- and 12300^-. At the ultimate PS fluence of $1.5 \cdot 10^{15}\,\text{n}_{\text{eq}}\text{cm}^{-2}$ the signal of thFZ240 sensors is marginally above the 9600^- mark for annealing times between 20 and 60 weeks. The thFZ240 material could, therefore, be used for the PS region of the Phase-2 Outer Tracker.

The data presented in Figure 8.19 and Figure 8.20 show that there is a difference between the measured signals of thFZ240 sensors at the ultimate 2S ($\Phi_{\text{eq}} = 6 \cdot 10^{14}\,\text{n}_{\text{eq}}\text{cm}^{-2}$) and the high PS fluences ($\Phi_{\text{eq}} \geq 1 \cdot 10^{15}\,\text{n}_{\text{eq}}\text{cm}^{-2}$), although the depletion behavior is very similar (see Figure 8.16b). This coincides with the observations made on FZ290 sensors. The neutron share of these fluences is $4 \cdot 10^{14}\,\text{n}_{\text{eq}}\text{cm}^{-2}$ and $5 \cdot 10^{14}\,\text{n}_{\text{eq}}\text{cm}^{-2}$ which drives the degradation of the depletion behavior. The contribution of the proton induced radiation damage is mitigated due to the high oxygen concentration of the material. However, the high number of proton generated defects clearly has an impact on the degeneration of the sensor signal, which is most probably related to charge trapping.

8.8. Comparison of FZ290 and thFZ240

In order to evaluate the generated leakage current in both materials properly, one must normalize the leakage current to area. It was already mentioned, that the evaluation of the power consumption is difficult, since the applied bias voltage is dependent on signal, annealing and fluence, which change over the course of the HL-LHC operation. Such an evaluation is performed for FZ290 in Chapter 9. For simplicity, a comparison at a fixed bias voltage of 600 V is presented in Figure 8.21a and for 800 V in Figure 8.21b. The plots present mean values taken from measurements on miniature sensors after 2 and 20 weeks of annealing at room temperature and conducted at $T = -20\,^{\circ}\text{C}$. The largest difference can be observed at the highest available fluence of $1.5 \cdot 10^{15}\,\text{n}_{\text{eq}}\text{cm}^{-2}$ after 20 weeks of annealing. The FZ290 sensor show a high responsiveness towards leakage current annealing at this fluence, which is presented in Figure 8.8 in more detail. The leakage current generation of FZ290 is further suppressed by a *underdepletion* at high fluences even at $V_{\text{bias}} = 800\,\text{V}$. The generated leakage current can be used to estimated the power consumption per sensor at a certain bias voltage by using Equation (7.1). At a fixed bias voltage, the difference in power consumption of both materials corresponds to the difference in leakage current. According to these results, using thFZ240 sensors would lead to a higher power consumption at least at the end of the nominal HL-LHC runtime and during a extended run-time. The difference in leakage current at lower fluences is not significant. Overall, there is no significant benefit of using thFZ240 sensors in terms of leakage current neither for the 2S nor for the PS region of the CMS Phase-2 Outer Tracker.

Figure 8.22 shows the seed signal of FZ290 and thFZ240 for different fluences, measured at $T = -20\,^{\circ}\text{C}$ and after 20 weeks of annealing at room temperature, which is the envisaged annealing time at the end of the nominal HL-LHC operation. The signal values are obtained by calculating the average of data points of signals at 14 and 29 weeks from the the data sets shown in Section 8.5 and Section 8.7. The orange and yellow sectors highlight the desired signal range for strip sensors in the 2S and PS region, respectively.

The data show that the signal of FZ290 is sufficient at 600 V up to the nominal fluences of the 2S ($\Phi_{\text{eq}} = 3 \cdot 10^{14}\,\text{n}_{\text{eq}}\text{cm}^{-2}$) and PS ($\Phi_{\text{eq}} = 1 \cdot 10^{15}\,\text{n}_{\text{eq}}\text{cm}^{-2}$) region with respect to their

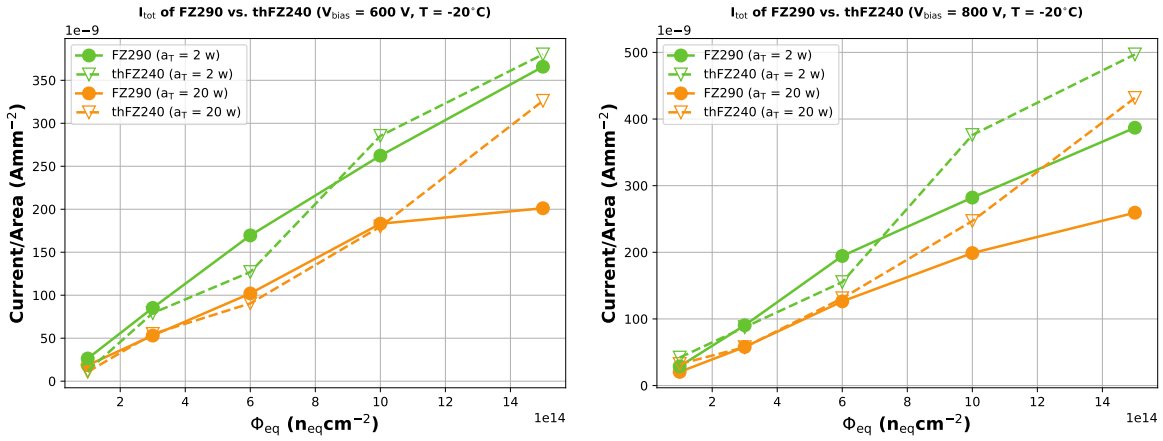

(a) (b)

Figure 8.21.: Mean leakage current over fluence for FZ290 and thFZ240 after 2 and 20 weeks of annealing at room temperature, measured at $T = -20\,°\mathrm{C}$ and a bias voltage of (a) 600 V and (b) 800 V. The leakage current is normalized to area in order to compare and evaluate the generated leakage current in both materials properly.

different signal specifications. The thFZ240 sensors lack the required signal for the 2S region. Their signal characteristic throughout the available fluence spectrum at said bias voltage is well-described by a linear fit (dashed line). The FZ290 sensors provide large signals if they are sufficiently depleted. However, the measured signals of FZ290 and thFZ240 sensors follow the same trend for $\Phi_{\mathrm{eq}} \geq 6 \cdot 10^{14}\,\mathrm{n_{eq}cm^{-2}}$ and $V_{\mathrm{bias}} = 600\,\mathrm{V}$, where FZ290 is significantly underdepleted. The 2S-specific FZ290 signals at $V_{\mathrm{bias}} = 600\,\mathrm{V}$ are represented by the dash-dotted line. The FZ290 sensors prove to be very responsive to bias voltage boosting (over $+2000\,\mathrm{e^-}$ for a $+200\,\mathrm{V}$ boost). The bias voltage boost is only required for a potential $4000\,\mathrm{fb^{-1}}$ extension of the HL-LHC, which is represented by the signal values at the ultimate 2S and PS fluence of $6 \cdot 10^{14}\,\mathrm{n_{eq}cm^{-2}}$ and $1.5 \cdot 10^{15}\,\mathrm{n_{eq}cm^{-2}}$. The thFZ240 sensors do not provide enough additional signal after bias voltage boosting at low fluences. The material could be used for the PS region, though, since it generates enough signal at the low and nominal PS fluences. The PS-s signal specification can be met at the ultimate PS fluence at 800 V if the annealing time is increased to about 30 weeks at room temperature. For an annealing time of 20 weeks at room temperature the measured signal is about $9600\,\mathrm{e^-}$, which is equal to the lower limit.

8.9. Conclusion

The oxygen concentration in FZ290 and thFZ240 is high enough in order to provide a similar radiation tolerance towards proton generated radiation damage. The degradation of the full depletion voltage is driven by neutron generated damage and is hardly impacted by additional proton irradiation. However, the impact of the proton generated radiation damage manifests itself in the increase of the bulk generated leakage current. The degradation of the charge collection efficiency is driven by the depletion behavior of the sensor and, therefore, also strongly depends on the neutron share of the irradiation. The data shows that large additional proton fluences are required (nominal PS and ultimate PS fluence) in order to further degenerate the sensor signal.

The data show that FZ290 sensors can provide high signals at 600 V at almost every stage of operation and are responsive to bias voltage boosting. The signal and, therefore, the efficiency

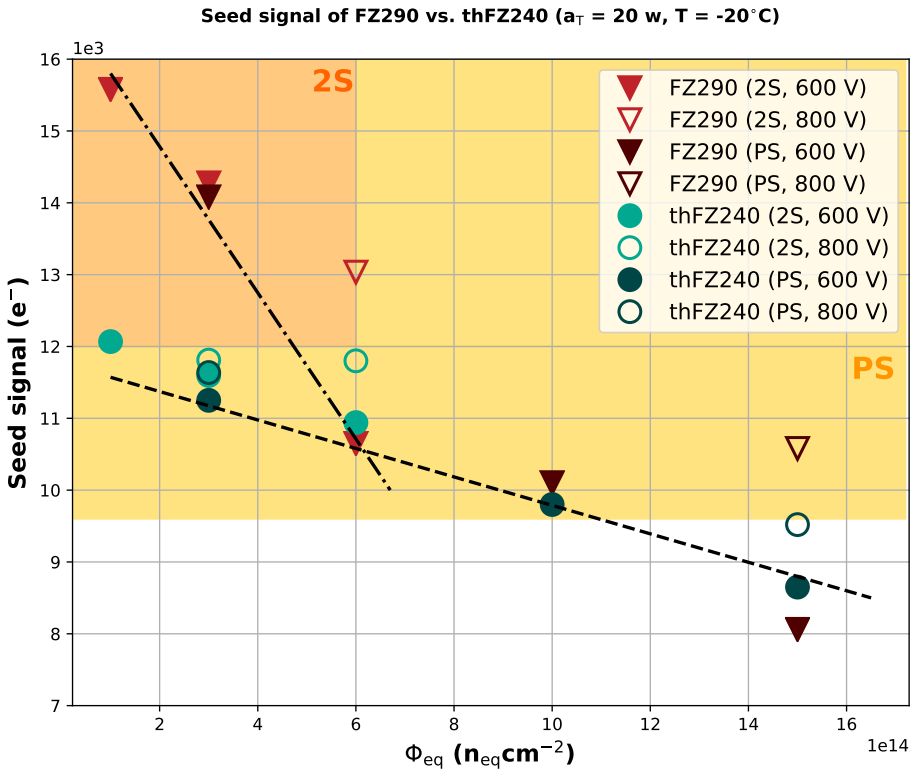

Figure 8.22.: Seed signal of FZ290 and thFZ240 for different fluences, measured at $T = -20\,°C$ and after 20 weeks of annealing at room temperature. The orange and yellow sectors highlight the required signal range for strip sensors in the 2S and PS region. The solid markers represent measurements conducted at 600 V. Measurement results conducted at 800 V are added in case the initially measured signal does not meet its specification in order to show the impact of a bias voltage boost. Data points of FZ290 and thFZ240 sensors are depicted in red and green, respectively. A lighter color tone indicates fluences which are expected in the 2S region. Darker color tones highlight fluences which are expected for the PS region. The data points at 600 V were fitted for each material to indicate the qualitative characteristic of the signal. The fit results are depicted by the dashed black lines.

of the sensor can easily be increased in case of a potential 4000 fb^{-1} extension scenario of the HL-LHC by boosting the bias voltage to 800 V. In this case, room temperature annealing can be used up to 30 weeks without risking a decrease in efficiency, as a means to reduce the leakage current during the operation. The thFZ240 sensors showed higher leakage currents before and after irradiation compared to FZ290. During the campaign, the thFZ240 sensors revealed a lack of mechanical robustness, which is not only required for measurements but especially for module assembly. It was shown that the signals provided by thFZ240 sensors are not sufficient for satisfying the requirements of the 2S signal specifications even with a boosted bias voltage. The sensors could potentially be used for the PS region, but only in a strict annealing scenario that ranges from 30 and 60 weeks at room temperature in case of a potential 4000 fb^{-1} extension.

In conclusion, thFZ240 did not show any significant advantage over FZ290. Therefore, the additional costs that are incurring due to the thinning process are not justifiable. In September 2019, the CMS Outer Tracker Sensor Working Group presented the outcome of the Final 2S irradiation campaign to the rest of the CMS community. As a consequence, it was decided to pick FZ290 as the base material for sensors of the 2S and PS region for the CMS Phase-2 Outer Tracker.

9

Estimated Performance of FZ290 during the HL-LHC Run-Time

The performance of FZ290 sensors during operation is quantified in terms power consumption and hit efficiency. The efficiency is the driving factor for the applied bias voltage, which then determines the leakage current generation and power consumption. According to Relation (5.5), a sensor operates efficiently if its signal is larger than 12σ of noise, which results in the lower limits of the 2S and PS-s signal specifications of $12000\,\mathrm{e}^-$ and $9600\,\mathrm{e}^-$, respectively. Due to the degeneration of the signal with increasing fluence one is forced to increase the bias voltage over time in order to stay efficient. Based on signal measurements conducted during the FZ290 irradiation study one can estimate the optimal bias voltage for different stages of the operation. Furthermore, the generated leakage current and power consumption can be approximated for every given voltage value.

9.1. General Discussion

An increase of the HL-LHC's instantaneous luminosity in the first three years between LS3 and LS4 is foreseen until the nominal peak luminosity of $5 \cdot 10^{34}\,\mathrm{cm}^{-2}\mathrm{s}^{-1}$ is reached. In case of the ultimate HL-LHC performance scenario the ramp-up would take place between LS3 and LS5 (first and sixth year of operation) up to the ultimate luminosity of $7.5 \cdot 10^{34}\,\mathrm{cm}^{-2}\mathrm{s}^{-1}$ [CER19]. The FZ290 performance evaluation is simplified by assuming a linear increase of the integrated luminosity and, therefore, a linear fluence accumulation over a run-time of ten years. In order to account for the ultimate HL-LHC performance scenario the FZ290 evaluation incorporates the expected fluences with respect to a yearly accumulated integrated luminosity of $400\,\mathrm{fb}^{-1}$ for the last three operation years. Therefore, the fluence projection is more conservative at the beginning, because the ramp-up of the instantaneous luminosity, and becomes more realistic at the end of the assumed operation time.

One has to address the fact, that the acquired measurement data does not reflect the realistic damage scaling and defect annealing of the sensors in the detector. The miniature sensors, which were used for irradiation studies, were irradiated to a target fluence with respect to typical fluences at $3000\,\mathrm{fb}^{-1}$ or $4000\,\mathrm{fb}^{-1}$. Hence, the annealing was performed on fully irradiated sensors. The sensors in the tracker are exposed to radiation for one year, which results in a steady increase of the full depletion voltage and the leakage current as well as a steady decrease of the signal. Thus, the degeneration of these sensor parameters peaks at the end of the year. The annealing takes place during the year-end shutdown. It is difficult to quantify how the impact of the step-wise fluence accumulation and defect annealing differs from the one observed in the laboratory measurements. It is fair to assume, that the annealing characteristic of leakage current deviates from the parameterization presented in Ref. [Mol99]. Moreover, one can assume that the annealing performed on a fully irradiated sensor is more impactful with respect to the evolution of N_{eff}. The mechanisms that drive the change of N_{eff}

are defect removal and defect formation. These mechanisms are proportional to fluence [Lin+01]. Hence, they are weaker in a realistic scenario, where the fluence is accumulated over time. The measurement data presented in Section 8.5 shows that reverse annealing significantly decreases the signal of sensors with $\Phi_{eq} \geq 6 \cdot 10^{14}\,n_{eq}cm^{-2}$ for annealing times larger than four weeks at room temperature. The signal of sensors with $\Phi_{eq} = 3 \cdot 10^{14}\,n_{eq}cm^{-2}$ shows reverse annealing for annealing times larger than ten weeks at room temperature. Following the argumentation above, one can assume that this effect is less pronounced in the real detector. Therefore, the signal approximation for the FZ290 performance evaluation based on the acquired data can be considered conservative during the final years of operation.

Another uncertain parameter is the sensor temperature in the future tracker, which heavily impacts the leakage current generation and power consumption. The measurements after irradiation were performed at $T = -20\,°C$. The FZ290 performance is evaluated with respect to said operation temperature. The coolant temperature in the Phase-2 Outer Tracker will be $-33\,°C$ at the first module in the cooling loop. The 2S sensors are mainly cooled by two Al-CF[1] bridges located along the short sensor edges perpendicular to the strips. The PS-s sensor is also cooled via Al-CF bridges. The PS-p is mainly cooled via the CFRP[2] baseplate covering nearly the entire backside of the sensor [CMS18]. At least for the strip sensors of the CMS Phase-2 Outer Tracker one can expect noticeable heat variations across the sensor bulk, the center being the warmest region. The temperatures between sensors of different modules will also vary because of the decreasing coolant temperature in the loop. Nevertheless, $T = -20\,°C$ can be considered as an upper limit for the FZ290 performance evaluation. This assumption is supported by thermal measurements and simulations performed by M. Rauch [Rau19][3].

9.2. Available Measurement Data

The measurement data was acquired during the FZ290 irradiation campaign presented in Chapter 8. The fluences that were chosen for this irradiation campaign correspond to the lowest and largest expected values for 2S and PS region after $3000\,fb^{-1}$ as well as the ultimate fluences at $4000\,fb^{-1}$ (see Table 8.3). An additional irradiation was carried out afterwards with `S62`, which accumulated a fluence of $1 \cdot 10^{12}\,n_{eq}cm^{-2}$ with reactor neutrons at JSI in order to check for unexpected behavior during the first weeks of operation. The measurement results of this sensor are helpful to approximate signals and leakage currents for fluences below the lowest available fluence of $1 \cdot 10^{14}\,n_{eq}cm^{-2}$. The data can be separated with respect to 2S-like and PS-like fluences depending on the neutron fraction.

The seed signals were measured in steps of 100 V from 300 V to 900 V. The value at the beginning of Phase-2 Outer Tracker operation can be assumed to be between 300 V and 350 V. This is slightly above the full depletion voltage of FZ290 sensors before irradiation (see Section 8.1). The maximum desired operation voltage is 600 V [CMS18] with an additional margin of +200 V in case of a $4000\,fb^{-1}$ extension. The envisaged annealing scenario for the Phase-2 Outer Tracker is two weeks during a short shutdown period at the end of every year. The nominal run-time is ten years. The envisaged annealing scenario for Outer Tracker sensors is, therefore, ranging from two weeks (after the first year) up to 20 weeks (after the tenth year) at room temperature. This is roughly covered by the annealing steps performed during

[1] Carbon fiber reinforced aluminum
[2] Carbon fiber reinforced polymer
[3] Internal presentation given in the scope of a meeting of the CMS Outer Tracker Modules Working Group in October 2019 at CERN

Table 9.1.: The CMS Phase-2 Outer Tracker is divided into six sectors with respect to the expected fluences in order to simplify the FZ290 performance evaluation.

Sector name	Accumulated fluence per year ($10^{14}\,\mathrm{n_{eq}cm^{-2}}$)	Accumulated fluence at $3000\,\mathrm{fb^{-1}}$($10^{14}\,\mathrm{n_{eq}cm^{-2}}$)	Affected modules (#)	Affected modules (%)
Low 2S	0.1	1	1862	24
Medium 2S	0.2	2	5322	70
Nominal 2S	0.3	3	424	6
Low PS	0.3	3	2380	43
Medium PS	0.5	5	2117	39
Nominal PS	1	10	1041	18

the measurements. The emphasized steps correspond to 2, 4, 7, 14 and 29 weeks at room temperature. The complete annealing program performed during the measurement campaign is listed in Table A.5. The leakage current was measured in 10 V steps up to 1000 V for every available fluence and annealing step at $T = -20\,^{\circ}\mathrm{C}$.

9.3. Fluence Spectrum

The expected fluence value for every single Phase-2 Outer Tracker module can be extracted from FLUKA simulations. Simulated results at $3000\,\mathrm{fb^{-1}}$ are presented in Figure 3.5. Even if one separates the fluences obtained by the simulation in $0.5 \cdot 10^{13}\,\mathrm{n_{eq}cm^{-2}}$ bins, this results in five different fluences for the 2S region and 15 fluences for the PS region. The measurements provide data for only six fluence values overall. For simplicity and because of the limited amount of data, the 2S and PS region are sectioned into three sectors: a low, medium and nominal sector. The nominal PS sector, for example, incorporates modules which accumulate fluences of $5 \cdot 10^{14}\,\mathrm{n_{eq}cm^{-2}} < \Phi_{\mathrm{eq}} \leq 1 \cdot 10^{15}\,\mathrm{n_{eq}cm^{-2}}$ during the nominal run-time of the HL-LHC. This represents the fluence spectrum of 18% of PS modules. Table 9.1 outlines the fluence accumulation as well as the total and relative amount of affected modules per sector. A sketch of one quarter of the Phase-2 Outer Tracker is shown in Figure 9.1. The colored areas highlight the different sectors.

9.4. Describing the General Course of Action

The time scope of the FZ290 performance evaluation is ten years. The yearly fluence accumulation per sector is estimated with respect to the nominal HL-LHC performance scenario of $3000\,\mathrm{fb^{-1}}$. Additionally, the fluences of the final three years of operation are estimated with respect to the ultimate HL-LHC performance scenario of $4000\,\mathrm{fb^{-1}}$. With an envisaged room temperature annealing of two weeks during the year-end shutdown results this results in 78 combinations of fluence-annealing states for the whole Outer Tracker. By approximating the seed signal S_{seed} for different bias voltages and fluence-annealing states, one can determine the minimum bias voltage that is required to operate FZ290 sensors efficiently at a given state. The signal has to be larger than 12σ in order to facilitate an efficient operation (see Section 5.7). Finally, the bias voltage is used to estimate the leakage current I_{tot} and power

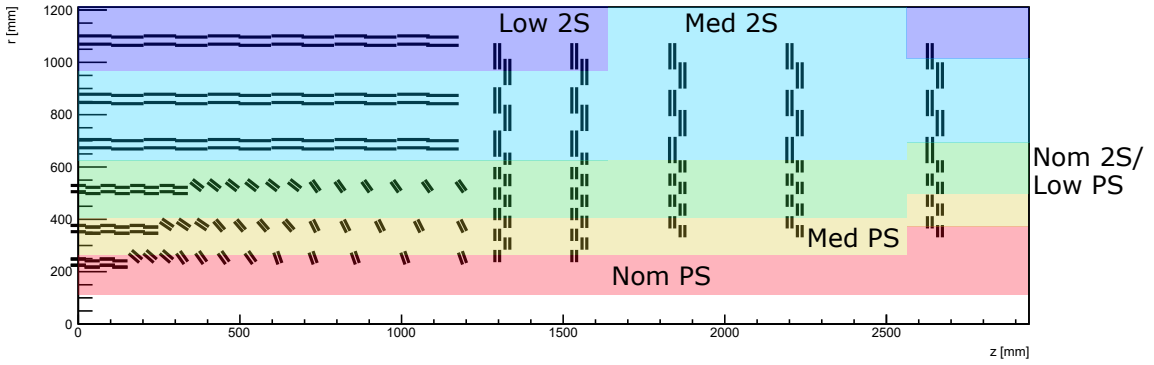

Figure 9.1.: Illustration of the CMS Phase-2 Outer Tracker sectors.

consumption P of a sensor. The minimum bias voltage, henceforth denoted by V_{opt}, reflects the optimal operation voltage for the corresponding sensors/modules in the CMS Phase-2 Outer Tracker. The 12σ margin ensures a hit efficiency of 99.5%. A higher bias voltage would only increase leakage current and power consumption without generating a significant gain in efficiency.

At first, the measurement data were used to create a set of reference data. The reference data included additional signal values for the available fluences (see Table 8.3) at uncovered annealing times and bias voltages. The additional annealing times that are required to fully cover the annealing scenario over ten years are 6, 8, 10, 12, 16, 18 and 20 weeks of room temperature annealing. The increase of the bias voltage during operation is assumed to be carried out in 50 V steps. Additionally required bias voltages are, therefore, 350 V, 450 V and so forth. The signal values were derived by linear interpolation, which is explained in Section 9.5. The course of action was similar in terms of creating the reference data of the leakage current. Leakage current values at unavailable annealing times were interpolated. Interpolations in order to increase the bias voltage coverage were not necessary, because the measurements were carried out in 10 V steps. As a next step, the remaining signal-fluence-annealing states were approximated by calculating bivariate B-spline representations of the available measurement data at every measured bias voltage. The reference data were used to tune the parameterizations if necessary. The procedure is explained in Section 9.6.

In order to account for the different radiation composition between 2S and PS region, the measurement data were separated with respect to 2S-like (neutron fraction of over 70%) and PS-like fluences (neutron fraction below 40%). An exception was made for the data of the 2S-like fluences $1 \cdot 10^{14}\,\text{n}_{\text{eq}}\text{cm}^{-2}$ and $1 \cdot 10^{12}\,\text{n}_{\text{eq}}\text{cm}^{-2}$. The corresponding signals and leakage currents had to be used for the PS region as well in order to approximate values below the lowest available PS fluence of $3 \cdot 10^{14}\,\text{n}_{\text{eq}}\text{cm}^{-2}$. The differences between neutron and proton generated defects on leakage current generation and charge collection are hardly observable for $\Phi_{\text{eq}} \leq 3 \cdot 10^{14}\,\text{n}_{\text{eq}}\text{cm}^{-2}$, which was shown in Chapter 8. Thus, using data generated from measurements of low, neutron irradiated sensors appears to be valid for approximations regarding the PS region.

9.5. Linear Interpolations

Linear interpolation was used as a means to create the reference data. Since parameterizations of the signal-fluence-annealing surfaces were only available for the measured bias voltages, linear interpolation was also used to create a 50 V bias voltage coverage for the values obtained from the parameterization. In order to approximate the signals for the required annealing times, the signal annealing is assumed to follow a linear characteristic within a reasonably narrow time window. Therefore, signals with respect to unavailable annealing times in the measurement data are obtained by calculating the weighted average of the signal of the next lower and next higher measured annealing time. The weighting is given by the difference between target annealing time a_t and the closest available annealing times $a_<$ and $a_>$ in the measurement data:

$$\Delta x_1 = a_\mathrm{t} - a_< \qquad (a_< < a_\mathrm{t}) \ , \tag{9.1}$$

$$\Delta x_2 = a_> - a_\mathrm{t} \qquad (a_> > a_\mathrm{t}) \ . \tag{9.2}$$

The weighting parameters are then calculated and multiplied with the measured signals $S_<$ and $S_>$. The sum of the results yields the weighted average signal S_t at the given annealing time a_t:

$$S_t = \frac{\Delta x_2}{\Delta x_1 + \Delta x_2} S_< + \frac{\Delta x_1}{\Delta x_1 + \Delta x_2} S_> \ . \tag{9.3}$$

Annealing is assumed to be a process that scales logarithmically [Mol99], which means that the extent of the time window between two annealing times is allowed to increase for large annealing times. To give an example, the signal for an annealing time of 6 weeks is calculated by using the signal values at 4 and 7 weeks, while the signal at 20 weeks is calculated from the signal at 14 and 29 weeks:

$$S_{t_\mathrm{a}=6} = S_{t_\mathrm{a}=4} \cdot 0.33 + S_{t_\mathrm{a}=7} \cdot 0.67 \tag{9.4}$$

$$S_{t_\mathrm{a}=20} = S_{t_\mathrm{a}=14} \cdot 0.6 + S_{t_\mathrm{a}=29} \cdot 0.4 \ , \tag{9.5}$$

where S denotes the signal and the index indicates the annealing time t_a in weeks at room temperature. In order to increase the bias voltage coverage to 50 V, the signals at 350 V, 450 V and so forth, were approximated by calculating the average signal between signals of the next higher and next lower available bias voltage. Such approximations were not required for the leakage current evaluation since it was measured in 10 V steps.

Scanning the reference data for signals that matched an expected fluence-annealing state of one of the six sectors of the CMS Phase-2 Outer Tracker yielded four matches for the 2S region and seven for the PS region. This covers 10% and 18% of the total number of fluence-annealing states for 2S and PS region, respectively. Hence, the majority of signal and leakage current values used for the evaluation of the FZ290 performance during the nominal operation time of the HL-LHC originates from spline interpolations, which are described in the next section.

9.6. Spline Interpolations

Spline interpolations were used in order to create parameterizations of the signal-fluence-annealing surfaces for every measured bias voltage. This reduces the amount of time and effort

that is required to retrieve the remaining fluence-annealing states for each sector compared to linearly interpolating every state *by hand*. It can also be understood as a first step towards developing a model for the FZ290 performance in the future tracker. Figure 9.2 shows the surface spanned by signals for different fluences and annealing times for the 2S region measured at $V_{\text{bias}} = 500\,\text{V}$ and $T = -20\,°\text{C}$. The number of data points was increased for this illustration in order to smoothen the surface. A similar procedure can be applied to the data retrieved from IV measurements, which is shown in Figure 9.3. The uncertainties are relatively small and given by the weighted sum of squared residuals of the spline approximation. The fit uncertainties for signals are approximately $240\,\text{e}^-$ and $\mathcal{O}(10^{-15})\,\text{A}\,\text{mm}^{-3}$ for the leakage currents. Signals are always rounded to nearest ten.

The values retrieved from spline interpolation are validated and tuned (if necessary) by comparing them to the reference data. The deviations originate from the fact that the spline interpolations are based on the measurement data rather then the reference data set. In order to illustrate the validation process, the reference signals and approximated signals for the nominal 2S sector were summarized in Table 9.2 for $V_{\text{bias}} = 500\,\text{V}$. The fluences during the third and tenth year of operation are matched by the measurement data. This results in two reference values for each bias voltage step for this sector. The reference values at $V_{\text{bias}} = 500\,\text{V}$ are used to tune the interpolated results. In this example, $S_{t_{\text{op}}=3}$ (index is indicating the operation time t_{op}) differs from the reference signal by $490\,\text{e}^-$. The signals for $t_{\text{op}} \leq 3\,\text{y}$ are corrected by that value. $S_{t_{\text{op}}=10}$ differs from the reference signal by $-160\,\text{e}^-$, which leads to a correction of signals with $t_{\text{op}} \geq 10\,\text{y}$ by said value. The correction of signals with $3\,\text{y} < t_{\text{op}} < 10\,\text{y}$ is determined similarly to the weighted average calculation described by Equation (9.1), Equation (9.2) and Equation (9.3).

After carrying out the calculation and the tuning of the signals, one compares the results to the lower limit of the signal specification of the region, which is in this case $12000\,\text{e}^-$. The results show that a bias voltage of 500 V is sufficient to provide signals larger than $12000\,\text{e}^-$ up to the tenth year of operation. By repeating this procedure for other available bias voltages one can estimate the optimal bias voltage for every remaining fluence-annealing state.

9.7. Results

Table 9.3 and Table 9.4 summarize the FZ290 performance evaluation of the nominal HL-LHC scenario of $3000\,\text{fb}^{-1}$ over the course of ten years. The last three columns represented the evaluation of the FZ290 performance with respect to a $4000\,\text{fb}^{-1}$ extension. The tables include the optimal bias voltage V_{opt}, the corresponding signal S_{seed}, total leakage current I_{tot} and power consumption P per sensor, for the expected fluences and annealing times on a yearly basis for the different sectors defined in Table 9.1. The reference values are depicted in bold characters. The obtained values for the volume generated leakage current were multiplied by $V_{2S} = 2668\,\text{mm}^3$ or $V_{PS-s} = 1314\,\text{mm}^3$ in order to reflect the expected total leakage current per 2S or PS-s sensor, $I_{\text{tot, 2S}}$ or $I_{\text{tot, PS-s}}$, respectively. The power consumption was calculated by multiplying V_{opt} and the total leakage current per sensor. The leakage current and power values are given with respect to an sensor temperature of $-20\,°\text{C}$. A sensor temperature of $-20\,°\text{C}$ can be considered a worst case scenario. The leakage current can be easily scaled to a more optimistic temperature if necessary. Following Equation (4.23), the leakage current and, hence, the power consumption would reduce by 45% at $T = -25\,°\text{C}$. The approximated signal and operation voltage values are not impacted by temperature.

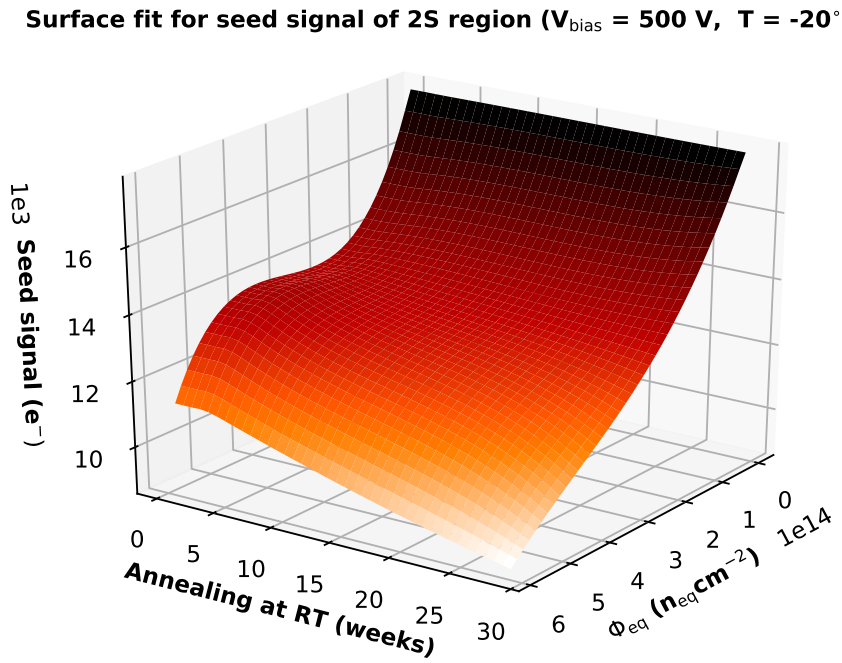

Figure 9.2.: Surface fit of the seed signal of the 2S region. The data was taken from signal measurements carried out with different fluences and annealing times, measured at $V_{\text{bias}} = 500\,\text{V}$ and $T = -20\,°\text{C}$.

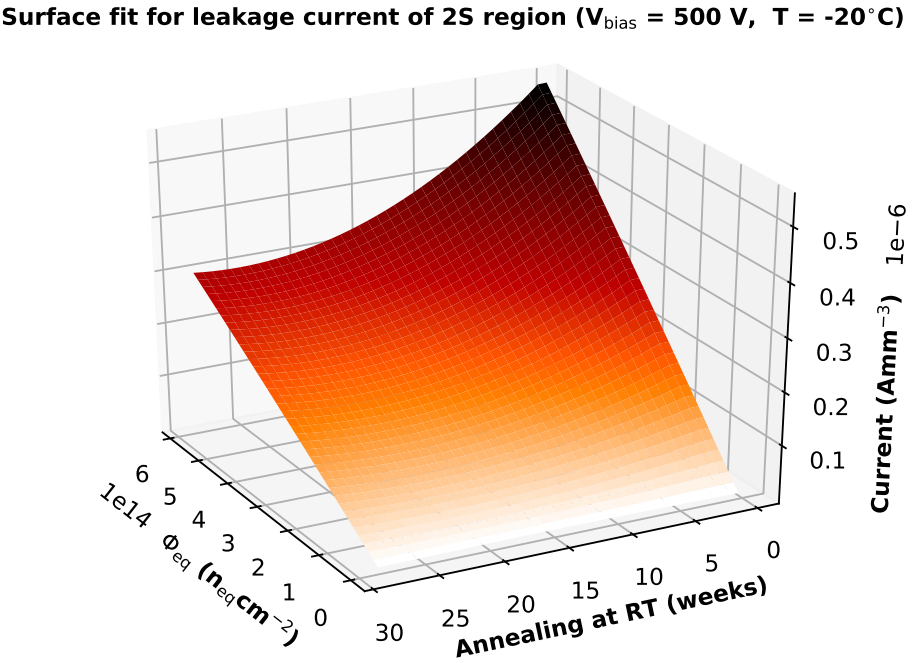

Figure 9.3.: Surface fit of leakage current of the 2S region. The data was taken from IV measurements carried out with different fluences and annealing times, measured at $V_{\text{bias}} = 500\,\text{V}$ and $T = -20\,°\text{C}$.

Table 9.2.: Approximated signals from spline interpolation S_{spline} at $V_{\text{bias}} = 500\,\text{V}$ with respect to the accumulated fluence and annealing time t_{a} expected for the nominal 2S sector per operation year t_{op}. The reference signals are used to tune the interpolated data which yields S_{seed}.

t_{op} (y)	t_{a} (w)	Φ_{eq} ($10^{14}\,\text{n}_{\text{eq}}\text{cm}^{-2}$)	S_{ref} (e^-)	S_{spline} (e^-)	S_{seed} (e^-)
1	2	1	-	16710	16230
2	4	2	-	15800	15310
3	6	3	14640	15130	14640
4	8	4	-	14600	14160
5	10	5	-	13810	13780
6	12	6	-	13520	13470
7	14	7	-	13560	13220
8	16	8	-	13270	13020
9	18	9	-	13040	12830
10	20	10	12630	12790	12630

The experimental data was obtained from measurements with miniature versions of the 2S sensor. The PS-s sensor design is very similar to the 2S, both are strip sensors and made from FZ290 material. Therefore, one can expect a similar performance in terms of leakage current and charge collection. The PS-p is a macro-pixel sensor. Nevertheless, the driving factor of leakage current generation and charge collection is the thickness. It is safe to assume that the values presented in Table 9.4 are also valid for the PS-p (both sensors have a similar active volume). The noise of the MPA is currently assumed to be about $200\,\text{e}^-$ which results in $2400\,\text{e}^-$ for the lower limit of the signal specification. Hence, the required operation voltage of the PS-p is much lower. However, the operation voltage in the future tracker cannot be individually adjusted for every module or, even less so, for every sensor. The chosen operation voltage for PS modules is, therefore, determined by the efficiency of the PS-s.

About 94% of 2S modules of the CMS Phase-2 Outer Tracker, represented by the low and medium 2S sector, can be operated in a bias voltage range of $300 + 150\,\text{V}$ even during the ultimate HL-LHC scenario. Due to the low noise of the SSA compared to the CBC, the expected operation voltages for about 82% of the PS modules are in the same bias voltage range even during the ultimate HL-LHC scenario. Only the innermost PS modules have to be operated at the desired maximum operation voltage of 600 V at the end of the nominal run-time. These modules require a bias voltage boost of +50 V at the end of operation if the ultimate HL-LHC scenario is realized. Figure 9.4 shows the power consumption per sensor and year for different sectors during the nominal HL-LHC operation at $T = -20\,^{\circ}\text{C}$ and the optimal operation voltage. The power consumption for sensors of the low and medium 2S and PS sector is fairly similar. The expected maximum power consumption is given by the innermost PS modules after ten years of operation, where P amounts to 507 mW per sensor for $T = -20\,^{\circ}\text{C}$. The expected maximum power consumption for a 2S sensor at the same time period is 55% lower.

Based on these results the CMS collaboration is strongly advised to not exceed annealing times of 20 weeks at room temperature during operation, because of the significant impact of reverse

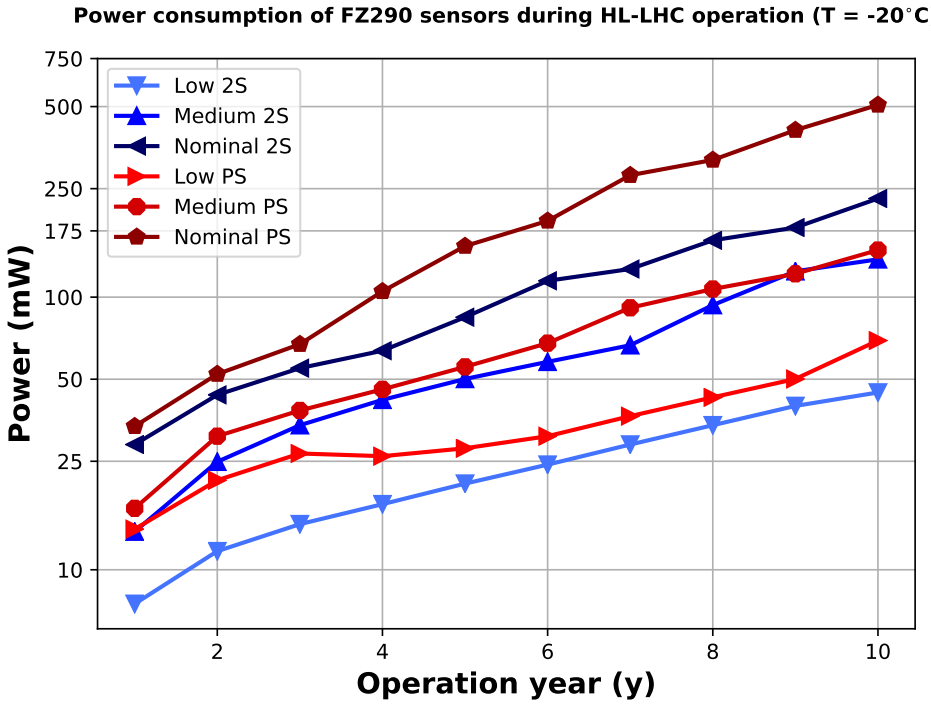

Figure 9.4.: Power consumption of FZ290 sensors for the nominal HL-LHC performance scenario at $T = -20\,°\mathrm{C}$.

annealing, especially for a $4000\,\mathrm{fb}^{-1}$ extension. If one were to assume annealing times of 22, 24 and 26 weeks at room temperature for the last three years of operation during the ultimate HL-LHC scenario, the optimal bias voltages would increase between 50 V and 150 V. The increase of the bias voltage outweighs the benefit of short-term leakage current annealing at this stage and would, therefore, result in a significant increase of leakage current generation and power consumption.

9.8. Conclusion

The goal of this analysis was to predict and evaluate the performance of FZ290 sensors in the CMS Phase-2 Outer Tracker over course of the nominal HL-LHC run-time. The future Outer Tracker was divided into six sectors in order to simplify the evaluation process. The FZ290 performance was evaluated by approximating the required minimum operation voltage and the respective signal, leakage current and power consumption at $T = -20\,°\mathrm{C}$. The results presented in this chapter indicate that a vast majority of Phase-2 Outer Tracker modules can be operated at low bias voltages for the largest part of the operation time. The approximations can be considered conservative, which is explained in Section 9.1, and, therefore, compensate for potential FLUKA uncertainties. Most of the interpolations were carried out by using measurement data in order to generate parameterizations of the signal-annealing-fluence and current-annealng-fluence surfaces for every measured bias voltage and for each of the six sectors defined by Table 9.1. The analysis of the data reveals that a vast majority of 2S and PS modules can be operated at bias voltages between 300 V and 450 V even at the end of the ultimate HL-LHC scenario. The sensors generate less leakage current and require less cooling power at lower bias voltages, which minimizes the risk of thermal runaway.

Table 9.3.: Approximated FZ290 performance for the 2S region in terms of required minimum operation voltage, signal, leakage current and power consumption at $T = -20\,^{\circ}\mathrm{C}$.

HL-LHC scenario (fb^{-1})	3000										4000		
Operation time (y)	1	2	3	4	5	6	7	8	9	10	8	9	10
Annealing (w)	2	4	6	8	10	12	14	16	18	20	16	18	20
Low 2S ($10^{14}\,\mathrm{n_{eq}cm^{-2}}$)	0.1	0.2	0.3	0.4	0.5	0.6	0.7	0.8	0.9	**1**	1.1	1.2	1.3
V_{opt} (V)	300	300	300	300	300	300	300	300	300	**300**	300	300	350
S_{seed} (e^-)	17340	16990	16440	15895	15370	14870	14380	13880	13360	**12810**	12870	12330	12780
$I_{tot,2S}$ (µA)	25	49	68	84	97	109	119	130	141	**153**	165	174	197
P (mW)	7.5	14.7	20.4	25.2	29.1	32.7	35.7	39.0	42.3	**45.9**	45.9	49.5	69.0
Med. 2S ($10^{14}\,\mathrm{n_{eq}cm^{-2}}$)	0.2	0.4	0.6	0.8	**1.0**	1.2	1.4	1.6	1.8	2	2.2	2.4	2.6
V_{opt} (V)	300	300	300	300	**300**	300	300	350	400	400	400	450	450
S_{seed} (e^-)	17180	16454	15470	14560	**13740**	12970	12190	12300	12810	12375	12130	12470	12190
$I_{tot,2S}$ (µA)	48	89	121	147	**168**	183	195	219	242	261	305	330	349
P (mW)	14.4	26.7	36.3	44.1	**50.4**	54.9	58.5	76.7	96.8	104.4	122	148.5	157.1
Nom. 2S ($10^{14}\,\mathrm{n_{eq}cm^{-2}}$)	0.3	0.6	**0.9**	1.2	1.5	1.8	2.1	2.4	2.7	**3**	3.2	3.6	4
V_{opt} (V)	300	300	**300**	300	350	400	400	450	450	**500**	500	500	550
S_{seed} (e^-)	16160	15040	**13710**	12600	12700	12990	12028	12420	12050	**12630**	12640	12360	12480
$I_{tot,2S}$ (µA)	87	142	**184**	222	252	292	323	368	403	**468**	509	559	636
P (mW)	26.1	42.6	**55.2**	66.6	88.2	116.8	129.2	165.6	181.4	**234**	254.5	279.5	349.8

Table 9.4.: Approximated FZ290 performance for the PS region in terms of required minimum operation voltage, signal, leakage current and power consumption at $T = -20\,°\mathrm{C}$.

HL-LHC scenario (fb^{-1})	3000										4000			
Operation time (y)	1	2	3	4	5	6	7	8	9	10	8	9	10	
Annealing (w)	2	4	6	8	10	12	14	16	18	20	16	18	20	
Low PS ($10^{14}\,\mathrm{n_{eq}cm^{-2}}$)	0.3	0.6	**0.9**	1.2	1.5	1.8	2.1	2.4	2.7	**3**	3.2	3.6	4	
V_{opt} (V)	300	300	**300**	300	300	300	300	300	300	**350**	350	350	400	
S_{seed} (e^-)	16160	15040	**13710**	13010	12130	11340	10690	10190	9790	**10510**	10110	9790	10600	
$I_{tot,PS-s}$ (µA)	43	71	**87**	95	113	130	145	160	174	**197**	232	250	265	
P (mW)	12.9	21.3	26.1	28.5	33.9	39	36.6	43.5	52.2	69	81.2	87.5	92.8	
Med. PS ($10^{14}\,\mathrm{n_{eq}cm^{-2}}$)	0.5	**1**	1.5	2	2.5	**3**	3.5	4	4.5	5	5	**6**	7	
V_{opt} (V)	300	**300**	300	300	300	**300**	350	350	350	400	400	**400**	450	
S_{seed} (e^-)	15690	**13864**	12900	11720	10670	**9860**	10340	10040	9840	10810	10270	9810	10020	
$I_{tot,PS-s}$ (µA)	69	**92**	124	153	179	**201**	267	292	314	324	391	**439**	506	
P (W)	20.7	27.6	37.2	45.9	53.7	60.3	93.5	102.2	109.9	129.6	156.4	175.6	227.7	
Nom. PS ($10^{14}\,\mathrm{n_{eq}cm^{-2}}$)	**1**	2	**3**	4	5	6	7	8	9	**10**	11	12	13	
V_{opt} (V)	**300**	300	**300**	350	450	450	500	500	550	**600**	600	600	650	
S_{seed} (e^-)	**13870**	12260	**10390**	9728	10610	9990	10576	10060	10160	10300	10415	9805	9710	
$I_{tot,PS-s}$ (µA)	**111**	173	**225**	325	445	518	612	670	759	**845**	898	921	972	
P (W)	33.3	51.9	67.5	113.8	200.3	233.1	306	335	417.5	507	538.8	552.6	631.8	

9.9. Outlook

Ten surface parameterizations were necessary in order to approximate the signal and 14 for the leakage current approximations. Defining an accurate model which yields the signal value for every given period of the Phase-2 Outer Tracker operation, would be the more elegant approximation approach. The signal is a function of fluence, bias voltage and annealing, which would be the independent parameters of the model. The ansatz for a model could look like this:

$$S(\Phi_{\mathrm{eq}}, V_{\mathrm{bias}}, a_{\mathrm{t}}) = S_{\mathrm{base}}(\Phi_{\mathrm{eq}}, V_{\mathrm{bias}}) + S_{\mathrm{var}}(\Phi_{\mathrm{eq}}, V_{\mathrm{bias}}, a_{\mathrm{t}}) \ . \tag{9.6}$$

S_{base} represents the degenerated signal due to irradiation at a certain bias voltage. S_{var}, which can be positive or negative, represents the signal variation due to annealing, which is dependent on the annealing time, fluence and bias voltage. This correlation is indicated by Figure 8.12 and Figure 8.13. The bias voltage dependence of the annealing characteristic is indicated by the different amount of beneficial annealing between 600 V and 800 V. The suppression of reverse annealing is most pronounced for $\Phi_{\mathrm{eq}} \geq 6 \cdot 10^{14}\,\mathrm{n_{eq}cm^{-2}}$, which ultimately shows the fluence dependence of the annealing behavior. All in all, one has to fit a four dimensional parameter space. In fact, one needs to develop a second model to be able to approximate the leakage current for any given state of fluence, bias voltage and annealing. The parameter space increases even further if one is eager to create a uniform model for the whole Outer Tracker, since the annealing of the signal as well as the depletion behavior depends on the neutron share of the radiation process, which is different for 2S and PS region. Parameters like charge collection and depletion behavior also depend on the material properties (oxygen concentration, thickness and so forth). This must be considered if one wanted to create a more general model which is not overfitted to FZ290 data.

A model like the one proposed by Equation (9.6) was difficult to develop, because of the limited amount of data. The lack of data for $\Phi_{\mathrm{eq}} < 1 \cdot 10^{14}\,\mathrm{n_{eq}cm^{-2}}$ for the 2S region in addition to missing fluences between $3 \cdot 10^{14}\,\mathrm{n_{eq}cm^{-2}}$ and $1 \cdot 10^{15}\,\mathrm{n_{eq}cm^{-2}}$ for the PS region weighs especially heavy. The irradiation studies conducted in the course of the CMS Phase-2 Outer Tracker Upgrade always targeted the expected maximum fluences, in order to evaluate if a certain sensor material was able to generate sufficient signal at $3000\,\mathrm{fb^{-1}}$ and $4000\,\mathrm{fb^{-1}}$. This leaves the major part of the operation time uncovered. Now that the sensor performance at the end of the HL-LHC run-time is well-described by measurement data and the material choice is finalized, future irradiation tests could concentrate on these missing fluence ranges. Furthermore, the samples which were used for irradiation studies were always annealed after accumulating the target fluence. This approach is completely blind to potential low-fluence annealing or low-fluence leakage current effects. It would be interesting to investigate signal and leakage current following a step-by-step irradiation and annealing approach as it takes place in a real detector under laboratory conditions. Such a study is only feasible if a dedicated test setup is developed and installed at one of the available irradiation sites.

10
Frontside Biasing

The conventional biasing scheme for silicon sensors was introduced in Section 4.8 and is known as backside biasing (BSB). Sensor backside and bias ring are connected to a voltage source and then operated in reverse bias mode. The 2S module of the CMS Phase-2 Outer Tracker contains two 2S sensors with their backsides facing inwards. Therefore, the backside is not accessible during the final wire-bonding step, which builds the frontside connections (bias ring to service electronics and strips to readout channels). The backside has to be processed individually at the beginning of the module assembly. One has to attach, glue and wire-bond a special connector to the backside of each sensor. The wire-bonds need to be encapsulated afterwards. Firstly, building a reliable connection is a difficult task. Secondly, wire bonding is a potential bottle neck during module production. The wire-bond connection of the backside will use up valuable bonding capacity. Thirdly, in order to attach the connector to the backside, one has to place a sensor face down on a support carrier, which bears the risk of damaging the sensitive frontside of the sensor. By utilizing frontside biasing as the baseline for CMS Phase-2 Outer Tracker modules, one could avoid the usage of this backside connector. Risky and time-consuming assembly steps would be eliminated and the module construction would be facilitated.

The concept of frontside biasing (FSB) was initially introduced in Ref. [Nak+00]. Instead of applying a high voltage (HV) connection to the sensor backside, one can apply HV to the aluminum ring at the edge region (edge ring) of the sensor. Edge ring and backside are interconnected as a consequence of the conductive characteristic of the edge region. They are always set to the same electric potential. In the case of an n-in-p sensor, reverse bias is established by applying negative HV to the edge ring and a ground connection to the bias ring. The FSB scheme is illustrated in Figure 10.1.

This study investigates the validity of frontside biasing as an alternative biasing scheme for the CMS Phase-2 Outer Tracker Upgrade, but also for high energy physics experiments in general. Therefore, one has to compare the sensor characteristics under frontside-biased and backside-biased modes of operation especially after irradiation. The irradiation studies presented in the previous chapters focused on the properties of the active sensor region, whereas this study mainly investigates the properties of the sensor edge. The most important parameter is the resistivity of the material and its dependence on temperature, fluence, annealing and bias voltage. The measurement data used as a basis for this study were mainly obtained at ETP. Simulations were performed by E. Pree at HEPHY, Vienna, Austria. The results were combined and published in Ref. [Bas+18] which was authored by myself. This chapter does not contain discussions about the bias voltage and annealing dependency of the resistivity included in Ref. [Bas+18]. These topics were mainly investigated by the research team at HEPHY.

The nomenclature of the sensors differs from the one described in Chapter 6. The reason being, that this study uses sensors of different materials. The names indicate the sensor type (first character) and the active thickness (3-digit number) in order to improve the comprehensibility

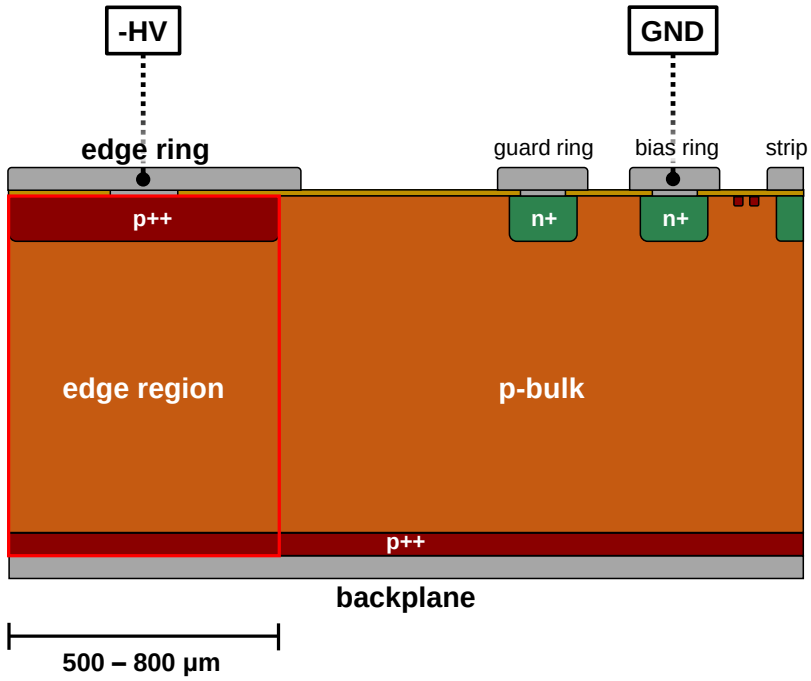

Figure 10.1.: Illustration of the FSB scheme on an n-in-p silicon strip sensor. The red box highlights the edge region, which is defined by the lateral dimensions of the highly doped edge implant at the sensor frontside [Bas+18].

Table 10.1.: List of sensor types used for this study. The sensor nomenclature indicates the active thickness of the sample (3-digit number) and the sensor type (first character). The D sensors were produced by IFX and are physically thinned to 200 µm. The other sensors were processed by HPK. These sensors stem from the ddFZ240 and ddFZ200 batches which were characterized in Chapter 7.

Abbreviation	Sensor name	A_{sensor} (cm)	A_{edge} (cm)
A200	`ddFZ200 Irradiation`	1.83	0.38
A240	`ddFZ240 Irradiation`	1.83	0.38
B200	`ddFZ200 KIT Test`	3.10	0.46
B240	`ddFZ240 KIT Test`	3.10	0.46
C240	`ddFZ240 Baby`	6.96	0.81
X240	`ddFZ240 2S`	96.66	2.54
D200	`thFZ200 Baby IFX`	13.49	1.01

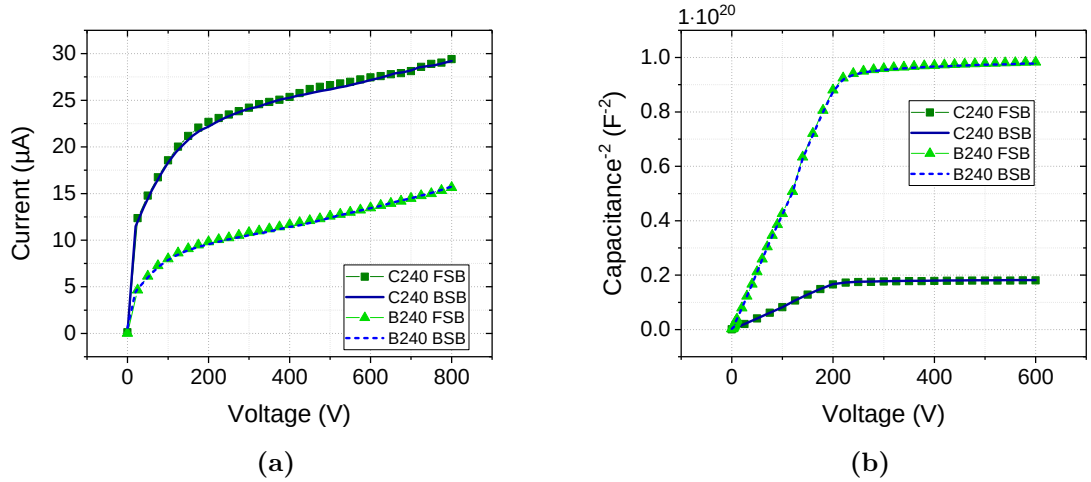

(a) (b)

Figure 10.2.: (a) Typical IV measurement of two different sensors measured at $T = 20\,°\text{C}$. (b) CV characteristics of the same sensors. Green markers represent measurements utilizing the FSB approach while the blue lines represent measurements utilizing the BSB approach [Bas+18].

of the plots. Table 10.1 summarizes the sensor names and abbreviations used in this chapter in addition to the respective areas of the edge region A_{edge} and the surface areas of the sensors A_{sensor}. The measurements conducted at HEPHY were carried out with sensors processed by Infineon Technologies Austria AG (IFX) [Inf]. The sensors were physically thinned to a thickness of 200 µm (D200). Their design is comparable to the design of the Baby sensor of the 2S wafer. The base resistivity of the IFX material is about $6\,\text{k}\Omega\,\text{cm}$. The other samples presented in this chapter stem from the ddFZ240 and ddFZ200 batches, which were processed by HPK and characterized in Chapter 7. The HPK material has a base resistivity of about $3\,\text{k}\Omega\,\text{cm}$.

10.1. Characteristic Measurements before Irradiation

The probe stations at ETP and HEPHY were used to conduct IV and CV measurements. The probe stations can be easily modified for frontside biasing by adding a second bias needle, which is connected to the HV output of a power supply. There are several contact pads located on the edge ring which are not passivated. The needle tip is positioned on such a contact pad and used for applying negative HV to the sensor edge. For IV and CV measurements the chuck on, which the sensor is placed in the probe station, is always floating. Figure 10.2a and Figure 10.2b show typical IV and CV characteristics of two different unirradiated sensors measured by utilizing the BSB and FSB scheme. One can observe no significant difference between both modes of operation. Strip and signal measurement were also conducted under frontside-biased conditions. No variations were observed between FSB and BSB. This behavior is expected, since edge ring and backside are always on the same potential independent of the biasing scheme. The electric field in the active region is the same for BSB and FSB. Therefore, FSB is a valid approach to operate and test silicon strip sensors before irradiation.

10.2. Impact of Edge Dimension

The edge is assumed to act as an ohmic connection between frontside and backside. The edge dimensions of the sensors used for this study are precisely known. Therefore, one can calculate the resistivity ρ of the edge based on the measured resistance R_{edge} by following the well-known resistor formula:

$$\rho = R_{\text{edge}} \cdot \frac{A_{\text{edge}}}{L} \ . \tag{10.1}$$

The width of the edge area A_{edge} is defined by the distance between cut edge and the inner border of the edge implant. The edge length L is determined by the active thickness of the sensor. Highly doped backside implants of at 30 µm are typical for HPK sensors. The deep-diffused sensors examined in this chapter provide even larger backside implants (between 80 µm and 120 µm). With a doping concentration of about $1 \cdot 10^{19}\,\text{cm}^{-3}$ (see Table 6.1) the resistivity of the highly doped backside layer is below 1 Ω cm and, therefore, several orders of magnitude smaller than the bulk resistivity [Zeg07]. The statement that ρ is driven by the active region of the sensor bulk is important for accurately determining the edge resistivity with Equation (10.1).

The characterization of the sensor edge was performed by utilizing edge resistivity (ER) measurements. The edge resistance is measured by applying low voltage offsets between edge ring and backside. The edge resistances are retrieved from the inverse slopes of the IV characteristics which follow Ohm's law. Finally, the resistivity can be calculated by using Equation (10.1). The circuitry of ER measurements, which is shown in Figure A.6, also allows for measuring R_{edge} while depleting the sensor bulk at the same time. The impact of bias voltage and the explanation of the underlying mechanism are shown in Ref. [Bas+18]. Figure 10.3 presents the results of ER measurements on unirradiated sensors with different edge dimensions, conducted at $T = 20\,°\text{C}$. Voltage ramps were performed in steps of 1 mV up to 1 V, which depended on the edge area and the bulk resistivity of the sample. A few millivolts suffice to generate currents of several 100 µA for large A_{edge}. The comparison of the ddFZ200 and ddFZ240 sensor corroborates the assumption that only the active thickness contributes to the resistance:

$$\frac{L_{200}}{L_{240}} = 0.83 \approx \frac{R_{200}}{R_{240}} = 0.88 \tag{10.2}$$

This observation was also validated by TCAD simulations with a typical bulk resistivity of 3 kΩ cm from HPK material. Details regarding the simulations can be found in Ref. [Bas+18]. The simulated results state a resistance of 113 Ω for $L = 200$ µm and 137 Ω for $L = 240$ µm which coincides with the experimental results.

For an additional justification for using Equation (10.1) in this context, one can compare the extracted resistivities from ER measurements ρ_{ER} with the reference resistivities ρ_{CV} presented in Ref. [Ber+16]. Following Equation (4.12), the resistivity is inversely proportional to the full depletion voltage. One can, therefore, extract the reference values from CV measurements on diodes of the respective material. The results are summarized in Table 10.2. Both methods yield comparable results, which further supports the validity of extracting the resistivity of the material from ER measurements.

The statistical uncertainty of R_{edge} from the straight line fit is negligible. The uncertainty of ρ_{ER} is given by the standard deviation of the resistivity among the measured samples of

Table 10.2.: Mean resistivities for different materials resulting from CV measurements on diodes [Ber+16] and edge resistivity measurements [Bas+18].

Material	ρ_{ER} (kΩcm)	ρ_{CV} (kΩcm)	ρ_{ER}/ρ_{CV}
240 µm, ddFZ (HPK)	2.7 ± 0.4	3.0 ± 0.1	0.90 ± 0.13
200 µm, ddFZ (HPK)	2.7 ± 0.5	3.3 ± 0.1	0.81 ± 0.12
200 µm, FZ (IFX)	6.3 ± 0.6	6.5 ± 0.3	0.97 ± 0.05

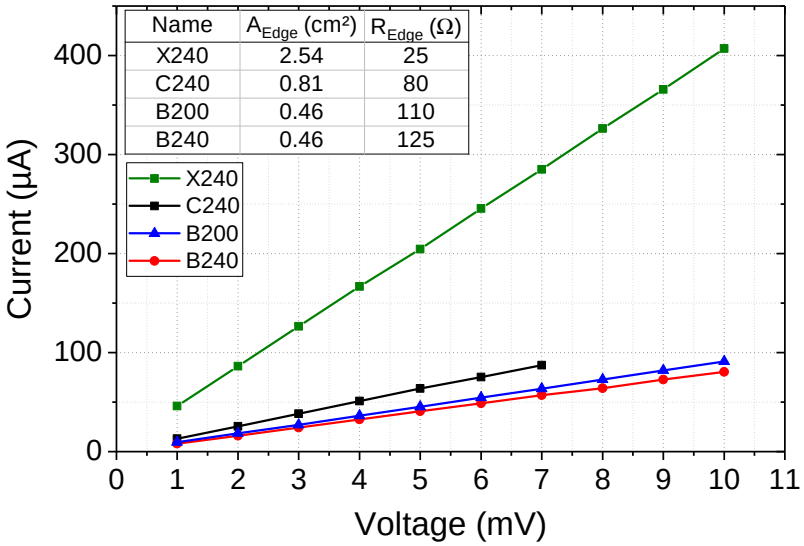

Figure 10.3.: R_{edge} measurements of unirradiated sensors with different edge dimensions conducted at $T = 20\,°\text{C}$ [Bas+18].

a certain material. Based on the measurement results and the given variations of ρ_{ER}, one can state that the resistivity is not constant among wafers of a single batch or even sensors of the same wafer. This can be related to variations of the active thickness and the doping profile. Similar assumptions were already made in Chapter 7 and Chapter 8 in order to explain variations of V_{fd} among different sample designs. The sensors used for FSB studies and the ones presented in Chapter 7 are the same. The uncertainty of the active thickness given by the vendors is ±10 µm. This corresponds to an uncertainty of about 5%, which equates to the uncertainty of ρ_{CV}. The difference between the two methods for determining the resistivity is small for the physically thinned IFX samples (3%). The variations for deep diffused material are 10% for ddFZ240 and 19% for ddFZ200. This indicates that the knee of the doping profile in the transition region between deep diffused implant and active region is less well-defined for deeper implants. Hence, the uncertainty of the active thickness increases as well as the uncertainty of the resistivity.

10.3. Temperature Dependence before Irradiation

As explained in Section 4.4, the temperature dependence of ρ is driven by an impairment of the carrier mobility due to phonon scattering for the temperature range of the measurements shown in this chapter. The expected temperature dependence is given by Equation (4.16).

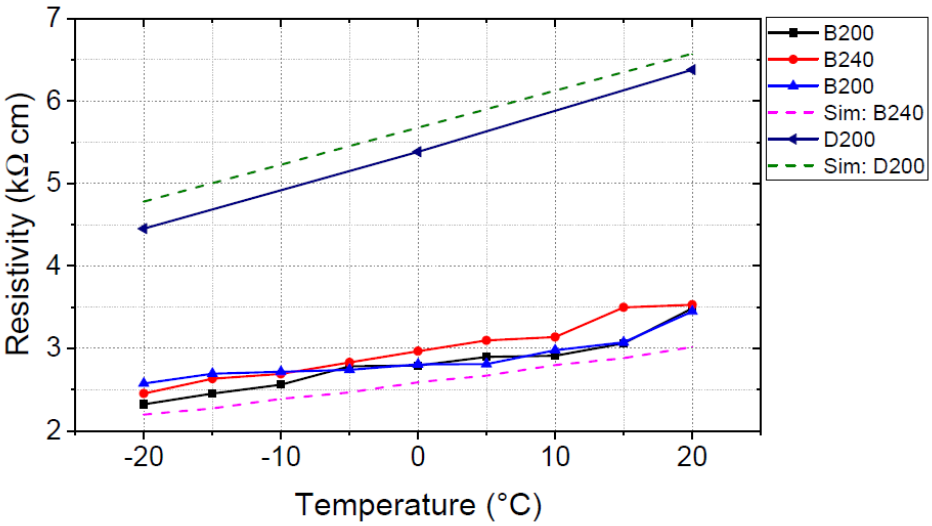

Figure 10.4.: Resistivity over temperature characteristic of unirradiated sensors [Bas+18].

The resistivity is expected to follow a T^a-characteristic with $a = 2.42$. The value is derived from the measured temperature dependency of the electron and hole mobility in extrinsic silicon over a temperature range of about 400 K and for a typical bulk doping concentration of $1 \cdot 10^{12}\,\mathrm{cm}^{-3}$ [Sze81]. Figure 10.4 shows the results of ER measurements of unirradiated sensors for $-20\,°\mathrm{C} \leq T \geq 20\,°\mathrm{C}$. The solid lines represent measurement data. The dashed lines represent results obtained by simulations. The increase from T_{min} to T_{max} corresponds to roughly 29% for HPK samples and 30% for the IFX sample. The almost linear characteristic shown in Figure 10.4 is a consequence of the small temperature range of 40 K. Therefore, a validation of the reference value a is not possible. As shown in Ref. [Bas+18], the resistivity follows Equation (10.3):

$$R = R_0 + R_1 \cdot T^{2.42}. \tag{10.3}$$

10.4. Impact of Radiation Damage

Understanding the impact of radiation damage on the edge resistivity of silicon sensors is especially important for HEP experiments. Figure 10.5 shows the IV characteristics of an irradiated sensor to a fluence of $1 \cdot 10^{15}\,\mathrm{n_{eq}cm}^{-2}$ operated via BSB and FSB. The measurement was conducted at $T = -20\,°\mathrm{C}$. The spread between the curves originates from a voltage drop ΔV along the sensor edge which emerged after the irradiation. The effective bias voltage V_{eff} of the sensor is given by:

$$V_{\mathrm{eff}} = V_{\mathrm{bias}} - \Delta V. \tag{10.4}$$

The offset between the curves at $I_{\mathrm{tot}} = 50\,\mu\mathrm{A}$ corresponds to a voltage drop of about 100 V. If one assumes an ohmic behavior of the irradiated edge then ΔV can then be calculated by:

$$\Delta V = R_{\mathrm{edge}} \cdot I_{\mathrm{tot}}, \tag{10.5}$$

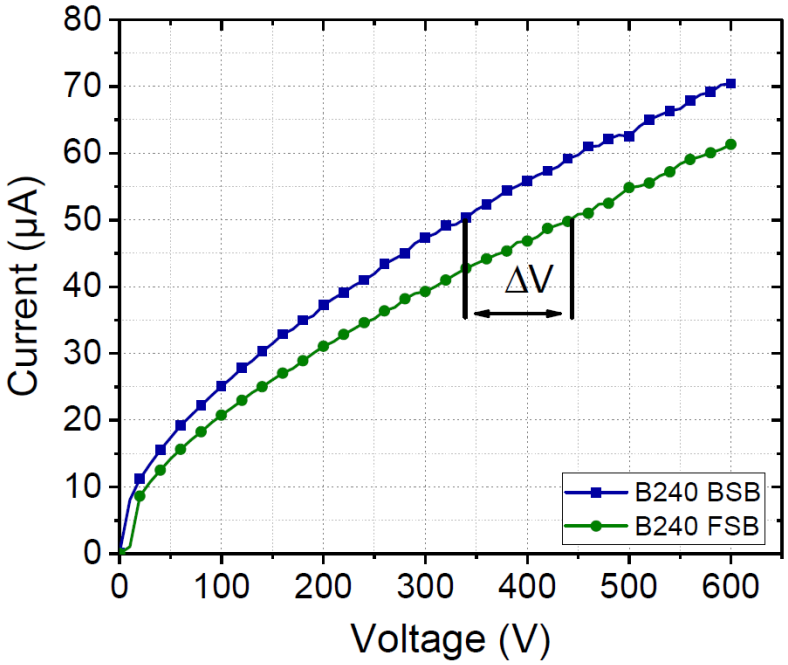

Figure 10.5.: IV characteristic of a sensor irradiated to a fluence of $1 \cdot 10^{15}\,\mathrm{n_{eq}cm^{-2}}$ with HV applied via BSB (blue) and FSB (green). The measurement was conducted at $T = -20\,°\mathrm{C}$ [Bas+18].

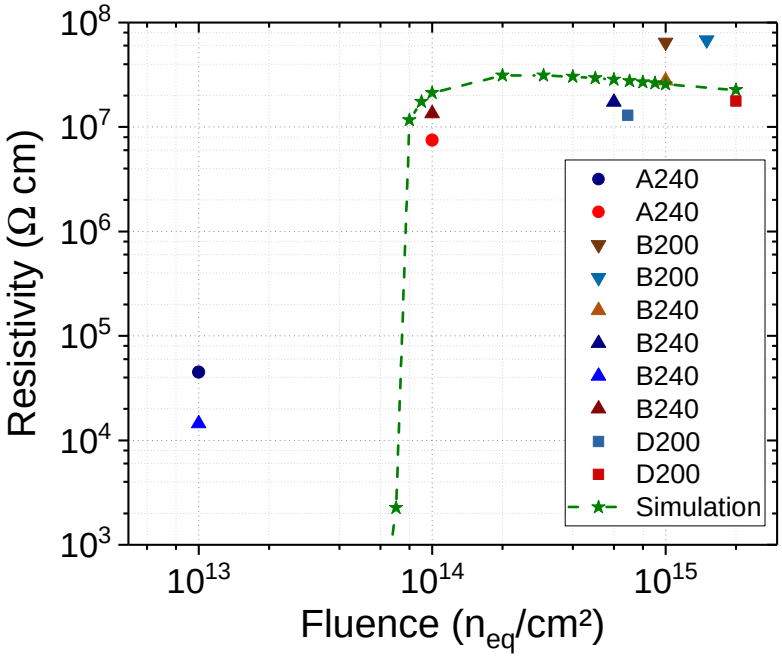

Figure 10.6.: Edge resistivity obtained from ER measurements on sensors with different fluences measured at $T = -20\,°\mathrm{C}$ [Bas+18].

where both R_{edge} and I_{tot} are proportional to fluence. The edge resistance can be determined from ER measurements in order to calculate ΔV. The voltage offset between edge rings and backside, which is applied during ER measurements, had to be increased after irradiation in order to produce currents comparable to those before irradiation. Depending on the edge dimensions and the accumulated fluences of the sensors, one had to apply 50 V and more. Moreover, the uncertainties of the straight line fit on the IV characteristics increase because the characteristics are not exactly linear for lower currents.

The measurements reveal that the resistivity of the material is significantly increased after irradiation. Figure 10.6 depicts the results of ER measurements for sensors with different accumulated fluences at $T = -20\,^{\circ}\text{C}$. The resistivity before irradiation is in the order of $10^3\,\Omega\,\text{cm}$. The increase of the resistivity at a fluence of $1 \cdot 10^{13}\,\text{n}_{\text{eq}}\text{cm}^{-2}$ is about one order of magnitude. This fluence roughly corresponds to a fluence accumulation of a 2S module during the first year of operation of the HL-LHC. The resistivity increases by four orders of magnitude at a fluence of $1 \cdot 10^{14}\,\text{n}_{\text{eq}}\text{cm}^{-2}$. The characteristic appears to saturate between $10^7\,\Omega\,\text{cm}$ and $10^8\,\Omega\,\text{cm}$ for fluences beyond $6 \cdot 10^{14}\,\text{n}_{\text{eq}}\text{cm}^{-2}$. The dashed green line represents the calculated resistivity with respect to the simulated edge current for different fluences. The results correlate well with the experimental findings for $\Phi_{\text{eq}} \geq 1 \cdot 10^{14}\,\text{n}_{\text{eq}}\text{cm}^{-2}$. The irradiation model that was used for the simulations is only valid in a fluence range of $1 \cdot 10^{14}\,\text{n}_{\text{eq}}\text{cm}^{-2} \leq \Phi_{\text{eq}} \leq 1 \cdot 10^{15}\,\text{n}_{\text{eq}}\text{cm}^{-2}$ [Ebe13] and is, therefore, not suitable for describing the edge properties for lower fluences.

Figure 10.7 shows the electron density and hole density for $-20\,^{\circ}\text{C} \leq T \leq 20\,^{\circ}\text{C}$ before and after irradiation ($\Phi_{\text{eq}} = 6 \cdot 10^{14}\,\text{n}_{\text{eq}}\text{cm}^{-2}$) from TCAD simulations. The values were simulated at the center of the edge region. As stated by Equation (4.7), a reduction of the sum of p and n leads to an increase of the resistivity of approximately the same order. In case of a p-doped bulk this sum is dominated by the hole density. The simulations reveal a decrease of the hole density due to irradiation by about two orders of magnitude at $T = +20\,^{\circ}\text{C}$. This corresponds to the measured increase of the resistivity which was reported in Ref. [Dez+99]. The study investigated the change in resistivity of simple silicon resistors with resistivities between $400\,\Omega\,\text{cm}$ and $4\,\text{k}\Omega\,\text{cm}$ at room temperature and after neutron irradiation. The measured resistivities after irradiation saturated at a value of about $300\,\text{k}\Omega\,\text{cm}$. This slightly exceeds the theoretically calculated limit of $230\,\text{k}\Omega\,\text{cm}$, which is given by the intrinsic resistivity of silicon at room temperature [Sze81]. This corresponds to the relation of n and p in an intrinsic semiconductor, where the carrier densities are equal. A decrease or increase of both quantities at the same time is forbidden by the mass action law presented by Equation (4.9). Therefore, the intrinsic resistivity of silicon determines the theoretical limit of ρ at a given temperature.

The decrease of the hole density at $T = -20\,^{\circ}\text{C}$ shown in Figure 10.7 is about four orders of magnitude, which coincides with the increase of the resistivity presented in Figure 10.6. Furthermore, the shift of the carrier densities is also responsible for the saturation of the resistivity that was observed during the measurements. One can see that electron and hole density are almost equal at a fluence of $6 \cdot 10^{14}\,\text{n}_{\text{eq}}\text{cm}^{-2}$. This corresponds to the relation of n and p in an intrinsic semiconductor, where the carrier densities are equal. A decrease or increase of both quantities at the same time is forbidden by the mass action law presented by Equation (4.9). Therefore, the intrinsic resistivity of silicon determines the theoretical limit of ρ at a given temperature. Additional contributions to the resistivity, which are observed in this study at $T = -20\,^{\circ}\text{C}$ as well as in the study of silicon resistors at $T = +20\,^{\circ}\text{C}$, are assumed to be related to a decrease of the carrier mobility due to defect clustering [Dez+99] or trapping.

The carrier mobility determines the temperature dependence of the resistivity before irra-

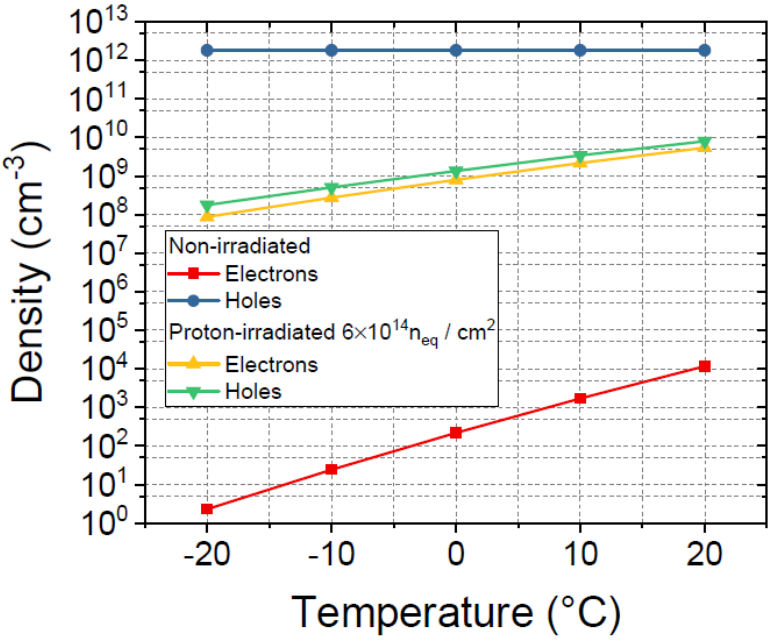

Figure 10.7.: Simulation of the electron and hole density of the edge region for a temperature range of $-20\,°\mathrm{C} \leq T \leq 20\,°\mathrm{C}$ [Bas+18].

diation. The dominant mechanism after irradiation, however, is the temperature dependency of the hole density, which is shown in Figure 10.7. As stated by Equation (4.10), the intrinsic carrier density has a temperature dependence of $\mathrm{T}^{\frac{3}{2}}$. Since $n_\mathrm{i} \sim \rho^{-1}$, one can conclude a proportionality between ρ and $\mathrm{T}^{-\frac{3}{2}}$. The curves presented in Figure 10.8 seem to follow that characteristic, even though the measurements were carried out with extrinsic sensor material.

10.5. Additional Power Consumption of Frontside-Biased Sensors

The voltage drop at the edge, which emerges after irradiation, ultimately demands for higher operation voltages, since the ΔV reduces the effective bias voltage of the sensor. The additional power consumption of a frontside-biased sensor increases the required cooling capacity of the detector and is, therefore, an undesired feature. From Equation (10.4) one can deduce:

$$P = I_{tot} \cdot (\Delta V + V_\mathrm{eff}\ . \tag{10.6}$$

The additional power consumption ΔP can be calculated by multiplying the leakage current of the sensor by ΔV. By merging Equation (10.1) and Equation (10.5) one can directly calculate ΔV and ΔP from the resistivity and the leakage current at certain fluence:

$$\Delta P = \Delta V \cdot I_\mathrm{tot} = \rho \frac{L}{A_\mathrm{edge}} \cdot I_\mathrm{tot}^2\ . \tag{10.7}$$

The additional power consumption is strongly dependent on temperature. An increase in operation temperature leads to an decrease of the resistivity (see Figure 10.8). At a fluence of $\Phi_{\mathrm{eq,\ low}} = 1 \cdot 10^{13}\,\mathrm{n_{eq}cm^{-2}}$ the resistivity decreases by about 43% for a temperature increase from $-20\,°\mathrm{C}$ to $-10\,°\mathrm{C}$. For a fluence of $\Phi_{\mathrm{eq,\ high}} = 6 \cdot 10^{14}\,\mathrm{n_{eq}cm^{-2}}$ the resistivity decreases

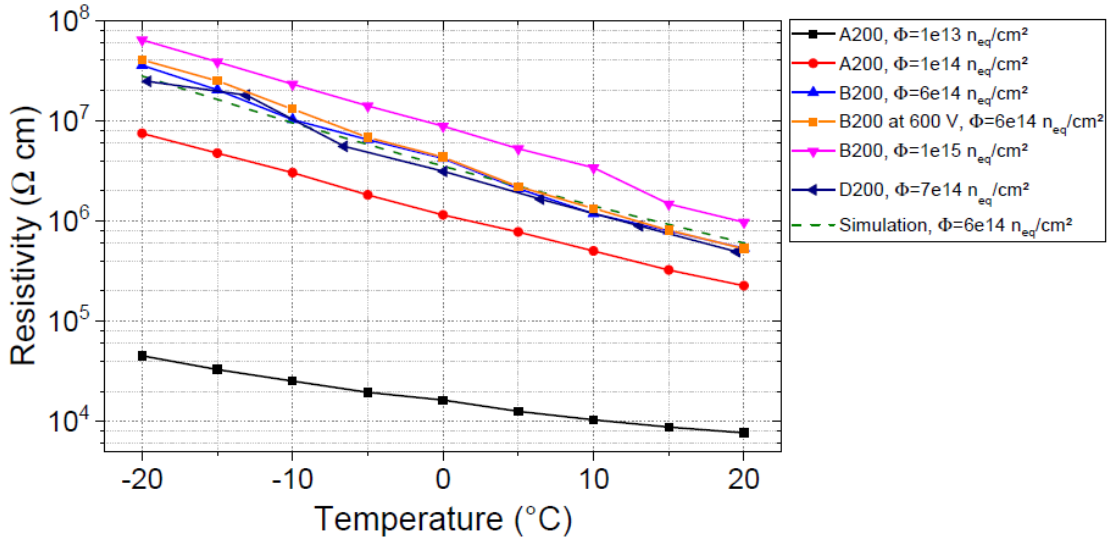

Figure 10.8.: Resistivity over temperature characteristic of irradiated sensors [Bas+18].

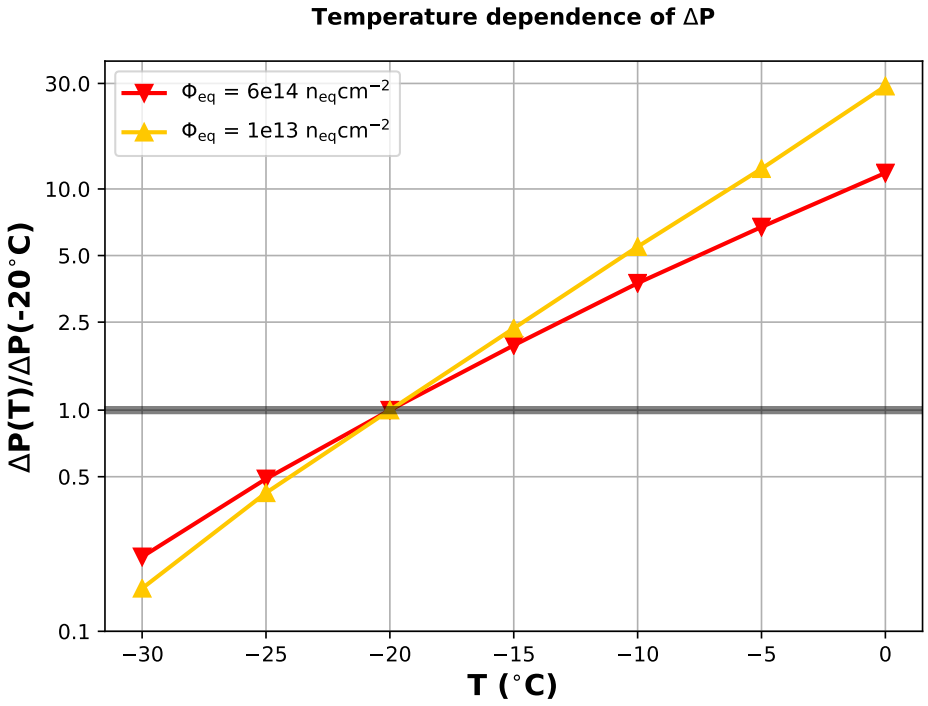

Figure 10.9.: Temperature dependence of additional power consumption of an irradiated 2S sensor for a temperature range of $-30\,°\mathrm{C} \leq T \leq 0\,°\mathrm{C}$. The relative change of ΔP is normalized by the additional power consumption at $T = -20\,°\mathrm{C}$.

by about 61% for the same temperature increase. According to Equation (4.23), the leakage current simultaneously increases by about 210%. Eventually, the temperature dependence of the additional power consumption is determined by the change of leakage current because of its quadratic dependency on temperature. Inserting the respective factors into Equation (10.7) yields an increase of ΔP by 448% for $\Phi_{\text{eq, low}}$ and 275% for $\Phi_{\text{eq, high}}$. The factors are presented in Table A.8 for a temperature range of $-30\,°\text{C} \leq T \leq 0\,°\text{C}$. The temperature dependence of $\Delta P(T)$ normalized to ΔP at $T = -20\,°\text{C}$ is depicted in Figure 10.9.

10.6. Extrapolations for the CMS Phase-2 Upgrade

The results presented in the former sections can be used to extrapolate the performance of a frontside biased 2S sensor during the extended HL-LHC run-time. The sensor material used for all sensors of the CMS Phase-2 Outer Tracker will be FZ290. The expected generated leakage currents of 2S sensors at $T = -20\,°\text{C}$ and the required minimum operation voltage per yearly accumulated fluence can be found in Table 9.3. The 2S region was sectioned into three sectors for these approximations, accounting for the different levels of radiation in the detector. The low, medium and nominal sectors correspond to a yearly fluence accumulation of $1 \cdot 10^{13}\,\text{n}_{\text{eq}}\text{cm}^{-2}$, $2 \cdot 10^{13}\,\text{n}_{\text{eq}}\text{cm}^{-2}$ and $3 \cdot 10^{13}\,\text{n}_{\text{eq}}\text{cm}^{-2}$, respectively. This is described in more detail in Section 9.3. The resistivity after irradiation was interpolated from the results for ddFZ240 and ddFZ200 sensors shown in Figure 10.6. The resistivity of the active region of HPK sensors should be comparable since the base material of the deep-diffused sensors and FZ290 is identical. The resistivity over fluence characteristic is sufficiently described by a fourth degree polynomial as depicted in Figure A.7. The coefficients of the polynomial are listed in Table A.7. Annealing effects of the resistivity were not taken into account.

Figure 10.10 shows the approximated voltage drop and additional power consumption of a frontside-biased 2S sensor over ten years for the nominal performance scenario of the HL-LHC of $3000\,\text{fb}^{-1}$. The low 2S sector represents the accumulated fluences of about 24% of all 2S modules in the CMS Phase-2 Outer Tracker. The additional power consumption for these modules is negligible for the majority of the HL-LHC run-time. However, the FSB approach is more problematic for higher fluences. The voltage drop of the most severely exposed 2S sensors after ten years of operation is 91.3 V which corresponds to an additional power consumption of 42 mW per sensor. This corresponds to an increase in power consumption by 18% per sensor. The medium 2S sector represents fluences which are accumulated by the majority of 2S modules (70%). The voltage drop after ten years for a 2S sensor of this sector is expected to be 57 V, which corresponds to an additional power consumption of 24.4 mW or an increase by 18%. With two sensors per module and the currently envisaged number of modules per sector which are shown in Table 9.1, one can calculate the total additional power consumption for the 2S region of the CMS Phase-2 Outer Tracker per year. The results are shown in Figure 10.11. After ten years of operation the total additional power consumption amounts to 153 W. The tracker should be able to cope with such a number.

The approximations shown in the last paragraph are very dependent on temperature, operation voltage and leakage current. Generally, the average 2S sensor temperature is assumed to vary between $-30\,°\text{C}$ and $-20\,°\text{C}$. The cooling mechanisms of the CMS Phase-2 Outer Tracker modules was already described in Section 9.1. Two of the four 2S sensor edges are in contact with Al-CF bridges, which represent the main cooling path in the module. The majority of the sensor surface is not directly cooled. Hence, the temperature at the edges should be lower than temperature at the center of the sensor. According to Equation (10.5), a low edge temperature,

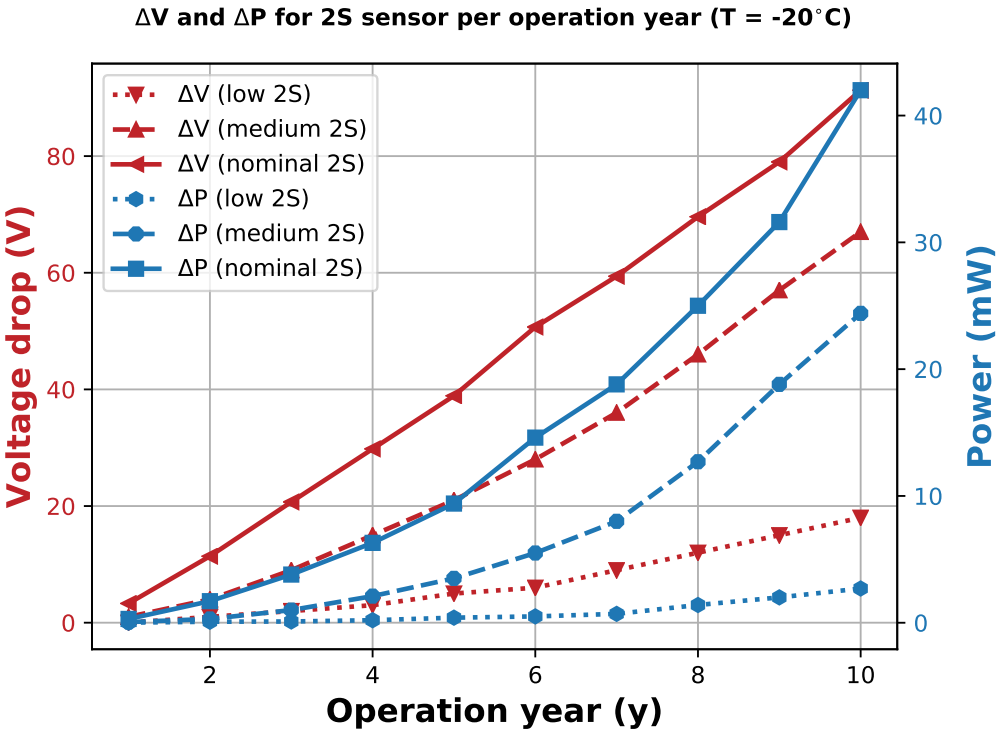

Figure 10.10.: Approximated voltage drop and additional power consumption of frontside-biased 2S sensors over ten years for the nominal performance scenario of the HL-LHC at $T = -20\,°\mathrm{C}$. The low, medium and nominal sector correspond to a yearly fluence accumulation of $1 \cdot 10^{13}\,\mathrm{n_{eq}cm^{-2}}$, $2 \cdot 10^{13}\,\mathrm{n_{eq}cm^{-2}}$ and $3 \cdot 10^{13}\,\mathrm{n_{eq}cm^{-2}}$, respectively.

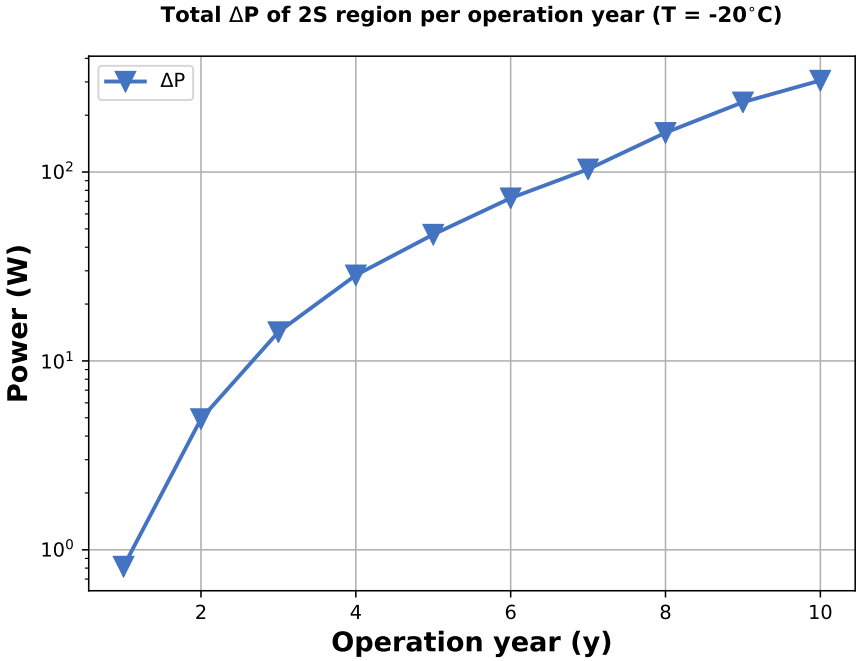

Figure 10.11.: Approximated additional power consumption of 2S region during the extended run-time of the HL-LHC with frontside biased sensors.

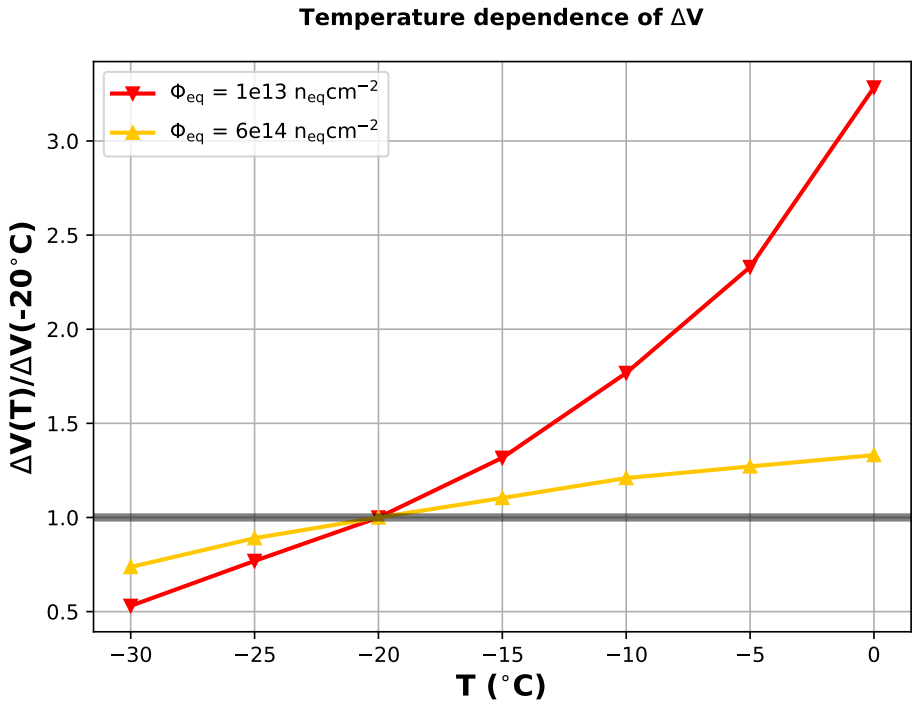

Figure 10.12.: temperature dependence of the voltage drop of an irradiated 2S sensor for a temperature range of $-30\,°\mathrm{C} \leq T \leq 0\,°\mathrm{C}$. The relative change of ΔV is normalized by the expected voltage drop at $T = -20\,°\mathrm{C}$.

which increases the edge resistance, in combination with a high temperature in the center of the sensor, where most of the leakage current is generated, can be considered the worst case scenario for FSB. The estimated operation voltages and leakage currents increase for a more conservatively estimated fluence accumulation or in case of a $4000\,\mathrm{fb}^{-1}$ extension of the HL-LHC, which further increases the expected voltage drop and additional power consumption per sensor.

The high voltage robustness of CMS Phase-2 Outer Tracker modules is restricted to 800 V [CMS18]. Therefore, a high voltage drop is a showstopper for FSB since it increases the required operation voltage in order to increase the effective bias voltage of a sensor. This becomes especially problematic with respect to a potential $4000\,\mathrm{fb}^{-1}$ extension of the HL-LHC. The voltage drop of the most severely exposed 2S modules increases to about 120 V after ten years ($\Phi_{\mathrm{eq}} = 4 \cdot 10^{14}\,\mathrm{n_{eq}cm}^{-2}$). According to Table 9.3 this increases the optimal operation voltage to 670 V. This is still acceptable. The expected voltage drops for the most severely exposed PS modules can amount to over 200 V. Hence, the optimal operation voltage would exceed the high voltage robustness of the modules at the end of the HL-LHC operation. This conclusion is of course dependent on sensor temperature. The temperature dependence of $\Delta V(T)$ normalized to ΔV at $T = -20\,°\mathrm{C}$ is depicted in Figure 10.12. The voltage drop increases with T. The increase at high fluences is rather slow, because the decreasing resistivity almost matches the increase of leakage current.

10.7. Conclusion

Measurements with miniature versions of the 2S sensor were conducted in order to study the characteristics of FSB before and after irradiation. The results lead to a better understanding of the properties of the sensor edge. The edge region can be characterized by utilizing edge resistivity measurements. There is no observable difference of the sensor performance between a frontside biased and a backside biased sensor before irradiation. However, the voltage drop at the edge increases after irradiation as a consequence of an increasing resistivity. The increase in resistivity saturates above fluences of $6 \cdot 10^{14}\,\mathrm{n_{eq}cm^{-2}}$. The limit is determined by the intrinsic resisitivity of silicon. At $T = -20\,^{\circ}\mathrm{C}$ the resistivity saturates about four orders of magnitude above the initial bulk resistivity, which coincides with the decrease of the hole density by the same order of magnitude. The phenomenon is, therefore, related the change of carrier density. This voltage drop requires higher operation voltages in order to increase the effective bias voltage and sufficiently deplete the sensor. Moreover, the study revealed an inverted temperature dependency of the resistivity before and after irradiation. The edge resistivity is proportional to temperature before irradiation, which is driven by an impairment of the carrier mobility due to phonon scattering. After irradiation the temperature dependency of the resistivity is driven by the temperature dependency of the carrier density.

The measured characteristics of the resistivity over fluence and temperature, in combination with the approximated leakage current generation per 2S sensor over the course of the nominal HL-LHC run-time, were used to estimate the voltage drop and the additional power consumption. The result is an estimated total power consumption of 153 W for the 2S region of the CMS Phase-2 Outer Tracker for an operation temperature of $-20\,^{\circ}\mathrm{C}$. The extimated maximum voltage drop for 2S sensors is 91.3 V, which would result in an optimal operation voltage below the voltage restriction of 800 V. The estimation given by Ref. [Bas+18] include the expected leakage current at a fluence of $6 \cdot 10^{14}\,\mathrm{n_{eq}cm^{-2}}$ and 600 V. For these parameters the reference states $\Delta V = 158\,\mathrm{V}$ and $\Delta P = 0.15\,\mathrm{W}$ per sensor. The total additional power consumption for the whole tracker was estimated by using these values. In hindsight, this approximation is way too conservative. However, the estimations strongly depend on the sensor temperature. One can expect lower edge temperatures in combination with higher temperatures at the sensor center, which increase the leakage current generation as well as the edge resistivity and, hence, the voltage drop and power consumption. These uncertainties make it hard to justify the usage of FSB as a baseline for 2S modules. The usage for the PS region is even more critical, because of the high fluence accumulation. The required operation voltages and the additional power consumption per sensor would be become unacceptably high. In conclusion, FSB is a viable biasing scheme for low-temperature, low-fluence HEP experiments where the voltage drop at the sensor edge can be considered negligible.

Part III.

Summary and Outlook

11
Summary and Outlook

The CMS Phase-2 Upgrade comprises a full replacement of the current CMS tracker in order to cope with the more challenging experimental environment of the HL-LHC. One of the key parameters is the radiation tolerance of the sensor material. The expected fluences for silicon sensors in the CMS Phase-2 Outer Tracker range between $1 \cdot 10^{14}\,\mathrm{n_{eq}cm^{-2}}$ and $1 \cdot 10^{15}\,\mathrm{n_{eq}cm^{-2}}$ after the nominal HL-LHC run-time of ten years ($3000\,\mathrm{fb^{-1}}$). Based on the results of a long R&D period, which basically started in 2002 with the foundation of the RD50 Collaboration at CERN, the CMS Outer Tracker Sensor Working Group eventually focused on n-in-p float zone silicon sensors with active thicknesses between 200 µm and 300 µm processed by HPK as a base material for sensors of the new Outer Tracker by 2015.

In order to finalize the material choice, the CMS Outer Tracker Sensor Working Group conducted four qualification campaigns within the last five years. The first two campaigns were carried out with deep diffused float zone material with active thicknesses of 240 µm (ddFZ240) and 200 µm (ddFZ200). The wafers contained the final design of the 2S sensor next to several miniature versions of the 2S sensor, which were used for irradiation studies. Characteristic measurements performed on these sensors validated the 2S design. The p-stop interstrip isolation technology was found to be the more reliable approach and became the baseline for the following wafer productions. Irradiation studies were mostly performed at ETP, where an emphasis was put on the evolution of the signal annealing. The targeted minimum efficiency of Outer Tracker sensors is 99.5% throughout the HL-LHC operation. The efficiency can be approximated by comparing the MPV of the seed signal generated by traversing particles with the readout threshold, which is determined by the noise of the readout electronics. The lower limit of the 2S and PS-s seed signal specification is $12000\,\mathrm{e^-}$ and $9600\,\mathrm{e^-}$, respectively. The desired maximum operation voltage of the CMS Phase-2 Outer Tracker is 600 V with an additional margin of up to +200 V in case of a potential $4000\,\mathrm{fb^{-1}}$ extension of the HL-LHC. The envisaged room temperature annealing per year is two weeks in order to reduce the leakage current generation of the sensors.

The studies revealed that the performance of ddFZ240 sensors is sufficient. The sensors provide a signal that is well-above the lower limits of the 2S and PS-s signal specification. However, these sensors were mostly irradiated with 23 MeV protons. The high oxygen concentration of the material significantly increases the radiation tolerance towards proton generated radiation damage. Even though this feature is considered well-understood, the extent of the additional radiation hardness was not expected. Since neutron radiation dominates in the 2S region during the HL-LHC operation, it was concluded that neutron and mixed irradiations are mandatory for the following irradiation studies. The performance of ddFZ200 sensors, which already included neutron irradiated samples, was not convincing. The charge collection did not meet the requirements. Moreover, the thickness reduction did not result in a significant reduction of the generated leakage current after irradiation compared to ddFZ240 sensors.

After HPK decided not to offer the deep diffused sensor material anymore, the final ma-

terial decision had to be made between the HPK standard material with an active thickness of 290 µm (FZ290) and physically thinned wafers with a thickness of 240 µm (thFZ240). Sensor were irradiated according to the expected composition of neutral and charged hadrons in the 2S and PS region. The annealing studies revealed that FZ290 sensors are efficiently operable at $V_{\text{bias}} \leq 600\,\text{V}$ for the nominal run-time of the HL-LHC. A potential bias voltage boost might be necessary during the $4000\,\text{fb}^{-1}$ extension. The relatively large active thickness of these sensors make them very responsive towards bias voltage boosting. The thFZ240 sensors, on the other hand, lack the required signal for the 2S region. The bulk is sufficiently depleted at around 600 V even at the highest available fluence, which mitigates the impact of bias voltage boosting. The sensors could potentially be used for the PS region in terms of signal. However, the benefit in terms of leakage current was not significant. Moreover, the thFZ240 turned out to be very sensitive towards mechanical stress and scratches at the backside, both of which are unavoidable during the characterization process and the module assembly. This resulted in breakdowns and increased leakage currents.

The collected data from the FZ290 irradiation campaign was used to approximate the sensor performance for the 2S and PS region over the course of the nominal HL-LHC run-time of ten years. The performance was evaluated with respect to the minimum operation voltage that is required to operate the sensors efficiently and the resulting signal, leakage current and power consumption. In order to simplify the problem the regions were separated into three fluence sectors. A HL-LHC run-time of ten years was estimated for this study. With a yearly fluence accumulation of one tenth of the expected fluence at $3000\,\text{fb}^{-1}$ and two weeks of room temperature annealing one has to determine the performance parameters for 78 fluence-annealing states. This was realized by parameterizing the surface spanned by the measured signal values for different fluence and annealing times for every available bias voltage. The results indicate that the majority of CMS Phase-2 Outer Tracker modules can be operated at low bias voltages for the largest part of the operation time. In order to improve the validity of the predictions, future irradiation studies with FZ290 sensors should target the as yet uncovered fluence range of $\Phi_{\text{eq}} < 1 \cdot 10^{14}\,\text{n}_{\text{eq}}\text{cm}^{-2}$ for the 2S and $3 \cdot 10^{14}\,\text{n}_{\text{eq}}\text{cm}^{-2} < \Phi_{\text{eq}} < 1 \cdot 10^{15}\,\text{n}_{\text{eq}}\text{cm}^{-2}$ for the PS region.

Lastly, the sensors of the ddFZ240 and ddFZ200 batches were used to improve the understanding of the sensor edge before and after irradiation. Irradiation studies usually investigate the properties of the sensor bulk. Next to the academic motivation, understanding the properties of the sensor edge is necessary for the evaluation of frontside biasing (FSB). The conductive characteristic of the non-depleted sensor bulk in the edge region interconnects the backside and the frontside of the sensor periphery (edge ring). One can utilize this feature to deplete a silicon sensor by applying solely frontside connections in contrast to backside biasing (BSB), where the sensor backside is connected to the high voltage output of a power supply. The FSB approach would facilitate the module assembly for the CMS Phase-2 Outer Tracker, because risky and time-consuming assembly steps would be avoided. Measurements have shown that the sensor performance of a frontside biased and a backside biased sensor is identical. However, the edge resistivty increases significantly after irradiation, which results in a non-negligible voltage drop at the edge. At $\Phi_{\text{eq}} \leq 1 \cdot 10^{14}\,\text{n}_{\text{eq}}\text{cm}^{-2}$ the voltage drop is negligible. For high fluences the approximated voltage drop at the edge of a 2S sensor amounts to over 100 V. This significantly increases the power consumption per sensor. The impact on temperature, bias voltage and annealing on the edge resistivity was investigated as well and initially published in Ref. [Bas+18]. In conclusion, the FSB approach is a viable only for low-fluence, low-temperature HEP experiments. The usage for the PS modules can be ruled out because of the high fluence accumulation. The usage for the 2S region is also not recommended because of a noticeable

voltage drop and the end of the HL-LHC run-time for the most severely exposed modules.

The studies performed on irradiated silicon sensors presented this thesis have made an important contribution to the choice of the silicon sensor material for the future Outer Tracker of the CMS experiement. The results of the various qualification and irradiation campaigns demonstrated that the sensors fabricated on FZ290 base material are ideal for the CMS Phase-2 Outer Tracker, even for a potential extension of the HL-LHC performance scenario to $4000\,\mathrm{fb}^{-1}$. Based on these results, which were presented to the CMS Collaboration in September 2019, it was concluded to choose FZ290 as the sensor material for the whole Outer Tracker. Now that the final material decision was made, the members of the CMS Outer Tracker community prepare for the upcoming (pre-)production of 2S and PS modules, which shifts the focus of the participating institutes like ETP from R&D to the preparation for module mass production. The specifications for sensor quality control (SQC) centers, process quality (PQC) control and irradiation test (IT) centers need to be finalized. The SQC center, PQC center and IT center candidates need to prepare and update their laboratories and equipment in order to cope with these specifications. ETP will play an important role in the 2S module production chain as they will act as a SQC and IT center. Moreover, ETP pledged to build over 2000 2S modules.

Part IV.

Appendix

A
Appendix

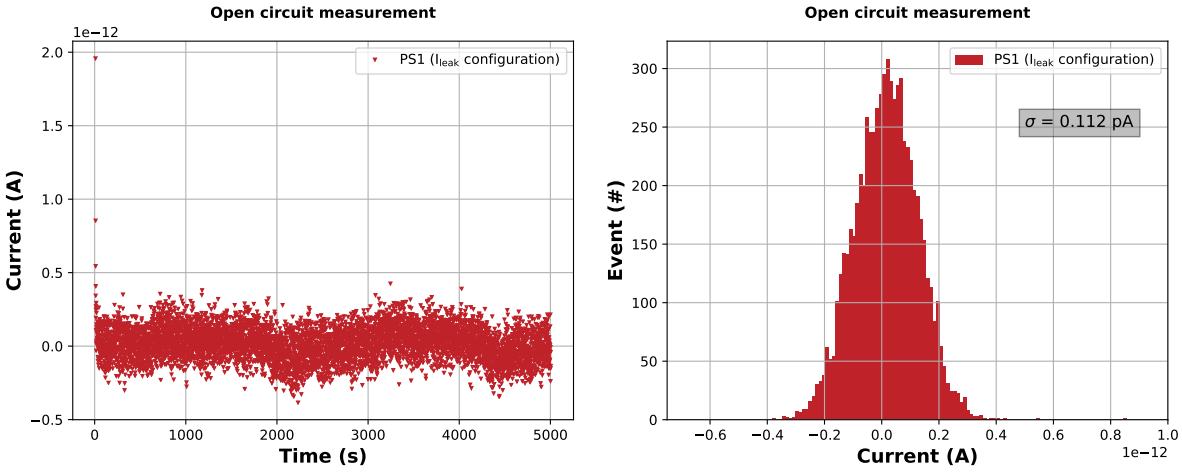

(a) (b)

Figure A.1.: Open circuit measurement with the I_{leak} relay configuration of one of the ETP probe stations. The current was measured repeatedly for about 1.4 h, which corresponds to about 6600 data points.

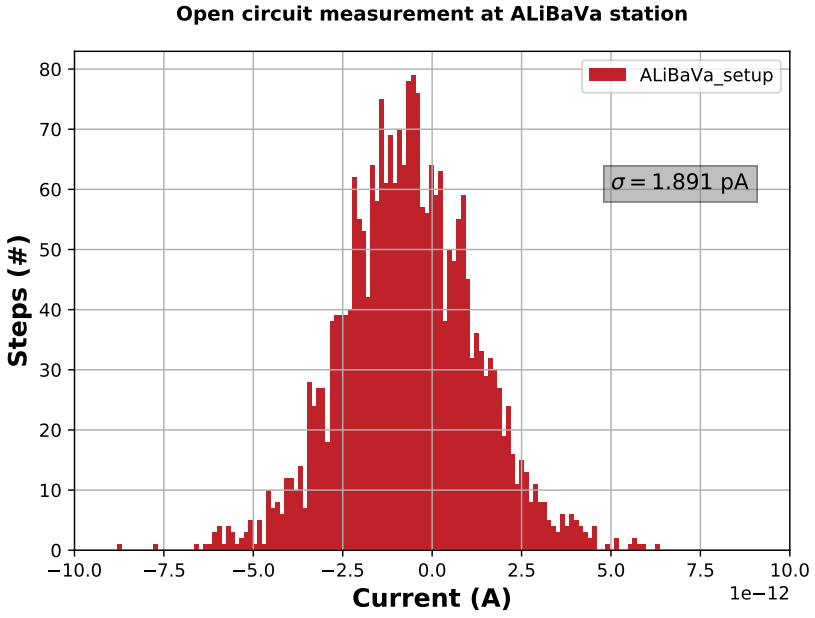

Figure A.2.: Histogram of open circuit measurement at the ETP ALiBaVa setup. The standard deviation of the distribution is $\sigma = 1.891$.

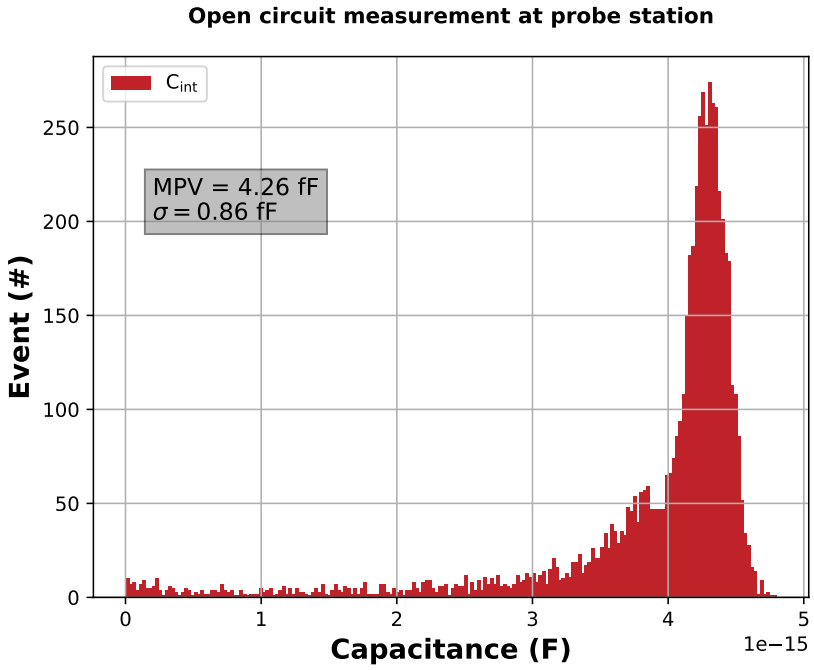

Figure A.3.: Histogram of open circuit measurement with the C_{int} relay configuration of one of the ETP probe stations. The capacitance was measured at 1 MHz repeatedly for about 1.4 h, which corresponds to about 6600 data points.

Table A.1.: List of samples that were flagged during the qualification process. Samples were excluded, if the leakage current was significantly larger than the representative value for the specific material or did not meet the specifications of $|I_{500}| \leq 2\,\text{nA/mm}^3$.

Sample	$\lvert I_{500}\rvert$ (nA/mm^3)	Misc	Flag
`ddFZ200 14 Irradiation`	-	Breakdown at 450 V	Excluded
`ddFZ200 19 Irradiation` (S54)	3.29	-	Out of specs
`ddFZ200 10 KIT Test`	2.14	-	Out of specs
`ddFZ200 15 KIT Test`	2.21	-	Out of specs
`ddFZ200 16 KIT Test`	2.84	-	Out of specs
`ddFZ200 19 Baby`	2.61	-	Out of specs
`FZ290 19 Baby`	1363	Hard breakdown	Excluded
`FZ290 14 TS12 DiodeL`	88.95	Soft breakdown	Excluded
`thFZ240 32 TS12 DiodeL`	3.10	Soft breakdown	Excluded
`thFZ240 41 2S` (S86)	26.70	thFZ240 issue	Excluded
`thFZ240 40 2S` (S85)	11.71	thFZ240 issue	Excluded

Table A.2.: List of samples for which high strip leakage currents were measured. The TDR specifications state an allowed maximum strip leakage current of $I_{\text{leak}} \leq 2\,\text{nA/cm}$. These strips were excluded from mean value calculation.

Sample	No. of strips	$\lvert I_{\text{leak}} \rvert$ (nA/cm)
ddFZ240 03 PCommon	1	~ 6
ddFZ240 03 Baby	1	~ 9
ddFZ240 18 Irradiation	1	> 1000
ddFZ240 15 KIT Test	1	~ 5
ddFZ240 12 KIT Test	29	~ 10
ddFZ240 18 KIT Test	23	~ 10
ddFZ200 14 Irradiation	2	~ 4
ddFZ200 11 KIT Test	1	~ 40
ddFZ200 25 KIT Test	1	~ 6
FZ290 19 KIT Test	1	> 1000
FZ290 37 PCommon	2	> 1000
thFZ240 21 Baby	1	~ 8
thFZ240 15 KIT Test	1	> 1000

Table A.3.: List of samples for which pinholes were detected. The pinhole definition of the TDR demands to flag a strip if $I_{\text{diel}} < 2\,\text{nA}$ at 10 V. The check was carried out before and after irradiation.

Sample	No. of strips	$\lvert I_{\text{leak}} \rvert$ (nA)	Irrad. ?
ddFZ240 22 Irradiation	1	~ 6318	Yes
ddFZ240 07 KIT Test	1	~ 812	Yes
ddFZ200 22 KIT Test	1	~ 2	No
ddFZ200 22 Irradiation	1	~ 6250	Yes
ddFZ200 07 KIT Test	1	~ 18835	Yes
ddFZ200 15 KIT Test	1	~ 473	Yes
FZ290 04 Baby	3	~ 92100	Yes
FZ290 11 Baby	2	~ 98000	Yes
FZ290 33 Irradiation	3	~ 92157	Yes
thFZ240 21 Baby	27	~ 6	No
thFZ240 22 Baby	2	~ 99000	Yes

Table A.4.: Overview of the annealing program for the ddFZ240 and ddFZ200 irradiation campaign. The parameters are annealing time t_a, annealing temperature T_a and the collected equivalent annealing time at room temperature $\sum t_{eq}$ in hours and weeks. The anticipated annealing time of the CMS Phase-2 Tracker after 10 years is 20 weeks at room temperature.

Step	t_a (min)	T_a (°C)	$\sum t_{eq}$ (h)	$\approx \sum t_{eq}$ (w)
1	20	60	90	0.5
2	20	60	165	1
3	40	60	318	2
4	76	60	650	4
5	15	80	1871	11
6	30	80	4894	29
7	60	80	10007	60

Table A.5.: Overview of the annealing program of the FZ290 and thFZ240 irradiation campaign for sensors. The parameters are annealing time t_a, annealing temperature T_a and the equivalent annealing time at room temperature t_{eq} in hours and weeks.

Step	t_a (min)	T_a (°C)	$\sum t_{eq}$ (h)	$\approx \sum t_{eq}$ (w)
1	10	60	51	0.3
2	20	60	130	1
3	40	60	280	2
4	80	60	620	4
5	100	60	1217	7
6	140	60	2321	14
7	25	80	4838	29
8	57	80	9705	58
9	120	80	19717	117

Table A.6.: Overview of the reduced annealing program of the FZ290 and thFZ240 irradiation campaign for diodes. The parameters are annealing time t_a, annealing temperature T_a and the equivalent annealing time at room temperature t_{eq} in hours and weeks.

Step	t_a (min)	T_a (°C)	$\sum t_{eq}$ (h)	$\approx \sum t_{eq}$ (w)
1	20	60	90	0.5
1	20	60	165	1
1	40	60	318	2
1	80	60	668	4
1	100	60	1287	7
1	25	80	3870	23

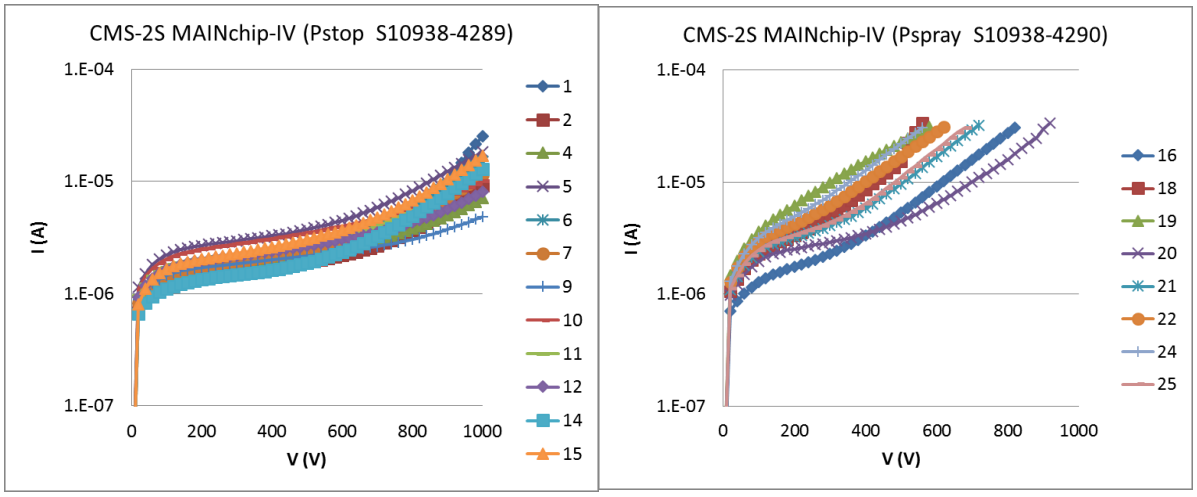

(a) (b)

Figure A.4.: IV characteristics of ddFZ200 2S sensors with (a) p-stop and (b) p-spray technology [CMS17c].

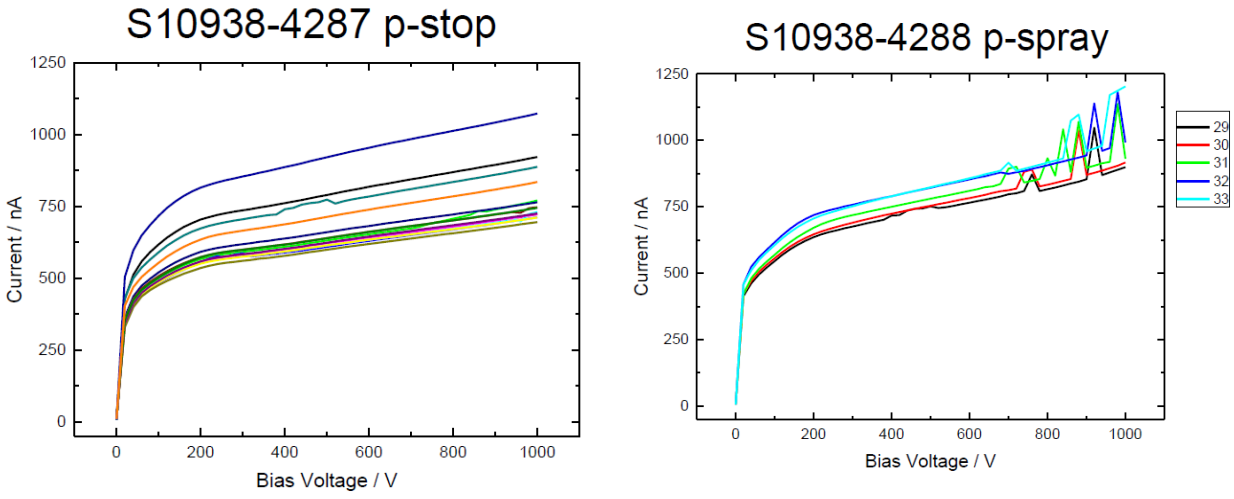

(a) (b)

Figure A.5.: IV characteristics of ddFZ240 2S sensors with (a) p-stop and (b) p-spray technology [CMS17c].

Table A.7.: Coefficients of the forth degree polynomial which was used to fit the data presented in Figure A.7. The index i of the coefficient a_i indicates the degree of the term.

Coefficient	Value
a_0	$-2.17939622 \cdot 10^{-52}$
a_1	$6.20692504 \cdot 10^{-37}$
a_2	$-5.23065862 \cdot 10^{-22}$
a_3	$1.70334689 \cdot 10^{-7}$
a_4	$-1.62170882 \cdot 10^{6}$

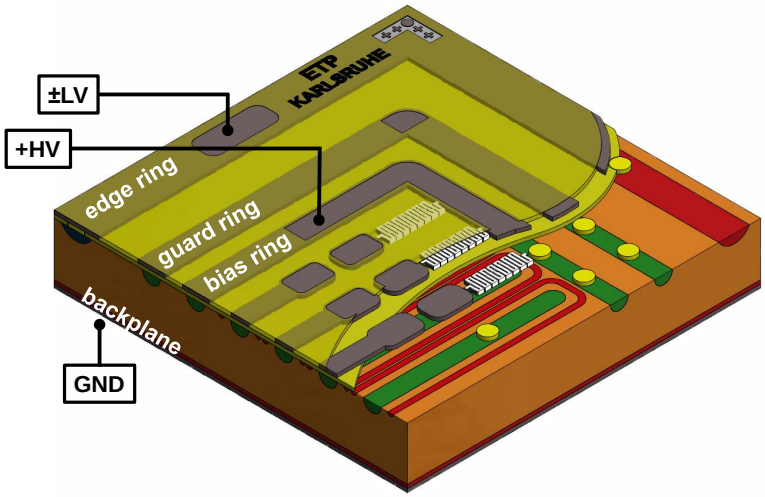

Figure A.6.: Illustration of the circuitry of ER measurements.

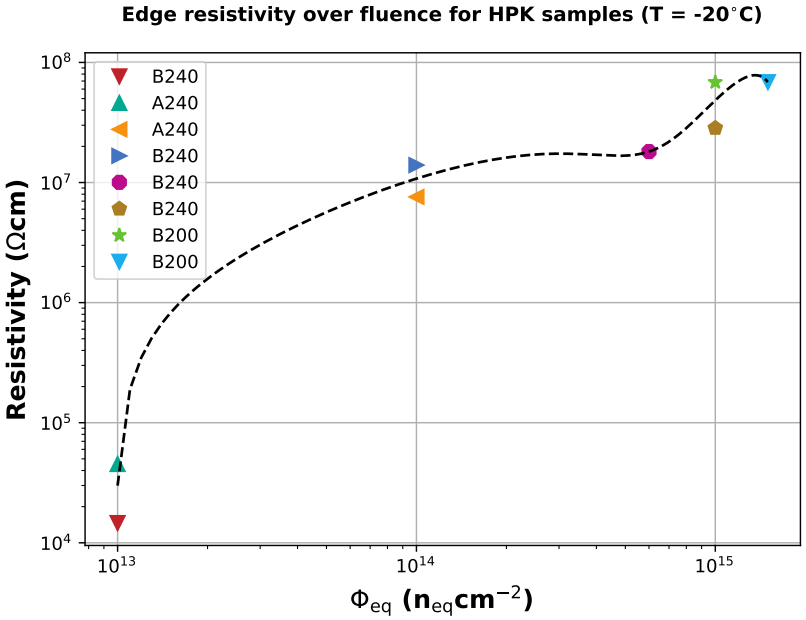

Figure A.7.: Illustration of the resisitvity versus fluence fit of the data of HPK sensors presented in Figure 10.6.

Table A.8.: Relative change of leakage current and resistivity with respect to the reference values at $T = -20\,°\mathrm{C}$.

Temperature T (°C)	-30	-24	-20	-15	-10	-5	0
$I_{\mathrm{tot}}(T)/I_{\mathrm{tot}}(-20\,°\mathrm{C})$	0.30	0.55	1	1.78	3.10	5.30	8.88
$\rho(T)/\rho(-20\,°\mathrm{C})$ (low fluence)	1.8	1.4	1	0.74	0.57	0.44	0.37
$\rho(T)/\rho(-20\,°\mathrm{C})$ (high fluence)	2.5	1.62	1	0.62	0.39	0.24	0.15

List of Figures

List of Tables

Bibliography

[Aad+12] G. Aad et al. *Observation of a new particle in the search for the Standard Model Higgs boson with the ATLAS detector at the LHC*. In: Physics Letters B 716.1 (2012), pp. 1–29. ISSN: 0370-2693. DOI: https://doi.org/10.1016/j.physletb.2012.08.020 (cited on p. 3).

[Ada+17] W. Adam et al. *P-Type Silicon Strip Sensors for the new CMS Tracker at HL-LHC*. In: Journal of Instrumentation 12.06 (2017), P06018–P06018. DOI: 10.1088/1748-0221/12/06/p06018 (cited on pp. 43, 48, 51, 52, 64).

[Adu07] Adundovi. *A p-n junction in thermal equilibrium*. Aug. 14, 2007. URL: https://de.wikipedia.org/wiki/P-n-%C3%9Cbergang#/media/Datei:Pn-junction-equilibrium-graph.svg (cited on p. 20).

[Akh+19] A. Akhmerov et al. *Lecture notes for the TN2844 solid state physics*. Aug. 8, 2019. URL: https://solidstate.quantumtinkerer.tudelft.nl/11_nearly_free_electron_model/ (cited on p. 18).

[All+17] P. Allport et al. *Recent results and experience with the Birmingham MC40 irradiation facility*. In: Journal of Instrumentation 12.03 (Mar. 2017). DOI: 10.1088/1748-0221/12/03/c03075 (cited on p. 57).

[AM11] N. Ashcroft and N. Mermin. *Solid State Physics*. Cengage Learning, 2011. ISBN: 9788131500521 (cited on pp. 17, 18).

[Ard] Arduino. URL: https://www.arduino.cc/ (cited on p. 35).

[Bar+94] E. Barberis et al. *Capacitances in silicon microstrip detectors*. In: Nuclear Instruments and Methods in Physics Research Section A: Accelerators, Spectrometers, Detectors and Associated Equipment 342.1 (1994), pp. 90–95. ISSN: 0168-9002. DOI: https://doi.org/10.1016/0168-9002(94)91414-1 (cited on pp. 20, 30).

[Bas+18] M. Baselga et al. *Front-side biasing of n-in-p silicon strip detectors*. In: Journal of Instrumentation 13.11 (2018), P11007. DOI: 10.1088/1748-0221/13/11/p11007 (cited on pp. 21, 123–129, 131, 132, 136, 140).

[BD11] J. Baglio and A. Djouadi. *Higgs production at the lHC*. In: Journal of High Energy Physics 2011.3 (Mar. 2011). ISSN: 1029-8479. DOI: 10.1007/jhep03(2011)055 (cited on p. 5).

[Ber+16] T. Bergauer et al. *First thin AC-coupled silicon strip sensors on 8-inch wafers*. In: Nucl. Instrum. and Meth. 830 (2016), pp. 473–479 (cited on pp. 126, 127).

[BK16] H. Bichsel and S. R. Klein. *Passage of particles through matter*. In: 2016 (cited on pp. 23, 24).

[Bra17] J. Braach. *Qualification of 200m n-in-p Silicon Strip Sensors for the CMS Tracker Upgrade*. Karlsruher Institut für Technologie, Bachelorarbeit. 2017. URL: https://publish.etp.kit.edu/record/21402 (cited on pp. 41, 61).

[Car+16] A. Caratelli et al. *Readout architecture for the Pixel-Strip module of the CMS Outer Tracker Phase-2 upgrade*. In: (Nov. 2016) (cited on p. 14).

[Cer+14] D. Ceresa et al. *Macro Pixel ASIC (MPA): the readout ASIC for the pixel-strip (PS) module of the CMS outer tracker at HL-LHC*. In: Journal of Instrumentation 9.11 (Nov. 2014), pp. C11012–C11012. DOI: 10.1088/1748-0221/9/11/c11012 (cited on p. 14).

[CER18a] CERN. *Accelerator Performance and Statistics*. Oct. 1, 2018. URL: http://acc-stats.web.cern.ch/acc-stats/#lhc/ (cited on p. 6).

[CER18b] CERN. *The RD50 collaboration*. 2018. URL: https://rd50.web.cern.ch/rd50/ (visited on 08/10/2018) (cited on p. 51).

[CER19] CERN. *LHC Commissioning with beam*. Dec. 10, 2019. URL: https://lhc-commissioning.web.cern.ch/lhc-commissioning/schedule/HL-LHC-plots.htm (cited on p. 111).

[Cha+12] S. Chatrchyan et al. *Observation of a new boson at a mass of 125 GeV with the CMS experiment at the LHC*. In: Physics Letters B 716.1 (2012), pp. 30–61. ISSN: 0370-2693. DOI: https://doi.org/10.1016/j.physletb.2012.08.021 (cited on p. 3).

[Chi13] A. Chilingarov. *Temperature dependence of the current generated in Si bulk*. In: Journal of Instrumentation 8.10 (Oct. 2013), P10003–P10003. DOI: 10.1088/1748-0221/8/10/p10003 (cited on p. 30).

[Cie+17] D. Cieri et al. *An FPGA based track finder for the L1 trigger of the CMS experiment at the High Luminosity LHC*. In: Journal of Instrumentation 12.12 (Dec. 2017), P12019–P12019. DOI: 10.1088/1748-0221/12/12/P12019 (cited on p. 14).

[CMS11] CMS Collaboration. *Technical proposal for the upgrade of the CMS detector through 2020*. Tech. rep. CERN-LHCC-2011-006. LHCC-P-004. CERN, 2011. URL: https://cds.cern.ch/record/1355706 (cited on p. 6).

[CMS12] CMS Collaboration. *CMS Technical Design Report for the Pixel Detector Upgrade*. Tech. rep. CERN-LHCC-2012-016. CMS-TDR-11. CERN, 2012. URL: https://cds.cern.ch/record/1481838 (cited on p. 7).

[CMS15] CMS Collaboration. *1-D plot covering CMS tracker, showing FLUKA simulated 1 MeV neutron equivalent in Silicon including contributions from various particle types.* In: (July 2015). URL: http://cds.cern.ch/record/2039908 (cited on p. 16).

[CMS17a] CMS Collaboration. *CMS TriDAS project: Technical Design Report, Volume 1: The Trigger Systems*. Technical Design Report CMS. July 26, 2017. URL: http://cds.cern.ch/record/706847 (cited on p. 9).

[CMS17b] CMS Collaboration. *High-Luminosity Large Hadron Collider (HL-LHC) Technical Design Report V. 0.1*. CERN, 2017. ISBN: 978-92-9083-471-7. DOI: http://dx.doi.org/10.23731/CYRM-2017-004 (cited on pp. 11, 12).

[CMS17c] CMS Outer Tracker Sensor Working Group. *Measurements of 2S sensors from HPK*. Oct. 24, 2017. URL: https://indico.cern.ch/event/671608/contributions/2759733/attachments/1546002/2430753/2Smeasurements_171024.pdf (cited on pp. 63, 150).

[CMS18] CMS Collaboration. *The Phase-2 Upgrade of the CMS Tracker*. Tech. rep. CERN-LHCC-2017-009. CMS-TDR-014. CERN, Apr. 16, 2018. URL: https://cds.cern.ch/record/2272264 (cited on pp. 3, 8, 11–15, 36, 37, 44, 46, 62, 83, 85, 86, 92, 105, 112, 135).

[CMS97] CMS Collaboration. *The CMS electromagnetic calorimeter project: Technical Design Report*. Technical Design Report CMS. Geneva: CERN, 1997. URL: http://cds.cern.ch/record/349375 (cited on p. 7).

[Czo18] J. Czochralski. *Ein neues Verfahren zur Messung der Kristallisationsgeschwindigkeit der Metalle*. In: Zeitschrift für Physikalische Chemie (1918) (cited on p. 51).

[Dez+99] B. Dezillie et al. *Improved neutron radiation hardness for Si detectors: application of low resistivity starting material and/or manipulation of N/sub eff/ by selective filling of radiation-induced traps at low temperatures*. In: IEEE Transactions on Nuclear Science 46.3 (June 1999), pp. 221–227. ISSN: 1558-1578. DOI: 10.1109/23.775518 (cited on p. 130).

[EB08] L. Evans and P. Bryant. *LHC Machine*. In: Journal of Instrumentation 3.08 (Aug. 2008), S08001–S08001. DOI: 10.1088/1748-0221/3/08/s08001 (cited on p. 5).

[Ebe13] R. Eber. *Untersuchung neuartiger Sensorkonzepte und Entwicklung eines effektiven Modells der Strahlenschädigung für die Simulation hochbestrahlter Silizium-Teilchendetektoren*. PhD thesis. Karlsruher Institut für Technologie (KIT), Nov. 29, 2013. URL: https://publish.etp.kit.edu/record/21516 (cited on pp. 31, 130).

[Eli19] U. Elicabuk. *Characterization of n-in-p Strip Sensors for the Phase 2 Upgrade of CMS*. Bachelor's thesis. Karlsruher Institut für Technologie (KIT), 2019. URL: https://publish.etp.kit.edu/record/21760 (cited on p. 85).

[Fer+05] A. Ferrari et al. *FLUKA: A multi-particle transport code (Program version 2005)*. In: (2005) (cited on pp. 12, 64, 92).

[Fou+05] C. Foudas et al. *A Study for a Tracking Trigger at First Level for CMS at SLHC*. In: (Oct. 2005) (cited on p. 14).

[Gos18] J.-O. Gosewisch. *Irradiation Studies of Charge Collection and Interstrip Resistance of Silicon Strip Sensors in the Course of the CMS Phase-2 Upgrade*. Master's thesis. Karlsruher Institut für Technologie (KIT), 2018. URL: https://ekp-invenio.physik.uni-karlsruhe.de/record/49066 (cited on pp. 85, 100).

[Gru10] M. Grundmann. *The Physics of Semiconductors: An Introduction Including Nanophysics and Applications*. Springer Berlin Heidelberg, 2010. ISBN: 9783642138843 (cited on p. 22).

[Ham19] Hamamatsu Photonics K.K., Japan. 2019. URL: http://www.hamamatsu.com (cited on p. 51).

[Har+16] K. Hara et al. *Charge collection and field profile studies of heavily irradiated strip sensors for the ATLAS inner tracker upgrade*. In: Nuclear Instruments and Methods in Physics Research Section A: Accelerators, Spectrometers, Detectors and Associated Equipment 831 (2016). Proceedings of the 10th International "Hiroshima" Symposium on the Development and Application of Semiconductor Tracking Detectors, pp. 181–188. ISSN: 0168-9002. DOI: https://doi.org/10.1016/j.nima.2016.04.035 (cited on p. 49).

[Har17] F. Hartmann. *Evolution of Silicon Sensor Technology in Particle Physics*. Springer Tracts in Modern Physics. Springer International Publishing, 2017. ISBN: 9783319644363. URL: https://books.google.de/books?id=7WY9DwAAQBAJ (cited on pp. 19, 21, 25, 27–31).

[Hen15a] M. A. Henning. *n-Dotierung im Siliziumkristallgitter mit Phosphor*. Apr. 2, 2015. URL: https://de.wikipedia.org/wiki/Dotierung#/media/Datei:Schema_-_n-dotiertes_Silicium.svg (cited on p. 19).

[Hen15b] M. A. Henning. *p-Dotierung im Siliziumkristallgitter mit Aluminium*. Apr. 2, 2015. URL: https://de.wikipedia.org/wiki/Dotierung#/media/Datei:Schema_-_p-dotiertes_Silicium.svg (cited on p. 19).

[HM03] W. Herr and B. Muratori. *Concept of luminosity*. In: *Intermediate accelerator physics. Proceedings, CERN Accelerator School, Zeuthen, Germany, September 15-26, 2003*. 2003, pp. 361–377. URL: http://doc.cern.ch/yellowrep/2006/2006-002/p361.pdf (cited on pp. 5, 6).

[Huh02] M. Huhtinen. *Simulation of non-ionising energy loss and defect formation in silicon*. In: Nucl. Instrum. Meth. A491 (2002), pp. 194–215. DOI: 10.1016/S0168-9002(02)01227-5 (cited on p. 80).

[Inf] Infineon Technologies Austria AG. URL: https://www.infineon.com (cited on p. 125).

[Insa] Institut für Hochenergiephysik, Austria. http://www.hephy.at/ (cited on p. 89).

[Insb] Institut Jozef Stefan, Slovenia. URL: https://www.ijs.si (cited on p. 54).

[Jac+77] C. Jacoboni et al. *A review of some charge transport properties of silicon*. In: Solid-State Electronics 20.2 (1977), pp. 77–89. ISSN: 0038-1101 (cited on p. 22).

[Jun11] A. Junkes. *Influence of radiation induced defect clusters on silicon particle detectors*. PhD thesis. Universität Hamburg, 2011 (cited on p. 63).

[Kei10] Keithley - A Tectronix Company. 2010. URL: https://www.tek.com (cited on p. 45).

[Lin+01] G. Lindström et al. *Radiation hard silicon detectors—developments by the RD48 (ROSE) collaboration*. In: Nuclear Instruments and Methods in Physics Research 466.2 (2001). 4th Int. Symp. on Development and Application of Semiconductor Tracking Detectors, pp. 308–326. ISSN: 0168-9002. DOI: https://doi.org/10.1016/S0168-9002(01)00560-5 (cited on pp. 79, 80, 100, 112).

[Lin+80] V. A. J. V. Lint et al. *Mechanisms of radiation effects in electronic materials*. 1st ed. Vol. 1. Wiley, 1980. ISBN: 978-0471041061 (cited on p. 24).

[Löc02] S. Löchner. *Performance of the Beetle Readout Chip for LHCb*. LHCb-TALK-2002-038 LHCb-TALK-2002-038. CERN, Sept. 9, 2002. URL: https://cds.cern.ch/record/1744659 (cited on p. 40).

[Löc06] S. Löchner. *Development, Optimisation and Characterisation of a Radiation Hard Mixed-Signal Readout Chip for LHCb*. PhD thesis. Ruperto-Carola University of Heidelberg, 2006. DOI: http://doi.org/10.11588/heidok.00006708 (cited on p. 49).

[Lut07] G. Lutz. *Semiconductor Radiation Detectors*. ISBN: 978-3-540-71678-5 (Print) 978-3-540-71679-2 (Online). Springer, 2007. DOI: 10.1007/978-3-540-71679-2 (cited on pp. 22, 24).

[Man+12] J. Mans et al. *CMS Technical Design Report for the Phase 1 Upgrade of the Hadron Calorimeter*. Tech. rep. CERN-LHCC-2012-015. CMS-TDR-10. CERN, 2012. URL: https://cds.cern.ch/record/1481837 (cited on p. 6).

[Mar+07] R. Marco-Hernández et al. *ALIBAVA: A portable readout system for silicon microstrip sensors*. In: IEEE Trans. Nuc. Sci. (Jan. 2007). DOI: 10.5170/CERN-2007-001.412 (cited on p. 40).

[Mes05] D. Meschede. *Gerthsen Physik*. 23rd ed. Berlin: Springer, 2005 (cited on p. 5).

[Met16] M. Metzler. *Radiation Hardness of n-in-p Strip Sensors for the Phase II Upgrade of CMS*. Master's thesis. Karlsruher Institut für Technologie (KIT), 2016. URL: https://publish.etp.kit.edu/record/21322 (cited on p. 61).

[Mob16] E. Mobs. *The CERN accelerator complex. Complexe des accélérateurs du CERN*. General Photo. July 2016. URL: https://cds.cern.ch/record/2197559 (cited on p. 6).

[Mol99] M. Moll. *Radiation Damage in Silicon Particle Detectors*. PhD thesis. University of Hamburg, 1999. URL: https://mmoll.web.cern.ch/mmoll/thesis/ (cited on pp. 25, 29–33, 66, 71, 77, 94, 95, 98, 101, 103, 111, 115).

[Nak+00] T. Nakayama et al. *Radiation Damage Studies of Silicon Microstrip Sensors*. In: IEEE Trans. Nuc. Sci. 47 (2000) (cited on p. 123).

[Nat17] National Instruments Corp. *LabWindows/CVI (C for Virtual Instrumentation) Development Environment*. Feb. 5, 2017. URL: http://www.ni.com/lwcvi/ (cited on p. 35).

[Par12] Particle Data Group. *Review of Particle Physics*. In: Physical Review D 86.1 (July 2012). DOI: 10.1103/PhysRevD.86.010001 (cited on p. 27).

[Pfa58] W. G. Pfann. *Zone melting*. Wiley series on the science and technology of materials. Wiley, 1958. URL: https://books.google.de/books?id=TMtTAAAAMAAJ (cited on p. 51).

[Pri16] M. Printz. *Analysis of n-in-p type silicon detectors for high radiation environment with fast analogue and binary readout systems*. PhD thesis. Karlsruher Institut für Technologie (KIT), 2016. URL: https://ekp-invenio.physik.uni-karlsruhe.de/record/48797 (cited on p. 28).

[Pyt14] Python Software Foundation. http://www.python.org. 2014 (cited on p. 35).

[Rau19] M. Rauch. *Summary of results of thermal measurements for the 2S Module*. Oct. 1, 2019. URL: https://indico.cern.ch/event/850567/contributions/3580870/attachments/1917806/3171688/MaxRauch_20191001.pdf (cited on p. 112).

[Rav06] F. Ravotti. *Development and Characterisation of Radiation Monitoring Sensors for the High Energy Physics Experiments of the CERN LHC Accelerator*. Presented on 17 Nov 2006. PhD thesis. Université Montpellier II, 2006. URL: https://cds.cern.ch/record/1014776 (cited on p. 25).

[Rie96] D. Riepe. *Naturalistic Tradition in Indian Thought*. Motilal Banarsidass Publishers (Pvt. Limited), 1996. ISBN: 9788120812932. URL: https://books.google.de/books?id=UZZGEhp8gasC (cited on p. 3).

[Sat+11] V. Satopaa et al. *Finding a "Kneedle" in a Haystack: Detecting Knee Points in System Behavior*. In: *2011 31st International Conference on Distributed Computing Systems Workshops*. June 2011, pp. 166–171. DOI: 10.1109/ICDCSW.2011.20 (cited on p. 38).

[Sch15] D. Schell. *Evaluation of Sensor Materials and Technologies for the Innermost Layer of the CMS Pixel Detector at the HL-LHC*. Master's thesis. Karlsruher Institut für Technologie (KIT), Aug. 19, 2015. URL: http://ekp-invenio.physik.uni-karlsruhe.de/record/48732 (visited on 01/08/2018) (cited on p. 18).

[Sch19] D. Schell. *Development of a Macro-Pixel sensor for the Phase-2 Upgrade of the CMS experiment*. PhD thesis. Karlsruhe Insitut für Technologie, Apr. 26, 2019 (cited on pp. 30, 52).

[Sze81] S. M. Sze. *Physics of Semiconductor Devices*. John Wiley & Sons, 1981. ISBN: 9780471056614 (cited on pp. 21, 22, 128, 130).

[SŽT11] L. Snoj, G. Žerovnik, and A. Trkov. *Computational analysis of irradiation facilities at the JSI TRIGA reactor*. In: Applied radiation and isotopes : including data, instrumentation and methods for use in agriculture, industry and medicine 70 (Dec. 2011), pp. 483–8. DOI: 10.1016/j.apradiso.2011.11.042 (cited on p. 54).

[Tan+18] M. Tanabashi et al. *Review of Particle Physics*. In: Phys. Rev. D 98 (3 Aug. 2018), p. 030001. DOI: 10.1103/PhysRevD.98.030001 (cited on pp. 23, 24).

[Tay11] L. Taylor. *CMS detector design*. Nov. 23, 2011. URL: http://cms.web.cern.ch/news/cms-detector-design (cited on p. 8).

[The08] The CMS Collaboration. *The CMS experiment at the CERN LHC*. In: Journal of Instrumentation 3.08 (Aug. 2008), S08004–S08004. DOI: 10.1088/1748-0221/3/08/s08004 (cited on pp. 6, 7).

[The20] The Tracker Group of the CMS Collaboration. *Evaluation of Silicon Sensor Properties for the Upgrade of the CMS Outer Tracker*. In: JINST (2020) (cited on p. 80).

[Uch+18] K. Uchida et al. *The CBC3 readout ASIC for CMS 2S-modules*. Tech. rep. CMS-CR-2018-017. Geneva: CERN, 2018. URL: https://cds.cern.ch/record/2312215 (cited on p. 14).

[WVK02] S. Watts, C. da Via, and A. Karpenko. *Macroscopic results for a novel oxygenated silicon material*. In: Nucl. Instrum. Methods Phys. Res. 485.1 (2002). Proceedings of the 5th International Conference on Large Scale Ap plications and Radiation Hardness of Semiconductor Detectors, pp. 153–158. ISSN: 0168-9002. DOI: https://doi.org/10.1016/S0168-9002(02)00547-8 (cited on pp. 79, 80, 100).

[Zeg07] V. Zeghbroeck. *Principles of Semiconductor Devices and Heterojunctions*. Prentice Hall PTR, 2007. ISBN: 9780130409041 (cited on pp. 22, 126).

[Zyk] Zyklotron AG, Germany. http://www.zyklotron-ag.de (cited on p. 57).

Acknowledgments – Danksagung

The present work would not have been possible without the support of many people, to whom I express my greatest thanks!

Die vorliegende Arbeit wäre ohne die Unterstützung zahlreicher Mitmenschen nicht möglich gewesen.

Danke Viki. Ich liebe dich. Danke Leni, du kleine süße Maus, auch wenn du mich die letzten Nächte wieder verprügelt hast im Schlaf. Ich hätte ihn gebrauchen können :)

Danke Mama, Papa, Lea-Pea-Hosali, mein Schwesterherz. Danke Oma.

Danke an meine Referenten, Thomas Müller und Ulrich Husemann, für die Möglichkeit meine Promotion am Institut für Experimentelle Teilchenphysik durchzuführen.

Danke Alex für die Betreuung seit dem Anfang meiner Masterzeit. Alex, Ulrich, Andreas, ihr habt dieses brilliante Jahrhundertwerk, diesen Meilenstein der Wissenschaft, in Form gebügelt. Danke dafür.

Danke an den berühmt-berüchtigten Competence Room in 316. Hier wurde Geschichte geschrieben. Danke Stefan, Daniel und Bene (auch wenn du's nie in 316 geschafft hast), Roland und Jan. Danke nochmal an meine Bachelor und Masterstudenten, die mir beim Messen geholfen haben: Justus, Jan und Umut. Danke an alle Mitglieder der ETP Hardware Gruppe, besonders den Technikern Felix, Tobias, Pia und Anita für's fixen und wire-bonden, und natürlich Frau Fellner.

Danke, Danke, Danke!

Declaration

I declare that the work in this dissertation was carried out in accordance with the requirements of the University's Regulations and that it has not been submitted for any other academic award. Except where indicated by specific reference in the text, the work is the candidate's own work. Work done in collaboration with, or with the assistance of, others is indicated as such.

Karlsruhe, January 2020

Marius Metzler